

**School of Physics  
and Astronomy**



Optical Properties and Exciton Dynamics of Colloidal  
Quantum Dots, Rods, and Platelets

Ali Naeem

PhD Thesis

24-02-2016

# Abstract

The linear optical properties and exciton dynamics of different semiconductor nanostructures have been studied. A model to describe the absorption spectra of cadmium selenide (CdSe) nanoplatelets (NPLs) has been developed, which allows the extraction of parameters relating to excitons confined within the thickness of the NPLs. Giant oscillator strength transitions (GOST) have been observed in NPLs with a lifetime limited dephasing of the ground state excitons at low temperature of about 1 ps, using transient resonant four wave mixing in heterodyne detection. The observation of the GOST effect has been affirmed by a decrease in the low temperature dephasing time with increasing NPL area. In addition, in cadmium selenide/cadmium sulphide (CdSe/CdS) quantum dot in rod (QDR) samples, dephasing dynamics at low temperature have been described by a Gaussian distribution of decay rates. Density dynamics have shown a fast initial decay followed by a signal rise attributed to an interplay between acoustic phonons and fast population dynamics related to the QDR fine structure. Density dynamics at longer delays have been attributed to an ensemble including both excitons and trions. The low temperature dephasing has been attributed to relaxation of excitons from a bright state to a lower lying dark state. Finally, a homebuilt scanning probe microscopy instrument has been modified to allow simultaneous optical and scanning probe imaging for the study of correlation between charge state and optical properties of nanostructures.

# Contents

|   |           |
|---|-----------|
| <b>Acknowledgements</b>                                     | <b>2</b>  |
| <b>Introduction</b>   | <b>2</b>  |
| <b>1 Background theory</b>                                  | <b>4</b>  |
| 1.1 Properties of semiconductors . . . . .                  | 4         |
| 1.1.1 Bulk CdSe . . . . .                                   | 5         |
| 1.1.2 Excitons . . . . .                                    | 6         |
| 1.1.3 Quantum confinement . . . . .                         | 8         |
| 1.1.4 Quantum wells . . . . .                               | 9         |
| 1.1.5 Giant oscillator strength . . . . .                   | 11        |
| 1.1.6 Quantum dots . . . . .                                | 13        |
| 1.1.7 Dielectric enhancement . . . . .                      | 15        |
| 1.2 Two level systems . . . . .                             | 17        |
| 1.3 Non-linear optics and FWM experiments . . . . .         | 18        |
| 1.3.1 The density matrix . . . . .                          | 18        |
| 1.3.2 Relaxation processes . . . . .                        | 19        |
| 1.3.3 Optical Bloch equations . . . . .                     | 20        |
| 1.3.4 Three beam FWM . . . . .                              | 22        |
| <b>2 Experiment</b>   | <b>25</b> |
| 2.1 Absorption and photoluminescence . . . . .              | 25        |
| 2.2 Three beam four-wave mixing . . . . .                   | 26        |
| 2.2.1 Heterodyne detection . . . . .                        | 26        |
| 2.2.2 Optical setup . . . . .                               | 29        |
| 2.2.3 Determination of photon echo amplitude . . . . .      | 34        |
| <b>3 Nanoplatelets</b>                                      | <b>37</b> |
| 3.1 Studied nanoplatelet samples . . . . .                  | 38        |
| 3.1.1 NPL synthesis and sample preparation . . . . .        | 39        |
| 3.2 Linear Optical Properties . . . . .                     | 43        |
| 3.2.1 Model for the nanoplatelet absorption . . . . .       | 44        |
| 3.2.2 Thickness Dependence . . . . .                        | 52        |
| 3.2.3 Size dependence . . . . .                             | 55        |
| 3.3 FWM measurements . . . . .                              | 66        |
| 3.3.1 Temperature dependent absorption . . . . .            | 67        |
| 3.3.2 Dephasing and density grating measurements . . . . .  | 68        |
| 3.3.3 Temperature dependence . . . . .                      | 72        |
| 3.3.4 Physical interpretation of FWM measurements . . . . . | 74        |

|          |   |            |
|----------|---|------------|
| 3.4      | Size dependent four wave mixing . . . . .           | 75         |
| 3.4.1    | Dephasing . . . . .                                 | 75         |
| 3.4.2    | Density dynamics . . . . .                          | 76         |
| 3.4.3    | Temperature Dependence . . . . .                    | 79         |
| <b>4</b> | <b>CdSe/CdS core shell quantum dots in rods</b>     | <b>82</b>  |
| 4.1      | Studied quantum dot in rod samples . . . . .        | 82         |
| 4.1.1    | Growth techniques . . . . .                         | 82         |
| 4.1.2    | Studied Samples . . . . .                           | 83         |
| 4.2      | Linear optical properties . . . . .                 | 84         |
| 4.3      | Exciton dephasing . . . . .                         | 85         |
| 4.3.1    | Dephasing fit function . . . . .                    | 86         |
| 4.3.2    | Dephasing fits and temperature dependence . . . . . | 89         |
| 4.4      | Exciton density dynamics . . . . .                  | 92         |
| 4.4.1    | Temperature dependent density dynamics . . . . .    | 93         |
| 4.4.2    | Initial dynamics . . . . .                          | 96         |
| 4.4.3    | Bright to dark relaxation time . . . . .            | 100        |
| 4.4.4    | Acoustic phonon oscillations . . . . .              | 102        |
| <b>5</b> | <b>Scanning probe microscope development</b>        | <b>108</b> |
| 5.1      | Background theory . . . . .                         | 108        |
| 5.1.1    | Atomic force microscopy . . . . .                   | 108        |
| 5.1.2    | Electrostatic force microscopy . . . . .            | 110        |
| 5.2      | Working principles of the instrument . . . . .      | 110        |
| 5.2.1    | Setup . . . . .                                     | 110        |
| 5.2.2    | Quartz tuning forks . . . . .                       | 111        |
| 5.2.3    | Electronics setup . . . . .                         | 114        |
| 5.3      | Developments of the instrument . . . . .            | 118        |
| 5.3.1    | Modifications to the electronics . . . . .          | 118        |
| 5.3.2    | Scanning probe microscopy tips . . . . .            | 126        |
| 5.3.3    | Home built positioner . . . . .                     | 130        |
| 5.3.4    | Quartz tuning fork holder . . . . .                 | 133        |
| 5.3.5    | Printed circuit board holder . . . . .              | 135        |
| 5.3.6    | Sample holder and preparation setup . . . . .       | 136        |
| 5.3.7    | Tip mounting setup . . . . .                        | 139        |
| 5.3.8    | Future work . . . . .                               | 140        |
|          | <b>Summary</b>                                      | <b>143</b> |
|          | <b>Bibliography</b>                                 | <b>143</b> |





# Acknowledgements

I would like to express my gratitude to my main supervisor, Prof. W Langbein, who has always pushed me to do my best. His knowledge and skill have always impressed me, and I would like to thank him for all the stimulating discussions. He has exemplified the amount of effort he has expected from me in the high quality of his own work, as well as giving his best effort to help me overcome difficult challenges in relation to my work. I would also like to thank my other supervisors Dr. M Elliott and Prof. P Borri for their guidance and support throughout my PhD.

I must also thank Dr. F Masia, who was my supervising postdoctoral researcher. He was always available to have often lengthy discussions to aid my understanding, and spent countless hours teaching and helping me during difficult experiments.

Finally, I would like to thank my girlfriend Natasha for her support, and her belief in me. My PhD, especially the final stages, were made much less daunting through her supportive and motivating words. Without her love and guidance, I would have found it substantially more difficult to reach this final stage.

# Introduction

The demonstration of the first laser in 1960 by Theodore Maimann opened up the possibility to probe matter with much higher intensities of light, making non-linear effects relevant. This was followed in the late 1960s by the development of pulsed laser, which are after further development since, are capable of producing pulses as short as several femtoseconds. A review of laser spectroscopy techniques can be found in [1].

Among the many types of structures that may be investigated using non-linear coherent spectroscopy techniques are colloidal nanostructures. Synthesis methods for quantum dots, as well as the more recently reported nanoplatelets (NPLs) [2], can readily be found in the literature (see for example, [3] wherein a growth procedure for core shell quantum dots in rods, or QDRs is described). Varying geometries and core shell configurations are accessible providing a large variety of nanostructures that can be investigated. Colloidal synthesis has the advantage of being more flexible than for example, epitaxial growth techniques in the sense that a crystalline substrate is not required for growth. Colloidally grown structures can easily be transferred between solution and otherwise manipulated more easily. Nanoplatelets with large lateral sizes, for example, can be allowed to "roll up" into tubes.

Semiconductor nanostructures can be utilized in numerous devices and applications, such as in quantum computing and photovoltaics to name a few. In order for these applications to be realized, the optical properties and exciton dynamics of these structures must be understood. In this work, we have used a transient resonant four-wave mixing (FWM) technique in heterodyne detection [4] [5] in order to study the exciton dynamics in CdSe nanoplatelets and CdSe/CdS core shell quantum dots in rods. We have also investigated the linear optical properties of nanoplatelets as a function of thickness and lateral size. Furthermore, we describe a combined scanning probe (SPM) and optical instrument intended for studying the correlation between the charge state and optical properties of nanostructures, which may be useful for sensing applications. Modifications have been made to a homebuilt SPM instrument to allow simultaneous optical and scanning probe measurements. The outline of the content is described below.

We begin by introducing the relevant background theory in chapter 1 before moving on to describing the experimental setups used in this work in chapter 2. Chapter 3 starts with the study of the linear optical properties of NPLs as function of both lateral size and thickness. FWM measurements are then presented in detail for a selected NPL sample which exemplifies the observed exciton dynamics. In the final sections of chapter 3, a size dependent study of the exciton dynamics is presented, affirming the physical interpretations made in the previous sections, and demonstrating the novel effects dependent on lateral size which have been predicted but not directly observed in the literature. We refer here to the observation of the

"giant oscillator strength" effect.

In chapter 4, a study of the exciton dynamics within QDR structures of varying core and shell sizes (and geometries) using the transient resonant FWM technique is presented.

In the final chapter of this work, chapter 5, the above mentioned combined SPM and optical instrument is described. The instrument has been modified, as described, to allow the study of the correlation between the charge properties and optical properties of nanostructures.

# Chapter 1

## Background theory

In this chapter, we present theory considered relevant to the subject matter of this work. We begin by discussing properties of semiconductor materials including the effects of quantum confinement. We then present the theory related to the experimental techniques used in this work under the general heading of 'Light Matter Interaction'. Insofar as there are a limited number of ways to differently describe well known concepts of physics, we make use of the content in cited works to aid us in describing relevant concepts herein. It is to be noted that the theory presented in this chapter is not claimed to be original work; formulas and figures are taken from the cited works as indicated.

### 1.1 Properties of semiconductors

In materials classified as insulators or semiconductors, the highest energy band that contains electrons is completely filled. This is referred to as the valence band. The next energy band up is known as the conduction band with a separation in energy known as the band gap  $E_g$  of the material. At a temperature  $T=0$  K, the conduction band is empty. A semiconductor material differs from an insulator in that the band gap is smaller. The distinction is not well defined, however band gaps above 3-4 eV are typically considered insulators. This is motivated by the thermal electron concentration in the conduction band, which for these band gaps leads to a conductivity low enough for these materials to be considered insulators. The band gap of semiconductor materials is typically 1 eV, for example the band gap of silicon (a semiconductor material) is around 1.1 eV at room temperature [6]. Due to the smaller band gap in semiconductor materials, a small number of electrons can be thermally excited into the conduction band, and allow the material to conduct electricity.

Pure semiconductor materials are known as intrinsic semiconductors. The electrical properties of a semiconductor material can be modified by adding impurities. Adding p-type impurities results in empty acceptor levels close to the top of the valence band, whereas adding n-type impurities results in empty donor levels close to the bottom of the conduction band [7]. The gap in energy between the acceptor (donor) levels and the valence (conduction) band is much smaller than the band gap of the intrinsic semiconductor causing electrons to easily become thermally excited into the acceptor level (conduction band) from the valence band (donor level) respectively. For example the energy gap between the acceptor level present as a result of the addition of boron to silicon and the valence band is approximately 0.05 eV,

much less than the band gap of silicon.

### 1.1.1 Bulk CdSe

The most stable crystal structure of CdSe is wurtzite, however zinc-blende CdSe can also be grown. Both of these crystal structures are shown in Fig 1.1. The hexagonal planes of the wurtzite structure have a stacking order of ABAB. The bonds between the atoms are coordinated tetrahedrally with each cadmium atom bonded to four selenium atoms and vice versa. The zincblende structure is characterized by a face-centered cubic lattice of Cd atoms arranged so that it interpenetrates a face-centered cubic lattice of Se atoms [8] as depicted in Fig 1.1 b). As in wurtzite, the bonds between the atoms are tetrahedrally coordinated.

This figure has been redacted by the author for copyright reasons

**Figure 1.1:** a) Sketch of wurtzite crystal structure [9], and b) sketch of zinc-blende crystal structure [10].

Let us now consider in general, the treatment of charge carriers in a periodic potential. Following the discussion in [11], wave packets described by Wannier-functions can be utilised when considering the motion of charge carriers influenced by an external field within a semiconductor material. These wave packets are formed using Bloch waves as given by:

$$\phi_{\vec{k}_0}(\vec{r}) = \sum_{\vec{k}} a_{\vec{k}} e^{i\vec{k} \cdot \vec{r}} u_{\vec{k}}(\vec{r}) \quad (1.1)$$

where a range of wavevectors  $\vec{k}$  is chosen about a wavevector value  $\vec{k}_0$  (see [11] for details of the choice of wavevector range). The change in energy of the wave packet under influence of a force  $\vec{F}$  can then be written as:

$$dE(\vec{k}) = \vec{F} \cdot \vec{v}_g dt \quad (1.2)$$

where  $\vec{v}_g$  is the group velocity of the wave packet which can most simply be expressed as:

$$\vec{v}_g = \frac{1}{\hbar} \frac{dE}{dk} \quad (1.3)$$

Noting also that we can write  $dE(\vec{k}) = \hbar \vec{v}_g d\vec{k}$  we obtain an expression for the external force:

$$\vec{F} = \hbar \frac{d\vec{k}}{dt} \quad (1.4)$$

Combining the above with the expression for group velocity yields

$$\vec{a} = \frac{1}{\hbar^2} \frac{\partial^2 E}{\partial k^2} \vec{F} \quad (1.5)$$

where  $\vec{a}$  is the acceleration of the wave packet. The above analysis elucidates the fact that charge carriers within the semiconductor crystal have an effective mass which is a tensor:

$$\frac{1}{m^*} = \frac{1}{\hbar^2} \frac{\partial^2 E}{\partial k_i \partial k_j} \quad (1.6)$$

where  $m^*$  is the effective mass and the indices  $i$  and  $j$  can be  $x$ ,  $y$  or  $z$ . In the effective mass approximation, electrons and holes in a periodic potential can be treated as having an effective mass given by Eq. 1.6 in a free potential. It should be noted that a hole is a quasi particle which represents the absence of an electron. An electron can be promoted to a higher energy level, leaving behind a hole which has the inverse mass, charge and energy of an electron. A consequence of the above expression is that the effective mass of an electron or hole can depend on the direction of movement. The effective mass approximation makes use of the fact that one may consider regions close to the band extrema only as these regions are most important, for example, for the optical properties of a material.

The band structure of semiconductors can be calculated using the tight binding approach in which the electrons are assumed to be tightly bound to their respective atoms or molecules. A limitation of this model however, is that in its simplicity it does not take into account interactions between electrons. One may resort to Green's function method or density functional theory to calculate the band structure of solids, both of which account for the many body problem of electron-electron interactions.

When the band structure of CdSe is examined, it can be seen that the minimum energy of the conduction band, and the maximum energy of the valence band are both located at the  $\Gamma$ -point of the Brillouin zone which makes CdSe a direct gap semiconductor. The 5s states of cadmium, and the 4p states of selenium are mixed resulting in  $sp^3$  hybridization. The top of the valence band is p-like, whereas the bottom of the conduction band is s-like.

The energy bands which will be considered in the following discussion can be seen in Fig 1.2 at the  $\Gamma$ -point close to the bandgap. These include the conduction band, and the three valence bands highest in energy at the  $\Gamma$ -point. The hole bands in order of increasing energy are labelled the heavy hole, light hole and the split off bands. It should be noted that the heavy hole (HH) and light hole (LH) bands do not have a splitting for zincblende crystal structure. For wurtzite however, there is a splitting between these bands due to the non-cubic unit cell with the c-axis asymmetry. A sketch of these bands is shown in Fig 1.4. The maxima and minima of the bands can be approximated as parabolic (and they are then called A, B and C bands) which allows us to approximate the dispersion relation close to these points as

$$E(\vec{k}) \approx E_0 + \frac{\hbar^2}{2m^*} \vec{k}^2 \quad (1.7)$$

### 1.1.2 Excitons

Light can be absorbed within a semiconductor material causing the transition of an electron from the valence to the conduction bands. The electron and the hole created as a result of this interband transition experience mutual Coulomb attraction. The Coulomb potential can be expressed as:

$$V_{\text{Coulomb}} = -\frac{e^2}{4\pi\epsilon_0\epsilon_r|\vec{r}_e - \vec{r}_h|} \quad (1.8)$$

This figure has been redacted by the author for copyright reasons

**Figure 1.2:** Band structure of wurtzite CdSe calculated using the local-density approximation in ref [12]. The dashed lines represent the band gap and the 4d states of selenium from other sources. The figure is taken from the Landolt-Börnstein database [13]

where  $e$  is the electronic charge, and  $\vec{r}_e$  and  $\vec{r}_h$  are the position vectors of the electron and hole respectively. The electron and hole can form a bound electron-hole pair which is a new quasi-particle known as an exciton. The above potential leads to a series of hydrogen like states below the bandgap of the material as depicted in Fig. 1.5 b).

In a direct gap semiconductor material, in the parabolic band approximation, we can consider the centre of mass (COM) motion of the exciton separately to the relative motion of the charge carriers [11]. A total wavevector for the exciton can be defined as  $\vec{K} = \vec{k}_e + \vec{k}_h$ ,  $M = m_e + m_h$  represents the COM mass. A dispersion relation for the excitons can then be written as:

$$E_x(n_B, \vec{K}) = E_g - R_y \frac{1}{n_B^2} + \frac{\hbar^2 \vec{K}^2}{2M} \quad (1.9)$$

where  $R_y$  is chosen to represent the exciton Rydberg energy defined as  $R_y = \frac{\mu}{m_0} \frac{1}{\epsilon_r^2} 13.6 \text{ eV}$ , wherein the reduced mass  $\mu = \frac{m_e m_h}{m_e + m_h}$  is utilized.  $n_B$  represents the principal quantum number of the exciton states depicted in Fig. 1.5 b). An exciton Bohr radius  $a_x$  can also be defined using the hydrogen Bohr radius  $a_B$  as expressed by:

$$a_x = a_B \epsilon_r \frac{m_0}{\mu} \quad (1.10)$$

Typically in semiconductor materials,  $R_y$  is much smaller than the band gap of the material. The exciton Bohr radius is here assumed to be large such that the



This figure has been redacted by the author for copyright reasons

**Figure 1.3:** Band structure of zincblende taken from [14]. For these calculations, the Fermi level was defined to be 0 eV.

exciton is extended over many unit cells allowing us to utilize the effective mass approximation [11] [15]. This type of excitons which are typical for semiconductor materials are known as Wannier-Mott excitons. On the other hand, tightly bound excitons are referred to as Frenkel excitons and are typically observed in molecular crystals and insulators [16]. Since these excitons are effectively restricted to one unit cell of the crystal (due to being tightly bound to a specific atom or molecule), they cannot be described in the effective mass approximation.

### 1.1.3 Quantum confinement

The small sizes of semiconductor nanocrystals result in the quantum confinement of the charge carriers within, leading to interesting size dependent characteristics. For example, the fluorescence wavelength of quantum dots varies with their size. Quantum confinement effects are typically observed when the size of the crystal concerned is similar to (or smaller than) the de Broglie wavelength of thermal motion in at least one direction. Assuming charge carriers are confined in a region of length  $\Delta x$ , the confinement energy can be written as

$$E_{QC} \approx \frac{\hbar^2}{2m(\Delta x)^2} \quad (1.11)$$

The two types of structures that we are concerned with are two dimensional (2D) quantum well like structures, and 0D quantum dots. 2D structures confine charge

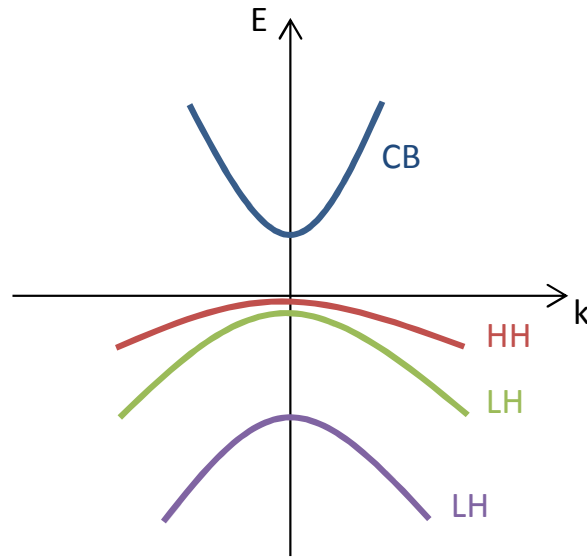


**Figure 1.4:** Sketch of the band structure of CdSe at the  $\Gamma$ -point close to zero energy. The conduction band, heavy hole band, light hole band and the split off band are shown as labelled.

This figure has been redacted by the author for copyright reasons

**Figure 1.5:** a) sketch depicting excitation of electron from valence to conduction band. b) exciton dispersion for direct gap semiconductor [11]

carriers in one dimension only, leaving them free in the other two thus the name. In 0D structures the particles are confined in all directions. The two properties of a material that are modified due to confinement are the density of states, and the energy of the charge carrier which is increased if the mass is positive (note that valence bands have negative masses).

#### 1.1.4 Quantum wells

One type of system studied in this work is thin sheets of CdSe. Due to their geometry (depicted in the sketch of Fig. 1.6), the confinement energy within the thickness is much larger than the confinement energy in plane, making these so called

nanoplatelets (NPLs) quantum well (QW) like. One can calculate the quantised energy levels within a QW by using the effective mass approximation and solving the Schrödinger equation. Because of the confinement in only one direction, chosen here as the  $z$ -direction, the part of the wavefunction of an electron or hole dependent on  $z$  can be separated. For the energy eigenvalues, we obtain the expression in Eq 1.12 below.

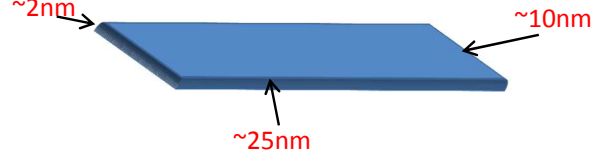


**Figure 1.6:** Sketch of geometry of nanoplatelets.

$$E(n, \vec{k}) = E_n + \frac{\hbar^2 \vec{k}^2}{2m^*} \quad (1.12)$$

where  $\vec{k}$  only contains the contribution in the  $x, y$  plane, and the last term above is derived from using plane wave solutions for the in-plane wavefunction. It must be noted that the solution given above is for an infinite potential well in which the  $z$  dependent wave function is zero outside of the QW thickness. For a finite potential well, the wave function will decay exponentially outside the well. The contribution due to the confinement is given by

$$E_n = \frac{\hbar^2 k_n^2}{2m^*} \quad (1.13)$$

where  $k_n = n\pi/d$  with  $d$  being the thickness of the QW.

The expected absorption spectrum for excitons in 2D systems is well explained in [17]. As outlined therein, the contribution to the absorption by the bound state is given by:

$$\alpha_B(\hbar\omega) = A_0 \sum_{i=1}^{\infty} \frac{2}{R_y a_x^2 \pi (i - 1/2)^3} \delta\left(\epsilon + \frac{1}{(i - 1/2)^2}\right) \quad (1.14)$$

where  $\epsilon = \frac{(\hbar\omega - E_g)}{R_y}$ . Noting that the 2D Sommerfeld enhancement factor is given by

$$S_{2D}(\epsilon) = \frac{2}{1 + e^{-2\pi/\sqrt{\epsilon}}} \quad (1.15)$$

we can write the continuum state contribution as given in Eq. 1.16 below.

$$\begin{aligned} \alpha_C(\hbar\omega) &= A_0 \int_0^{\infty} dE \frac{S_{2D}(E)}{2\pi R_y a_x^2} \delta(E + E_g - \hbar\omega) \\ &= A_0 \frac{\mu}{m_0 \pi \hbar^2} S_{2D}(\epsilon) \end{aligned} \quad (1.16)$$

The total absorption for an ideal 2D exciton is then given by the sum of the contributions in Eq. 1.14 and Eq. 1.16, as given in Eq. 1.17 below.

$$\alpha(\hbar\omega) = \frac{A_0}{2\pi R_y a_x^2} \left[ 4 \sum_{i=1}^{\infty} \frac{1}{(i - 1/2)^3} \delta\left(\epsilon + \frac{1}{(i - 1/2)^2}\right) + S_{2D}(\epsilon) \right] \quad (1.17)$$

It should be noted that  $\epsilon = (\hbar\omega - E_g)/R_y$ . The above expression for the ideal 2D exciton absorption reveals a four fold enhancement of the exciton binding energy over bulk. If we further consider the effect of finite linewidth  $\gamma$  of exciton transitions in a 2D system (as outlined in [17]), we obtain the following expression for the 2D exciton absorption:

$$\alpha(\hbar\omega) = \frac{A_0}{2\pi R_y a_x^2} \left[ 4 \sum_{i=1}^{\infty} \frac{1}{(i - 1/2)^3} \frac{\gamma}{\left[ \epsilon + \frac{1}{(i-1/2)^2} \right]^2 + \gamma^2} + \int_0^{\infty} \frac{d\epsilon'}{\pi} \frac{\gamma S_{2D}(\epsilon')}{(\epsilon' - \epsilon)^2 + \gamma^2} \right] \quad (1.18)$$

Exemplary absorption spectra for 2D excitons obtained from Eq. 1.17 and Eq. 1.18 (taken from [17]) are shown in Fig. 1.7

This figure has been redacted by the author for copyright reasons

**Figure 1.7:** a) absorption spectrum of 2D exciton with zero linewidth. b) absorption spectrum of 2D exciton with finite linewidth [17].

The excitons created due to inter-band transitions in QWs have a binding energy 4 times higher (for ideal 2D systems) than in bulk due to the confinement forcing the electron and hole closer together. Excitonic transitions are clearly evident in the absorption spectra of QWs where they appear at energies equal to the band gaps minus the binding energy of the excitons. A series of spectra [30] owing these absorption features is shown in Fig. 1.8. The NPL structures studied in this work also clearly exhibit the same features. Many examples of absorption spectra of NPLs of different thickness and lateral size can be found in ref [2][18][19][20][21][22][23][24][25][26][27][28][29].

### 1.1.5 Giant oscillator strength

Oscillator strength is a dimensionless quantity that represents the likelihood of an energy level transition due to interaction with a photon. We here present a series of steps that will lead us to the definition of the phenomenon known as Giant Oscillator Strength. These illustrative steps are taken from ref [31] in which a more complete discussion can be found.

For an unbound 1s exciton in 2D, the oscillator strength per unit cell can be described as:

$$f_x^{2D} = \frac{V_{\text{cell}} f_0 |\phi_{1s}^{2D}(0)|^2}{L_z} \quad (1.19)$$

for an infinite potential quantum well. Here  $f_0$  is the dipole matrix element,  $V_{\text{cell}}$  is the volume of a unit cell, and  $\phi_{1s}^{2D}(r_e - r_h)$  is the wavefunction of the 2D exciton which describes the in-plane electron-hole relative motion. The quantity  $|\phi_{1s}^{2D}(0)|^2$

This figure has been redacted by the author for copyright reasons

**Figure 1.8:** Absorption and PL spectra for NPLs of different thicknesses taken from ref [30]. The heavy and light hole absorption peaks can clearly be seen in all spectra. The heavy hole absorption peaks are the lowest energy features.

represents the probability of both the electron and hole being found in the same unit cell. In ref [31], this quantity is noted to be:

$$|\phi_{1s}^{2D}(0)|^2 = 2/A_x \quad (1.20)$$

with  $A_x$  being the area covered by the 2D exciton. The total oscillator strength is simply given by the oscillator strength per unit cell times the total number of unit cells which we here call  $N$ :

$$F_x^{2D} = N f_x^{2D} \quad (1.21)$$

$N$  can also be written as the total volume of the quantum well divided by the unit cell volume  $AL_z/V_{\text{cell}}$  where  $A$  represents the total quantum well area. We can then write down the total oscillator strength more explicitly as

$$F_x^{2D} = \frac{AL_z}{V_{\text{cell}}} V_{\text{cell}} f_0 \frac{2}{A_x} \frac{1}{L_z} = f_0 2 \frac{A}{A_x} \quad (1.22)$$

Let us now write the oscillator strength for an exciton bound in plane. The center of mass (COM) of an exciton that is bound in plane can be said to cover a number of unit cells which can be represented by  $N_{Bx}$ . We also define an area over which the center of mass of a confined exciton can move as  $A_{Bx}$ .  $A_{Bx}$  is clearly the area of  $N_{Bx}$  unit cells. We can then intuitively write the oscillator strength per impurity atom as

$$F_{Bx}^{2D} = f_0 \frac{A_{Bx}}{A_x} \quad (1.23)$$

This result is the effect known as "giant oscillator strength". The oscillator strength of excitons can be limited by scattering, and we can incorporate the coherence area

of the exciton  $A_{coh}$  into the above expression and write

$$F_{Bx}^{2D} = f_0 \frac{A_{coh}}{A_x} \quad (1.24)$$

It should be noted that in most materials,  $A_{coh}$  and  $A_{Bx}$  are similar. The oscillator strength thus scales with the area over which the center of mass of the exciton is extended. This means that in the NPL samples mentioned earlier, NPLs of a larger lateral size should exhibit faster radiative decay times due to Giant Oscillator Strength Transitions, or GOST. The term "giant" is used to signify the increase in the oscillator strength of transitions that results from varying confinement.

### 1.1.6 Quantum dots

In quantum dots (QD), charge carriers are confined in all three directions which makes them zero-dimensional (0D) structures. Due to the confinement, a QD has discrete quantised energy levels. Let us consider spherical dots, in which the wave function can be expressed in spherical polar coordinates due to the symmetry. For a potential which is only dependent on the radius, it is possible to separate the wave function into radial and angular parts, and subsequently solve the radial Schrödinger equation in order to find the energy eigenvalues [15].

$$E_{nl} = \frac{\hbar^2}{2m^*} \frac{C_{nl}^2 \pi^2}{R_0^2} \quad (1.25)$$

The values  $C_{nl}$  depend on the potential profile and are different for different values of the quantum numbers  $n$  and  $l \leq (n-1)$ . In experiments involving QDs it is important to consider the excitonic fine structure since the energy splitting between states, as well as states being either dark or bright, will effect the results of optical measurements. Note that optical transitions to dark states are not allowed by the quantum mechanical selection rules, whereas for bright states, optical transitions are allowed. Ekimov *et al* [32] present calculations of the energy level structure in spherical CdSe quantum dots. Since the conduction band minimum has s-like character, the angular quantum number for the lowest electron state in the conduction band is 0. The electrons have a spin of 1/2. The lowest hole states in the valence band have a total angular momentum of 3/2. The lowest excitonic state therefore has a total angular momentum  $F = 3/2 \pm 1/2$ , and the projection of  $F$  can have eight different values namely  $m_F = 0, \pm 1$  for  $F = 1$ , and  $m_F = 0, \pm 1, \pm 2$  for  $F = 2$ . The lowest excitonic state in CdSe QDs is therefore eightfold degenerate.

Several effects contribute to lifting the degeneracy of the aforementioned levels. Firstly, the crystal field splitting, which is the result of the hexagonal crystal structure in wurtzite dots, splits the light and heavy hole bands. Note that the total angular momentum  $j = 3/2$  of the holes in the valence band has the four projections  $\pm 3/2$  (heavy hole) and  $\pm 1/2$  (light hole) along the c-axis. These results are presented in ref [33]. The heavy-light hole band splitting is approximately 25 meV in bulk for wurtzite CdSe. CdSe QDs can be non-spherical which also results in the lifting of degeneracy. Finally, the electron hole exchange interaction which is enhanced due to the confinement causes further fine structure splitting. With all these effects taken into account, the fine structure comprises five separate excitonic energy levels with one for each magnitude of the possible values of  $F$  and  $m_F$ .

According to [35], the expected fine structure level ordering for perfectly spherical QDs is the one depicted in Fig 1.9 a). The size dependent fine structure for

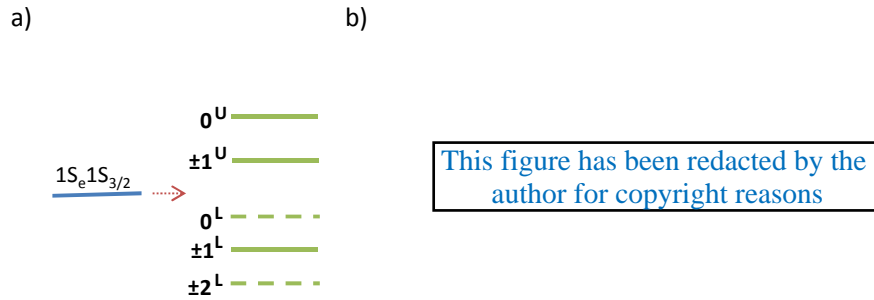


**Figure 1.9:** A sketch of the exciton energy level ordering is presented in a). The superscript L represents the lower branch due to the heavy hole exciton, and U represents the upper branch due to the light hole exciton. The calculated size dependent fine structure taken from ref [34] is presented in b). The energies are relative to the  $1^L$  state.

different shape types from this work is shown in Fig 1.10. Similar calculations are also presented in the work of Nirmal *et al* [36]. A comparison of the size dependent fine structure from experiments and theoretical calculations is given in ref [34]. The band structure from ref [34] is displayed in Fig 1.9 b). Good agreement between the experimental and theoretical values is reported. In both figures, the energy levels represented by dashed lines are dark states, whereas the solid lines represent bright state. Bright (dark) states have a non-zero (zero) dipole moment of the optical transition, respectively. Size dependent non-sphericity of the dots is taken into account in all the above mentioned works.

CdSe QDs with a CdS shell which is rod shaped have been studied herein. The CdS shell grows over the core asymmetrically so that the core is located towards one end of the rod. The edges of the valence and conduction bands are at different energies in these two materials. The difference in the energies of the corresponding bands between two materials is known as the band offset. In bulk, the low temperature CdSe bandgap is 1.84 eV, whereas for CdS it is 2.58 eV. The difference in the band gap is mainly due to the valence band offset. Calculations in [37] show that the band alignment between the materials depends on the strain between the core and the shell. In ref [38], [39] for strained CdSe/CdS superlattices the conduction band offset was found to be 0.15 eV. However in ref [40] it was reported to be in the range  $\pm 0.25$  eV for small core shell nanocrystals. This offset is therefore not well known at present and seems to be comparable to the energy shift due to strain as well as quantisation energies due to confinement.

Structures in which the band alignment is such that the conduction and valence band offsets have opposite sign are known as type-I. In these structures the electrons and holes are confined within the core. Due to the band alignment of CdSe/CdS core shell dots, the hole is confined within the core with a barrier of about 0.8 eV, while the electron, which is also lighter, has a barrier below 0.25 eV. The electron wave function can thus extend into the shell. These structures have been referred to in the literature as quasi type-II or type-I $_{\frac{1}{2}}$ . The hole confinement dominates the exciton confinement, and the electron is bound by the Coulomb interaction.

This figure has been redacted by the author for copyright reasons

**Figure 1.10:** The size dependent excitonic fine structure for CdSe quantum dots [35]. a) spherical dots, b) oblate dots with an ellipticity parameter  $\mu$  of -0.28, c) prolate dots with  $\mu = 0.28$ , and d) using an effective size taking into account size dependent non-sphericity.

In ref [41], the excitons in the dot in rod structures are still expected to approximately retain spherical symmetry with only a small leakage into the rod like shell of the electron wavefunction. This means that we can expect the exciton fine structure to be similar to spherical core shell dots. When the CdS shell is added to the QDs, the ordering of the energy levels is expected to stay the same, but the splitting between levels is expected to decrease due to the reduced electron hole overlap and thus exchange interaction. Measurements on core shell systems with small cores [41][42] indicate a dark bright splitting of approximately 2 meV. The dark bright splitting of core shell dots for different conduction band offsets is calculated by the group of Shabaev *et al* [43].

### 1.1.7 Dielectric enhancement

Colloidally grown nanostructures typically have their surface covered by ligands, and are in a medium with a low dielectric constant. There is therefore a large mismatch between the dielectric constant inside, and the dielectric constant outside the nanostructure. Let us recall that electric field strength is inversely proportional to the dielectric constant in a material. This means that if the electric field between two charges extends outside of a nanostructure, the total field strength will be greater due to the lower dielectric constant outside the nanostructure. As a result, the



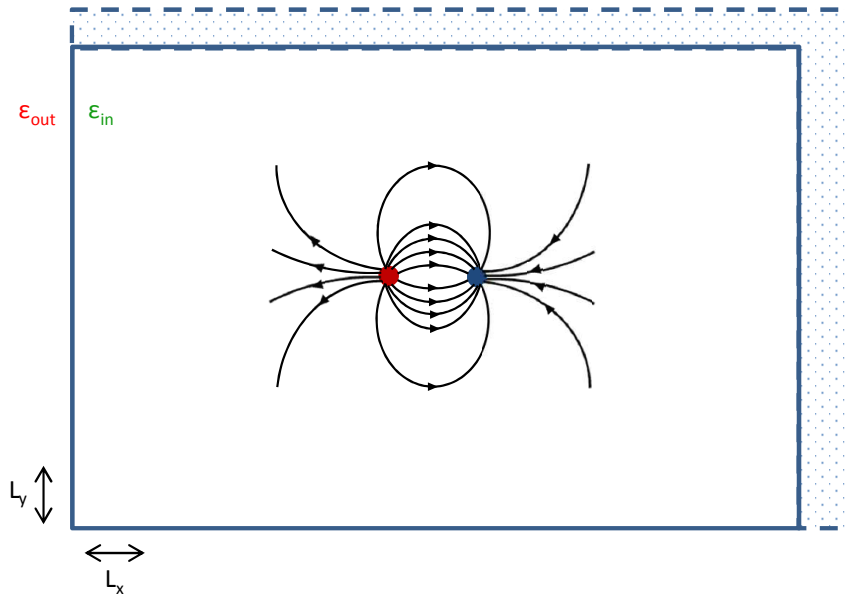


**Figure 1.11:** The figure illustrates that the effect of a change in lateral dimensions of the NPL does not impact significantly on the amount of dielectric enhancement if the exciton Bohr radius is smaller than the lateral dimensions. The dashed lines and the dotted region indicate an NPL with a larger lateral size.  $\epsilon_{out}$  represents the dielectric constant outside the NPL, and  $\epsilon_{in}$  represents the dielectric constant inside the NPL, with  $\epsilon_{out} < \epsilon_{in}$ .

binding energy of, for example, excitons in such a nanostructure will also be greater. This effect is known as dielectric enhancement.

The amount of dielectric enhancement will of course depend on the geometry of the nanostructure. For example, if the exciton Bohr radius within a structure is much smaller than the spatial dimensions of the structure, this effect will be reduced compared to a case in which one of the nanostructure dimensions is comparable to the Bohr radius of excitons. The NPL samples mentioned earlier have a thickness much smaller than their lateral size which means that dielectric enhancement will contribute to the change in exciton binding energy with changing thickness. Dielectric screening means that the exciton binding energies in NPLs will be larger than what is expected for ideal 2D systems, in other words more than 4 times larger than the exciton binding energies in bulk (see section 1.1.4).

On the other hand, for NPLs of a fixed thickness, dielectric enhancement will not impact significantly on the change in binding energy due to a change in lateral size. This assumes of course that the lateral size is larger than the exciton Bohr radius. In ref [16], calculations of binding energy as a function of different outside dielectric constants are presented for a range of NPL thicknesses. Unsurprisingly, the data in ref [16] show an increase in binding energy with a decrease in the outside dielectric constant with a more pronounced change for the thinner NPLs (see, for example, figure 2b of ref [16]).

## Light-matter interaction

The semiclassical picture of light matter interaction is suited to describing most of the experiments discussed in the present work. In this approach, matter is treated

quantum mechanically, and the classical description of electromagnetic radiation is used. Absorption and stimulated emission can be well described, while spontaneous emission is outside this treatment and is taken into account using phenomenological decay constants.

In this section, the essential theory required for an understanding of the three beam FWM experiments presented will be covered. In the experiments, we probe the semiconductor nanostructures with light of a frequency resonant with the ground state exciton. Ignoring the fine structure, we can treat this process as the interaction of light with a two level system. In the ensemble measurements performed in the present work, the light interacts with many similar two level systems simultaneously.

We begin our treatment by considering a simple two level system interacting with light. We then move on to considering the interaction of light with an ensemble of inhomogeneously broadened two level systems, and present the theory behind three beam FWM experiments which allow us to measure population decay, and dephasing times in these semiconductor nanostructures.

## 1.2 Two level systems

We start by considering a system with two energy levels with energies  $E_a$  and  $E_b$ , which interact with light of frequency  $\omega$ . We use  $a$  to refer to the ground state, and  $b$  to refer to the excited state of the system. The treatment of the two level system present below is described in further detail in [44] which has been utilized herein. In order to understand the behaviour of a two level system in the presence of light, we solve the time-dependent Schrödinger equation :

$$\mathcal{H}\Psi = i\hbar \frac{\partial \Psi}{\partial t} \quad (1.26)$$

The Hamiltonian can be split into two parts, the first part for the system in the absence of light, and a second part which represents the light matter interaction:

$$\hat{\mathcal{H}} = \mathcal{H}_0(\vec{r}) + \mathcal{H}_{int}(t, \vec{r}) \quad (1.27)$$

The general solution to the time-dependent Schrödinger equation for a two level system is given by:

$$\Psi(\vec{r}, t) = c_a(t) \psi_a(\vec{r}) \exp\left(\frac{-iE_a t}{\hbar}\right) + c_b(t) \psi_b(\vec{r}) \exp\left(\frac{-iE_b t}{\hbar}\right) \quad (1.28)$$

Substituting this into (1.26), allows the determination of the equations of motion for the coefficients  $c_a(t)$  and  $c_b(t)$ .

$$\begin{aligned} \dot{c}_a(t) &= -\frac{i}{\hbar} \left( c_a(t) \langle a | \mathcal{H}_{int} | a \rangle + c_b(t) \langle a | \mathcal{H}_{int} | b \rangle e^{-i\omega_0 t} \right) \\ \dot{c}_b(t) &= -\frac{i}{\hbar} \left( c_b(t) \langle b | \mathcal{H}_{int} | b \rangle + c_a(t) \langle b | \mathcal{H}_{int} | a \rangle e^{-i\omega_0 t} \right) \end{aligned} \quad (1.29)$$

Where  $\omega_0$  is defined as the resonant frequency of the two level system  $\frac{E_b - E_a}{\hbar}$ . The interaction hamiltonian can also be expressed in matrix form as follows:

$$\mathcal{H}_{ij}(t) = \int \psi_i^* \hat{\mathcal{H}}_{int}(t) \psi_j d^3\vec{r} \equiv \langle i | \hat{\mathcal{H}}_{int}(t) | j \rangle \quad (1.30)$$

In order to solve the above equations, we must first define the interaction term of the hamiltonian. For an electron of charge  $e$  in the dipole approximation we have  $\hat{\mathcal{H}}_{int}(t) = e\vec{r} \cdot \vec{\mathcal{E}}(t)$ , wherein  $\vec{\mathcal{E}}(t)$  relates to a time dependent electric fields. Choosing the direction of polarisation for the electric field to be in the x-direction allows us to rewrite the interaction hamiltonian more simply as:

$$\hat{\mathcal{H}}_{int}(t) = \frac{ex\mathcal{E}_0}{2} (e^{i\omega t} + e^{-i\omega t}) \quad (1.31)$$

Taking note of the definition of the dipole matrix element  $\mu_{ij} \equiv -e \langle i | x | j \rangle$ , we can express the interaction matrix elements as:

$$\mathcal{H}_{ij}(t) = -\frac{\mathcal{E}_0}{2} (e^{i\omega t} + e^{-i\omega t}) \mu_{ij} \quad (1.32)$$

Since the dipole moment is an odd parity operator, its diagonal components are zero (if the states have a defined parity). Note that the definition of the dipole matrix elements implies that  $\mu_{21} = \mu_{12}^*$ . By defining the quantity known as the Rabi frequency  $\Omega_R = |\mu_{ab}\mathcal{E}_0/\hbar|$ , we can rewrite equations 1.29 in the following way:

$$\begin{aligned} \dot{c}_a(t) &= \frac{i}{2}\Omega_R (e^{i(\omega-\omega_0)t} + e^{-i(\omega+\omega_0)t}) c_b(t) \\ \dot{c}_b(t) &= \frac{i}{2}\Omega_R (e^{-i(\omega-\omega_0)t} + e^{i(\omega+\omega_0)t}) c_a(t) \end{aligned} \quad (1.33)$$

In our experiments, we use strong light fields of frequencies resonant with the two level systems we want to probe ( $\omega \approx \omega_0$ ). We can therefore exclude the terms with frequency  $\omega - \omega_0$  assuming  $\omega - \omega_0 = 0$ . We can also make use of the rotating wave approximation in which the high frequency terms, the terms with frequency  $\omega + \omega_0$ , are ignored. Over a long enough time scale, the contribution of these high frequency terms is negligible. Solving the resulting coupled differential equations leads to the following solution:

$$\begin{aligned} c_a(t) &= \cos \frac{\Omega_R}{2} t \\ c_b(t) &= i \sin \frac{\Omega_R}{2} t \end{aligned} \quad (1.34)$$

The probability of an electron being in state  $a$  is given by  $|c_a(t)|^2 = \cos^2\left(\frac{\Omega_R}{2}t\right)$ , and similarly for state  $b$  the probability is given by  $|c_b(t)|^2 = \sin^2\left(\frac{\Omega_R}{2}t\right)$ . In the presence of strong electromagnetic fields resonant with the two level transition, the probabilities of occupation of the two states oscillate in time. This coherent superposition of the two states is known as Rabi oscillations which occur at the Rabi frequency  $\Omega_R/2\pi$ .

## 1.3 Non-linear optics and FWM experiments

### 1.3.1 The density matrix

In the experiments presented in this thesis, measurements are acquired on an ensemble of sample structures. These can be likened to an ensemble of inhomogeneously broadened two level systems. Such an ensemble of systems must have a long and

complicated wave function. It is therefore preferable to consider the statistical properties of the ensemble which can be measured. One has to therefore introduce the density matrix formalism which describes a system as a mixture of the states of many two level systems. The density matrix (which relates to properties observed over many repetitions of the experiment) is defined as:

$$\rho_{ij} = \begin{pmatrix} \rho_{bb} & \rho_{ba} \\ \rho_{ab} & \rho_{aa} \end{pmatrix} = \sum_k P_k \begin{pmatrix} |c_{b,k}|^2 & c_{b,k}c_{a,k}^* \\ c_{a,k}c_{b,k}^* & |c_{a,k}|^2 \end{pmatrix} \quad (1.35)$$

Where  $P_k$  is the probability of system number  $k$  being in the state  $\Psi_k = c_{a,k}\Psi_a + c_{b,k}\Psi_b$ . Examination of the density matrix elements reveals that the diagonal components are the probabilities of occupation of the two states. The off-diagonal elements represent a coherent superposition of the two states. In other words, they are related to the polarization created in the sample. The evolution of the statistical properties of the system is described by the Liouville variant of the Schrödinger equation :

$$i\hbar\dot{\rho} = [\hat{\mathcal{H}}, \rho] \quad (1.36)$$

### 1.3.2 Relaxation processes

When considering how an ensemble of two level systems will evolve after excitation, we must understand the relaxation processes that can occur within these systems. There are two different types of relaxation that must be considered. The longitudinal relaxation rate refers to the decay of the population in the upper state, or more generally towards its equilibrium. A system in its excited state can spontaneously emit and return to the ground state, and as a result interrupt the Rabi oscillations. The longitudinal relaxation rate is usually denoted as  $1/T_1$ .

The transverse relaxation rate  $1/T_2$  is related to any of the dephasing processes that can occur within a medium. Any process which does not effect the population of the excited state, but alters the phase of the wavefunction, contributes to the dephasing rate but not to the population decay. Such processes may comprise, for example, nearly elastic collisions with phonons in a solid which conserve the population in the excited state, but cause the phases to become randomized. The relaxation rate due to population conserving processes is referred to as the pure dephasing rate  $1/T_2'$ . The following relationship between these different reates can be expressed:

$$1/T_2 = 1/2T_1 + 1/T_2' \quad (1.37)$$

In order to include the effects of these damping processes into our treatment of ensembles of two level systems, we must incorporate them into the Hamiltonian. In addition to the unperturbed part  $\hat{\mathcal{H}}_0$  and the interaction part  $\hat{\mathcal{H}}_{int}$ , we can also include a relaxation Hamiltonian term  $\hat{\mathcal{H}}_R$ . The approximation we will use, makes use of the phenomenological relaxation rates described above and approximates the relaxation Hamiltonian in the following way:

$$\begin{aligned} [\hat{\mathcal{H}}_R, \rho]_{bb} &= -\rho_{bb}/T_1 \\ [\hat{\mathcal{H}}_R, \rho]_{ba} &= -\rho_{ba}/T_2 \end{aligned} \quad (1.38)$$

The dephasing time of an optical transition can be measured experimentally in different ways [45]. Since the homogeneous width of the spectral absorption is inversely proportional to the dephasing time, experiments can be performed either in the time domain to directly address the transient decay of the polarization induced by a pulsed coherent light field, or in the spectral domain by measuring the steady-state optical absorption lineshape. The response of the medium to the incident field depends on the field intensity. For example, only in the linear response limit (in the first order of the incident field amplitude), is the absorption lineshape Lorentzian with the half-width at half-maximum (HWHM) in angular frequency given by  $\gamma = 1/T_2$ .

One important limitation of linear spectroscopy in determining the homogeneous linewidth is inhomogeneous broadening within the measured ensemble. In the time domain, this translates into an additional decay rate  $1/T_2'$  of the macroscopic first order polarization. It is inversely proportional to the inhomogeneous spectral width, which is assumed to be Gaussian of standard deviation  $\sigma$  and FWHM  $\sigma\sqrt{8\ln 2}$ . In strongly inhomogeneously broadened systems (where  $\gamma \ll \sigma$ ), linear spectroscopy usually fails in measuring the dephasing time, with the exception of speckle analysis of the resonant Rayleigh scattering Ref [46] [47].

It is possible to isolate a single system from the inhomogeneous ensemble to circumvent the inhomogeneous broadening, and perform linear spectroscopy. However, resonant spectroscopy of this type is typically severely limited by background light, as the directional selection is not valid for single emitters of sizes smaller than the light wavelength. Background light can be suppressed by using for example, non-resonant excitation as in photoluminescence experiments [48] [49], and exciting the sample using an internal waveguide mode or at the Brewster angle. However, even a single emitter can show an effective inhomogeneous broadening due to a slow spectral diffusion during the required measurement time, which is much longer than the coherence time.

Experiments based on third order signals, such as FWM in the transient coherent domain after pulse excitation [1] or spectral hole-burning in the frequency domain with continuous wave excitation, allow one to overcome the presence of an inhomogeneous distribution. In these experiments, the signal can be detected free of background with appropriate selection in the direction and/or the frequency domain. The application of transient FWM to the measurement of the dephasing time in semiconductors was recently reviewed in ref [50] and [51].

### 1.3.3 Optical Bloch equations

In general, the electric polarisation  $P$  is a non-linear function of the electric field  $\mathcal{E}$ . When low intensities of light are being considered, the polarisation can be assumed to be linear with respect to  $E$ . However, higher intensities of light present the need to consider higher order terms. The electric polarisation can be written as:

$$P = \chi^{(1)}\mathcal{E} + \chi^{(2)}\mathcal{E}^2 + \chi^{(3)}\mathcal{E}^3 \dots \quad (1.39)$$

where  $\chi^{(n)}$  is the  $n^{th}$  order dielectric susceptibility of the material in question, and all parameters are functions of the wavevector  $k$  and the angular frequency  $\omega$  of the field. In four wave mixing (FWM) experiments, we consider the field generated by the third order polarisation.

In order to predict the behaviour of an ensemble of two level systems, we need to calculate the time evolution of the elements of the density matrix. We can relabel

the matrix elements to better reflect their physical meaning. The diagonal elements are related to the population of the two states, and the off-diagonal elements are related to the polarization. Assuming a closed system for the density, we can thus rewrite the density matrix as a power series in the field:

$$\rho_{ij} = \begin{pmatrix} \rho_{aa} & \rho_{ab} \\ \rho_{ba} & \rho_{bb} \end{pmatrix} = \begin{pmatrix} n & p \\ p^* & 1 - n \end{pmatrix} \quad (1.40)$$

The equations of motion describing the time evolution of the density matrix elements are referred to as the optical Bloch equations [1].

$$\begin{aligned} \dot{n} + n/T_1 + \frac{i}{\hbar} (\mathcal{H}_{ba} p^* - p \mathcal{H}_{ba}^*) &= 0 \\ \dot{p} + (i\Omega + 1/T_2) p + \frac{i}{\hbar} \mathcal{H}_{ba} (1 - 2n) &= 0 \end{aligned} \quad (1.41)$$

To solve the optical Bloch equations, the population  $n$  and the polarization  $p$  can be expanded in a Taylor series. The zeroth order terms in these series are zero since we assume states of a given parity. We must also note that for the initial conditions  $n = 0$  and  $p = 0$ , only the even powers of the population, and the odd powers for the polarization remain. Up to third order, the Optical Bloch Equations then become:

$$\begin{aligned} \dot{p}^{(1)} + (i\Omega + 1/T_2) p^{(1)} + \frac{i}{\hbar} \mathcal{H}_{ba} &= 0 \\ \dot{n}^{(2)} + \frac{1}{T_1} n^{(2)} + \frac{i}{\hbar} (\mathcal{H}_{ba} p^{(1)*} - p^{(1)} \mathcal{H}_{ba}^*) &= 0 \\ \dot{p}^{(3)} + (i\Omega + 1/T_2) p^{(3)} - 2 \frac{i}{\hbar} \mathcal{H}_{ba} n^{(2)} &= 0 \end{aligned} \quad (1.42)$$

Let us consider a two beam FWM experiment in which two pulses with wave vectors  $\vec{k}_1$  and  $\vec{k}_2$  impinge on the sample with a temporal delay of  $\tau_p$ . A grating can be created due to interference of the two pulses causing the second pulse to be diffracted in the direction  $2\vec{k}_2 - \vec{k}_1$ . The signal in this direction is related to  $p_{221}^{(3)*}$  meaning that for the density, only the  $\vec{k}_2 - \vec{k}_1$  component, namely  $n_{21}^{(2)}$ , needs to be calculated. The solution to equations 1.42 for the two beam FWM experiment with incident delta pulses (defined by the Dirac delta function  $\delta$ ) is calculated in [1], where this discussion is provided in much greater detail. These solutions are reproduced here as follows:

$$\begin{aligned} n_{21}^{(2)*} &= \frac{-\mu_{ba}^2}{\hbar^2} \mathcal{E}_2 \mathcal{E}_1 [\Theta(-\tau_p) \Theta(t) e^{-\frac{t}{T_1} + g\tau_p} \\ &\quad + \Theta(\tau_p) \Theta(t - \tau_p) e^{-\frac{(t-\tau_p)}{T_1} - g^* \tau_p}] \end{aligned} \quad (1.43)$$

$$\begin{aligned} p_{221}^{(3)*} &= i \frac{\mu_{ba}^3}{\hbar^3} e^{-i\omega t} e^{i(2\vec{k}_2 - \vec{k}_1) \cdot \vec{r}} \mathcal{E}_1 \mathcal{E}_2^2 \\ &\quad \times \Theta(\tau_p) \Theta(t - \tau_p) e^{-(g-i\omega)(t-\tau_p)} e^{-(g^*+i\omega)\tau_p} \end{aligned} \quad (1.44)$$

where  $\Theta$  is the Heaviside function. For convenience, we have also defined a quantity  $g = 1/T_2 + i\Omega$  where  $\hbar\Omega = E_b - E_a$ . For a particular positive pulse delay, the population decreases exponentially after the arrival of the second pulse with the longitudinal decay time  $T_1$ . The population also decreases exponentially with respect to  $\tau_p$ . Experimentally, if measurements where the signal is proportional to

the population are taken at a fixed time after the arrival of the second pulse, the population decay time can be recovered by varying  $\tau_p$ .

The expression for the third order polarization states that it is non zero only for positive pulse delays and positive times. The signal decays exponentially with the transverse time constant  $T_2$ . In the ensemble measurements we will be presenting, we expect there to be an inhomogeneous distribution of transition frequencies. We can consider a Gaussian distribution as follows [52]:

$$G(\Omega) = \frac{1}{\sigma\sqrt{2\pi}} \exp\left[-\frac{(\Omega' - \Omega)^2}{2\sigma^2}\right] \quad (1.45)$$

We then average the third order polarization over this distribution to include its effects in our discussion.

$$\int_{-\infty}^{+\infty} p_{221}^{(3)*}(\Omega', t) \frac{1}{\sigma\sqrt{2\pi}} e^{-\frac{(\Omega' - \Omega)^2}{2\sigma^2}} d\Omega' = p_{221}^{(3)*}(\Omega, t) e^{-\frac{\sigma^2(t - 2\tau_p)^2}{2}} \quad (1.46)$$

The above expression demonstrates that the third order polarization signal appears as a pulse at a time equal to twice the pulse delay, i.e a pulse delay after the arrival of the second pulse. This is known as a photon echo. In the FWM experiments presented in this thesis, we are concerned with this photon echo signal.

### 1.3.4 Three beam FWM

In the experiments to be presented, three beam FWM measurements are conducted on the nanostructures in question which allow the determination of the dephasing time, and the exciton lifetime in the same experiment. In a three beam experiment, three pulses spectrally centered at the same optical frequency as the transition we want to probe are used. The pulses can be described in terms of complex electric fields centered at time  $t = 0$ . We can introduce a delay between the three pulses, and label the delay times  $\tau_{12}$  and  $\tau_{23}$  where the later is the delay between the second and third pulse, and the former is the delay between the second and first pulse. The total electric field that impinges on the sample can therefore be written as:

$$\mathcal{E}(t) = \mathcal{E}_1(t) + \mathcal{E}_2(t - \tau_{12}) + \mathcal{E}_3(t - \tau_{13}) \quad (1.47)$$

Where  $\tau_{13} = \tau_{12} + \tau_{23}$ . In general the  $n$ -th order polarization in a three beam experiment is proportional to the electric field in the following way:

$$P^{(n)} \propto \mathcal{E}_1^{n_1} \mathcal{E}_1^{*m_1} \mathcal{E}_2^{n_2} \mathcal{E}_2^{*m_2} \mathcal{E}_3^{n_3} \mathcal{E}_3^{*m_3} \quad (1.48)$$

where  $n = (n_1, m_1, n_2, m_2, n_3, m_3)$ , and  $n_j$  and  $m_j$  are natural numbers including zero. The light due to this polarization is emitted in the direction  $l_1\vec{k}_1 + l_2\vec{k}_2 + l_3\vec{k}_3$  where  $l_j = n_j - m_j$ . In the previous section we noted that the direction in which the third order polarization signal is non-zero for positive pulse delay and positive times is  $2\vec{k}_2 - \vec{k}_1$  for the two beam case. Similarly, an echo signal for positive pulse delay for the three beam case corresponds to  $n_1 = 0, m_1 = 1, n_2 = 1, m_2 = 0, n_3 = 1, m_3 = 0$ . Thus the direction of emission will be  $\vec{k}_3 + \vec{k}_2 - \vec{k}_1$ . As before, the process can be understood in terms of a density grating being generated due to the polarization created by pulse 1 interfering with the field of pulse 2. The third pulse is then

diffracted into the direction of emission defined by  $\vec{k}_3 + \vec{k}_2 - \vec{k}_1$ . Pulse 3 is also referred to as the probe.

In order to gain an intuitive understanding of how the three beam experiment can allow us to probe the population decay time as well as the dephasing time, we can use the picture of the Bloch sphere. This description is traditionally used to explain the spin echo in magnetic resonance imaging, but is a very intuitive way to elucidate how the three beam experiment works. Lets start by defining the Bloch vector:

$$\vec{U} = U\vec{e}_1 + V\vec{e}_2 + W\vec{e}_3 \quad (1.49)$$

Where  $\vec{e}_j$  is a set of orthonormal basis. The components of the Bloch vector are defined in terms of the components of the density matrix.

$$\begin{aligned} U &= \rho_{ba}e^{i\omega t} + c.c. \\ V &= i\rho_{ba}e^{i\omega t} + c.c. \\ W &= \rho_{bb} - \rho_{aa} \end{aligned} \quad (1.50)$$

The component  $W$  of the Bloch vector is related to the population of the two levels, whereas the other two components are related to the polarization. If the Bloch vector points downwards, along the  $\vec{e}_3$  axis, it means that the probability of the lower state  $a$  being occupied is 1, and the probability of the upper state  $b$  being occupied is 0 (see Fig. 1.12 a)). This is the case before the arrival of any excitation pulses. After the arrival of the first pulse of pulse area  $\pi/2$  (where the pulse area is the product of  $\Omega_R$  and the temporal width of the pulse), a polarization is created within the sample which results in a coherent superposition of the two possible states. The Bloch vector now points along the  $\vec{e}_2$  axis in the  $\vec{e}_1\vec{e}_2$  plane as shown in Fig. 1.12 b). The  $\vec{e}_3$  component of the vector is zero. The phases of the two level systems within the inhomogeneously distributed ensemble are evolving independently. This results in the polarizations within the ensemble going out of phase as depicted in Fig. 1.12 c). During this time, dephasing occurs due to the homogenous broadening which is characteristic to the two level systems. The arrival of the second  $\pi/2$  pulse, a time  $\tau_{12}$  after the first, results in the  $W$  component of the vector acquiring a positive value with all other components being zero. A population has now been created in the upper state  $b$  which decays exponentially with time. The information about the phase evolution of the two level systems is still stored within the excitation (not depicted in Fig. 1.12).

The third pulse (also a  $\pi/2$  pulse) arrives at a time  $\tau_{23}$  after the second, and causes the Bloch vector to be in the  $\vec{e}_1\vec{e}_2$  plane once more. This time however, the vector points in the negative direction along the  $\vec{e}_2$  axis, but the direction in which the phases evolve remains the same as depicted in Fig. 1.12 e). After the arrival of the first pulse, the phases were allowed to evolve for a time  $\tau_{12}$ . It therefore takes the same amount of time for the phases to become realigned along the negative  $\vec{e}_2$  axis. Therefore, a time  $\tau_{12}$  after the arrival of the third pulse, a photon echo pulse is emitted (Fig. 1.12 f)). In this way, the effect on the dephasing due to inhomogeneous broadening is reversed, and the reduction of the amplitude observed in the photon echo compared to the original amplitude is due only to the processes that contribute to the homogeneous broadening. The time for which the phases have been allowed to evolve is  $2\tau_{12}$ , which means the dephasing time can be acquired by measuring the photon echo amplitude while varying the delay between the first and second pulses. Since the population is allowed to decay for a time  $\tau_{23}$ , measuring the photon echo amplitude versus  $\tau_{23}$  gives a measure of the population lifetime in the ensemble.



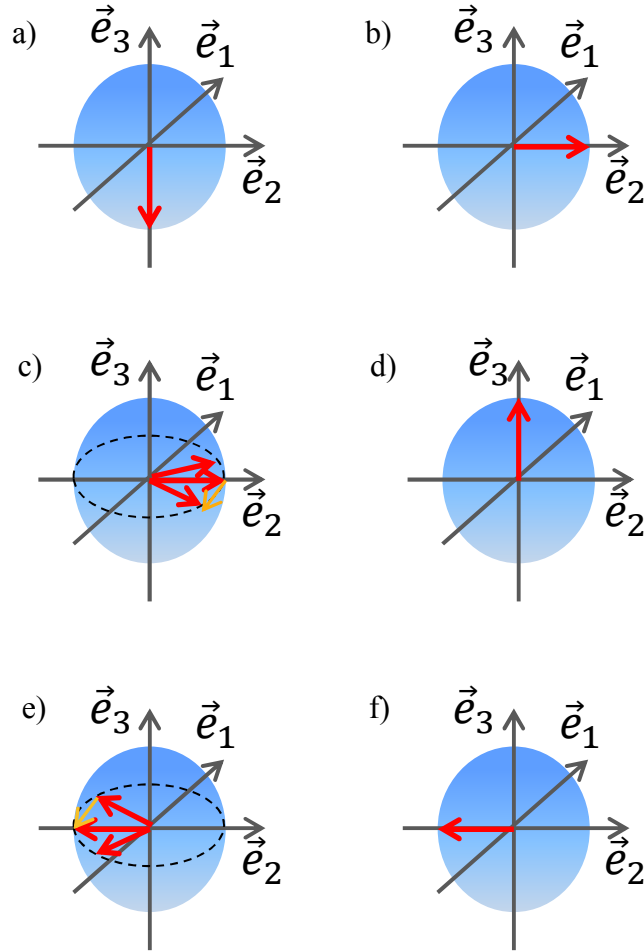


**Figure 1.12:** Sketch of the evolution of the Bloch vector upon sequential arrival of three pulses of  $\pi/2$  pulse area.

## Chapter 2

# Experiment

Content included in this chapter has been published in [45] and its supplement, the copyright for which belongs to the American Physical Society.

The experimental setups used for room temperature absorption and photoluminescence measurements, as well as the three beam FWM setup used for low temperature measurements are described herein.

### 2.1 Absorption and photoluminescence

A setup was developed to measure spatially resolved absorption and photoluminescence (PL) spectra for the purposes of conducting room temperature absorption and PL studies, as well as characterizing sample preparation methods for FWM experiments. An Olympus BX-50 transmission microscope was adapted to provide an input for a Ocean Optics HR4000 spectrometer. In order to achieve this, a home built eye piece adapter was constructed to fit into the opening for the right-hand side eye piece as shown in the images given in Fig. 2.1 a) and c). An internal thread within the opening of the eye piece adapter allowed an SMA multimode optical fibre to be inserted with the aid of a Thorlabs SM05 SMA adapter as shown in Fig. 2.1 c). The end of the optical fibre was positioned within the eye piece adapter at the intermediate image plane when the adapter was inserted into the eye piece opening. The opposite end of the optical fibre was connected to the spectrometer as shown in Fig. 2.1 b).

A Canon EOS 500D camera body was mounted onto the microscope with the sensor in the intermediate image plane to allow real time viewing of the sample on a computer using the EOS utility software. With the eyepiece adapter mounted, the microscope could be used to acquire spectral data through measurements made using the HR4000, while the use of the camera in real time allowed spatial selection of specific sample areas.

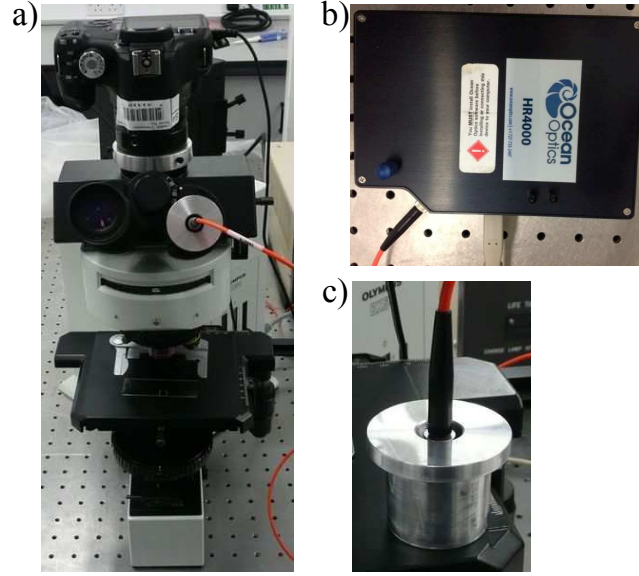


**Figure 2.1:** a) picture of the Olympus BX-50 transmission microscope showing the modifications that allow spatially resolved absorption and PL measurements.

## 2.2 Three beam four-wave mixing

In the following subsections, the optical setup used to acquire three beam FWM measurements at cryogenic temperatures is described. It should be noted that this setup is the same as the one used in our published work [45].

### 2.2.1 Heterodyne detection

An arrangement illustrating a heterodyne detection technique which can be used for transient FWM experiments without directional selection is shown in Fig. 2.2. Rather than detecting the signal intensity, the heterodyne technique allows the measurement of field amplitude and phase. The technique also allows for a much greater sensitivity, and specifically selectivity, as incoherent signals are not detected, and the detection frequency selects a specific wave mixing process. The heterodyne "amplification" also allows the effect of detector dark noise to be suppressed. The pulse train provided by a mode-locked laser source is divided into the excitation and reference pulses. The spectrum of the pulse train consists of series of longitudinal modes of frequencies separated by the repetition rate of the laser. The time period of the pulse train is  $T_p = 2\pi/\Omega_p$ , which means that a pulse arrives at times equal to integer multiples of  $T_p$ . The electric field  $E(t)$  of a pulse train can be written as a Fourier series [53].

$$E(t) = \mathcal{E}(t) + c.c., \quad \mathcal{E}(t) = e^{-i\omega_0 t} \sum_{n \in \mathbb{Z}} A_n e^{-in\Omega_p t} \quad (2.1)$$

The complex field  $\mathcal{E}(t)$  has the Fourier coefficients  $A_n$ . The frequency spectrum of a single pulse in the train is given by  $|A_n|^2$ . In the heterodyne experiment, the three excitation pulses are frequency upshifted by  $\sim 80$  MHz by acousto-optic

modulators (AOM). Let us denote the fields of the excitation pulses as follows:

$$\begin{aligned}
 \mathcal{E}_1(t) &= e^{-i(\omega_0+\Omega_1)(t+2\tau_{12}+\tau_{23})} \sum_n A_n^1 e^{-in\Omega_p(t+2\tau_{12}+\tau_{23})} + c.c. \\
 \mathcal{E}_2(t) &= e^{-i(\omega_0+\Omega_2)(t+\tau_{12}+\tau_{23})} \sum_n A_n^2 e^{-in\Omega_p(t+\tau_{12}+\tau_{23})} + c.c. \\
 \mathcal{E}_3(t) &= e^{-i(\omega_0+\Omega_3)(t+\tau_{12})} \sum_n A_n^3 e^{-in\Omega_p(t+\tau_{12})} + c.c.
 \end{aligned} \tag{2.2}$$

As discussed in section 1.3, we should expect the photon echo signal to arrive a time  $\tau_{12}$  after the last pulse. The above expressions imply that the pulse arrive in the order pump1, pump2, and finally the probe (for positive  $\tau_{12,23}$ ). For the purpose of this description, we have chosen the time at which the photon echo arrives to be  $t = 0$ . The shifts in frequency  $\Omega_{1,2,3}$  of the three pulses are due to the interaction with the acoustic wave within the AOMs. We note that we are concerned with the third order signal in the direction  $\vec{k}_s = \vec{k}_3 + \vec{k}_2 - \vec{k}_1$  which has the frequency:

$$\omega_s = \omega_0 + \Omega_3 + \Omega_2 - \Omega_1 = \omega_0 + \Omega_s \tag{2.3}$$

We assume that the pulse is close to Fourier-limited, and that its duration is much smaller than the period of the AOM  $2\pi/\Omega_{\text{AOM}}$ , i.e. that the spectral width  $\Delta$  of the envelope of  $|A_n|^2$  is much larger than  $\Omega_{\text{AOM}}$ . The complex fields of the reference and signal pulse trains are then given by

$$\mathcal{E}_r(t) = e^{-i\omega_0(t-\tau_r)} \sum_n A_n^r e^{-in\Omega_p(t-\tau_r)} \tag{2.4}$$

$$\mathcal{E}_s(t) = e^{-i(\omega_0+\Omega_s)t} \sum_n A_n^s e^{-in\Omega_p t} \tag{2.5}$$

The signal collected from the sample is combined with the reference signal at a 50:50 beam splitter. The amplitudes of the fields recieved by the two photodiodes are given by:

$$\mathcal{E}_{a,b} = \frac{\mathcal{E}_r \mp \mathcal{E}_s}{\sqrt{2}} \tag{2.6}$$

Each photodiode in the detection scheme generates a photocurrent proportional to the square of the incoming field, time integrated over the response time of the diodes  $T_{\text{det}}$ . In the balanced detection we measure the photocurrent difference  $I_d = I_b - I_a$ ,

$$\begin{aligned}
 I_d \propto \int_{T_{\text{det}}} dt (E_b^2 - E_a^2) &\propto \int_{T_{\text{det}}} dt E_r E_s = \int_{T_{\text{det}}} dt [ \\
 &e^{-i(2\omega_0+\Omega_s)t+i\omega_0\tau_r} \sum_{n,m} A_n^s A_m^r e^{-i(n+m)\Omega_p t+im\Omega_p\tau_r} \\
 &+ e^{-i\Omega_s t-i\omega_0\tau_r} \sum_{n,m} A_n^s A_m^{*r} e^{-i(n-m)\Omega_p t-im\Omega_p\tau_r} + c.c. ]
 \end{aligned} \tag{2.7}$$

where Eq. 2.4 has been used, and  $n$  and  $m$  are integers. The terms in Eq. 2.7 which are rapidly oscillating with a frequency  $2\omega_0$ , average to zero over the diode response time  $T_{\text{det}} \gg 2\pi/\omega_0$ . Conversely, terms oscillating at the frequency  $\Omega_s$  or smaller can be time resolved by the detector, i.e.  $T_{\text{det}} \gg 2\pi/\Omega_s$ . We note that the second term of the integrand in Eq. 2.7 has the oscillating part  $\sum_{n,m} e^{-i[\Omega_s+(n-m)\Omega_p]t}$ .

A lock-in amplifier can then filter the photocurrent oscillating at  $\Omega_s$  given by the terms for which  $m = n$ . Alternatively, the lock-in can filter the signal at sidebands of the laser repetition rate. To reach a detection frequency range of around one MHz providing low  $1/f$  noise and acoustics, and low radiation pickup, we can arrange that  $\Omega_s$  is only slightly larger than  $\Omega_p$  (e.g. 78 MHz and 76MHz respectively), and choose  $m = n + 1$ . The detected current can then be expressed as

$$I_d \propto e^{-i(\Omega_s - \Omega_p)t} \sum_n A_n^s A_{n+1}^{*r} e^{-in\Omega_p\tau_r} + c.c. \quad (2.8)$$

The integration over  $T_{\text{det}}$  does not appear in Eq. 2.8 since the oscillation with frequency  $\Omega_s - \Omega_p$  is slowly varying over  $T_{\text{det}}$  which means that the integrand can be treated as constant. Note that the terms being summed over  $n$  which multiply the term  $e^{-i(\Omega_s - \Omega_p)t}$  have the form of a Fourier series with the amplitude of the  $n$ -th Fourier component being  $A_n^s A_{n+1}^{*r}$ . The previously imposed condition that the spectral width of the laser pulses is much larger than the AOM frequency ( $\Delta \gg \Omega_{\text{AOM}}$ ) implies that we can approximate  $A_{n+1}^{*r}$  with  $A_n^{*r}$ . The resulting term  $A_n^s A_n^{*r}$  is therefore actually the  $n$ -th Fourier component of the cross-correlation  $C(\tau_r)$  between the complex reference and signal fields, meaning that the sum in Eq.(2.8) is  $C(\tau_r)$ . The selection of the different signals is accomplished by choosing the corresponding detection frequency  $\Omega_d$ , which is used as reference for a dual-phase lock-in measuring the photocurrent, and retrieving both real and imaginary parts of  $C(\tau_r)$ . The AOM frequencies, as well as the laser repetition frequency are mixed in order to provide the appropriate reference for the lock-in. The excitation pulses are detected at  $\Omega_d = \Omega_j - \Omega_p$  where  $j$  represents the three excitation pulses, and the FWM is detected at  $\Omega_d = \Omega_3 + \Omega_2 - \Omega_1 - \Omega_p$ . In choosing the AOM frequencies and the laser repetition rate appropriately we make sure that all these frequencies are well separated, typically by about a MHz. In the reported experiments we used  $\Omega_p/2\pi = 76.11$  MHz,  $\Omega_1/2\pi = 80$  MHz,  $\Omega_2/2\pi = 79$  MHz, and  $\Omega_3/2\pi = 78.6$  MHz. These result in a FWM detection frequency of  $(\Omega_3 + \Omega_2 - \Omega_1 - \Omega_p)/2\pi = 1.49$  MHz.

We assume that the pulses have a gaussian profile. We also know that the amplitude of the photon echo signal is dependent on  $\tau_{12}$  and  $\tau_{23}$ , decreasing with increasing  $\tau_{12}$  due to the dephasing, and decreasing with increasing  $\tau_{23}$  due to population decay. The pulse amplitudes can therefore be expressed as

$$\begin{aligned} A_n^s &= A^s(\tau_{12}, \tau_{23}) e^{-(n\Omega_p/\sqrt{2}\sigma)^2} \\ A_n^r &= A^r e^{-(n\Omega_p\sqrt{2}\Delta)^2} \end{aligned} \quad (2.9)$$

Carrying out the Fourier transform of the magnitude of the cross correlation  $C(\tau_r) = \sum_n A_n^s A_n^r e^{-in\Omega_p\tau_r}$  with the gaussian pulses yields

$$C(\tau_r) \simeq A^s(\tau_{12}, \tau_{23}) A^r e^{-(n\Omega_p\tau_r)^2/(\sigma^2 + \Delta^2)} \quad (2.10)$$

The above is a gaussian profile with a maximum occuring when the reference and signal pulses overlap in time, i.e.  $\tau_r = 0$ . The width of the gaussian profile is dependent on both the spectral width of the signal  $\sigma$ , and the laser  $\Delta$ . By scanning the reference delay around the photon echo at time  $\tau_{12}$ , one can map out the gaussian profile of the photon echo. This is known as the time resolved FWM (TR-FWM) signal, whereas integrating over the reference delay scan yields the time integrated FWM (TI-FWM) signal.

### 2.2.2 Optical setup

The following description is for the setup used in our recent work Ref [45]. The same setup was also used in the works [54] and [4]. The heterodyne detected three beam FWM data were taken using the experimental setup shown in Fig. 2.2. The setup is situated on an optical table with pneumatic legs in a temperature stabilized ( $\pm 1^\circ\text{C}$ ) room. To achieve passive optical phase stability over a period of seconds to minutes, the setup is encapsulated by a cover to reduce air convection. In order to produce the laser pulses to be used for the experiment, first an intracavity frequency doubled Nd:Yag laser, which is itself pumped by semiconductor diode lasers, is used to pump a Kerr-lens mode locked Ti:Sapphire laser. The signal beam from the Ti:Sapphire laser is first input into a optical parametric oscillator (OPO) in order to create a beam at 100-1600 nm which then undergoes intracavity frequency doubling. The result is a train of  $(100\pm 10)$ fs intensity FWHM pulses with a repetition rate of 76 MHz. This source can cover a wavelength range from 350 nm to  $1.6\mu$ . To compensate for the significant group velocity dispersion introduced by the optical components, especially the acousto-optical modulators (AOMs), we use a grating based pulse shaper. The pulse shaper is adjusted while observing the autocorrelation of the pulses, with an autocorrelator (AC) picking up the beam after an AOM. Some of the optical components must be exchanged depending on the wavelength range being used for the experiment. These include the beamsplitters (PBS, NPBS), the AOMs, the waveplates (QWP, HWP), and the photodiodes (PD). The elements specified in Table 2.1 refer to the wavelength range around 500 nm used in the present work.

A polarizing beam splitter (PBS) is used to split the beam with a splitting ratio adjustable with a half wave plate (HWP). This beam is further split by a non-polarizing beam splitter into beams 1 and 2. A beam expander (BE) changes the beam size by a factor of 3/10, and creates a Gaussian tail in all the three AOMs. The AOMs deflect a part of the beam by Bragg reflection with a frequency shift given by the carrier frequency of the electrical drive  $\Omega_{1,2,3}$ , and an amplitude given by the amplitude of the electrical drive. The amplitude of the drive is controlled via the analog input of the drivers, which is connected to the analog outputs of the lock-in amplifier, and a 5:1 voltage divider able to drive 40 mA current into 50 Ohm input impedance. After the AOMs, the beams are expanded by a factor of 10/3 back to their original size, and have a radial field amplitude  $\propto \exp(-(r/w_0)^2)$  with the radius  $r$ . This provides a sufficiently collimated beam with a Rayleigh length  $z_R = \pi w_0^2/\lambda$ . For  $w_0 = 1$  mm, as used in the setup, we have  $z_R = 6.3$  m for  $\lambda = 500$  nm which is much larger than the maximum path length difference in the setup of about 0.5 m to create the pulse delays. The BEs are also used to adjust the beam divergence. Beam 2 is passed over a delay line controlling  $\tau_{12}$  made of a linear stage and a corner cube retro-reflector and is then recombined with beam 1.

Corner-cubes are used since their reflection direction is opposite to the direction of the incoming beam independent of their tip-tilt. The divergence of the beam is  $\lambda/(\pi w_0) \approx 0.16$  mrad, and a typical tip/tilt accuracy of a linear stage is similar. This means that using a right-angle mirror, which has the advantage of simplicity and conservation of horizontal and vertical beam polarizations, would produce significant beam pointing errors. A motion of 150 mm corresponds to 1 ns pulse delay, and the unidirectional repeatability of the stages of  $1\mu\text{m}$  corresponds to 7 fs pulse delay which can sufficiently resolve the 100 fs pulse duration. The stages have an accuracy of  $100\mu\text{m}$  per 50 mm travel. The overlap between the photon echo and the reference pulse therefore has a maximum variation of about 1 ps per 200 ps delay. We have

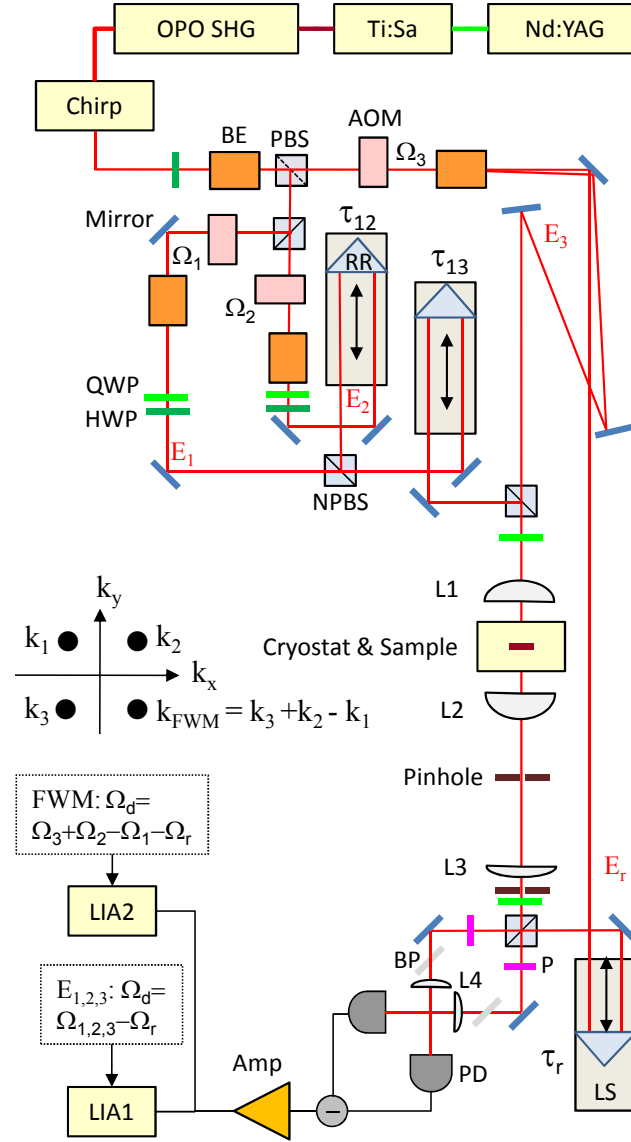


**Figure 2.2:** Sketch of the setup used to measure heterodyne detected four-wave mixing. Details of the components included in the setup are given in Table 2.1

[45]

found a relative scaling error of about  $10^{-3}$  between the stages, which we corrected. This resulted in a remaining variation of only about 300 fs, which is taken into account in the measurement procedure by scanning the reference delay over the nominal photon echo position, and fitting the photon echo amplitude as explained later. Both beams 1 and 2 are passed over another delay line controlling  $\tau_{13}$  with a total range of 2 ns.

The beam transmitted by the first PBS is split by an AOM into the deflected beam 3 (Probe), and the undeflected beam which is used as the reference beam. Beams 1, 2, and 3 are recombined by a NPBS and focussed by L1 onto the sample. The focused spot is of Gaussian profile with a spot size of  $r_0 = f\lambda/(\pi w_0) \approx 7 \mu\text{m}$  (intensity FWHM is  $r_0\sqrt{2\ln 2} \approx 10 \mu\text{m}$ ). The polarization of the three beams impinging on the sample is adjusted by waveplates. Beam 3 is horizontally linearly polarized after the PBS, and can be converted to circular polarization rotating the

QWP in front of L1. The polarization of beams 1 and 2 is adjusted using the QWP-HWP combinations in their beam paths.

The sample is mounted into a cold finger helium flow cryostat. The NPLs are embedded in a thin polymer film as described in section 3.1.1, which is squeezed between two 1 mm thick c-axis cut quartz plates providing a high thermal conductivity. The circular dichroism of quartz along the c-axis leads to the rotation of a linear polarization by about 27 degrees per mm, but does not affect a circular polarization.

The transmitted beam is imaged onto a pinhole by L2 which is blocking spurious reflections, then collimated by L3 and transmitted through a QWP which is converting the circular polarization back to linear polarization. The beam is then spatially selected using an iris aperture, to select the direction of the signal to be detected, and combined in a NPBS with the reference beam, which has an adjustable delay  $\tau_r$ . The reference beam is spatially and directionally overlapped with the signal beam. The two outputs are then projected onto horizontal polarization by polarizers, and detected by photodiodes. The beam size is adjusted to the active photodiode area by lenses, and the detected currents are equalized to within  $10^{-3}$  relative error by adjusting the rotation of Brewster plates, to suppress common mode noise of the reference beam.

The diodes are reverse biased with opposite voltages yielding opposite photocurrents, which are combined and amplified by a current preamplifier. At a current gain of  $10^5$  V/A the amplifier has an input current noise of  $2.1 \text{ pA}/\sqrt{\text{Hz}}$  and an input voltage noise of  $2.8 \text{ nV}/\sqrt{\text{Hz}}$ . At a frequency of 2 MHz and a diode and cable capacity of about 50 pF, the voltage noise corresponds to a current noise of  $1.8 \text{ pA}/\sqrt{\text{Hz}}$ , resulting in a total current noise of about  $3 \text{ pA}/\sqrt{\text{Hz}}$ . The 0.3 mW optical power of the reference beam per diode with a quantum efficiency of 0.75 at a wavelength of 500 nm creates a current of  $91 \mu\text{A}$  per diode, resulting in a total shot noise of  $\sqrt{2eI} = 7.6 \text{ pA}/\sqrt{\text{Hz}}$ . The electronic noise thus contributes less than 10% to the total noise, so that the detection is shot-noise limited. The current amplifier voltage is analyzed by a dual-channel lock-in amplifier at the frequency  $\Omega_d$  corresponding to the signal to be detected. The input voltage noise of the lock-in is between 4 and 80 nV/ $\sqrt{\text{Hz}}$  depending on the sensitivity setting, well below the preamplifier output noise of  $760 \text{ nV}/\sqrt{\text{Hz}}$ .

The lock-in reference frequency  $\Omega_d$  is created by analog mixing of the AOM driver reference outputs with +10dBm level and the laser repetition rate taken from the internal photodiode of the Ti:Sapphire laser. A sketch of the electronic layout is shown in Fig. 2.3, which provides reference frequencies for two lock-in amplifiers LIA1 and LIA2. The reference outputs of the AOM drivers are first passed through a 30dB attenuator and a 28dB amplifier to provide an additional isolation of about 56dB from back-propagating signals into the AOM driver which can create spurious signals. LIA1 is provided with the selectable reference frequencies of  $\Omega_1 - \Omega_p$ ,  $\Omega_2 - \Omega_p$ , or  $\Omega_3 - \Omega_p$  to detect the transmitted excitation pulses, which allows to determine the excitation pulse arrival times relative to the reference with 10 fs accuracy. These frequencies are created by mixing the low-pass filtered laser photodiode containing only the fundamental frequency, with one of the AOM reference outputs selectable via a switch, and subsequent low-pass filtering to select the difference frequency. LIA2 is provided with the reference frequency  $\Omega_3 + \Omega_2 - \Omega_1 - \Omega_p$  to detect the FWM. This is created by first mixing the reference outputs of AOM1 and AOM2 and low-pass filtering to provide the difference frequency  $\Omega_1 - \Omega_2$ . This frequency is then mixed with the reference of LIA1 and low-pass filtered. For a LIA1 reference



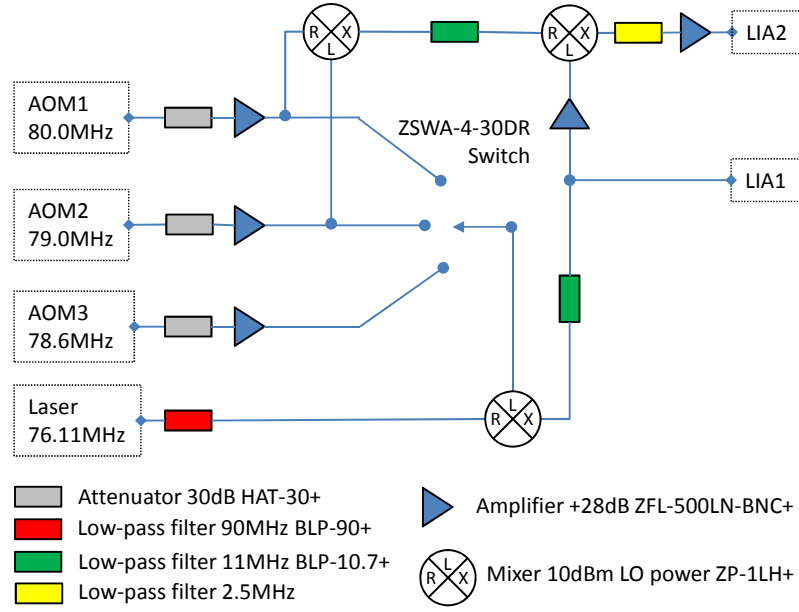


**Figure 2.3:** Sketch of the electronic mixing circuit to create the reference frequency  $\Omega_d$  for the lock-in. The listed components are from Mini-Circuits except the low-pass filter with 2.5 MHz cutoff frequency which is home built using a 3rd order Butterworth design.

of  $\Omega_3 - \Omega_p$  this provides the FWM reference frequency, allowing to measure  $\mathcal{E}_3$  and FWM simultaneously.

| Name    | Definition  | Make                                    |
|---------|---|---|
| Nd:YAG  | cw laser, frequency doubled, diode pumped Nd:YAG laser, power 10 W              | Coherent Verdi V10                      |
| Ti:Sa   | Kerr lens mode locked Ti:Sapphire laser, 100-150 fs pulse duration, power 1.5 W | Coherent Mira 900                       |
| OPO SHG | Optical parametric oscillator with intracavity frequency doubling, power 100 mW | APE OPO PP2                             |
| Chirp   | Grating based pulse shaper for spectral shaping and linear chirp compensation   | Home-build                              |
| QWP     | Achromatic quarter-wave plate   | Casix WPA1212 $\lambda/4$ 465-610 nm    |
| HWP     | Achromatic half-wave plate  | Casix WPA1212 $\lambda/2$ 465-610 nm    |
| PBS     | Polarizing cube beamsplitter  | Lambda Research Optics BPB-10SF2-550    |
| NPBS    | Non-polarizing broadband cube beamsplitter 45%/45%                              | Lambda Research Optics BNPB-10B-45R-550 |

| Name     | Definition  | Make  |
|----------|---|---|
| BE       | Beam expander to reduce beam size to AOM active beam diameter and adjust beam divergence, Galilean $f=-30$ mm and $+100$ mm | Casix MgF <sub>2</sub> coated Plano-convex and plano-concave lenses |
| AOM      | Acousto-optic modulator for frequency shifting and intensity control  | Intraaction ATM801-A1 & ME-802E6                                    |
| RR       | Retro-reflectors, enhanced aluminium first surface corner cubes   | Home-build from Edmund optics NT32-516                              |
| LS       | Linear stage to change pulse delay, range 150 mm for $\tau_{12}$ , 200 mm for $\tau_r$ , 300 mm for $\tau_{13}$             | Micos VT-80 2SM   |
| P        | Glan-Thompson polarizer, to define the detected linear polarization   | Casix PGM5210   |
| BP       | Brewster plate to fine-tune transmission by rotation to achieve balancing   | 1 mm thick glass plate cut from microscope slide                    |
| PD       | Si photodiode, 12 V bias, opposite polarity for current subtraction   | Home build using Hamamatsu S7836-01                                 |
| Amp      | Current amplifier, adjustable Gain  | Femto DHPA-100  |
| LIA      | Lock-in amplifier, reference frequency $\Omega_d$   | Stanford instruments SR844  |
| Pinhole  | Pinhole to remove scattered light   | 200 $\mu$ m diameter  |
| L1       | Lens to focus beams onto sample, Achromat $f=40$ mm MgF <sub>2</sub> coated   | Casix ACL0201   |
| L2       | Lens to image sample onto pinhole, Hastings triplet $f=25.4$ mm MgF <sub>2</sub> coated                                     | Edmund Optics 30120   |
| L3       | Lens to collimate beams from pinhole, plano-convex $f=100$ mm MgF <sub>2</sub> coated                                       | Casix PCX030  |
| L4       | Lens to reduce beam size on diodes, plano-convex $f=54$ mm MgF <sub>2</sub> coated  |   |
| Mirror   | Protected silver first surface mirrors $\lambda/10$ , 1" diameter   | Casix CAG0202   |
| Cryostat | Helium flow coldfinger cryostat, pancake-style  | Cryovac KONTI for microscopic measurements                          |
| AC       | Autocorrelator based on two-photon absorption   | APE Mini  |

| Name  | Definition                        | Make                        |
|-------|-----------------------------------|-----------------------------|
| Table | Optical table with pneumatic legs | Newport M-RS1000 and I-2000 |

**Table 2.1:** Elements shown in the sketch of the setup for heterodyne detected four-wave mixing in Fig. 2.2

The setup can be used in collinear geometry, with all beams having the same spatial mode, or in a box geometry indicated in Fig. 2.2. The former is used for FWM imaging of nanoparticles reported in ref [55] and [56]. However, the collinear geometry has the disadvantage that the detection is exposed to the directly transmitted excitation beams, which can give rise to saturation in the diodes which creates a spurious FWM signal at pulse overlap. When measuring in waveguides, the excitation powers are typically sufficiently small due to the small mode area so that this is not a significant problem. For thin polymer films however, the resonant absorbance is typically below 10% and the spot sizes are larger. In this case the box geometry can be used to select the non-linear signal directionally, suppressing the excitation beam power by typically 2-4 orders of magnitude. The box geometry has been used in the experiments reported in the present work, with a separation between the beams of about 3 mm, corresponding to an angle of about 4 degrees.

### 2.2.3 Determination of photon echo amplitude

To determine the photon echo amplitude for given delay times  $\tau_{12}$  and  $\tau_{13}$ , the reference delay  $\tau_r$  is stepped across the echo, and for each  $\tau_r$  the complex signal  $S$  is measured by the dual channel lock-in. Since the signal is phase sensitive, a phase drift during the measurement of  $\phi$  results in a factor on the signal amplitude of  $2 \sin(\phi/2)/\phi$ . To keep the signal reduction below 2%,  $|\phi| \lesssim 0.7$ , so that the motion of the reference delay stage has to be below  $\sim 50$  nm. To achieve this, we add a delay of about 100 ms after the stage motion is nominally completed before taking data. We use a 24dB filter with a time constant of  $\tau_{LI} = 10$  ms. Using this filter results in a rather symmetric temporal response function  $\propto t^3 \exp(-t/\tau_{LI})$  and a strong suppression of other components of frequency  $\Omega$  by  $((\Omega - \Omega_s)\tau_{LI} + i)^{-4}$ , reaching 8 orders of magnitude at 16 KHz frequency separation, sufficient to suppress the signals of the excitation pulses to below the noise floor. To create a nearly step-like response function suited to take the signal between the movements of  $\tau_r$ , the signal is read by the PC every 40 ms for 5 times, before the reference delay is moved again, and the average is used as a signal point  $S_m(\tau_r)$ .

The sampling of the photon echo is adjusted to resolve the photon echo and cover its width, which is given by the laser pulse duration or the inverse inhomogeneous broadening, whichever is longer. In the present case the inhomogeneous broadening is larger than the laser pulses, so that the measured echo is given by the autocorrelation of the laser pulse. We used 7 steps covering the range -300 fs to 300 fs centered at the nominal photon echo position  $\tau_e$ , which is

$$\tau_e = \begin{cases} \tau_{12} + \tau_{13} & \text{for } \tau_{12} \geq 0 \\ \tau_{13} & \text{for } \tau_{12} < 0 \end{cases}, \quad (2.11)$$

where  $\tau_{13}$  is  $\tau_{12} + \tau_{23}$ . Note that here, zero time is at the arrival of the first pulse. For  $\tau_{12} < 0$ , no echo is expected, but due to the finite pulse duration a part of the fields still arrive in the correct time ordering.

In order to allow for a large dynamic range in the delay  $\tau_{12}$  to be covered, we use a delay scan made of two sections. The region of small delays around pulse overlap is covered by  $N_{\text{lin}}+1$  equidistant points from  $\tau_{12}^s$  to  $\tau_{12}^e$  followed by  $N_{\text{log}} - 1$  points ending at  $\tau_{12}^{\text{log}}$  spaced by equal factors. Explicitly, at the  $n$ -th point we set

$$\tau_{12} = \begin{cases} \tau_{12}^s + (\tau_{12}^e - \tau_{12}^s) \frac{n}{N_{\text{lin}}} & \text{for } n \leq N_{\text{lin}} \\ \tau_{12}^e \exp\left(\frac{n - N_{\text{lin}}}{N_{\text{log}}} \log\left(\frac{\tau_{12}^{\text{log}}}{\tau_{12}^e}\right)\right) & \text{for } n > N_{\text{lin}} \end{cases} \quad (2.12)$$

where  $n = 0, 1, \dots, N_{\text{lin}} + N_{\text{log}}$ . The value of  $N_{\text{log}}$  is chosen so that the step size is approximately continuous across the junction of the two sections. The data shown in Fig. 2.4 was taken using  $\tau_{12}^s = -0.3$  ps,  $\tau_{12}^e = 1$  ps,  $N_{\text{lin}} = 26$ ,  $\tau_{12}^{\text{log}} = 250$  ps, and  $N_{\text{log}} = 113$ .

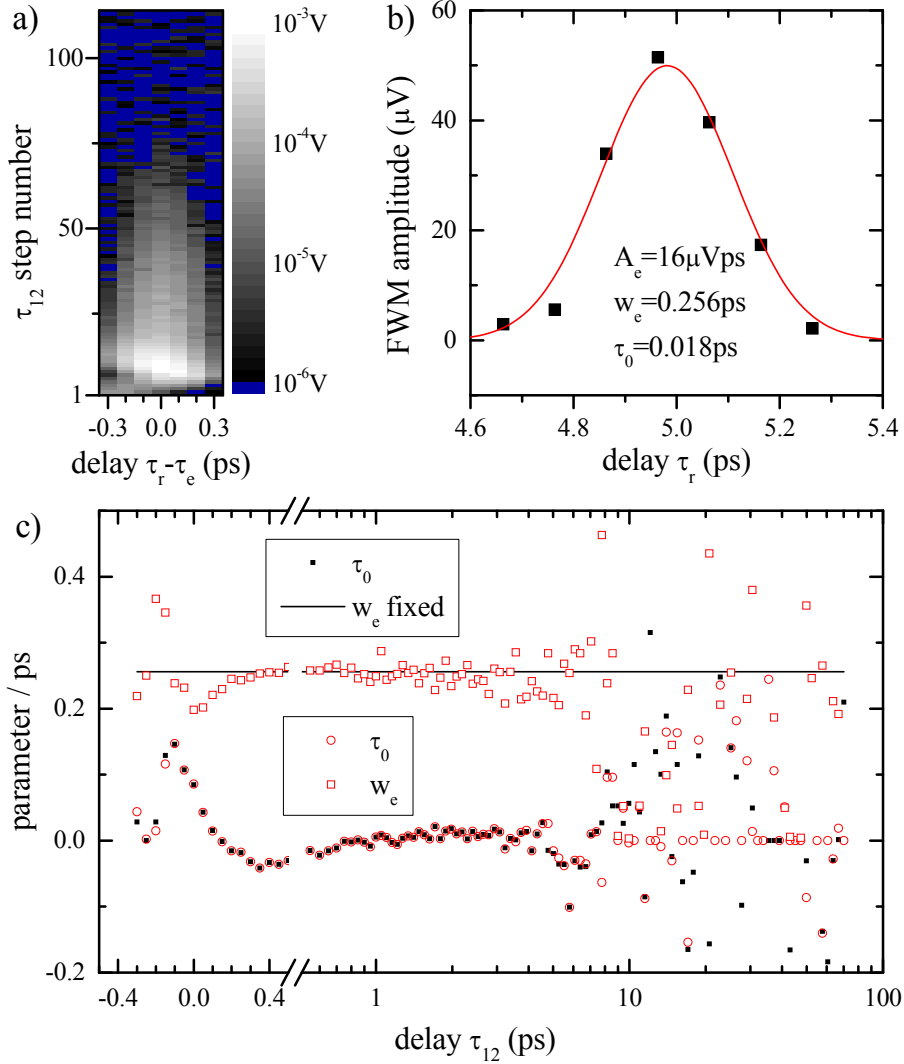


**Figure 2.4:** Photon echo analysis for the data shown in Fig. 3.23 a for  $T=5$  K. a) Measured FWM amplitude  $S_c(\tau_r)$  on a logarithmic grey scale as given, for  $\tau_{23} = 1$  ps as function of the  $\tau_{12}$  step number  $n$ . Values below  $10^{-6}$  V are shown as blue. b)  $S_c(\tau_r)$  for the step  $n = 40$ ,  $\tau_{12} = 1.982$  ps, with the Gaussian fit Eq.(2.14), resulting in the fit parameters as shown. c) Fitted relative position  $\tau_0$  (red open circle) and width  $w_e$  (red open square), and fitted  $\tau_0$  (black square) for constant  $w_e$  (black line), as function of  $\tau_{12}$ .

In order to retrieve the photon echo amplitude from  $S_m(\tau_r)$ , we first subtract an

offset  $S_0$  which is due to electronic cross-talk from the reference. Then, since the phase of the measured signal is relative to the reference, and the reference phase is not known, we analyze the amplitude of the signal. The noise component  $S_\sigma$  is superimposed on the signal  $S$  in  $S_m$ , and has an arbitrary phase. The corresponding amplitude square  $|S + S_\sigma|^2$  has a noise-averaged value of  $|S|^2 + 2\sigma^2$ , with the variance of  $\sigma$  of real and imaginary part of  $S_\sigma$ . We therefore calculate the corrected signal amplitude  $S_c$  from the measured data  $S_m$  using

$$S_c(\tau_r) = \pm \sqrt{\pm |S_m(\tau_r) - S_0|^2 \mp 2\sigma^2}, \quad (2.13)$$

where the sign is chosen to provide a real result. Both  $S_0$  and  $\sigma$  are determined using the histograms of the measured data in the absence of signal. For the data shown in Fig. 2.4, we found  $\sigma = 1.3 \mu\text{V}$ .

Example data of  $S_c$  are given in Fig. 2.4a.  $S_c(\tau_r)$  is then fitted by the Gaussian

$$S_e(\tau_r) = \frac{A_e}{w_e \sqrt{\pi/2}} \exp \left( -2 \frac{(\tau_r - \tau_e - \tau_0)^2}{w_e^2} \right) \quad (2.14)$$

with the echo area  $A_e$ , the relative center position  $\tau_0$ , and the width  $w_e$ . An example fit is shown in Fig. 2.4b. The width is expected to be independent of  $\tau_{12}$ , and therefore it is fixed to the average value found in a preliminary fit. The center position  $\tau_e$  is kept free within the limits of the data range to account for variations of the relative delay due to the limited positioning accuracy of the linear stages. An example of the fitted values for  $\tau_0$  and  $w_e$  is given in Fig. 2.4c). The systematic deviation at delays close to pulse overlap,  $\tau_{12} < 0.2 \text{ ps}$ , show the effect of the finite pulse width. The fitted amplitude  $A_e$  is used for further analysis, and is plotted in Fig. 3.23.

For delay scans probing the density dynamics which are not affecting the delay between photon echo and reference, which for the present setup are  $\tau_{13}$  scans, the reference delay stage is kept fixed and the measured signal  $S - S_0$  is directly used, given by the amplitude shown in Fig. 3.24. In this scan also the phase carries information during the passive phase stability of the setup, and can be used to identify changes of the effect of the density on the susceptibility, which can create both amplitude and phase changes of the transmitted  $\mathcal{E}_3$ . Measuring both  $\mathcal{E}_3$  and FWM at the same time and using an intensity modulation of  $\mathcal{E}_1$  instead of the interference of  $\mathcal{E}_1$  and  $\mathcal{E}_2$ , allows to reconstruct the phase of the nonlinear response [57] [58].

## Chapter 3

# Nanoplatelets

Content included in this chapter has been published in [45] and its supplement, the copyright for which belongs to the American Physical Society.

The use of semiconductor crystals with a thickness significantly smaller than the lateral dimensions is widespread in opto-electronic applications. Quantum wells, which confine charge carriers within their thickness, can be grown using techniques such as molecular beam epitaxy (MBE). More recently, semiconductor nanocrystals with thicknesses much smaller than their lateral dimensions have been grown by colloidal synthesis. Since colloidal growth of nanocrystals does not require a substrate and the resulting structures are in solution, these structures can more easily be manipulated for example, transferred between solutions. The shape of colloidal structures can also be adapted by suitable surface ligands during growth and other growth conditions.

Nanoplatelets (NPL) are colloiddally grown semiconductor crystals that have a thickness of only a few monolayers, much smaller than their lateral dimensions. In this work, we are concerned with CdSe NPLs. The first reference to CdSe "platelets" in the literature can be found in [2] wherein flat CdSe sheet like structure of a rectangular geometries are reported. Prior to this, magic sized nanocrystals with a disc shape were reported in [26] with an absorption spectrum similar to the expected spectrum for 2D structure. The observation of the 'giant oscillator strength transitions' (GOST) was predicted in [2]. Details of the growth of NPLs demonstrating the transition from 3D confinement (nanocrystal seeds) to 2D confinement as the NPLs grow was demonstrated in [18].

Much of the literature since the publication of [2], such as [25] has focused on the growth of NPLs. For example, photochemical etching resulting in wurtzite and zincblende CdSe NPLs is studied in [24], whereas synthesis of colloidal 'quantum disks' of CdSe is reported in [27]. A review of the growth techniques relating to 2D "nanoribbon" is given in [59].

Several publications exist which include theoretical studies relating to NPL structures. In [30], as well as a demonstration of growth of CdSe, CdS and CdTe NPLs, calculations of transition energies using the eight-band Pidgeon Brown model are presented. In this work, temperature dependent PL measurements also reveal short lifetimes giving an indication of GOST. On the other hand, [60] relates to tight-binding calculations including Coulomb interaction, self-energy corrections and enhanced electron hole interactions. Exciton binding energies up to several hundreds of meVs are reported as a result of image charge effects which relate to the dielectric mismatch with the surrounding medium. In addition, the electronic structure of NPLs has been studied theoretically by Hartree-renormalized k-p calculations including Coulomb interactions in [16] wherein time-resolved PL measurements as a

function of temperature are also presented.

Importantly for the subject of this work, [19] confirms QW like behaviour with confinement in one direction for NPLs, wherein time resolved PL and transient-absorption measurements are used. In this work, a high power pulsed laser is used to create a carrier population which reportedly cools in times of the order of picoseconds. In [61] however, in PL measurements on single NPLs, low temperature ultrafast lifetimes of about 200 ps have been reported. This work generally relates to the blinking behaviour of NPLs which is found to be similar to that of other nanocrystals. Another time-resolved PL study presented in [23] found that the measured PL emission from NPLs was due to relaxation from a bright state to a dark state with a splitting of a few meV.

A study conducted by Cherevko *et al* in [28] found that optical phonons are confined within the thickness of the NPLs when the exciton transitions are resonantly excited (in Raman spectroscopy). The observed phonon bands were not thickness dependent when the excitation was off-resonant. This result is highly relevant to the observation of phonon within this work as will be discussed in later sections. [29] and [62] on the other hand, are studies concerned with Auger recombination within NPLs. A review of the work in the literature can be found in [63].

Studies have also been carried out on stacked arrangements of NPL, for example in [64] which is a temperature dependent PL study, and [22] wherein CdSe NPLs form giant superparticles that organise themselves with the NPL surfaces perpendicular to the substrate. Studies have also appeared in the literature focused on core shell structure NPLs. For example, in [65] an atomic layer deposition technique is used to obtain CdSe/CdS NPLs. The growth of CdSe/CdS and CdSe/CdZnS core shell NPLs is reported in [21]. A quite unique study [66] also reports on quantum dot in plate structures. The beforementioned study [61] which is concerned with NPL blinking found the blinking to be suppressed upon the addition of a shell to NPLs. However, the most interesting application for core shell NPLs was recently in [67] wherein LEDs are demonstrated using CdSe/CdZnS core shell NPLs.

As is clear from the above, CdSe NPL structures have garnered much recent interest with an applications already demonstrated. However, there are no existing studies that use a technique like the three beam FWM technique used herein to probe the exciton dynamics within these structures in further detail.

### 3.1 Studied nanoplatelet samples

The studied NPL samples varied in lateral size as well as thickness. The different thicknesses were characterised by the energy of the heavy hole exciton ( $X_{hh}$ ) absorption peak (see the discussion in section 3.2.1 for the physical origin of the NPL absorption features). The details of all the investigated samples can be found in Table 3.1. Fig. 3.1 shows TEM images of all the studied samples. The data acquired from literature were digitized from the indicated published works. It can be seen from the TEM images of sample 120x60x1.4 that there is a variation in the lateral shape and lateral size. Their lateral size has therefore not been quantified in the same way as for the other NPL samples in Table 3.1. The information about the samples from literature is reported here as published in the original works except for the NPL thickness.

We have labelled the NPL thicknesses using a terminology that indicates a half-integer number of monolayers. In ref [30], the NPLs with the heavy hole exciton

| Thickness | $X_{\text{hh}}$ absorption (eV) | Name       | $L_x$ (nm)    | $L_y$ (nm) | Source    |
|-----------|---------------------------------|------------|---------------|------------|-----------|
| 6.5 ML    | 2.24                            | 35x8x2     | $35 \pm 5$    | $8 \pm 2$  | [2]       |
| 5.5 ML    | 2.42                            | 50x50x1.7  | 50            | 50         | [62]      |
|           | 2.41                            | 24x14x1.7  | $24 \pm 5$    | $14 \pm 3$ | This work |
|           | 2.41                            | 30x12x1.7  | $30 \pm 4$    | $12 \pm 3$ | This work |
|           | 2.41                            | 29x10x1.7  | $29 \pm 3$    | $10 \pm 1$ | This work |
|           | 2.42                            | 34x8x1.7   | $34 \pm 4$    | $8 \pm 2$  | This work |
|           | 2.42                            | 19x7x1.7   | $19 \pm 2$    | $7 \pm 1$  | This work |
|           | 2.44                            | 28x5x1.7   | $28 \pm 3$    | $5 \pm 1$  | This work |
|           | 2.47                            | 33x8x1.7   | $33 \pm 4$    | $8 \pm 1$  | This work |
|           | 2.44                            | 24x5x1.7   | $24 \pm 3$    | $5 \pm 1$  | This work |
|           | 2.44                            | 12x6x1.7   | $12 \pm 1$    | $6 \pm 1$  | This work |
| 4.5 ML    | 2.68                            | 120x60x1.4 | 120           | 60         | [68]      |
| 3.5 ML    | 3.13                            | 2x2x1.1    | 2 nm diameter | -          | [26]      |

**Table 3.1:** Properties of the investigated NPL samples.

absorption peak at 510 nm are reported to be 6 ML thick whereas in ref [16] they are reported to be 5 monolayers. In the work of Baghani *et al* [62], the authors claim that the surface of the NPLs is terminated with a layer of Cadmium atoms. Due to the presence of a Cadmium atom layer in addition to an integer number of CdSe layers, we label our 510 nm NPLs as 5.5 ML thick. We continue to use this labelling convention for the other thicknesses even though the works from which the data is taken report a thickness half a monolayer greater.

The data set includes NPLs of four different thicknesses. There are ten different samples which have a thickness characterised by a  $X_{\text{hh}}$  absorption energy of 2.42 eV (5.5 ML), nine of which form the subset of NPLs for which we have acquired data experimentally. This subset of nine NPL samples will be referred to as our size dependent subset (SDS) as it comprises NPLs of different lateral sizes as indicated in Table 3.1. Absorption spectra for all samples have been studied in the present work. PL spectra were studied for the SDS. FWM data was obtained on a subset of the SDS.

### 3.1.1 NPL synthesis and sample preparation

The NPLs in the SDS were synthesised by our collaborators [68]. The chemicals used in the synthesis included oleic acid, sodium myristate, cadmium nitrate tetrahydrate, cadmium acetate dihydrate  $\text{Cd}(\text{Ac})_2 \cdot 2\text{H}_2\text{O}$ , and technical grade 1-octadecene (ODE) purchased from Sigma-Aldrich. A 99.99% selenium (Se) mesh was purchased from STREM. In order to first synthesise the cadmium myristate ( $\text{Cd}(\text{myr})_2$ ), 0.02 mol (5 g) of sodium myristate was added to 150 mL of methanol. The mixture was stirred at room temperature for 60 minutes to dissolve the sodium myristate in the methanol. Separately, 3 g of cadmium nitrate is dissolved in 10 mL of methanol. This solution was added to the first, a white powder formed. The white powder was dried under vacuum for two days in order to completely remove the methanol. The NPLs were



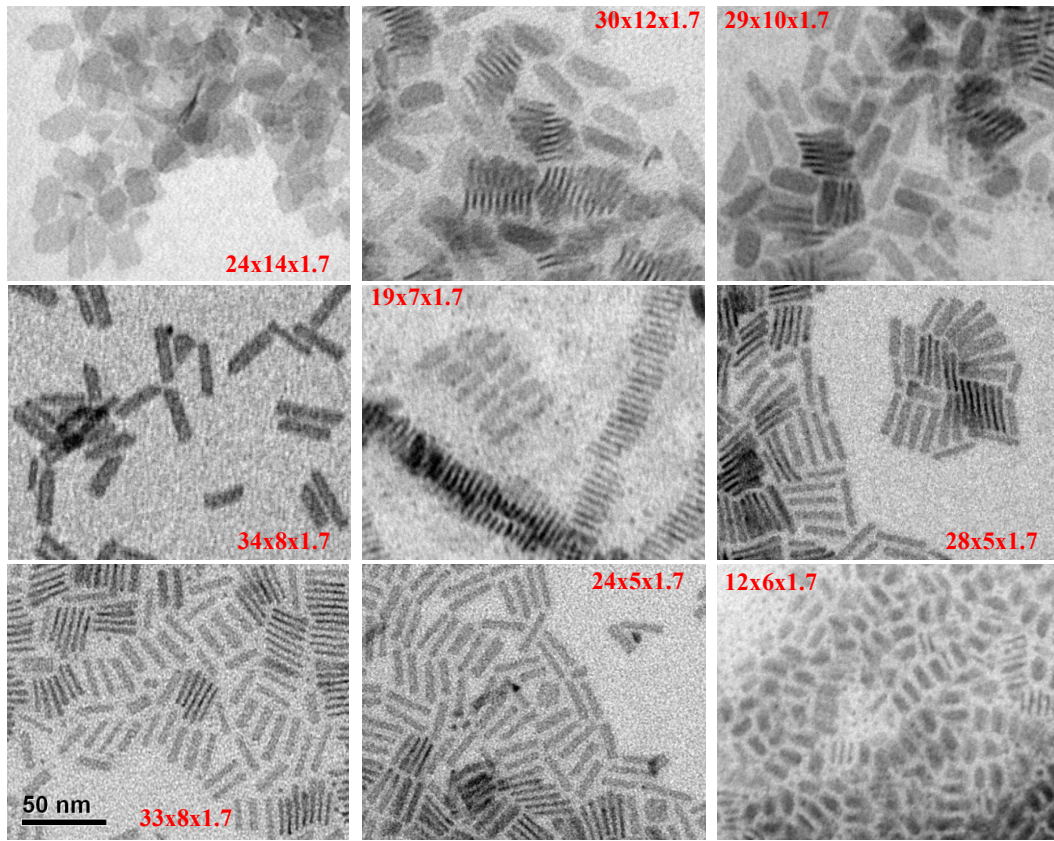


**Figure 3.1:** TEM images of selected NPL samples as labelled on equal scales (see scale bar in the bottom left image). The assigned sample names as given in Table 3.1 are indicated on the corresponding images. The 50 nm scale bar is applicable to all nine TEM images.

then synthesised using a method similar to the one reported by Ithuria *et al* in Ref [30].

To synthesize the samples, an amount of cadmium acetate 2.25 times larger, and a concentration of Se which is twice as large as that reported by Ithuria *at al* was used. A three-neck flask was used to mix 12 mg of Se, 170 mg of  $\text{Cd}(\text{myr})_2$  with a concentration of 0.3 mmol, and 15 mL of ODE and the resulting mixture was out-gased under vacuum. The mixture was then heated under argon flow to a temperature of 210°C. 90 mg of  $\text{Cd}(\text{Ac})_2$  were added as soon as this temperature was reached. The mixture was then heated to 240°C, and kept at this temperature for ten minutes before being allowed to cool down to room temperature. Selective precipitation was used to extract the NPLs from the resulting colloid which also contained spherical quantum dots. The resulting CdSe NPLs had a zinc-blende crystal structure which was determined when miscut silicon substrates were used to measure the X-Ray diffraction pattern on a drop-casted thin film of NPLs.

Measurements on colloidal structures can be taken in solution, or they can be deposited onto a transparent substrate for optical measurements. Colloidally grown structures therefore allow flexibility in terms of the way samples can be prepared for measurements. For the experiments on the NPL samples, the nanostructures needed to be homogeneously distributed on a transparent substrate to allow optical excitation and detection. It was important that the NPLs did not aggregate as

nanostructures being closer than approximately 10 nm may result in a change in the dynamics due to Förster-type interactions [64]. The samples also needed to be mounted in a way that would allow good thermal contact for low temperature measurements.

The studied samples were homogeneously dispersed in a polystyrene (PS) film for optical measurements probing their temperature dependent linear optical properties, and FWM. These were prepared as follows. We started from an NPL colloid in toluene. Two of the samples were delivered in hexane, which was exchanged with toluene by allowing the hexane to evaporate under a nitrogen atmosphere so that roughly half the volume of the original colloid remained, and replacing the lost volume with toluene. This evaporation and solvent replacement process was carried out at least five times. The starting point was the nanostructures dissolved in toluene in varying concentrations.

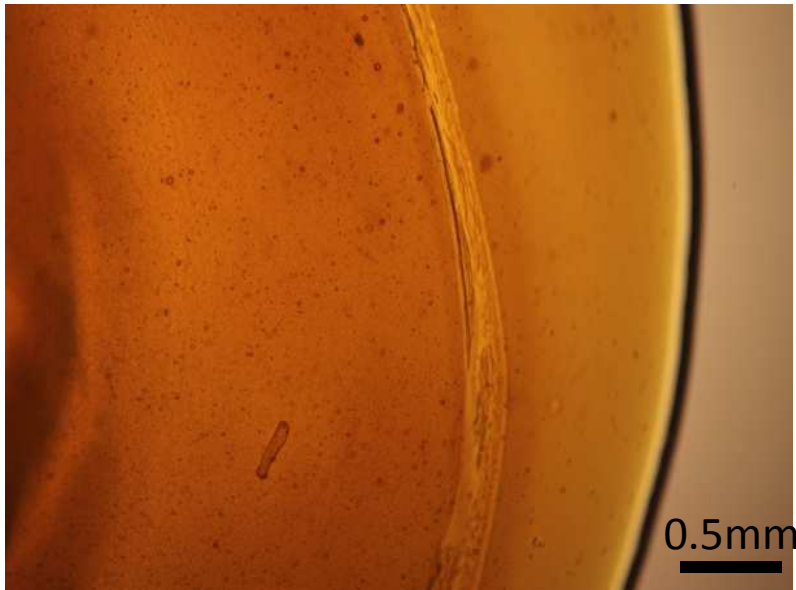


**Figure 3.2:** Transmission image of nanostructure PS sample film.

A solution of 5% polystyrene and 95% toluene, by weight, was prepared and added to the NPL toluene colloid in different volume/volume ratios depending on the initial concentration of the colloid, as well as the size and shape of the nanostructures. This mixture could be stored for multiple preparations. Before each preparation the NPL PS mixture was sonicated and slowly warmed (over a period of up to five minutes) on a hot plate in a small (1mL) glass vial to ensure a homogeneous distribution of NPLs within the mixture. A glass slide was first wiped clean with a lint free optics wipe lightly soaked in acetone followed by another wipe lightly soaked in ethanol. The slide was then placed on a hot plate in a fume cupboard set at a temperature between 60 and 80°C, and allowed to thermalize for several minutes. A 5  $\mu$ L drop cast of the NPL PS mixture was then made onto the slide using an adjustable pipette with a disposable tip. The drop cast was allowed to dry for at least 3 minutes. Several drop casts were made on top of each other after the previous drop had formed a dry layer in order to create a final layer of adequate absorbance. Typically, four stacked layers were drop cast for the samples investigated here.

Appropriate ratios of nanostructure colloid to PS solution had to be determined in order to avoid aggregation in the final film, and to give a high enough absorbance

so that measurements could be taken. The concentrations of the supplied colloid solutions were not known. Our procedure involved starting from a colloid to polystyrene solution ratio of 80:20. The resulting layers after the drop casting step were examined under a microscope, and absorbance spectra were acquired in order to assess the level of possible aggregation and the shape of the absorption spectra respectively. An example of a sample film showing a homogeneous distribution of nanostructures can be seen in an image acquired using the Olympus BX-50 microscope shown in Fig. 2.1. The colloid to PS solution ratio was subsequently adjusted, and the process was repeated until a suitable sample had been produced.

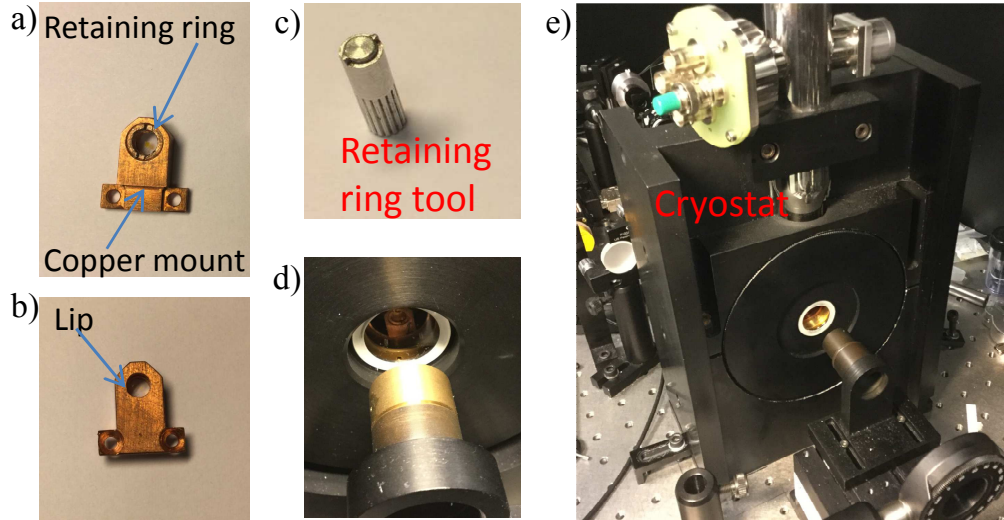


**Figure 3.3:** Front and back views of the copper mount in a) and b) respectively. c) shows a tool for screwing the retaining ring indicated in a). d) and e) are images of the cold finger cryostat in the optical setup shown in Fig. 2.2, including the input objective L1.

For the room temperature NPL absorption and PL data presented in the following sections, the measurements were taken with the polymer samples layers on the glass slide on which they were drop cast. For low temperature measurements, the sample polymer films were cut into square pieces with lateral dimensions of roughly 0.5 mm using a double edge shaving razor blade. These pieces were then squeezed between two quartz windows of 5 mm diameter and 1 mm thickness with the aid of a copper mount after it had been placed on a hotplate at 120°C for about 10 seconds. Fig. 3.3 a) and b) show images of the copper mount used. This mount was custom made to fit into the cold finger helium flow cryostat (see image of cryostat Fig. 3.3 e)) used for low temperature measurements as shown in Fig. 3.3 d). The mount comprised an opening with an internal thread, and a lip extending into the opening at one end. A quartz window could rest against this lip in order to be held inside the mount. A second window could be squeezed on top of the first with a piece of sample film in between as the retaining ring shown was screwed into the opening using the retaining ring tool shown in Fig. 3.3 c), from the side opposite to the one with the lip. Small amounts of vacuum grease were applied to the surfaces of the mount (including the retaining ring) that were in contact with the quartz windows to provide thermal contact in vacuum.

It was important to ensure that the samples resulting from the preparation method described above did not contain a significant fraction of aggregates. The



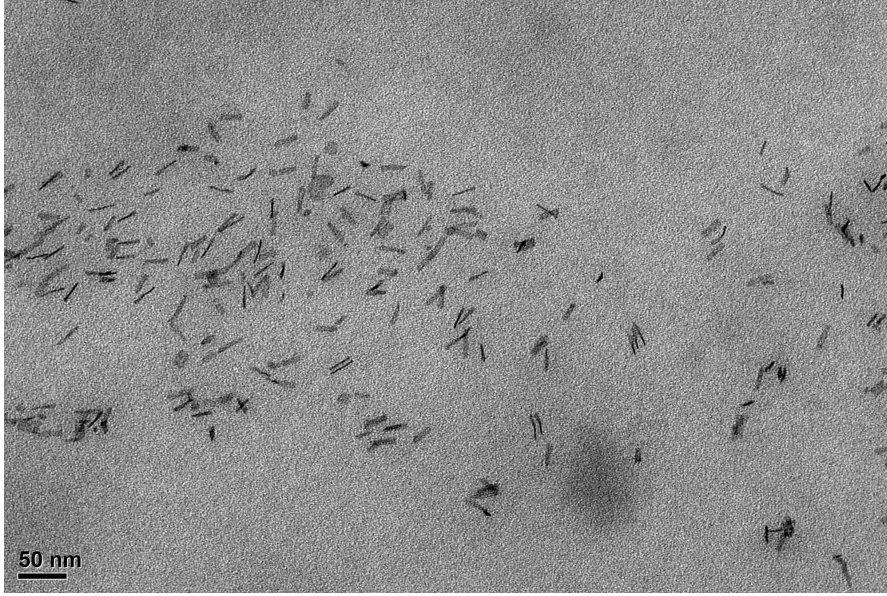


**Figure 3.4:** Transmission electron microscope images of a section of the sample film prepared using sample 12x6x1.7.

spatial distribution of NPLs in the polymer film samples was measured using TEM by our collaborators [68]. The samples were prepared for TEM by dispersing tiny fragments (approximately 1 mm diameter) in a drop of super glue on a polymeric support in order to handle the sample for cutting. A Diatome (diamond knife) on a Leica EM UC6 ultramicrotome was used to cut the pieces of sample film into approximately 70 nm thick slices. A FEI Tecnai G2 F20 was used to acquire the TEM images. An accelerating voltage of 200 kV was used for the field-emission gun, and the images were recorded using a 4 Mp Gatan BM UltraScan Charge-Coupled Device (CCD) camera.

The acquired TEM images indicate only a small amount of NPLs with a separation less than 10 nm, suggesting a lack of any significant aggregation. The TEM image of the sample film of sample 12x6x1.7 is shown in Fig 3.4. We should therefore not expect the dynamics to be significantly affected. Some bunching was observed on the micrometer scale in the lower resolution images which may cause Rayleigh scattering. This can be observed in the NPL absorption spectra presented in the next section.

## 3.2 Linear Optical Properties

We have investigated the linear optical properties of a range of sizes and thicknesses of NPLs. We have studied in detail the absorption spectra of the NPLs by fitting the spectra with a model that allows us to extract the parameters of the exciton states. The dependence of these parameters on size and thickness was studied.

For the samples in the SDS (see Table 3.1) we have measured the absorption, as well as the photoluminescence (PL) spectra of these samples using the modified Olympus BX-50 microscope as described in section 2.1. For these measurements, these NPLs were distributed in a PS matrix prepared as described in section 3.1.1. For all other studied samples, the absorption spectra were acquired from either our collaborators, or from literature. Our collaborators provided us with the absorption

measurements of the 4.5 ML thick NPLs labelled 120x60x1.4 in Table 3.1. The data acquired from literature include a spectrum of 6.5 ML thick NPLs labelled 35x8x2 taken from the work of Ithuria *et al* [2], a spectrum of 3.5 ML thick NPLs which we label 2x2x1.1 taken from the work of Ouyang *et al* [26], and finally an additional spectrum of NPLs of thickness 5.5 ML labelled 50x50x1.7 taken from the work of Baghani *et al* [62].

The absorption spectra not acquired experimentally by us, namely the spectrum provided by our collaborators and the spectra acquired from literature, were measured with the NPLs in solution. The spectrum for 4.5 ML NPLs (labelled 120x60x1.4) from our collaborators was acquired with the NPLs in a toluene solution. For the 6.5 ML NPL (labelled 35x8x2) spectrum taken from ref [2], the NPLs were dispersed in a hexane solution. The spectrum of the 3.5 ML NPLs (labelled 2x2x1.1) taken from ref [26] was acquired with the NPLs in a toluene solution. In ref [26], sample 2x2x1.1 is reported as magic-sized nanocrystals. They are disk shaped structures of a reported diameter of approximately 2 nm. Based on the TEM images found in the supplementary material of [26], as well as the heavy hole exciton absorption energy of the investigated magic-sized nanocrystals, we conclude that these structures are thin disk shaped NPLs with a diameter smaller than the lateral dimensions of the other NPL samples we will discuss. We therefore include these as part of our NPL thickness dependent study.

### 3.2.1 Model for the nanoplatelet absorption

The geometry of NPLs is similar to that of quantum wells in that one of the dimensions is much smaller than the other two. Therefore, models used to describe the absorption spectra of quantum wells are suitable for NPLs. We noticed from the absorption spectra of our size dependent NPL subset that the exciton absorption energies vary with lateral size (see section 3.2.3). We thus elected to describe the confinement within the NPLs using a factorised approach. In this approach, the exciton is quantized according to the COM mass, while the continuum edge, representing free carriers, is expected to be confined with the reduced mass. The exciton binding energy is also expected to increase due to the electron and hole effectively being forced closer together in-plane.

In the absorption spectra presented in this work, we show the absorbance as a function of photon energy as seen in Fig 3.5. The absorbance is defined as:

$$A = -\ln\left(\frac{I_1}{I_0}\right) \quad (3.1)$$

where  $I_0$  is the intensity of light incident on the sample, and  $I_1$  is the transmitted intensity.

The model used to describe the absorption spectra went through several iterations. This was because at each of the intermediate iteration stages of the model, we found inadequacies which we attempted to correct in subsequent iterations. We denote the different iterations of the model with numbers. The models are summarized in Table 3.2. A fit made to the absorption spectrum of sample 34x8x1.7 at 20 K with the first version, absorption model 1 (AM1), is shown in Fig 3.5. From the data, three absorption peaks, as well as a higher energy feature that appears to be a continuum edge are identifiable. Based on the energy ordering of the heavy hole (HH) and light hole (LH) valence bands due to confinement along the thickness direction (see Fig 1.4), we attribute the lowest energy peak to the 1s heavy hole exciton ( $X_{hh}$ )

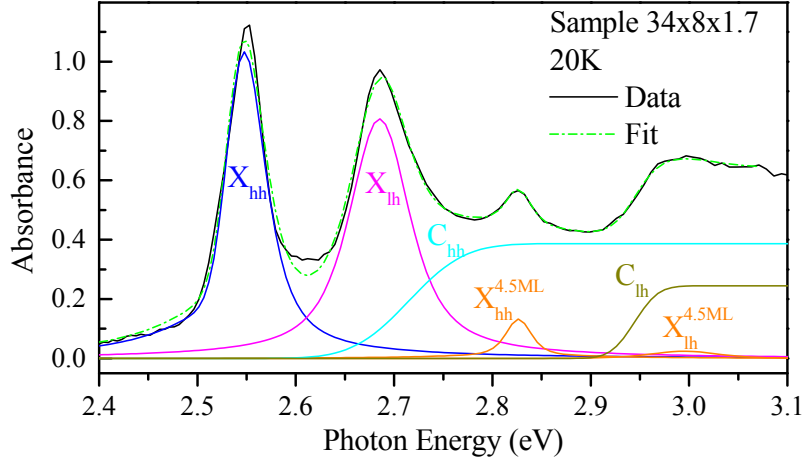


**Figure 3.5:** The absorption spectrum of sample 34x8x1.7 at 20 K is shown. The fit is made using AM1, and the individual components of the fit are shown as indicated.

absorption which is followed by the 1s light hole exciton ( $X_{lh}$ ) absorption peak. The third absorption peak observed at 2.83 eV in Fig. 3.5 is not characteristic of NPLs of this thickness (see Fig 1.8), and was attributed to the presence of platelets of a different thickness that contaminated this sample. Such contamination was observed in only two of the samples in the SDS. The feature at 3 eV in Fig. 3.5 was initially attributed to the LH continuum edge  $C_{lh}$  only. The continuum edge of the  $X_{hh}$  is expected to appear at lower energies since the predicted value from literature for the  $X_{hh}$  binding energy is 100-300 meV [16]. The energy separation between the continuum and the exciton absorption peak is the exciton binding energy. To take account of the 1s exciton absorption peak and the continuum, we fitted the absorption spectra with an expression as given in Eq. 3.2 for each conduction to valence band combination,

$$P_x(\omega) = p_x + \frac{A_{Cx}}{2} \left[ 1 + \operatorname{erf} \left( \frac{\Delta - R_x}{\gamma_{Cx}} \right) \right] \quad (3.2)$$

where  $p_x$  represents the 1s exciton absorption line shape and the second term is the continuum edge  $C$ . In the above expression,  $\Delta$  is  $\hbar\omega - E_x$ ,  $A_{Cx}$  and  $\gamma_{Cx}$  are the height and width of the continuum edge respectively,  $R_x$  is the exciton binding energy, and  $p_x$  is normalised to have unity area. The step-like density of states of the continuum in 2D is broadened by a Gaussian broadening, resulting in the error function used in the above expression. The Sommerfeld enhancement of the continuum absorption leads to an increased absorption decaying on the energy scale of the exciton binding energy. However, we elected not to consider this enhancement because at the large energy scales we are concerned with here, the effective mass approximation might break down, giving rise to non-parabolicity of the bands and accordingly a non-constant density of states. One could also use a  $\cosh^{-2}$  broadening which is analytically integrable and gives a  $1 + \tanh(x)$  term instead of  $1 + \operatorname{erf}(x)$ . This does not however change the shape and the resulting fit parameters significantly as we have verified. The Gaussian is better suited for inhomogeneous broadening (due to the size distribution).

The in-plane localisation of the COM of the excitons is expected to result in an assymmetric absorption lineshape as is the case for quantum wells [69] [70]. This lineshape was used to take the in-plane confinement into account, and was for the

$X_{\text{hh}}$  absorption lineshape.

$$p_{\text{hh}} = \frac{1}{2\eta} \left[ 1 + \operatorname{erf} \left( \frac{\Delta}{\gamma} - \frac{\gamma}{2\eta} \right) \right] \exp \left[ \frac{\gamma^2}{4\eta^2} - \frac{\Delta}{\eta} \right] \quad (3.3)$$

where the asymmetric broadening due to localisation is described by the parameter  $\eta$  (known as the localization energy parameter), and  $\gamma$  represents the standard deviation of the potential variation [69]. This lineshape does not take into account the homogeneous broadening of the transitions created, for example, by phonon scattering and radiative decay. At room temperature, this broadening is relevant. There is however, no analytical expression including this broadening.

We noticed from the absorption spectra that the light hole exciton absorption peak is in general much broader than the  $X_{\text{hh}}$ . This is attributed to the scattering of  $X_{\text{lh}}$  into  $X_{\text{hh}}$ . Depending on the  $X_{\text{hh}}$  binding energy, it is sometimes the case that the continuum edge of the HH overlaps the  $X_{\text{lh}}$  peak. If such an overlap exists, the  $X_{\text{lh}}$  may resonantly scatter into the HH continuum resulting in greater homogeneous broadening of the  $X_{\text{lh}}$  absorption peak [71]. We also notice that the LH exciton peak appears to be assymetric. Fig. 3.5 shows a fitted absorption spectrum for sample 34x8x1.7. It can be seen from the individual components of the fit plotted in the figure that the assymetry in the  $X_{\text{lh}}$  peak can be explained by the HH continuum edge, and the symmetric line shape given in Eq 3.4 has been used to describe the LH absorption lineshape.

$$p_{\text{lh}} = \frac{1}{2\gamma \cosh^2 \left( \frac{\Delta}{\gamma} \right)} \quad (3.4)$$

For the above lineshape the full width at half maximum (FWHM) is given by  $1.763 \gamma$ . Although we should still expect the  $X_{\text{lh}}$  lineshape to be assymetric just as for the HH, the homogeneous broadening by the scattering into the HH continuum is not taken into account in Eq. 3.3. Furthermore, the lineshape 3.3 has two parameters which are not resolvable in the experimental data. We have therefore used a simpler lineshape. A pure Gaussian does not describe the homogeneous broadening well, however the exponential tails of the chosen lineshape give a better description. Note that a lorentzian lineshape assumes a Markovian scattering, i.e. without memory in the outgoing channel. In reality there is always a finite memory time, which results in suppressed tails of the Lorentzian lineshape. Secondly, the energy position of the HH continuum shown in Fig. 3.5 agreed with theoretical predictions. We checked the agreement for the binding energy  $R_{\text{HH}}$  with theory by comparing the ratio  $R_{\text{LH}}/R_{\text{HH}}$  obtained from the fit with the one calculated from theory. We can do this because the position of the LH continuum is reasonably well defined in the spectrum shown in Fig. 3.5. We first calculated the in-plane HH and LH masses  $m_{\text{HH}}$  and  $m_{\text{LH}}$  using formulas from ref [72] for the in plane hole masses in quantum wells:

$$m_{\text{hh}} = \frac{m_e}{y_1 + \bar{y}} \quad (3.5)$$

$$m_{\text{lh}} = \frac{m_e}{y_1 - \bar{y}} \quad (3.6)$$

In the above expressions  $m_e$  is the free electron mass, and it is assumed that  $\bar{y} = y_2 = y_3$  with  $y_{1,2,3}$  being the Luttinger-Kohn parameters of the valence band with. Using these expressions, the in-plane heavy-hole mass is  $m_{\text{hh}} = 0.19m_e$  and the in-plane light-hole mass is  $m_{\text{lh}} = 0.67 m_e$ . Note that the heavy-hole has a smaller

mass in-plane but a larger mass for the confinement in the platelet thickness. The in-plane reduced mass can be calculated using the isotropic electron mass  $m_c = 0.18 m_e$ , resulting in  $\mu_{hh} = 0.092 m_e$  and  $\mu_{lh} = 0.14 m_e$ . Since the 2D exciton binding energy is proportional to the in-plane reduced mass, the difference in the in-plane hole dispersions results in the difference between light-hole and heavy-hole exciton binding energies (see section 1.1). Therefore, taking the ratio of these reduced mass values gives a predicted ratio value for the heavy-hole and light-hole exciton binding energies:  $R_{lh}/R_{hh} = \mu_{lh}/\mu_{hh} = 1.51$ . The value obtained from the fit parameters of the fit in Fig 3.5 is 1.46 which is close to the theoretical value. We thus conclude that the assymetry seen in the LH exciton absorption peak is dominated by the presence of the HH continuum.

The third absorption peak attributed to contamination seen at 2.83 eV in Fig. 3.5 at a temperature of 20 K was observed at 2.69 eV at room temperature. This energy is similar to the  $X_{hh}$  absorption peak of sample 120x60x1.4. Sample 120x60x1.4 is one monolayer thinner (4.5 ML), we thus concluded that sample 34x8x1.7 was contaminated with platelets of thickness 4.5 ML. To include the features of the contaminating NPL in AM1, we included a  $X_{hh}$  lineshape, a HH continuum, and a  $X_{lh}$  lineshape for the thinner NPLs. The  $X_{hh}$  and  $X_{lh}$  lineshapes used were of the form given in Eq. 3.4 for the contamination. It was important to include the  $X_{lh}$  absorption and  $C_{hh}$  as these features would overlap the  $C_{lh}$  of the contaminated sample, modifying the shape of the spectrum in this region to a degree depending on the level of contamination. However, since these features ( $C_{hh}$  and  $X_{lh}$  peak of the contaminating NPLs) could not clearly be seen in the spectrum of Fig. 3.5, their parameters needed to be fixed. We used a fit of the 4.5 ML spectrum to fix the ratio between the  $X_{hh}$  and the  $X_{lh}$  peak areas, the HH and LH energy separation, and the ratio between the widths of the lineshape. We also fixed  $R_{hh}$ , and the ratio between  $X_{hh}$  peak area and the continuum step height. The only free parameters were the ones directly related to the  $X_{hh}$  of the contaminating (4.5 ML) NPLs.

It was noticed from the spectrum in Fig. 3.5 that the  $X_{hh}$  peak has tails visible on the low energy side. These tails could be due to resonant Rayleigh scattering which would have Lorentzian tails. To approximate the effect of this resonant scattering in AM1, we added Lorentzian lineshapes centered at the exciton absorption energies.

$$\frac{L/\pi}{(\gamma_L + \Delta^2/\gamma_L)} \quad (3.7)$$

In the above,  $L$  and  $\gamma_L$  are the area and width of the Lorentzian respectively. In the fit shown in Fig 3.5, the only exciton absorption peak included in the model for which these scattering tails were not included was the  $X_{lh}$  absorption peak of the 4.5 ML contamination. The fit function for AM1 thus included the following components:

$$\alpha_{abs} = A_{hh}P_{hh} + A_{lh}P_{lh} + \alpha_{abs}^{4.5ML} \quad (3.8)$$

$$\alpha_{abs}^{4.5ML} = A_{hh}P_{hh} + A_{lh}p_{lh} \quad (3.9)$$

where  $P_{hh,lh}$  is defined in Eq. 3.2. Note that  $P_x$  includes an exciton transition lineshape and the continuum, whereas  $p_x$  includes only the transition lineshape (without the continuum) as defined in Eq. 3.2, Eq. 3.3 and Eq. 3.4.

| Model | Components | Details | Problems |
|-------|------------|---------|----------|
|-------|------------|---------|----------|



| Model | Components                                    | Details  | Problems  |
|-------|---|--|---|
| 1     | $X_{hh}, X_{lh}, C_{hh}, C_{lh}$              | All parameters unconstrained. Lorentzian centered at absorption energy of exciton included for resonant scattering   | $X_{so}$ not included   |
| 2     | $X_{hh}, X_{lh}, C_{hh}, C_{lh}, X_{so}$      | All parameters unconstrained. Only one Lorentzian centered at HH absorption energy included  | Width of $X_{so}$ too large, essential contributing to background |
| 3     | $X_{hh}, X_{lh}, C_{hh}, C_{lh}, \propto E^4$ | $X_{hh}$ tail on low energy side masked from fit. No Lorentzian component included. Rayleigh scattering term included. Constraints $R_{hh} = \frac{R_{lh}^{6.5ML}}{R_{hh}^{6.5ML}} \times R_{lh}$ and $C_{hh} = \frac{R_{lh}^{6.5ML}}{R_{hh}^{6.5ML}} \times C_{lh}$ imposed using values of $R_{hh}^{6.5ML}$ and $R_{lh}^{6.5ML}$ taken from a AM2 fit of the spectrum of sample 35x8x2 | The fitted width of $C_{lh}$ too large                            |
| 4     | $X_{hh}, X_{lh}, C_{hh}, C_{lh}, X_{so}$      | An offset $\propto E^2$ subtracted from spectra prior to fit. Using parameter values from fit of 120x60x1.4 shown in Fig 3.9, the fits were constrained as indicated in Eq. 3.11. The tails on the low and high energy side of $X_{hh}$ masked to exclude data affected by resonant scattering   | N/A   |

**Table 3.2:** The progression of the model for the NPL absorption spectra is shown.

Moving on from this initial model for the NPL absorption on to AM2 (see Table 3.2), it was noticed that the splitting between the heavy and light holes, and the split off hole is expected to be  $\Delta_{so} \approx 0.39$  eV for CdSe with a zincblende structure, and  $\Delta_{so} \approx 0.42$  eV for wurtzite CdSe. This means that the absorption peak of the split off exciton  $X_{so}$  should appear at the position of the high energy feature at 3 eV in Fig. 3.5. We realized as a result that by not including a lineshape for the  $X_{so}$ , we underestimated the LH binding energy in AM1. In AM2 we therefore included a lineshape of the form given in Eq. 3.3 centered at an energy  $[\Delta_{hh} + \Delta_{lh}]/2 + \Delta_{so}$  to account for  $X_{so}$ . The energy was related to the HH and LH exciton energies to reduce the number of free parameters as the  $X_{so}$  feature is overlapping the  $C_{lh}$ , and the fit tends not to be well defined. AM2 did not require the inclusion of Lorentzian scattering tails for all the exciton absorption peaks in order to give good quality data fits because of the large width of the  $X_{so}$  peak. Therefore, AM2 included a Lorentzian lineshape centered only at the  $X_{hh}$  absorption energy. AM2 also included

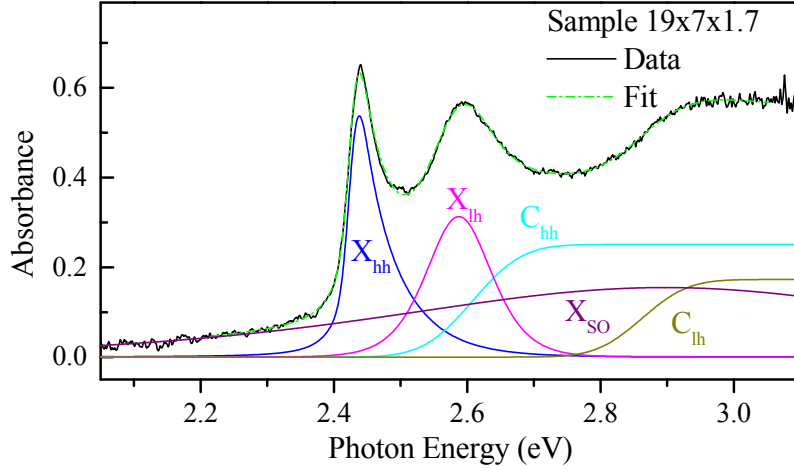


**Figure 3.6:** Fitted absorption spectrum of sample 19x7x1.7 at room temperature. The fit is made using AM2. The individual components of the fit are shown as indicated.

a general offset. Fig. 3.6 shows a fit made to the room temperature absorption spectrum of sample 19x7x1.7 with AM2. It can be seen from the components of the fit plotted in the figure that when left unconstrained, the width of the  $X_{so}$  absorption peak converged to a very large value. This resulted in the SO lineshape simply contributing to the background. Constraining the width of the  $X_{so}$  resulted in the HH binding energy values  $R_{hh}$  converging outside of the expected range ( $<100$  meV).

Before moving on to the next version of the NPL absorption model, let us first discuss the spectrum for the thicker sample 35x8x2.0 shown in Fig 3.9 taken from ref [2] where the arrangement in energy of the  $C_{lh}$  and  $X_{lh}$  absorption, as well as the area of the  $X_{so}$  peak is such that the SO peak is clearly visible. In addition, this spectrum shows a low amount of Rayleigh scattering, reducing the number of free parameters in the fit. The position of the split off absorption peak, is expected to stay at the same energy in relation to the heavy and light hole exciton absorption peaks. The exciton binding energies however varies depending on the size and thickness of the NPL, so that the position of the continua relative to their respective absorption peaks will vary. The energy splitting of the split off band (0.39 eV from the central position between the heavy and light hole exciton peaks) means that the position of the SO exciton will in general somewhat overlap with the LH continuum edge based on the observed absorption spectra. This means that based on the level of quantisation, the energy position of the SO exciton absorption peak will vary in relation to the LH continuum edge, specifically the  $C_{lh}$  will shift to higher energies relative to  $X_{so}$  with decreasing thickness, i.e. increasing confinement energy. Since the high energy features of the spectrum could be seen clearly for sample 35x8x2 compared to the spectra of any other studied sample, it was decided that parameter values from a fit made to this spectrum (using AM2) could be used to constrain the parameters of the fits for the other investigated NPL samples. The problem with AM2 described previously was that the complexity of the expected features of the spectra, especially the high energy feature that combines the  $C_{lh}$  and the  $X_{so}$ , does not allow for an unconstrained fit. In AM3, we therefore fixed the ratio of the binding energies  $R_{hh}/R_{lh}$  to the value obtained from a AM2 fit to the spectrum in Fig 3.9.  $R_{hh}$  was then expressed in terms of  $R_{lh}$  in the fit function. We also fixed

the ratio between the product of the HH continuum height and binding energy, and the product of the LH continuum height and binding energy  $A_{Chh}R_{hh}/(A_{Clh}R_{lh})$  in the same way.

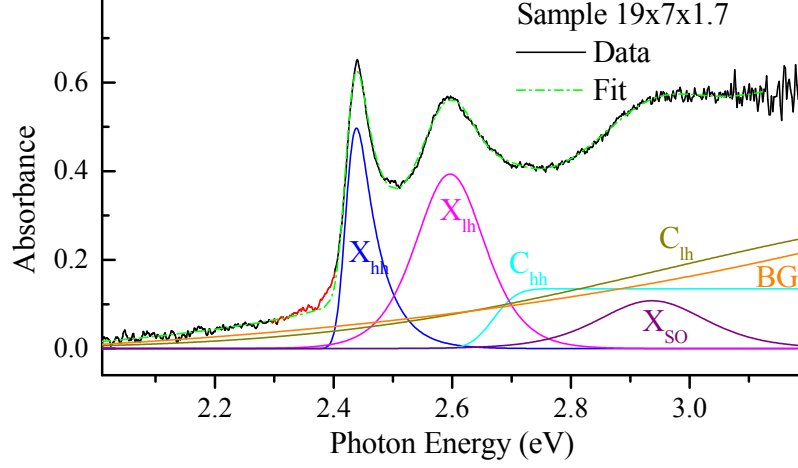


**Figure 3.7:** Fitted absorption spectrum of sample 19x7x1.7 at room temperature. The fit is made using AM3 with the region of data shown in red masked from the fit. The individual components of the fit are shown as indicated, and the component labelled BG is the background proportional to  $E^4$ .

In addition to the above constraints for AM3, we removed the Lorentzian for the resonant scattering contribution. It was noted that resonant scattering should result in a  $X_{hh}$  lineshape that is the convolution of a Lorentzian function with  $p_{hh}$ . However, this calculation does not have an analytical solution. Instead of describing this effect in our fit function, we masked the Lorentzian tails on the low energy side of the  $X_{hh}$ , where they were most obviously contributing to the spectrum, in order to reduce the influence of this shortcoming of the fit function on the fit. This masked region of the absorption spectrum is highlighted in red in Fig 3.7 which shows a fit made with AM3 for the spectrum of sample 19x7x1.7. To account for the scattering background which can clearly be seen at energies much lower than the  $X_{hh}$  absorption peak for a majority of the studied samples, we included a term proportional to the fourth power of energy  $E^4$  which describes Rayleigh scattering. It can be seen from Fig 3.7 that the  $C_{lh}$  resulting from the AM3 fit is very broad. The NPL absorption model has many features with some that overlap complicating the fit. It was decided that to achieve fits with physically meaningful parameters, the fit function needed to be further constrained. To this end, we proceeded to fit the low energy parts of the spectra (for energies below 2.1 eV) with a Rayleigh scattering term proportional to  $E^4$ , and subtract the resultant background from the NPL spectrum in question. This approach resulted in the subtraction of too high a background at high energies, distorting the shape of the spectra at the  $C_{lh}$  position as can be seen from the background subtracted spectrum of sample 120x60x1.4 shown in Fig 3.8.

In order to correctly account for the scattering background seen in the NPL spectra, it must be noted that these NPLs can have areas as large as several hundred square nanometers (see Table 3.1). For Rayleigh scattering to be the dominating process, the particle size in the concerned medium must be significantly smaller than the wavelength of light, typically less than 10% of the wavelength. However, Mie scattering dominates if the particle size is comparable to the wavelength of

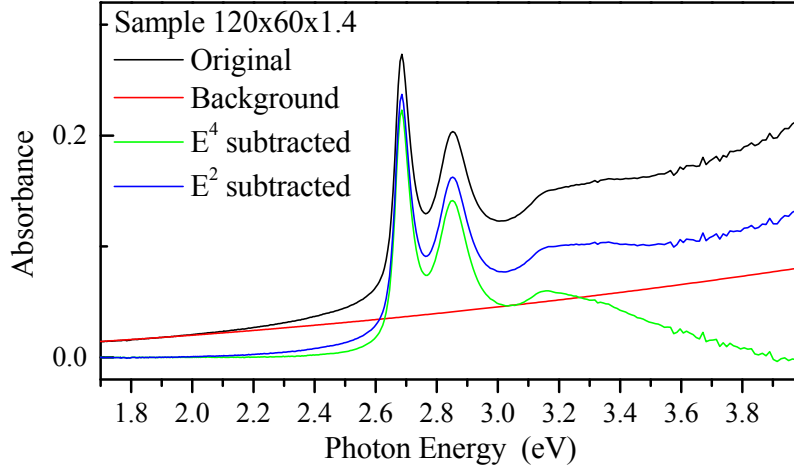


**Figure 3.8:** The room temperature absorption spectrum of sample 120x60x1.4 is shown in black. The blue trace is the spectrum with a background proportional to  $E^2$  subtracted from it. The background proportional to  $E^2$  is shown in red. The green trace is the spectrum with a background proportional to  $E^4$  subtracted from it.

light [73]. Mie scattering is dependent on the particle size and shape, and has a much weaker wavelength dependence. It is possible that the observed scattering background is a mixture of the two processes due to the fact that at higher energies the wavelength of light becomes comparable to the NPL size, whereas at much lower energies this is not the case. At higher energies therefore, the Mie scattering process is more relevant. In addition,  $\epsilon_r$  is decreasing with increasing energy, reducing the Rayleigh scattering. We found that the background in the NPL spectra could overall be described by a scattering term proportional to  $E^2$  as can be seen from the example shown in Fig 3.8. This was checked over several of the samples showing the strongest Rayleigh scattering by examining the the continuum absorption. Before fitting the absorption spectra, the region at low energies in the spectra (well below the HH exciton peak) was fit with this scattering term, and the resultant background was subtracted from the NPL spectra. In AM4 we also included an offset to account for incorrect referencing.

AM4 exercised more stringent constraints over the parameters of the excitons in order to ensure that they were physically meaningful (see details of the evolution of the model in Table 3.2). First the spectrum of sample 35x8x2 was fit with the following function:

$$\alpha_{\text{abs}} = A_{\text{hh}}P_{\text{hh}} + A_{\text{lh}}P_{\text{lh}} + A_{\text{so}}p_{\text{so}} \quad (3.10)$$

In addition to the tail on the low energy side of the  $X_{\text{hh}}$  peak, the region between the  $X_{\text{hh}}$  and  $X_{\text{lh}}$  peak was also masked from the fit to exclude any part of the spectrum strongly influenced by the missing homogeneous broadening of the  $X_{\text{hh}}$  model, and possibly resonant Rayleigh scattering. The fit to the 120x60x1.4 data made in this way is shown in Fig 3.9. We then used the parameter values from this fit as a guide to constrain the parameter values in the fits made to the spectra of all other NPLs. This was because the spectrum in Fig 3.9 has the most clearly defined parameter values out of all the studied spectra because of a small scattering contribution and the sharpest linewidths due to its larger thickness. This is also due to the clear visibility of the  $X_{\text{so}}$  peak which is not as obscured by the overlapping LH continuum

edge as it is for the spectra for all other thicknesses of NPLs as shown in Fig 3.9. We chose to fix the ratios between certain parameters in the following way:

$$\begin{aligned}
 A_{lh} &= \rho_{Alh} A_{hh} c_{Alh} \\
 R_{hh} &= \rho_{Rhh} R_{lh} c_{Rhh} \\
 A_{Chh} &= \rho_{Chh} A_{hh} / R_{hh} c_{Chh} \\
 A_{Clh} &= \rho_{Clh} A_{lh} / R_{lh} c_{Clh} \\
 A_{so} &= \rho_{so} A_{hh} c_{so}
 \end{aligned} \tag{3.11}$$

where the values  $\rho_{Alh,Rhh,\dots}$  are fixed using the parameter values for the fit in Fig 3.9. The normalization parameters  $c_{Alh,Rhh,\dots}$  were included to allow defined tolerances on these constraints, typically between 0.8 and 1.2. The parameters  $c_{Clh,so}$  were allowed to exceed this range in some cases in order to obtain reasonable fits. These instances will be pointed out when the fits in question are presented in the following subsections.

These constraints are based on the following logic. Firstly, the ratio between the areas of the different lineshapes should not vary significantly between the different samples, as they are given by the exciton binding energy and the dipole matrix elements of the bands. There could be a geometry dependent local field for different aspect ratios which is neglected here. Secondly, The ratio between the HH and LH reduced mass should not be changed greatly in the different NPLs leading to the constraint between  $R_{lh}$  and  $R_{hh}$ . Applying these constraints for all other fits to the NPL spectra allowed us to obtain physically meaningful exciton parameters, and good fits to all the data, that were consistent between the various fitted spectra.

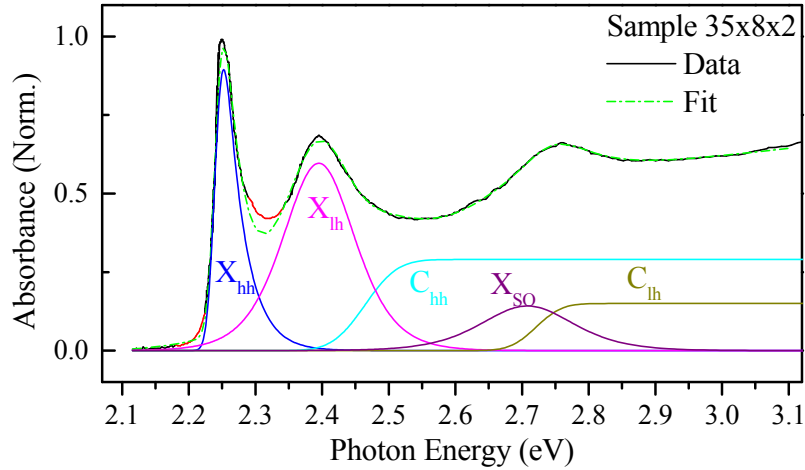


**Figure 3.9:** The absorption spectrum for sample 35x8x2 is shown with a fit made to the data using AM4 indicated by a green dash-dot line. The regions of data shown in red are masked for the fit. The individual components of the fit are plotted as indicated.

### 3.2.2 Thickness Dependence

In order to examine the exciton parameter as a function of NPL thickness, we fitted the absorption spectra of NPLs with four different thicknesses. In addition to sample 35x8x2 shown in Fig. 3.9, we present the spectra for samples 35x8x2, 120x60x1.4 and 2x2x1.1.

The fitted absorption spectra for samples 50x50x1.7 and 120x60x1.4 are shown in Fig 3.10 a) and b) respectively. The fits shown are made with the tolerances to the constraints 3.11 (see Table 3.3). The validity of the constrained fit used is supported by the fit of the spectrum for sample 50x50x1.7 which has very little background due to scattering. For the smallest considered thickness however, the fit could not well reproduce the spectrum of the sample. The fit to the spectra for these NPLs, sample 2x2x1.1 is shown in Fig 3.11. We can see from the individual components of this fit, and the fit parameters presented in Table 3.3 that the  $X_{so}$  absorption peak cannot be well fit even with the SO and HH-LH splitting at the upper limit of 0.42 eV (note that 0.42 eV is the splitting in wurtzite CdSe whereas the NPLs have a zincblende structure so that a splitting of 0.39 eV is expected). It is also clear from the components of the fit that it is not possible to fit the  $X_{hh}$  and  $X_{lh}$  absorption lineshapes well using the constraints in Eq. 3.11 with the maximum tolerance to these constraints being 20% (i.e. the value of parameter  $c_{Alh,Rhh}$ ... constrained between 0.8 and 1.2). Fig 3.11 also shows that the fitted HH continuum is very broad.

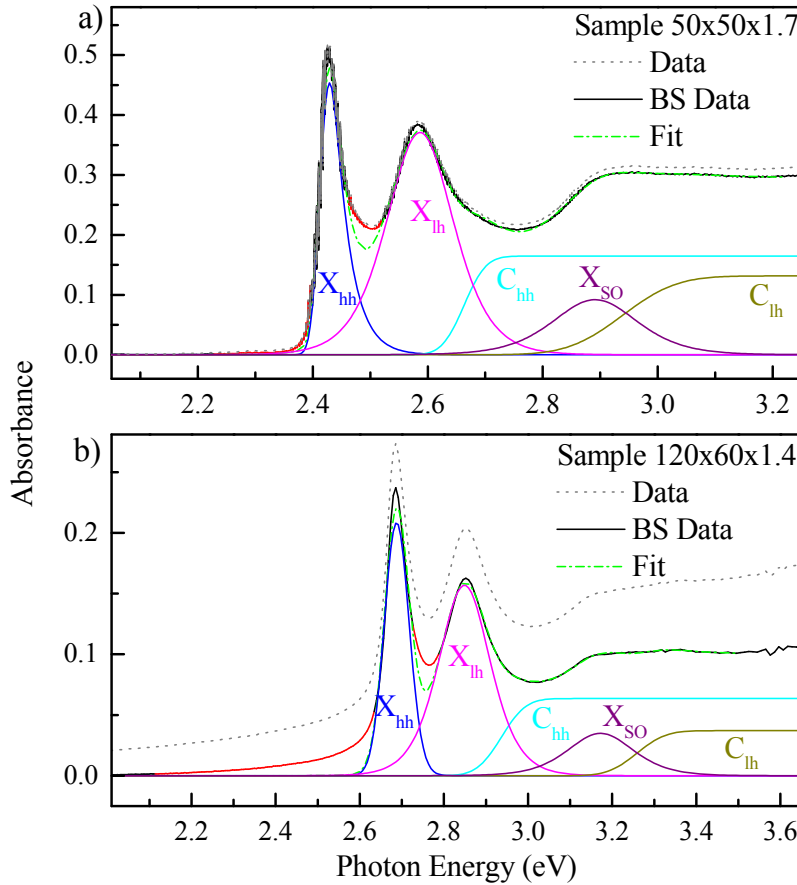


**Figure 3.10:** a) absorption spectrum for sample 50x50x1.7 with a fit using AM4. b), as a) for sample 120x60x1.4. The background subtracted data is shown in black, the original data is shown using a grey dotted line, and the fits are shown as green dash-dot lines with the regions of data shown in red being masked from the fit. Individual components of the fit are plotted as indicated.

The quantisation energy in an ideal 2D structure at a constant effective mass is proportional to the inverse square of the thickness of the structure. As previously discussed, the NPL thickness that leads to a specific  $X_{hh}$  absorption energy is a

| Fit parameters             | 50x50x1.7           | 120x60x1.4          | 2x2x1.1             |
|----------------------------|---------------------|---------------------|---------------------|
| $A_{hh}$                   | $0.0256 \pm 0.0007$ | $0.0154 \pm 0.0003$ | $0.0588 \pm 0.0081$ |
| $\eta$                     | $0.0277 \pm 0.0017$ | $0.0102 \pm 0.0089$ | $0.0073 \pm 0.0010$ |
| $\Delta_{hh}(\text{eV})$   | $2.4155 \pm 0.0005$ | $2.6783 \pm 0.0078$ | $3.1324 \pm 0.0012$ |
| $\gamma_{hh}(\text{eV})$   | $0.0184 \pm 0.0002$ | $0.0395 \pm 0.0004$ | $0.0631 \pm 0.0031$ |
| $c_{Chh}$                  | $1.07 \pm 0.17$     | $0.8 \pm 0.076$     | $0.8 \pm 1.19$      |
| $c_{Rhh}$                  | $1.03 \pm 0.14$     | $0.919 \pm 0.062$   | $1.18 \pm 1.46$     |
| $\gamma_{Chh}/\gamma_{hh}$ | $2.32 \pm 0.36$     | $1.65 \pm 0.32$     | $3.92 \pm 14.58$    |
| $c_{Alh}$                  | $1.168 \pm 0.073$   | $0.865 \pm 0.059$   | $0.8 \pm 0.29$      |
| $\Delta_{lh}(\text{eV})$   | $2.5865 \pm 0.0017$ | $2.8489 \pm 0.0026$ | $3.3083 \pm 0.0033$ |
| $\gamma_{lh}(\text{eV})$   | $0.0781 \pm 0.0029$ | $0.0822 \pm 0.0029$ | $0.1 \pm 0.013$     |
| $c_{Clh}$                  | $1.42 \pm 0.23$     | $1.05 \pm 0.13$     | $0.93 \pm 2.62$     |
| $R_{lh}(\text{eV})$        | $0.352 \pm 0.049$   | $0.410 \pm 0.018$   | $0.419 \pm 0.041$   |
| $\gamma_{Clh}/\gamma_{lh}$ | $1.34 \pm 0.79$     | $0.93 \pm 0.15$     | $0.65 \pm 0.72$     |
| $c_{so}$                   | $1.2 \pm 0.56$      | $0.8 \pm 0.24$      | $0.5 \pm 2.92$      |
| $\Delta_{so}(\text{eV})$   | $0.39$              | $0.409 \pm 0.012$   | $0.42 \pm 0.069$    |
| $\gamma_{so}(\text{eV})$   | $0.099 \pm 0.020$   | $0.105 \pm 0.015$   | $0.14 \pm 0.30$     |

**Table 3.3:** Fitted parameter values for the fits to NPL absorption spectra presented in Figs 3.10 and 3.11.

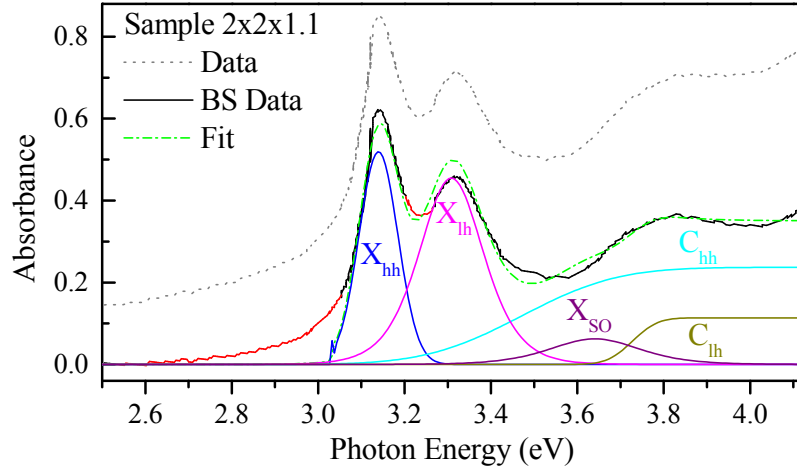


**Figure 3.11:** The absorption spectrum for sample 2x2x1.1, data fit using AM4 indicated by a green dash-dot line. The regions of data shown in red are masked for the fit. The individual components of the fit are plotted as indicated.

contentious issue in the literature. For the purpose of analysing the exciton parameters as a function of thickness, we relate the  $X_{hh}$  absorption peaks seen at 2.24 eV, 2.42 eV, 2.68 eV and 3.13 eV to NPLs with thicknesses 1.97 nm (6.5 ML), 1.67 nm (5.5 ML), 1.37 nm (4.5 ML) and 1.07 nm (3.5 ML) respectively. The  $X_{hh}$  and  $X_{lh}$  absorption energies are plotted in Fig 3.12 a) and the  $X_{hh}$  and  $X_{lh}$  binding energies are plotted in Fig 3.12 b) as a function of the inverse square of the NPL thickness  $L_z$ . As expected, an approximately linear increase in all four parameters is observed due to the quantisation of the excitons within the NPL thickness. Notably, the obtained exciton binding energies are similar to the binding energies given in ref[16], which takes dielectric screening into account, for a low outside dielectric constant. From the linear fits shown in Fig 3.12 a), we extracted the reduced masses of the HH and

LH exciton confined in the NPL thickness of  $\mu_{\text{hh}} = 0.262m_e$  and  $\mu_{\text{hh}} = 0.257m_e$  respectively. We notice also from Fig 3.12 c) that the linewidths of the HH and LH exciton transitions are not changing significantly with thickness.

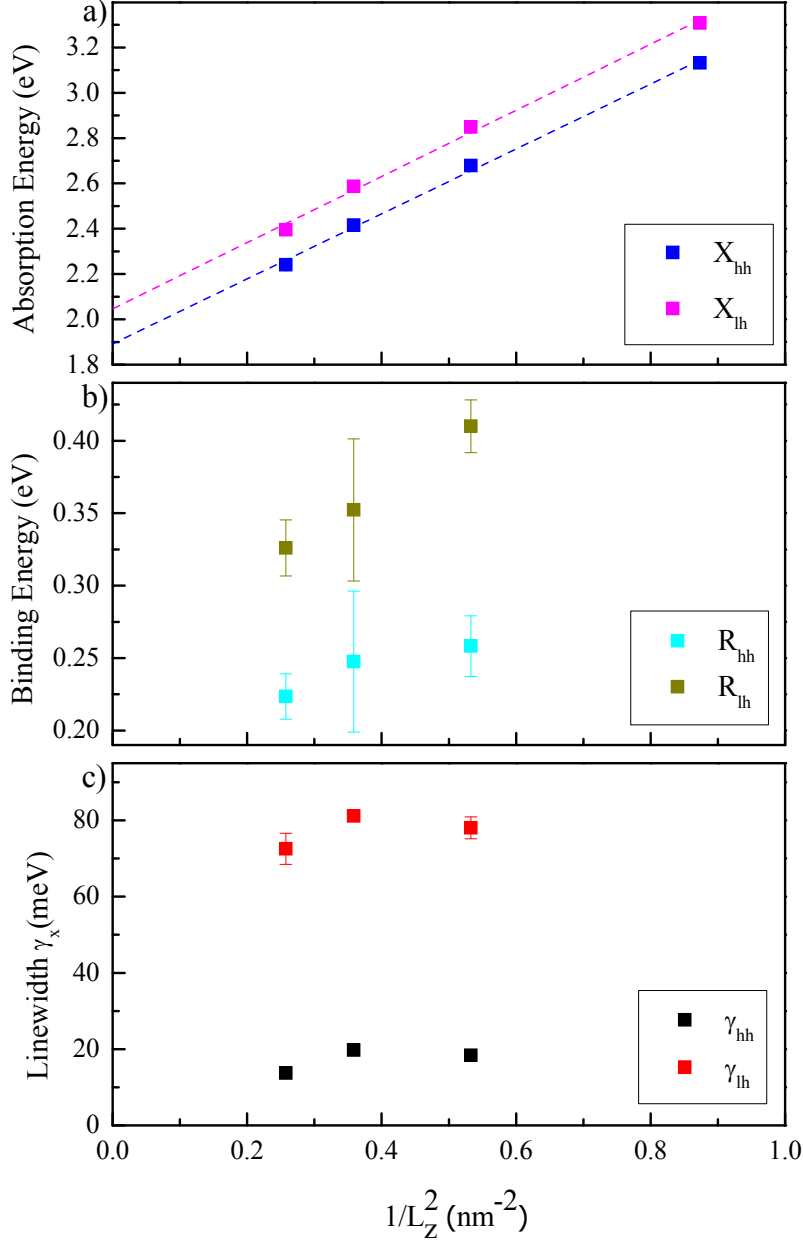


**Figure 3.12:** Exciton parameters as a function of  $1/L_z^2$ , where  $L_z$  is the NPL thickness, extracted from the fits shown in Figs 3.9, 3.10 and 3.11 are shown. a) shows the fitted  $X_{\text{hh}}$  and  $X_{\text{lh}}$  absorption peak energies as indicated. b) shows the fitted binding energies  $R_{\text{hh}}$  and  $R_{\text{lh}}$ . c) shows the linewidths  $\gamma_{\text{hh}}$  and  $\gamma_{\text{lh}}$ . Dashed lines in a) indicate linear fits.

### 3.2.3 Size dependence

In order to study the dependence of the exciton absorption and binding energies on the lateral size of the NPLs, we fitted the spectra of the SDS with AM4. The fits for all the sample in this subset, along with the individual components of the



fits, are given in Figs. 3.13, 3.14 and 3.15.  $\Delta_{\text{so}}$  was fixed to 0.39 eV for all of the fits shown. This is the literature value for zincblende CdSe, and is also extracted from the unconstrained fit to sample 35x8x2 in Fig 3.9. We also noted that the constraints  $c_{\text{lh}}$  and  $c_{\text{so}}$  needed to be relaxed to some extent (see tables 3.4 and 3.5). It could be the case that the scattering background subtracted from the data prior to fitting did not describe the scattering well at higher energies where the  $C_{\text{lh}}$  and  $X_{\text{so}}$  peak are found. This may have caused enough inconsistency in the resultant background subtracted spectra shape at high energies to require a relaxation of the two aforementioned constraints in order to achieve reasonable fits. An example of a 'good quality' fit is shown in Fig 3.16 which displays a fit to the spectrum of sample 24x5x1.7 with the tolerance for these two constraints relaxed beyond 20%, and another fit with the more stringent constraints. We can see that the more stringent constraints lead to the high energy feature close to  $X_{\text{so}}$  peak not being well described by the model. All fitted parameter values can be found in Tables 3.4 and 3.5.

The reader may notice that the NPL absorption spectra of a range of thicknesses and lateral sizes of NPLs can be reasonably well described by our model. Although this is a testament to the validity of the model used, it must also be noticed that the fit is complicated by the presence of several overlapping features namely  $C_{\text{hh}}$  which overlaps with the  $X_{\text{lh}}$  peak, and  $C_{\text{lh}}$  which overlaps the  $X_{\text{so}}$  absorption peak. As a result, the extracted values of the exciton binding energies have a significant error as shown in Table 3.5. Nonetheless we examined the dependence of the exciton absorption and binding energies on the lateral size of the NPLs using the exciton parameter values obtained from the fits shown. As discussed in section 3.2.1, after considering the strong confinement by the NPL thickness, there is an additional confinement of the exciton COM within the lateral dimensions of the NPL. The 1s exciton COM confinement energy can be expressed as follows:

$$E_{\text{x}} = \frac{\hbar^2 \pi^2}{2M} \left( \frac{1}{(L_{\text{x}} - a_{\text{x}})^2} + \frac{1}{(L_{\text{y}} - a_{\text{x}})^2} \right) \quad (3.12)$$

where  $M$  is the 'centre of mass' exciton mass, and  $a_{\text{x}}$  is the in-plane exciton Bohr radius. Let us refer to the Bohr radii of the HH and LH excitons as  $a_{\text{hh}}$  and  $a_{\text{lh}}$  respectively. Considering the expression for the exciton Bohr radius Eq. 1.10, the exciton Bohr radius is proportional to  $1/\mu_{\text{x}}$ . We thus estimated that given a  $a_{\text{hh}}$  of 2 nm, we should expect  $a_{\text{lh}} = 1.37$  nm taking the ratio  $\mu_{\text{lh}}/\mu_{\text{hh}}$  to be 1.46 as calculated from the exciton binding energies extracted from the best quality, and unconstrained absorption fit for sample 35x8x2 in Fig 3.9. One would expect the exciton energy to increase with decreasing size due to greater in-plane confinement. Fig 3.17 shows the 1s  $X_{\text{hh}}$  and  $X_{\text{lh}}$  absorption energies plotted as a function of  $\frac{1}{L_{\text{x}}^2} + \frac{1}{L_{\text{y}}^2}$ , as well as  $\frac{1}{(L_{\text{x}} - a_{\text{x}})^2} + \frac{1}{(L_{\text{y}} - a_{\text{x}})^2}$ . For the NPLs with lateral dimensions larger than  $a_{\text{x}}$  (i.e. all data points apart from the three with the largest values of  $\frac{1}{(L_{\text{x}} - a_{\text{x}})^2} + \frac{1}{(L_{\text{y}} - a_{\text{x}})^2}$ ), a linear increase in the exciton absorption energy can be seen. From linear fits made to these data points shown in Fig 3.17 c) and d), we extracted a COM mass of  $0.8 m_{\text{e}}$  for the HH exciton and  $1.3 m_{\text{e}}$  for the LH exciton. Note that in section 3.2.1, we calculated the values  $\mu_{\text{hh}} = 0.092 m_{\text{e}}$ ,  $\mu_{\text{lh}} = 0.14 m_{\text{e}}$ ,  $M_{\text{hh}} = 0.37 m_{\text{e}}$ , and  $M_{\text{lh}} = 0.85 m_{\text{e}}$  from the in-plane charge carrier masses derived from the Pidgeon-Brown model.

As the lateral size of the NPLs decreases, the energy of the continuum (due to stronger confinement) is expected to increase faster than the exciton absorption

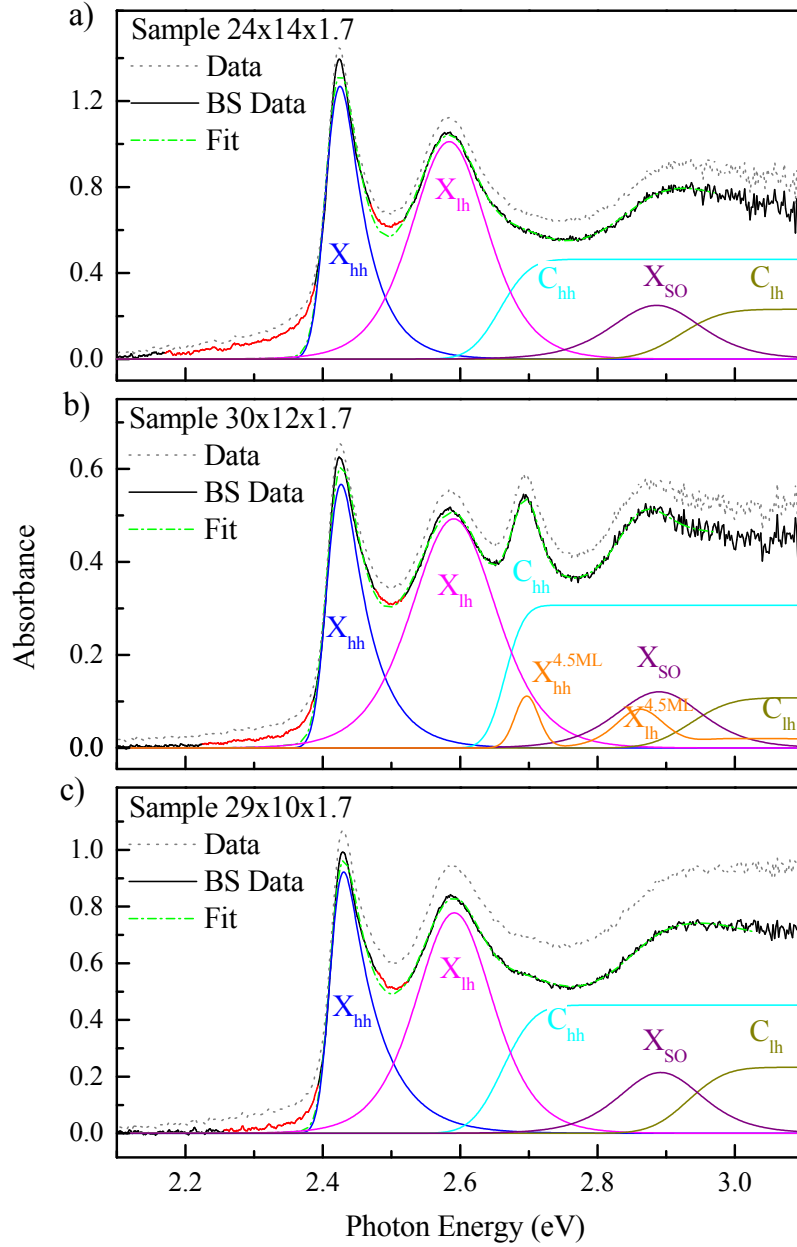


**Figure 3.13:** The room temperature background subtracted NPL absorption spectra are shown in black, and fits to the data using AM4 (see Table 3.2) are indicated with green dash-dot lines. The individual components of the fits are shown as indicated. a) is the fitted spectrum of sample 24x14x1.7, b) is the fitted spectrum of sample 30x12x1.7, and c) is the fitted spectrum of sample 29x10x1.7.

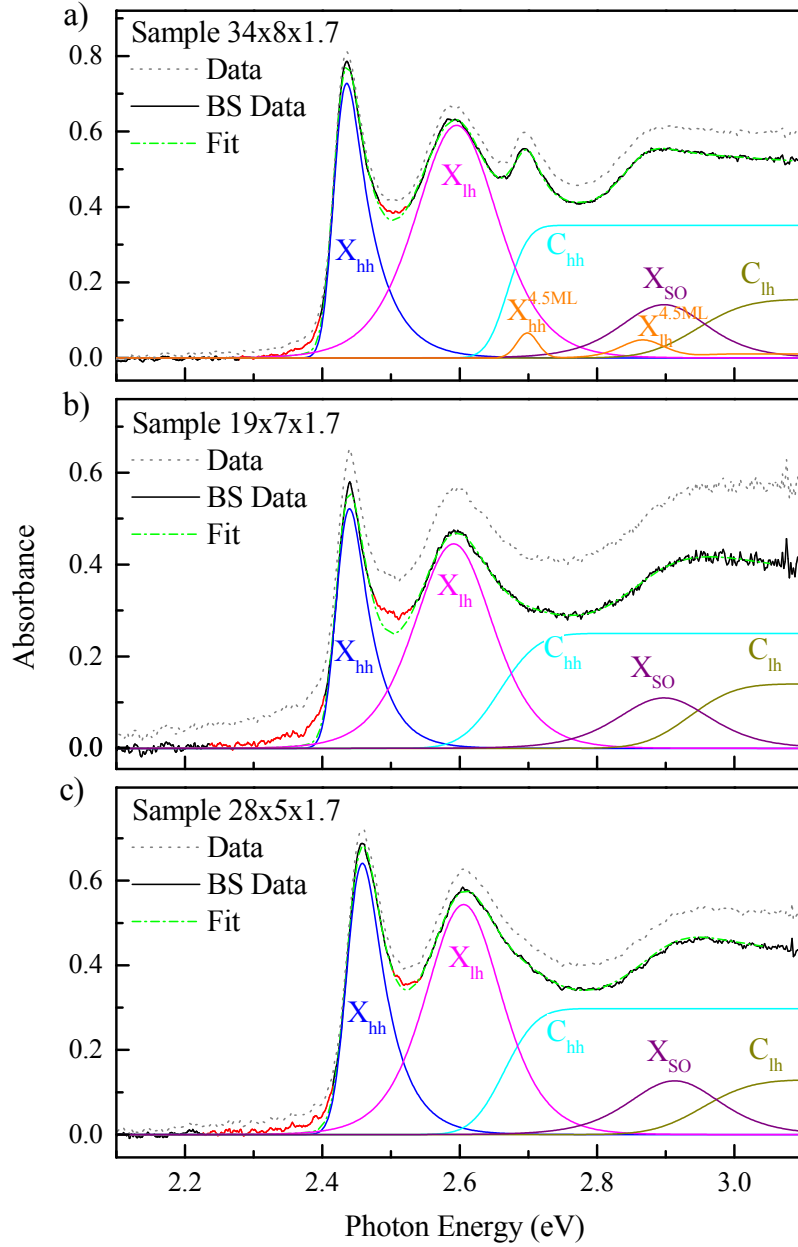


**Figure 3.14:** The room temperature background subtracted NPL absorption spectra are shown in black, and fits to the data using AM4 (see Table 3.2) are indicated with green dash-dot lines. The individual components of the fits are shown as indicated. a) is the fitted spectrum of sample 34x8x1.7, b) is the fitted spectrum of sample 19x7x1.7, and c) is the fitted spectrum of sample 28x5x1.7.

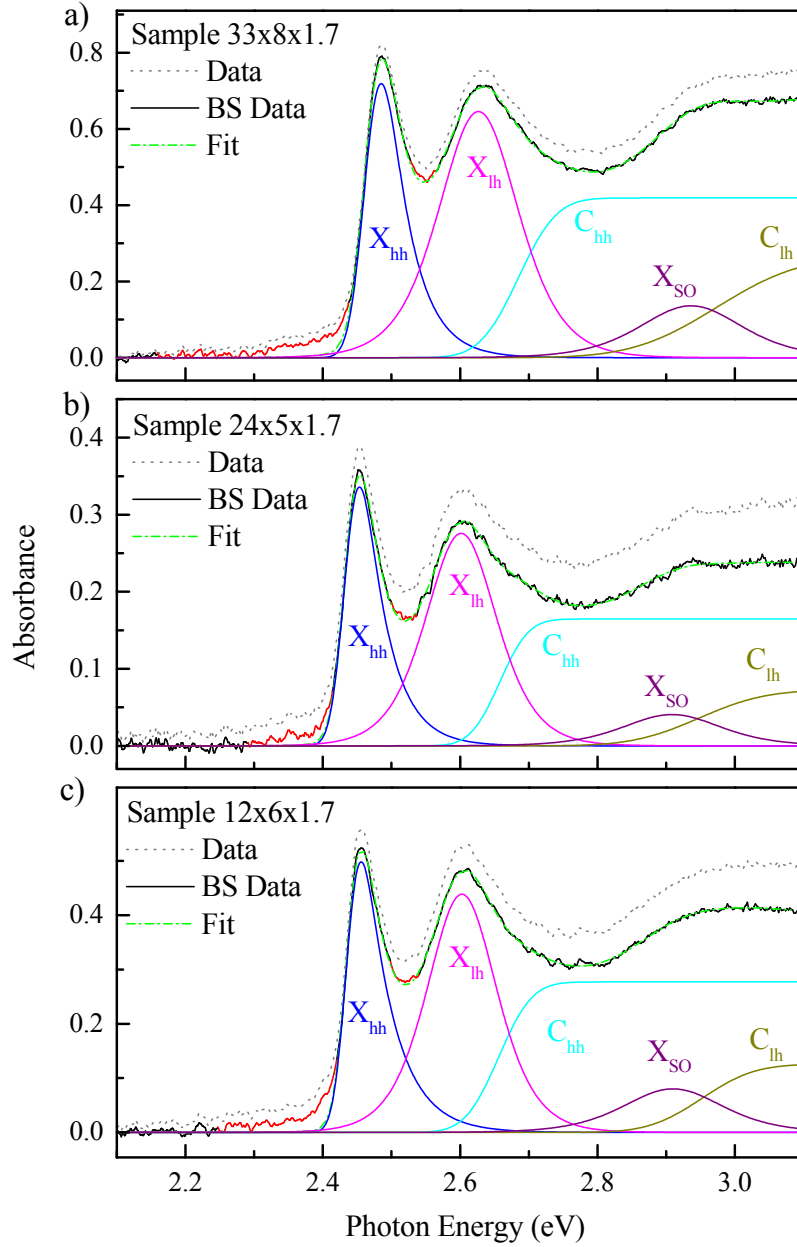


**Figure 3.15:** The room temperature background subtracted NPL absorption spectra are shown in black, and fits to the data using AM4 (see Table 3.2) are indicated with green dash-dot lines. The individual components of the fits are shown as indicated. a) is the fitted spectrum of sample 33x8x1.7, b) is the fitted spectrum of sample 24x5x1.7, and c) is the fitted spectrum of sample 12x6x1.7.

| Parameter                  | 24x14x1.7     | 30x12x1.7     | 29x10x1.7     | 34x8x1.7      |
|----------------------------|---------------|---------------|---------------|---------------|
| $A_{hh}$                   | 0.0925±0.0017 | 0.0429±0.0009 | 0.0739±0.0013 | 0.0504±0.0005 |
| $\eta$                     | 0.0369±0.0015 | 0.0410±0.0015 | 0.0487±0.0015 | 0.0381±0.0007 |
| $\Delta_{hh}$ (eV)         | 2.4075±0.0004 | 2.4088±0.0003 | 2.4124±0.0003 | 2.4193±0.0002 |
| $\gamma_{hh}$ (eV)         | 0.0230±0.0002 | 0.0220±0.0002 | 0.0196±0.0002 | 0.0197±0.0001 |
| $c_{Chh}$                  | 0.800±0.073   | 1.169±0.085   | 0.986±0.027   | 1.155±0.022   |
| $c_{Rhh}$                  | 1.084±0.054   | 1.083±0.077   | 1.067±0.017   | 1.042±0.019   |
| $\gamma_{Chh}/\gamma_{hh}$ | 2.10±0.18     | 1.42±0.21     | 2.58±0.13     | 1.731±0.096   |
| $c_{Alh}$                  | 0.846±0.039   | 0.994±0.043   | 0.818±0.038   | 1.026±0.023   |
| $\Delta_{lh}$ (eV)         | 2.5841±0.0011 | 2.5907±0.0008 | 2.5915±0.0012 | 2.5956±0.0004 |
| $\gamma_{lh}$ (eV)         | 0.0748±0.0018 | 0.0838±0.0018 | 0.0752±0.0015 | 0.0812±0.0009 |
| $c_{Clh}$                  | 0.91±0.21     | 0.80±0.66     | 1.200±0.030   | 0.962±0.037   |
| $R_{lh}$ (eV)              | 0.337±0.015   | 0.345±0.024   | 0.3406±0.0031 | 0.3503±0.0067 |
| $\gamma_{Clh}/\gamma_{lh}$ | 0.89±0.76     | 0.77±1.20     | 0.80±0.13     | 0.99±0.13     |
| $c_{so}$                   | 0.80±0.11     | 0.80±0.26     | 0.800±0.090   | 0.800±0.093   |
| $\Delta_{so}$ (eV)         | 0.39          | 0.39          | 0.39          | 0.39          |
| $\gamma_{so}$ (eV)         | 0.088±0.021   | 0.084±0.023   | 0.0820±0.0070 | 0.0850±0.0047 |

| Fit parameters             | 19x7x1.7      | 28x5x1.7      | 33x8x1.7      | 24x5x1.7      |
|----------------------------|---------------|---------------|---------------|---------------|
| $A_{hh}$                   | 0.0339±0.0009 | 0.0478±0.0007 | 0.0573±0.0012 | 0.0248±0.0005 |
| $\eta$                     | 0.0321±0.0019 | 0.0357±0.0011 | 0.0368±0.0015 | 0.0360±0.0018 |
| $\Delta_{hh}$ (eV)         | 2.4238±0.0005 | 2.4403±0.0003 | 2.4658±0.0004 | 2.4356±0.0005 |
| $\gamma_{hh}$ (eV)         | 0.0211±0.0002 | 0.0248±0.0001 | 0.0276±0.0002 | 0.0242±0.0003 |
| $c_{Chh}$                  | 1.20±0.10     | 1.027±0.049   | 1.20±0.45     | 1.09±0.23     |
| $c_{Rhh}$                  | 0.994±0.065   | 0.939±0.038   | 0.92±0.36     | 0.93±0.21     |
| $\gamma_{Chh}/\gamma_{hh}$ | 2.93±0.37     | 2.113±0.080   | 2.26±0.12     | 1.95±0.11     |
| $c_{Alh}$                  | 1.049±0.092   | 0.877±0.038   | 0.906±0.058   | 0.800±0.052   |
| $\Delta_{lh}$ (eV)         | 2.5912±0.0031 | 2.6057±0.0013 | 2.6267±0.0021 | 2.6015±0.0019 |
| $\gamma_{lh}$ (eV)         | 0.0774±0.0025 | 0.0746±0.0014 | 0.0778±0.0016 | 0.0695±0.0020 |
| $c_{Clh}$                  | 1.240±0.041   | 0.984±0.045   | 1.6171±0.5576 | 1.16±0.20     |
| $R_{lh}$ (eV)              | 0.344±0.013   | 0.348±0.012   | 0.35±0.14     | 0.347±0.078   |
| $\gamma_{Clh}/\gamma_{lh}$ | 0.99±0.36     | 1.06±0.41     | 1.74±1.23     | 1.55±1.19     |
| $c_{so}$                   | 0.99±0.22     | 0.800±0.091   | 0.80±1.26     | 0.53±0.55     |
| $\Delta_{so}$ (eV)         | 0.39          | 0.39          | 0.39          | 0.39          |
| $\gamma_{so}$ (eV)         | 0.091±0.020   | 0.0895±0.0091 | 0.100±0.029   | 0.0958±0.011  |

**Table 3.4:** Fitted parameters for the AM4 fits to the absorption spectra of NPL samples 24x14x1.7, 30x12x1.7, 29x10x1.7, 34x8x1.7, 19x7x1.7, 28x5x1.7, 33x8x1.7, and 24x5x1.7 are shown.

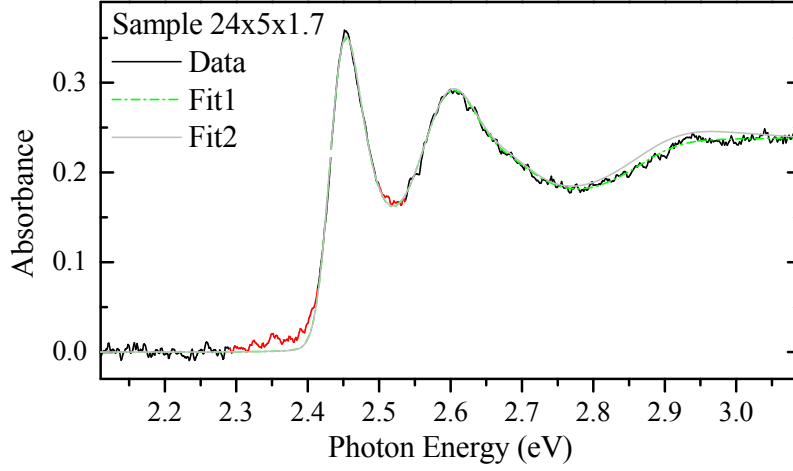


**Figure 3.16:** The background subtracted absorption spectrum for sample 24x5x1.7 is shown. Fit1, represented by the green dash-dot line, is made with the both parameters (see description of AM4 in Table 3.2) error4 and error5 allowed to have values greater and smaller than 1.2 and 0.8 respectively. Fit2, represented by the solid grey line, is made with all parameter cAlh,Rhh... constrained in the range 0.8-1.2. See Eq. 3.11 for the meaning of parameters cAlh,Rhh....

| Parameter                  | 12x6x1.7            |
|----------------------------|---------------------|
| $A_{hh}$                   | $0.0388 \pm 0.0008$ |
| $\eta$                     | $0.0420 \pm 0.0017$ |
| $\Delta_{hh}(\text{eV})$   | $2.4375 \pm 0.0003$ |
| $\gamma_{hh}(\text{eV})$   | $0.0227 \pm 0.0002$ |
| $c_{Chh}$                  | $1.183 \pm 0.066$   |
| $c_{Rhh}$                  | $0.912 \pm 0.049$   |
| $\gamma_{Chh}/\gamma_{hh}$ | $2.40 \pm 0.15$     |
| $c_{Alh}$                  | $0.800 \pm 0.053$   |
| $\Delta_{lh}(\text{eV})$   | $2.6026 \pm 0.0021$ |
| $\gamma_{lh}(\text{eV})$   | $0.0684 \pm 0.0015$ |
| $c_{Clh}$                  | $1.296 \pm 0.038$   |
| $R_{lh}(\text{eV})$        | $0.350 \pm 0.014$   |
| $\gamma_{Clh}/\gamma_{lh}$ | $1.25 \pm 0.38$     |
| $c_{so}$                   | $0.68 \pm 0.12$     |
| $\Delta_{so}(\text{eV})$   | 0.39                |
| $\gamma_{so}(\text{eV})$   | $0.098 \pm 0.016$   |

**Table 3.5:** Fitted parameters for the AM4 fits to the absorption spectra of NPL sample 12x6x1.7 are shown.

energy. The change in the exciton binding energy is given by the relative change in the energy position of the continuum edge and the excitonic absorption. We thus expected the binding energies of the HH and LH excitons to increase with decreasing size. As can be seen from both binding energies plotted in Fig 3.18, the opposite relationship was observed for the HH binding energy where a decrease in binding energy with lateral size was observed.

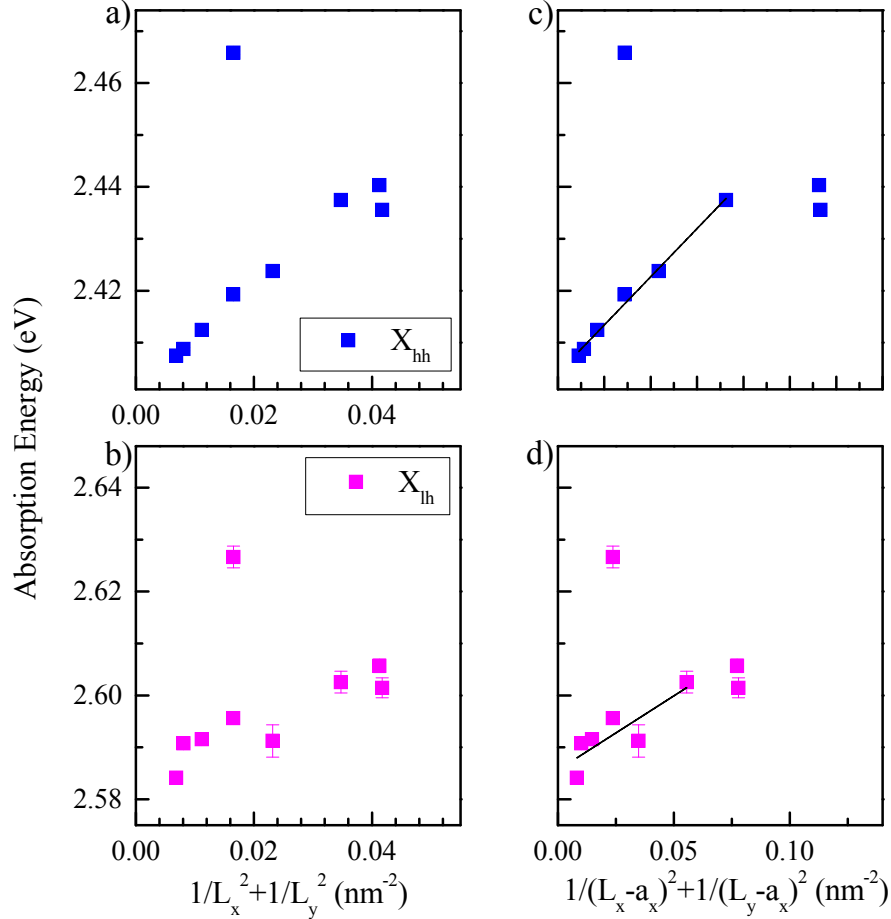


**Figure 3.17:** The size dependence of  $X_{hh}$  and  $X_{lh}$  absorption energies are shown. a) and c) show the  $X_{hh}$  absorption peak energies with  $a_{hh} = 2$  nm. b) and d) show the  $X_{lh}$  peak energies with  $a_{lh} = 1.37$  nm.

It is possible to make a theoretical prediction about the change in exciton binding energy by calculating the difference in the energy shift of the exciton absorption energy and the relevant continuum edge. This expected change in binding energy is given by:

$$\Delta R_x = \frac{\hbar^2 \pi^2}{2} \left[ \frac{1}{\mu} \left( \frac{1}{L_x^2} + \frac{1}{L_y^2} \right) - \frac{1}{M} \left( \frac{1}{(L_x - a_x)^2} + \frac{1}{(L_y - a_x)^2} \right) \right] \quad (3.13)$$

where  $\mu$  is the reduced mass of the electron and hole. The COM mass, reduced mass, and the exciton Bohr radius will all be different for the HH and LH excitons. We used the values  $\mu_{hh} = 0.092m_e$ ,  $\mu_{lh} = 0.14m_e$ ,  $M_{hh} = 0.37m_e$ , and  $M_{lh} = 0.85m_e$  calculated from the in-plane charge carrier masses derived from the Pidgeon-Brown model. Using these parameter values in Eq 3.13, we calculated the expected shifts in binding energy with varying lateral size presented in Fig 3.18 c) and d).

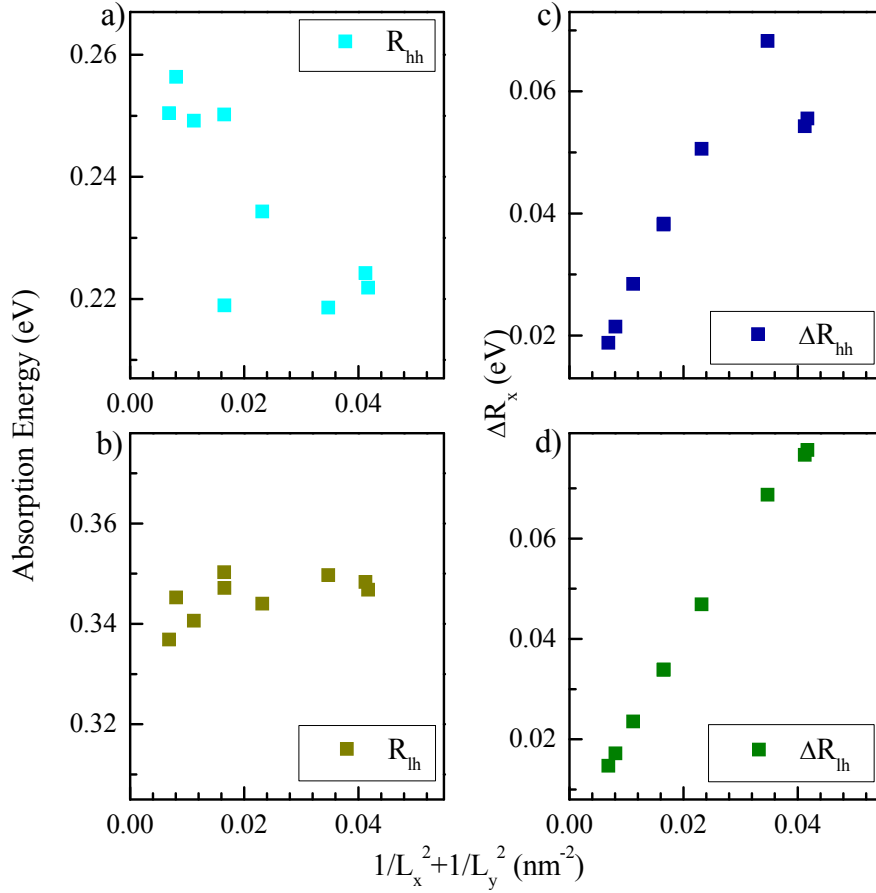


**Figure 3.18:** The size dependence of  $X_{hh}$  and  $X_{lh}$  binding energies are shown. a) shows the  $X_{hh}$  binding energies and b) shows the  $X_{lh}$  binding energies. The change in exciton binding energies calculated using Eq 3.13 is shown for  $X_{hh}$  binding energy in c) and for  $X_{lh}$  in d). For a) and c)  $a_{hh} = 2 \text{ nm}$  is used whereas for b) and d)  $a_{lh} = 1.37 \text{ nm}$  is used. The scale range on the vertical axes is the same for a) and c), and for b) and d) for comparison.

Our simple theoretical model predicts an increase in binding energy for the  $X_{hh}$  with decreasing size for all NPLs except for the two with the smallest lateral size (indicated by the largest values of  $\frac{1}{(L_x - a_x)^2} + \frac{1}{(L_y - a_y)^2}$ ). As previously mentioned, the continua are expected to increase in energy faster than the exciton absorption with increasing lateral confinement resulting in an increase in binding energy. The observed relationship for the  $X_{hh}$  binding energy implies that the  $X_{hh}$  absorption energy increases faster with confinement than the continuum. We found that the predicted relationship is strongly dependent on the exciton Bohr radius used in the calculation. We noticed that as the exciton Bohr radius value is increased, the exciton binding energies transition from increasing with decreasing size, to decreasing with decreasing lateral NPL size. If  $a_x$  is comparable to the shortest lateral dimension of the NPL, the COM confinement energy of the exciton has a greater bearing as it becomes more sensitive to the lateral size.



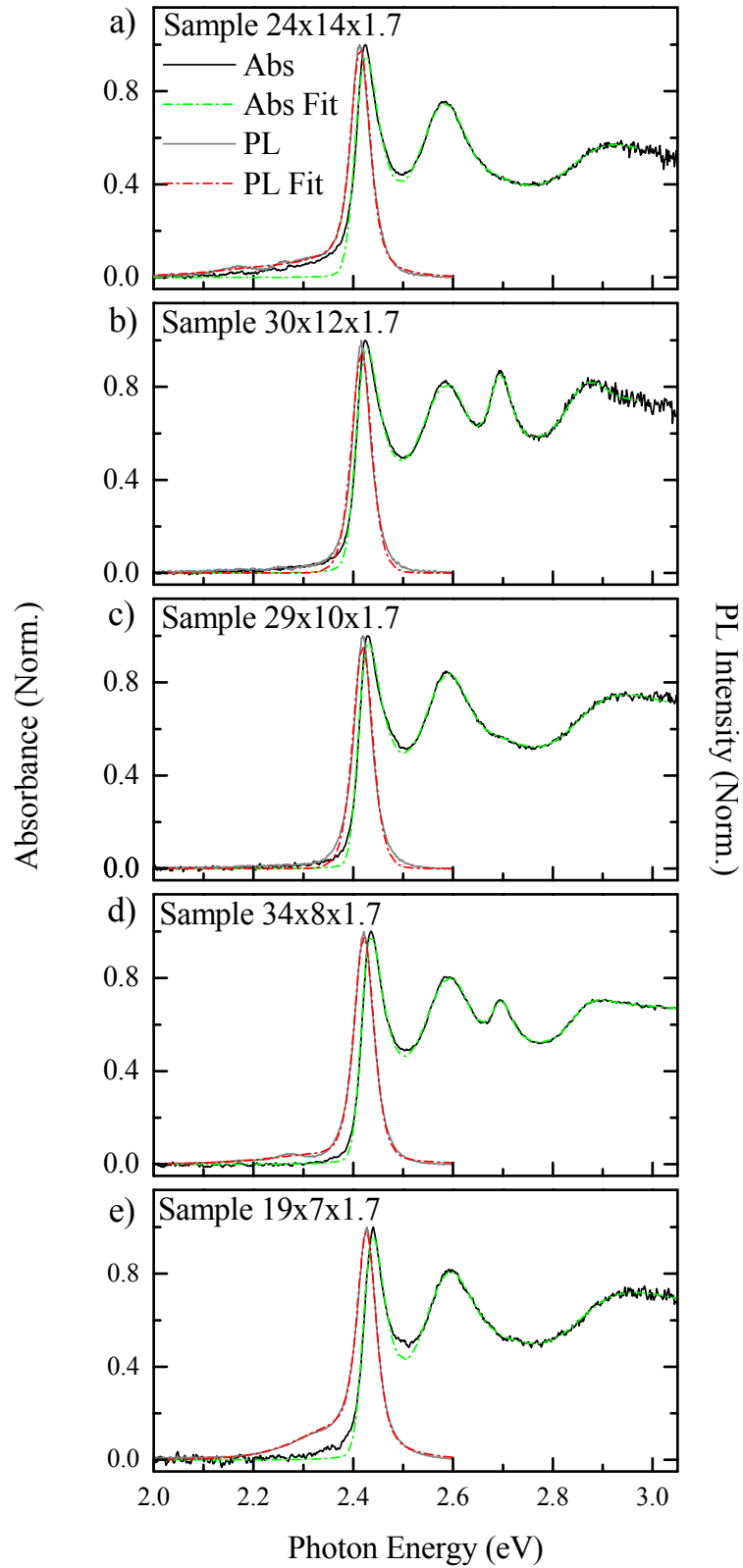


**Figure 3.19:** Normalised room temperature absorption and PL spectra of samples a) 24x14x1.7, b) 30x12x1.7, c) 29x10x1.7, d) 34x8x1.7, and e) 19x7x1.7. The data is shown using solid lines, and fits to the data are shown using dash-dot coloured lines.

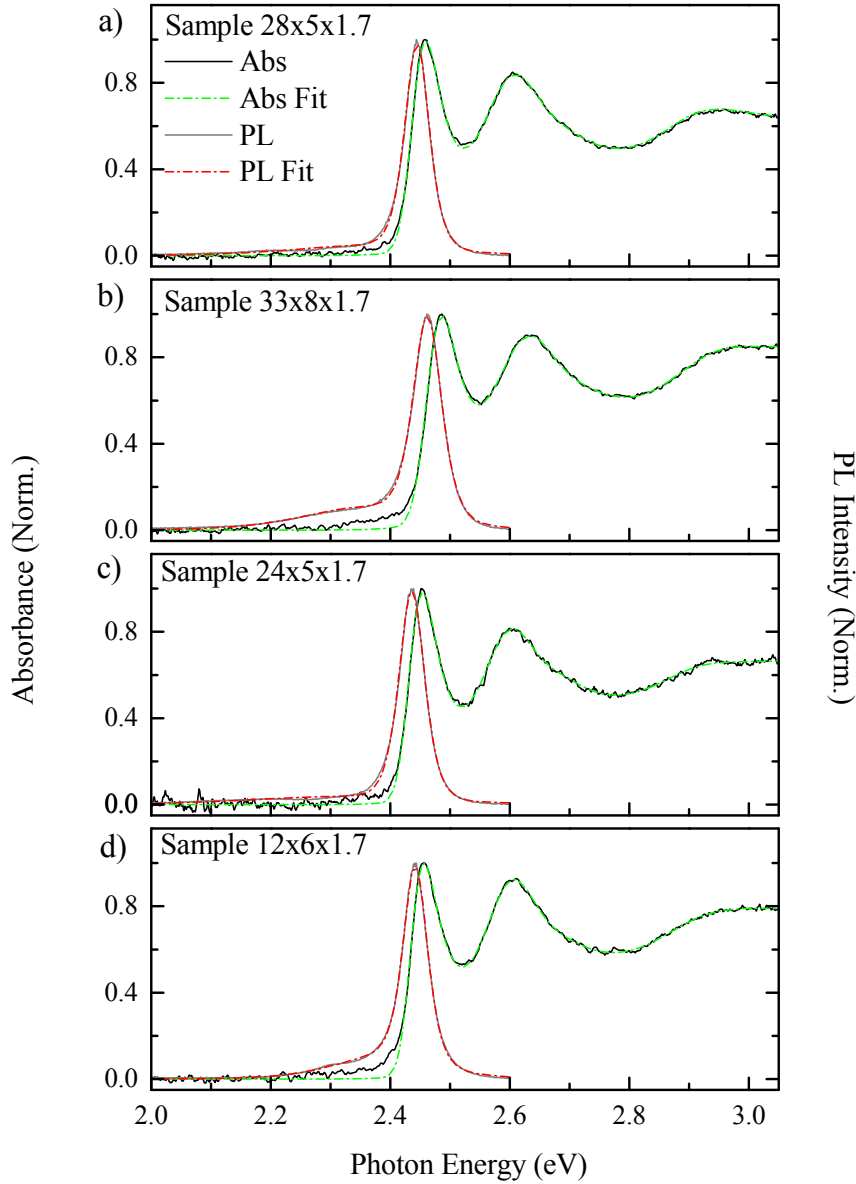


**Figure 3.20:** Normalised room temperature absorption and PL spectra of samples a) 28x5x1.7, b) 33x8x1.7, c) 24x5x1.7, and d) 12x6x1.7 are shown. The normalised data is shown using solid lines, and fits to the data are shown using dash-dot coloured lines.

It should also be noted that in the limit that the shorter NPL dimension is equal to the exciton Bohr radius, the expressions in Eq 3.13 and 3.12 are no longer valid. This is because the confinement in the shorter lateral direction starts to become almost as strong as the thickness confinement, and the structure is no longer 2D. Another factor that must be considered when one of the lateral dimensions becomes comparable to the exciton Bohr radius is the effect of dielectric enhancement. However, calculations taking account of dielectric enhancement are beyond the scope of this thesis.

Figs 3.19 and 3.20 show normalised fitted NPL absorption and PL spectra for the SDS. The PL spectra were fit with the sum of a number of  $1/\cosh^2(x)$  lineshapes

| Sample    | $A$        | $E_{PL1}(\text{eV})$ | $\gamma_{PL1}(\text{eV})$ |
|-----------|------------|----------------------|---------------------------|
| 24x14x1.7 | 424.9±1.3  | 2.41435±0.00004      | 0.02521±0.00009           |
| 30x12x1.7 | 406.4±0.9  | 2.41656±0.00005      | 0.02669±0.00007           |
| 29x10x1.7 | 661.6±1.3  | 2.41894±0.00005      | 0.02675±0.00006           |
| 34x8x1.7  | 975.5±1.0  | 2.42145±0.00002      | 0.02668±0.00004           |
| 19x7x1.7  | 940.4±1.2  | 2.42671±0.00003      | 0.02511±0.00005           |
| 28x5x1.7  | 837.6±0.8  | 2.44478±0.00002      | 0.0276±0.00004            |
| 33x8x1.7  | 1009.4±1.1 | 2.46206±0.00003      | 0.03182±0.00005           |
| 24x5x1.7  | 964.0±0.9  | 2.43607±0.00002      | 0.02876±0.00004           |
| 12x6x1.7  | 910.6±1.1  | 2.44195±0.00003      | 0.02725±0.00005           |

| Sample     | $B$       | $E_{PL2}(\text{eV})$ | $\gamma_{PL2}(\text{eV})$ |
|------------|-----------|----------------------|---------------------------|
| 24x14x1.7  | 40.7±1.5  | 2.390±0.003          | 0.091±0.005               |
| 30x12x1.7  | -         | -                    | -                         |
| 29x10x1.7  | -         | -                    | -                         |
| 34x8x1.7   | 48.6±0.6  | 2.35381±0.001        | 0.148±0.001               |
| 19x7x1.7   | 163.7±0.8 | 2.3763±0.0004        | 0.1126±0.0004             |
| 28x5x1.7   | 41.8±0.4  | 2.359±0.001          | 0.164±0.001               |
| 33x8x1.7   | 114.9±0.5 | 2.3578±0.0008        | 0.1380±0.0007             |
| 24x5x1.7   | 38.0±0.4  | 2.319±0.002          | 0.200±0.002               |
| 12x6x1.7   | 109.0±0.8 | 2.3905±0.0006        | 0.1127±0.0006             |
| Extra Comp | $C$       | $E_{PL3}(\text{eV})$ | $\gamma_{PL3}(\text{eV})$ |
| 24x14x1.7  | 19.7±1.5  | 2.24±0.01            | 0.166±0.005               |

**Table 3.6:** Fitted parameters for the fits to the PL spectra (shown in Fig 3.19 and 3.20) of all NPL samples in the size dependent sample subset.

depending on the number of separate monolayer peaks that were visible.

$$I_{PL}(E) = A \frac{1}{\cosh^2\left(\frac{E-E_{PL1}}{\gamma_{PL1}}\right)} + B \frac{1}{\cosh^2\left(\frac{E-E_{PL2}}{\gamma_{PL2}}\right)} + C \frac{1}{\cosh^2\left(\frac{E-E_{PL3}}{\gamma_{PL3}}\right)} \quad (3.14)$$

A summary of all the fit parameters can be found in Table 3.6. As expected from PL studies carried out in the literature on CdSe NPLs, only a minute stokes shift was observed as can be seen from the data presented. In addition, the small FWHM (full width at half maximum) characteristic of these structures due to a very small inhomogeneous broadening (due to a well controlled thickness) was also observed.

### 3.3 FWM measurements

By studying these NPL samples using the three beam FWM technique described in section 1.3, we wanted to probe the exciton dephasing and density dynamics within. The first sample to be studied using the three beam FWM technique comprised NPLs of thickness 5.5 ML, and size  $L_x=30.8\pm 2.6$  nm and  $L_y=7.1\pm 0.9$  nm, namely the 30×7 NPLs. Dephasing and density grating measurements were acquired as a function of temperature with measurements acquired at intervals of 2.5 K from 5 K upto 15 K, at intervals of 5 K from 15 K to 30 K, and in increments of 10 K upto 50 K. A discussion of the obtained results and their physical interpretation is presented in the following subsections.

### 3.3.1 Temperature dependent absorption

Temperature dependent absorption spectra were acquired as the sample was cooled to 20 K in order to find the appropriate excitation wavelengths to be used for the experiments. Fig 3.21 a) shows the absorption spectra at a few different temperatures. Fig 3.21 b) shows the room temperature spectrum alongside a spectrum taken at 20 K. With decreasing temperature, the shift of the absorption spectrum to higher energies is accompanied by a reduction in the linewidths. This can be seen in both the heavy and light hole absorption peaks. The linewidth is reduced due to reduced homogeneous broadening related to phonon scattering [61] [16].

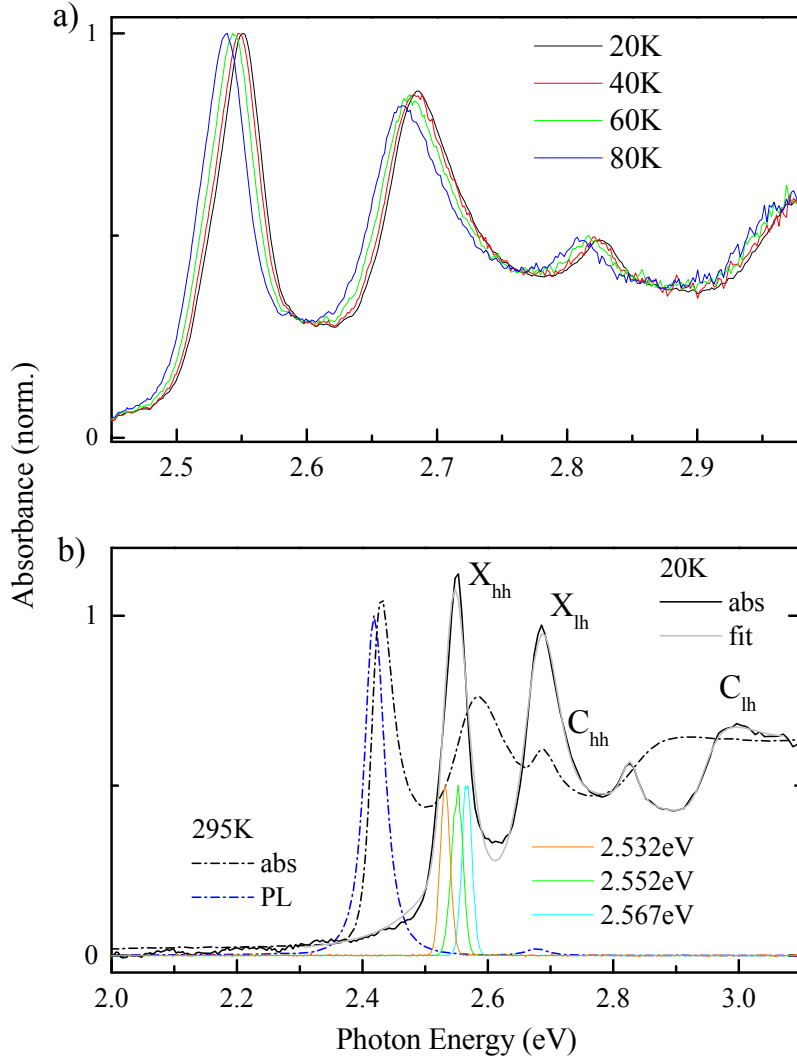


**Figure 3.21:** Linear optical properties of sample 30x7. Figure a) shows absorption spectra of the NPLs prepared in a PS film at the indicated temperatures. b) shows the absorption and PL spectra at 295K using the black and blue dashed lines respectively. The black solid line is the absorption at 20 K with the grey showing a fit to the data. The spectrum of the laser with the wavelengths used for FWM measurements are indicated by the orange, green, and cyan lines. The inset shows a TEM image of the NPLs with a scale bar of 50 nm.

The absorption spectrum is fit using the same procedure described in section 3.2.1. The fit reveals a heavy hole exciton peak linewidth of  $46 \pm 1$  meV (FWHM), and HH

and LH binding energies of  $(178 \pm 34)$  meV, and  $(259 \pm 3)$  meV respectively [45]. Note that the same fixed ratio for binding energies as the fits in section 3.2.3 is used. The peak linewidth is dominated by inhomogeneous broadening.

Our intention was to probe the dynamics of the bright HH exciton. We therefore excited the sample with a wavelength close to the HH excitonic absorption peak. Since the change in the HH exciton peak position between 20 K and 50 K is small compared to the laser linewidth (see Fig. 3.21 a)), we elected to use the same excitation wavelength in this temperature range. The peak position is not expected to shift further to higher energies below 20 K.

The laser spectra are shown in Fig. 3.21 b). These indicate the excitation wavelengths used for energy dependent dephasing measurements acquired at 20 K to be presented in the following subsection.

### 3.3.2 Dephasing and density grating measurements

As discussed in section 1.3.3, measuring the FWM field amplitude as a function of  $\tau_{12}$  reveals the dephasing dynamics, whereas the FWM field amplitude versus  $\tau_{23}$  reveals the population dynamics of the sample. For the dephasing measurements on the NPLs,  $\tau_{23}$  was fixed at 1 ps in order to exclude non-resonant non-linearities. Power dependent measurements were first acquired in order to ensure that the beam power used in the subsequent experiments did not effect the dynamics due to local heating. Power dependent dephasing measurements at 20 K are shown in Fig. 3.22. We can see that there is no difference in the dephasing dynamics as a function of excitation power in the range investigated. The time averaged excitation intensity of each beam was  $17 \text{ W/cm}^2$  which is within the third order non-linear response regime (confirmed by checking that the amplitude of the signal scaled as third order). The sample, prepared as described in section 3.1.1, had a distribution of randomly oriented NPLs. In order to minimize the selective excitation of linearly polarised transitions in the ensemble, all pulses were co-circularly polarised at the sample.

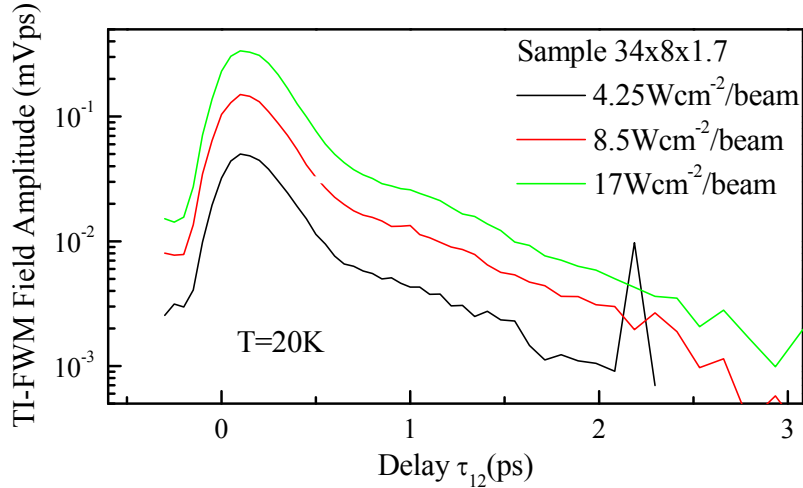


**Figure 3.22:** The time-integrated (TI) FWM field amplitude as a function of  $\tau_{12}$  for sample 34x8x1.7 at 20 K for three different excitation powers as indicated.

Measurements of the dephasing for different temperatures, and for different excitation energies at a constant temperature are shown in Figures 3.23 a) and 3.23 b) respectively. The decay of the photon echo field amplitude was fit using a sum of

exponential decays. The fit function is expressed as follows:

$$y = Ae^{-2\gamma_1\tau_{12}} + Be^{-2\gamma_2\tau_{12}} + Ce^{-2\gamma_3\tau_{12}} \quad (3.15)$$

The fits were made for  $\tau_{12} > 0.3$  ps. Two exponential decay components were needed to describe the dynamics for temperatures greater than 10 K, where as for lower temperatures three components were needed. We denote the fastest dephasing rate with  $\gamma_1$  and the slowest with  $\gamma_3$ . The fits to the energy dependent dephasing curves yield a  $\gamma_1$  which increases slightly with excitation energy, and a  $\gamma_2$  which slightly decreases with energy. The relative weight of  $\gamma_1$ , labelled the ZPL weight in the figure, shows a decrease with increasing energy. The physical origins of the different decay rates as well as the reason for relating  $\gamma_2$  to purely radiative decay are discussed in the next section.

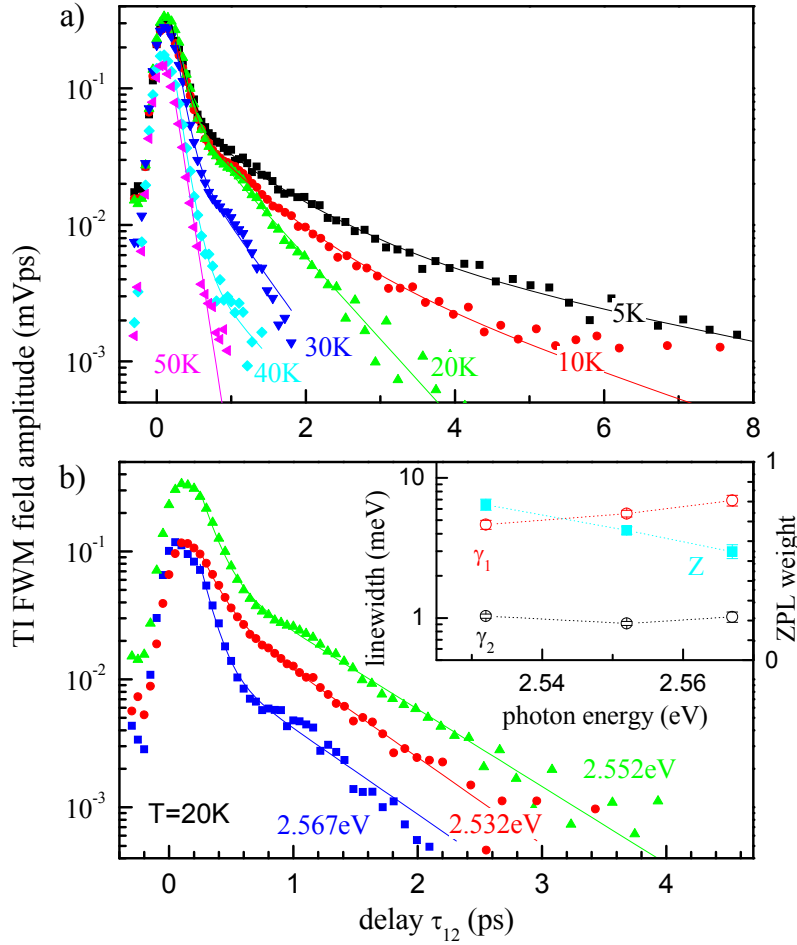


**Figure 3.23:** The time-integrated (TI) FWM field amplitude as a function of  $\tau_{12}$  at  $\tau_{23} = 1$  ps for sample 34x8x1.7 is shown. The solid lines are fits to the data. a) for a range of temperature and an excitation energy of 2.552 eV. b) for 20 K and the three indicated excitation energies. The linewidths  $2\hbar\gamma_{1,2}$ , and the ZPL weight extracted from the fits to these three curves are shown in the inset as a function of excitation energy.

The FWM signal versus  $\tau_{23}$  curves that result from the density grating (DG) measurements are shown in Fig 3.24. Fig 3.24 a) shows DG curves for different values of  $\tau_{12}$  at a fixed temperature of 12.5 K. Temperature dependent curves can be

seen for  $\tau_{12} = 0$  ps in Fig 3.24 b). The  $\tau_{12}$  dependence was initially acquired because these measurements can eluminate details about the density dynamics related to the fine structure. When  $\tau_{12} > 0$ , the density grating is spectrally modulated and the excitation can probe the density dynamics of nearby energy levels. Enlightening results from such measurements have been obtained for CdSe/ZnS CQDs and Cd-Se/CdS QDs presented in our group's previous works [4] and [5]. In the case of the NPL samples, these measurements provided useful information about damped oscillations which could already be observed in the temperature dependent DG curves for  $\tau_{12} = 0$  in Fig 3.24 b).

All fits to the DG curves are made with the following function:

$$S(t) = \sum_{n=1}^j A_n \exp\left\{\frac{\tau_{ac}^2}{2T_n^2} - \frac{t}{T_n}\right\} \left[ \frac{1}{e^{\frac{T_p}{T_n}} - 1} + \frac{1 + Be^{-\gamma_p t} \cos(\omega_p t)}{2} \left(1 + \operatorname{erf}\left(\frac{t}{\tau_{ac}} - \frac{\tau_{ac}}{2T_n}\right)\right) \right] \quad (3.16)$$

where  $\tau_{ac}$  is the autocorrelation time, and  $T_p$  is the laser period. In order to describe the physical origin of the terms in the above expression, let us first consider the population decay of a simple two level system. The time dependent population of the upper state after excitation can be written as:

$$N(t) = N_0 \theta(t) e^{-t/T_1} \quad (3.17)$$

where  $T_1$  is the population decay time and  $N_0$  is the population of the upper state at  $t = 0$ . If the population in the upper state is created at  $t = 0$ , a signal proportionla to the population will depend on time as shown in Fig ??

However, to account for the fact that in our experiments we excite the population with Gaussian pulses of finite width, we must calculate the convolution integral between Eq 3.17 and a Gaussian lineshape. The result of this calculation yields the terms  $\exp\left\{\frac{\tau_{ac}^2}{2T_n^2} - \frac{t}{T_n}\right\}$  and  $\left(1 + \operatorname{erf}\left(\frac{t}{\tau_{ac}} - \frac{\tau_{ac}}{2T_n}\right)\right)$  in Eq 3.16. Eq 3.16 accounts for a number of exponential population decays equal to  $j$ . It could also be the case that decay times  $T_n$  exist that are longer than the laser period  $T_p$ . In such a case, the signal from previous pulses wil "pile-up" and create a non-zero population signal before the arrival of the excitation pulses. To account for this, we take the sum of the geometric progression  $\sum_{k=1}^{\infty} e^{-\frac{T_p}{T_n} k}$  which results in the term  $1/\left(e^{\frac{T_p}{T_n}} - 1\right)$  in Eq 3.16. The part of the function  $(1 + Be^{-\gamma_p t} \cos(\omega_p t))$  was added to fit the observed damped oscillations.

The fits to the DG data are made two exponential decays with amplitudes  $A_{1,2}$  and decay rates  $\Gamma_1 > \Gamma_2$ .  $\Gamma_2$  is longer than the pulse period and results in a pile up of the signal. It is interesting to note from the  $\tau_{12}$  dependence in Fig. 3.24 a) that the inportance of the long lived component decreases as the delay  $\tau_{12}$  increases. The decay rates however are unaffected whithin error. The macroscopic polarization generated in the ensemble after the first pulse will decay due to dephasing effects untill the second pulse arrives. The fact that the amplitude of the long lived component decreases more than the short lived one with increasing  $\tau_{12}$  indicates that the long lived component has a faster dephasing rate and is thus spectrally broader.

As mentioned before, the density dynamics for  $\tau_{12} \neq 0$ , if modified, reveal information about the fine structure. Since modified dynamics for  $\tau_{12} \neq 0$  are not observed, it is unlikely that this time constant is due to relaxation between the different dark/bright excitonic states as was the case for spherical nanocrystals [4] [5]. The decay of a spin-forbidden dark state excited by the pulses could also give

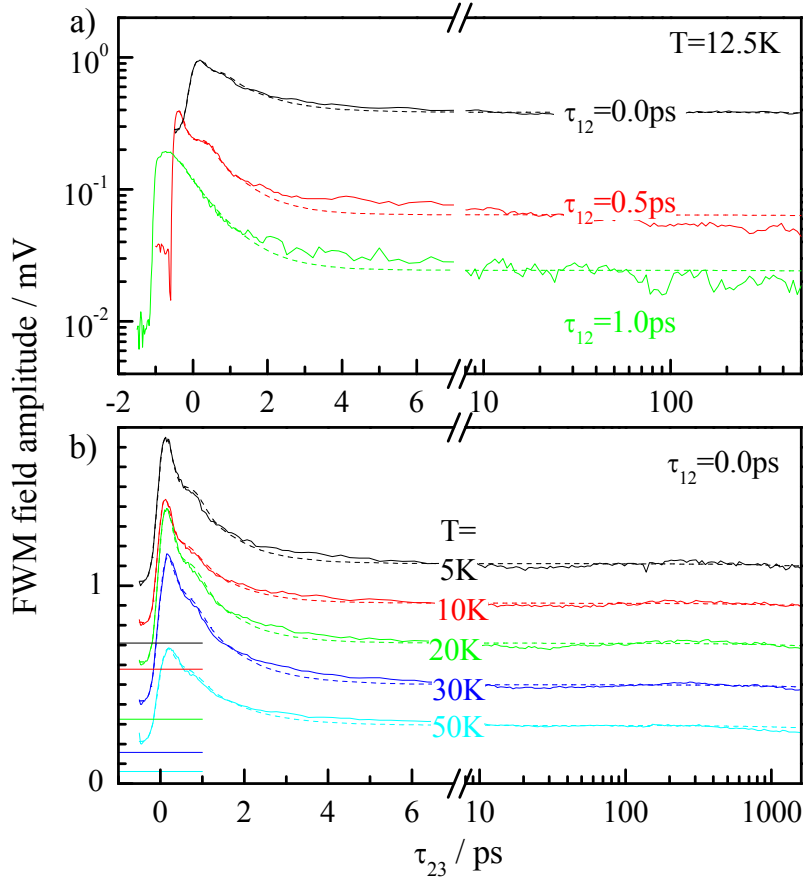


**Figure 3.24:** Exciton density dynamics measured from the TI-FWM field amplitude versus  $\tau_{23}$  at fixed  $\tau_{12}$ . Dashed lines are fits to the data. a) Measurements at 12.5 K for different values of  $\tau_{12}$ , as indicated. b) Measurements at  $\tau_{12} = 0$  ps for different temperatures, as indicated.

a long lived component. We note from the data that the time  $1/\Gamma_2$  does not vary significantly within the temperature dependence from 5 to 50 K. This allows us to estimate a lower limit of the energy splitting between the dark and bright states, if  $\Gamma_2$  is assumed to be the population decay from this dark state. We note that  $\delta_0 > k_B T \log\left(\frac{\Gamma_2}{\Gamma_1}\right) \approx 40$  meV using the temperature value 50 K. In colloidal CdSe dots, the dark bright splitting is of the order 1-10 meV. We would not expect this splitting to be so much larger in our NPLs, and we therefore disregard this explanation as a possibility.

We propose that the long lived component is due to charge carriers becoming trapped in the surroundings, and resulting in charging of the NPLs. Since this component does not only retain the specific bleaching of the directly excited state but also creates additional charged exciton transitions, it leads to a broad spectral response, as indicated by the data and previously discussed.

For the damped oscillations, we obtained an energy  $\hbar\omega_p = 4.1 \pm 0.1$  meV and a linewidth of  $\hbar\gamma_p = 1.5 \pm 0.2$  meV. One possibility for the origin of these oscillations are acoustic phonons generated by the exciton density. The creation of excitons is changing the equilibrium lattice constant within the structures causing acoustic oscillations. These would result in a time varying change in the dimensions of the NPLs, and since the exciton energy level separation depends on the quantum



confinement and therefore structure size, the result will be a time varying shift in energy of the bright excitonic state being probed. Thus, a signal proportional to the population of this energy level will also vary in time.

It turns out that the energy of the lowest longitudinal acoustic (LA) phonon mode confined by the NPL thickness is  $\hbar\omega_p = \hbar\nu/2L_z = 4.6$  meV. using the LA velocity in CdSe of  $v = 3.7 \times 10^3$  ms<sup>-1</sup> [74]. This result is remarkably close to the oscillation frequency observed in the data. We therefore attribute these oscillations to the LA phonon mode. It must be noted that the dimension  $L_z$  (the thickness of the NPLs) is much smaller than the lateral dimensions. This means that we can ignore any in-plane component of these phonons. Remembering that the NPLs are distributed in a polystyrene (PS) matrix, we can also try to estimate the decay rate of the phonons. The amplitude reflection coefficient can be calculated from the acoustic impedances of the materials either side of the boundary. It is given by

$$r = \frac{Z_{PS} - Z_{CdSe}}{Z_{PS} + Z_{CdSe}} \quad (3.18)$$

where the impedance ( $Z = v\rho$ ) is the product of the density and acoustic velocity. The amplitude reflection coefficient in this case is  $r = 0.75$ . We can equate this to the fraction of the amplitude remaining after the phonon meets one of the two boundaries once,  $r = e^{-\frac{L_z\gamma_p}{v}}$ . The estimated linewidth is therefore given by  $\hbar\gamma_p = -\hbar\ln(0.75)/L_z = 0.44$  meV. This is significantly smaller than measured because the NPL thickness corresponds to roughly 6 styrene ring diameters, we can expect a coupling to PS that varies within the ensemble. This would result in an inhomogeneous distribution of phonon oscillation frequencies, and account for the significantly larger than expected measured linewidth.

We can see from Fig. 3.24 a) that the oscillations are most prominent at  $\tau_{12} = 0.5$  ps. It seems to be the case that when the value  $\omega_p\tau_{12} = 0, 2\pi, \dots$  the phonon oscillations are suppressed, whereas for  $\omega_p\tau_{12} = \pi, 3\pi, \dots$  these oscillations are more apparent in the DG curves. We note that  $\omega_p\tau_{12} = \pi$  for  $\tau_{12} = 0.5$  ps, and  $\omega_p\tau_{12} = 0, 2\pi$  for  $\tau_{12} = 0, 1$  ps (see [75]).

### 3.3.3 Temperature dependence

The linewidths (FWHM) associated with the measured decay rates are given by  $2\hbar\gamma_i$  in the case of the dephasing measurements, and  $\hbar\Gamma_j$  in the case of the density grating measurements. The density decay linewidths, as well as the homogeneous linewidths are displayed as a function of temperature in Fig 3.25. We note that for temperatures of 10 K or below the homogeneous linewidth is the same as the density decay linewidth within error, namely  $2\gamma_2 \approx \Gamma_1$ . This means that at low temperatures the loss of the macroscopic polarization is limited by the lifetime of the excitonic state, and not by pure dephasing processes. We attribute  $\gamma_2$  to the zero-phonon-line (ZPL) dephasing of the lowest bright excitonic state. We therefore refer to the relative weight of the  $\gamma_2$  component as the ZPL weight. The ZPL linewidth obtained from the data at low temperatures is  $2\hbar\gamma_0 = 0.7$  meV, which is significantly larger than the linewidth of  $6 \mu\text{eV}$  found in spherical quantum dots deduced from dephasing times as long as 100 ps [4] [54]. The observed linewidth is however consistent with PL linewidths of single NPLs at low temperature [61], [16].

We have fit the temperature dependence of the ZPL width with the following

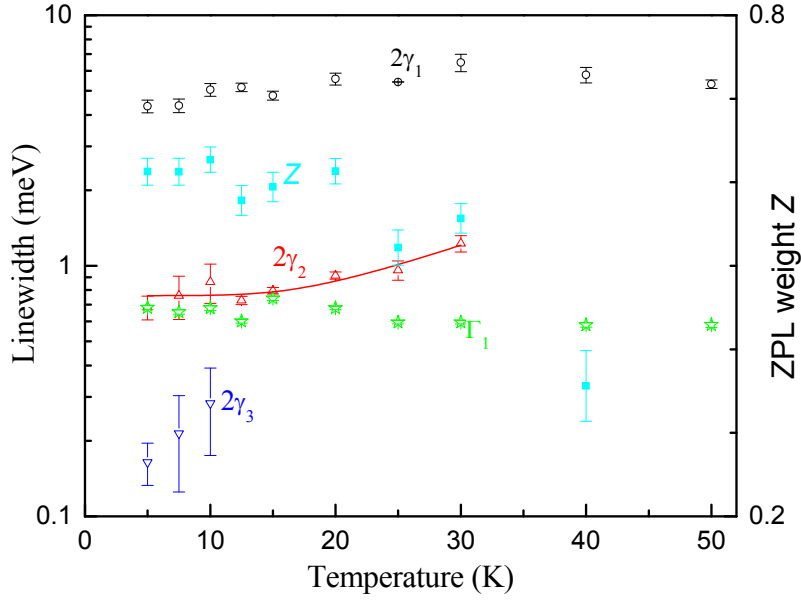


**Figure 3.25:** The homogeneous linewidths  $2\hbar\gamma_{1,2,3}$  and ZPL weight  $Z$  extracted from the dephasing measurements, and the lifetime-limited linewidth  $\hbar\Gamma_1$  from the DG measurements are shown as a function of temperature. The solid line is a fit to the linewidth data using a temperature activated behaviour.

temperature activated behaviour:

$$2\hbar\gamma_2 = 2\hbar\gamma_0 + \frac{b}{e^{\Delta/k_B T} - 1} \quad (3.19)$$

where  $b$  is the spontaneous scattering rate, and  $\Delta$  is the activation energy for the evolution of the linewidth away from its lower limit. Our fit reveals an activation energy of  $\Delta = 7 \pm 3$  meV and a scattering rate of  $b = 6$  meV. These values are also consistent with the observed narrowing of the heavy hole absorption exciton absorption peaks in the temperature dependent absorption data. The physical origin of the scattering process with this energy can be found by calculating the energy of excitonic states which are confined in terms of their centre of mass (COM) motion within the lateral size of the NPLs. We can use a particle in a box type calculation in which the energies are given by:

$$E_{n_x n_y} = \frac{\hbar^2 \pi^2}{2M} \left( \frac{n_x^2}{(L_x - 2a_B)^2} + \frac{n_y^2}{(L_y - 2a_B)^2} \right) \quad (3.20)$$

where  $a_B$  is the exciton Bohr radius in-plane, and  $M$  is the sum of the electron and hole mass calculated using the Pidgeon-Brown model. It is the exciton COM mass with a value of  $0.37 m_e$ . The numbers  $n_{x,y}$  are simply the integer quantum numbers. Interestingly, the energy separation between the bright ground exciton state ( $n_x = 1, n_y = 1$ ) and the next energy state up, i.e. the  $n_x = 2, n_y = 1$  state, is 4 meV. Since this is similar to the temperature activation energy within error, we can assume that the increase in linewidth seen with increasing temperature is due to scattering into this higher energy state. This scattering is facilitated by acoustic phonon absorption. The (2,1) state will be a dark state due to its odd parity.

In quantum dots, a non-Lorentzian lineshape which comprises a broad phonon band with a much narrower, typically a few meV broad, zero-phonon line on top due

to the exciton. This broad phonon band presents itself as a much faster initial decay of the FWM signal (seen in the dephasing curves) in the time domain. This combined with the fact that the weight of the  $\gamma_1$  component increases with temperature, as evidenced by a decreasing ZPL weight with increasing temperature, leads us to conclude that  $\gamma_1$  is due to the phonon broad band. Another interesting point is the maximum observed ZPL weight of 0.6. The ZPL weight is expected to scale with the volume of the nanostructure in question. In spherical CdSe nanocrystals of volume  $200 \text{ nm}^3$ , a similar ZPL weight is seen [4]. Since these NPLs have a volume of  $500 \text{ nm}^3$ , this result was unexpected. We have noticed however that in the PL spectra of NPLs provided in ref [61], there is a satellite emission peak on the high energy side roughly 4 meV away from the bright state. The amplitude of this satellite is approximately 10% of the bright state. We should expect that this satellite state has a similar absorption to the bright state due to the fact that for an energy separation of 4 meV, the Boltzmann factor of the thermal population is roughly 0.1. Since the two states have similar absorption, we would expect the ZPL weight to be roughly 0.5. The higher energy state will enhance the phonon broad band due to exciton-polaron transitions [76].

Finally, we attribute the weak longer dephasing component for  $T \leq 10 \text{ K}$  to the presence of a fraction of NPLs in which the coherence area of the exciton is reduced. This could be due to, for example, missing atoms in the top layer of the NPL. We would not expect such a small fraction ( $\frac{A_3}{A_3+A_2} \approx 13\%$ ) to make a significant difference to the density dynamics, so the two sets of data remain consistent with each other. We note that for  $\tau_{12} = 1 \text{ ps}$  (only when the offset is suppressed), a weak roughly 5 ps decay can be seen which is consistent with the dephasing time  $\frac{1}{2\gamma_3} \approx 5 \text{ ps}$ .

### 3.3.4 Physical interpretation of FWM measurements

The low temperature bright exciton lifetime of just 1 ps is the most significant result of these measurements. We have already noted that this lifetime is very short compared to the times seen in spherical nanocrystals which can be  $\approx 10 \text{ ns}$ . The NPLs are related to quantum well systems; they exhibit quantum confinement in only one direction. It therefore stands to reason that the lifetimes in the NPLs should be more comparable to those found in quantum wells. In 10 nm wide ZnSe/ZnMgSSe quantum wells [77], as well as 16-20 nm wide ZnSe/ZnMgSe wells [78], the radiative lifetime of the heavy hole exciton was measured to be  $\approx 1 \text{ ps}$ . It has also been calculated to be 12 ps in [79] for 10 nm wide GaAs/AlGaAs quantum wells. "Giant oscillator strength" is the phenomenon in which the radiative lifetime decreases with increasing extension of the exciton COM [16] [31] [80]. In laterally extended NPLs (much larger than investigated in this work), we would expect the lifetime to be even faster 1 ps. Considering that the binding energy of the exciton is large,  $R_{hh} \approx 250 \text{ meV}$  compared to 25 meV in ZnSe quantum wells, we can expect lifetimes as short as 100 fs. The NPLs are thus colloidal quantum wells of finite lateral size.

The exciton being confined in plane by the lateral size of the NPLs is consistent with the lifetime of about 1 ps that we have measured. Due to the giant oscillator strength effect, we would expect the radiative rate to be proportional to the NPL area. This is true for the cases where the exciton Bohr radius  $a_B$  is much smaller than the NPL size, and where the NPL size is much smaller than the excitation wavelength. In the next section we present measurements on a variety of sizes of NPLs in order to verify the physical interpretation we have presented here.

## 3.4 Size dependent four wave mixing

In this section we present the results of three beam FWM experiments on NPLs samples of thickness 5.5 ML and different lateral sizes, including samples 12x6x1.7, 24x5x1.7, 29x10x1.7, 24x14x1.7, and 30x12x1.7. We will refer to this set of samples, and sample 34x8x1.7, as our FWM SDS. We will compare the results obtained from these samples to those of sample 34x8x1.7 in the previous section in order to study the size dependence of the exciton dynamics. We begin by presenting the dephasing dynamics before moving on to the density dynamics, and finally discussing the dependence of the exciton dephasing times and lifetimes on temperature.

### 3.4.1 Dephasing

The dephasing dynamics for the samples in the FWM SDS are shown in Fig. 3.26 for a range of temperatures. We note that, as for sample 34x8x1.7, the data shows a fast initial decay of the signal attributed to the phonon broadband. For all samples, the data shows at longer times an exponential decay which we attribute to the ZPL emission. The data for sample 24x5x1.7 shows additionally a third, longer exponential decay at the lowest investigated temperature of 5 K. The fits to the data shown in Fig. 3.26 are made with the sum of two exponential components. Following the naming convention used in the previous section, we label the dephasing decay rates  $\gamma_1$  and  $\gamma_2$ , with  $\gamma_1$  corresponding to the faster initial decay. We included a third component  $\gamma_3$  in the fit to the 5 K data for sample 24x5x1.7.

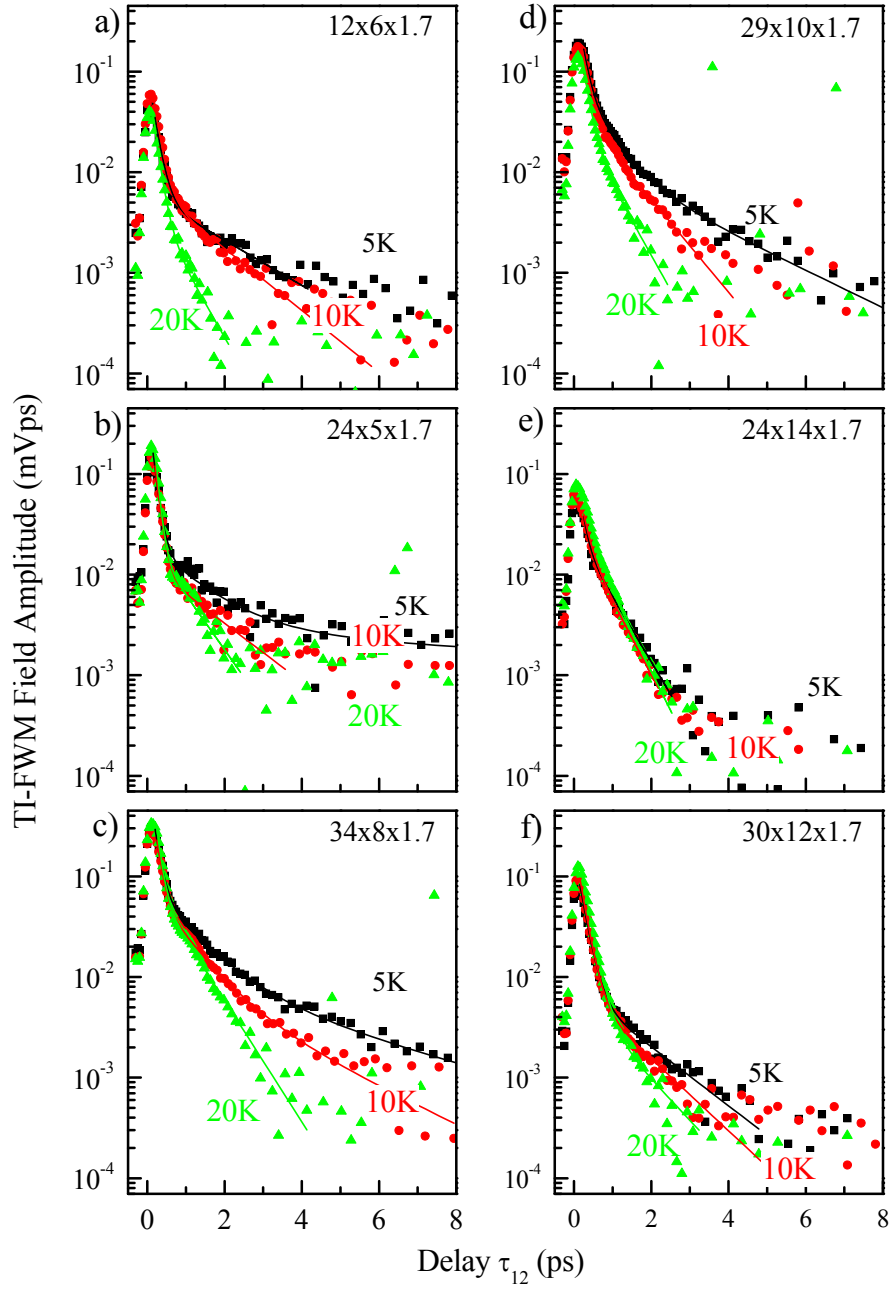


**Figure 3.26:** Time-integrated (TI) FWM field amplitude as a function of  $\tau_{12}$  at  $\tau_{23} = 1$  ps for the FWM NPL SDS as indicated. Data acquired at temperatures of 5, 10 and 20 K is shown for each sample. Fits to the data are shown using solid lines.

### 3.4.2 Density dynamics

The measured density dynamics for the FWM size dependent NPL subset are shown for a range of temperatures in Fig. 3.27. The fits to the data shown were made with Eq. 3.16 as for sample 34x8x1.7. Table 3.7 shows the fitting parameters for the fits to the 5 K density dynamics for all samples in the FWM SDS. We noticed that for all samples except 29x10x1.7 showed three decay times. For sample 29x10x1.7 only two decay times were needed for sample 34x8x1.7 in section 3.3. As in section 3.3.2, we attribute the shortest decay time in this data to the ground state exciton

| Samples                    | 12x6x1.7          | 24x5x1.7          | 34x8x1.7          |
|----------------------------|-------------------|-------------------|-------------------|
| $\tau_{ac}(\text{ps})$     | $0.103 \pm 0.005$ | $0.144 \pm 0.016$ | $0.239 \pm 0.005$ |
| $A_0(10^{-4}\text{Vps})$   | $1.54 \pm 0.01$   | $2.92 \pm 0.04$   | $9.0 \pm 0.1$     |
| $A_1$                      | $0.367 \pm 0.012$ | $0.776 \pm 0.008$ | $0.902 \pm 0.005$ |
| $T_1(\text{ps})$           | $1.91 \pm 0.13$   | $1.564 \pm 0.048$ | $0.967 \pm 0.018$ |
| $A_2$                      | $0.106 \pm 0.012$ | $0.098 \pm 0.008$ | 0                 |
| $T_2(\text{ps})$           | $21.3 \pm 4.3$    | $262 \pm 62$      | -                 |
| $A_3$                      | $0.527 \pm 0.017$ | $0.126 \pm 0.011$ | $0.033 \pm 0.005$ |
| $T_3(\text{ns})$           | $3.9 \pm 8.3$     | $83.2 \pm 7.8$    | $52.9 \pm 3.6$    |
| $K(\text{Vps})$            | $0.380 \pm 0.006$ | 0                 | 0                 |
| $t_0(\text{ps})$           | $0.029 \pm 0.003$ | 0                 | 0                 |
| B                          | 0                 | $0.65 \pm 0.03$   | $0.47 \pm 0.01$   |
| $\gamma_p(\text{ps}^{-1})$ | -                 | $0.088 \pm 0.020$ | 0.444             |
| $\omega_p(\text{ps}^{-1})$ | -                 | 6.21037           | 6.21037           |
| $\phi_p(\text{rad})$       | -                 | 0                 | 0                 |

| Samples                    | 29x10x1.7         | 24x14x1.7         | 30x12x1.7         |
|----------------------------|-------------------|-------------------|-------------------|
| $\tau_{ac}(\text{ps})$     | $0.120 \pm 0.007$ | $0.104 \pm 0.007$ | $0.112 \pm 0.004$ |
| $A_0(10^{-4}\text{Vps})$   | $7.95 \pm 0.085$  | $2.94 \pm 0.13$   | $1.62 \pm 0.03$   |
| $A_1$                      | $0.547 \pm 0.005$ | $0.800 \pm 0.008$ | $0.571 \pm 0.007$ |
| $T_1(\text{ps})$           | $1.040 \pm 0.015$ | $0.660 \pm 0.030$ | $1.050 \pm 0.041$ |
| $A_2$                      | 0                 | $0.097 \pm 0.016$ | $0.159 \pm 0.006$ |
| $T_2(\text{ps})$           | -                 | $610 \pm 180$     | $238 \pm 22$      |
| $A_3$                      | $0.132 \pm 0.007$ | $0.103 \pm 0.018$ | $0.270 \pm 0.009$ |
| $T_3(\text{ns})$           | $2340 \pm 140$    | $56.4 \pm 8.6$    | $51.3 \pm 1.5$    |
| $K(\text{Vps})$            | $0.321 \pm 0.005$ | 0                 | 0                 |
| $t_0(\text{ps})$           | $0.107 \pm 0.016$ | $0.015 \pm 0.007$ | 0                 |
| B                          | $1.58 \pm 0.07$   | $1.28 \pm 0.32$   | $1.336 \pm 0.058$ |
| $\gamma_p(\text{ps}^{-1})$ | $0.070 \pm 0.004$ | $0.159 \pm 0.029$ | $0.154 \pm 0.005$ |
| $\omega_p(\text{ps}^{-1})$ | 6.21037           | 6.21037           | 6.21037           |
| $\phi_p(\text{rad})$       | 0                 | 0                 | $4.645 \pm 0.016$ |

**Table 3.7:** Parameters of the fits to the FWM SDS DG data shown in Fig. 3.27.  $A_0$  is a prefactor that represents the amplitude, and the amplitudes  $A_{1,2,3}$  are relative amplitudes.

radiative lifetime. An offset ( $K$ ) was included in the fits for samples 12x6x1.7 and 29x10x1.7 as the non-zero signal at negative delays could not be described effectively by including an additional long decay (i.e. the resulting lifetime was so long that it could not be determined). Adding an offset is effectively the same as adding a time constant much longer than the scanned delay range. For these two samples however, adding such a long time constant resulted in its error being larger than the value itself. Following the reasoning presented in section 3.3.3, we attribute these longer density decays to the charging of NPLs.

It should be noted that the non-zero time offsets ( $t_0$ ) used for the density fits for samples 12x6x1.7, 29x10x1.7 and 24x14x1.7 simply imply that the delay between the second pulse (P2) and the Probe was not correctly calibrated to be zero when the two pulses arrive at the same time for these measurements. The non-zero  $t_0$

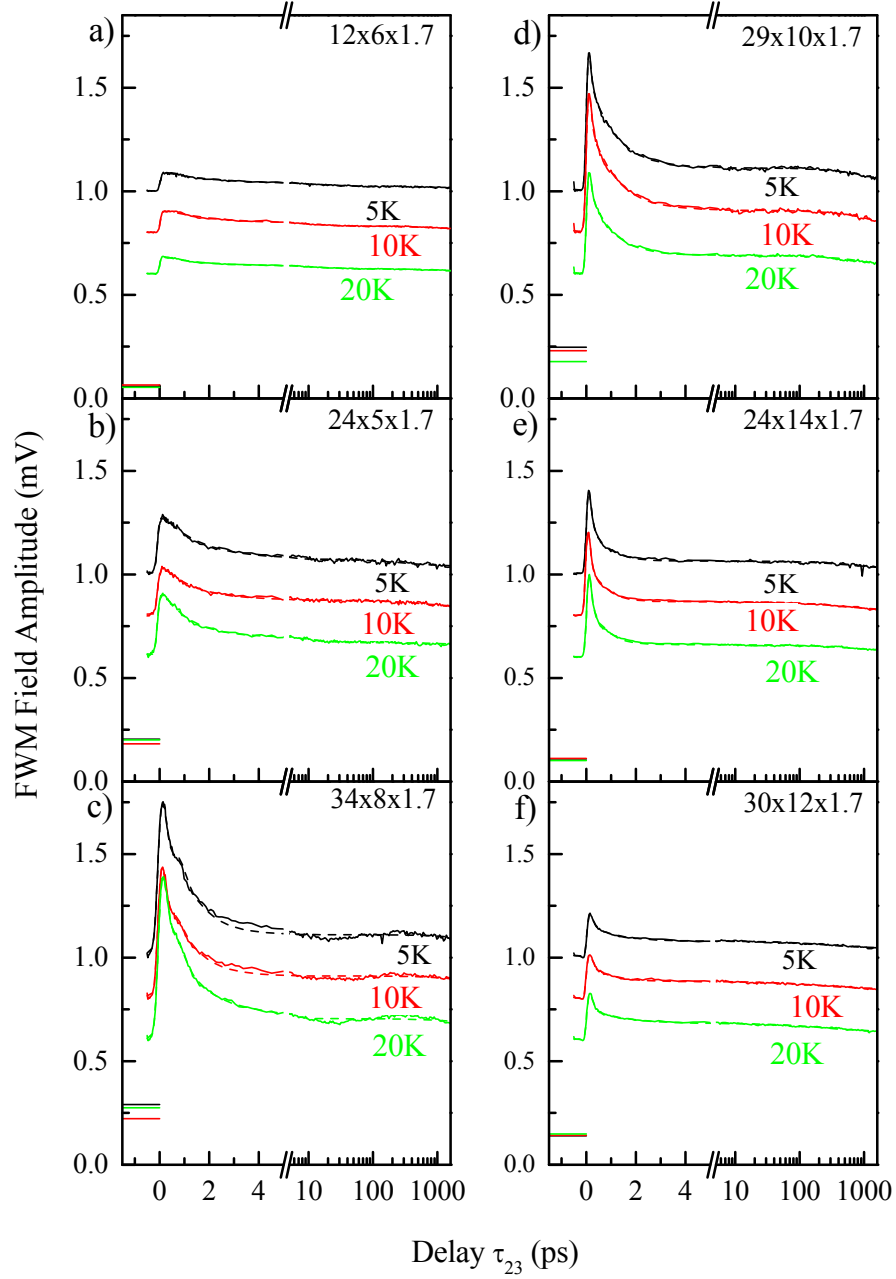


**Figure 3.27:** The FWM field amplitude as a function of  $\tau_{23}$  at  $\tau_{12} = 0$  for the FWM SDS as indicated for temperatures of 5, 10 and 20 K (black, red green) as labelled. Data is shown using solid lines and fits to the data are shown using dashed lines. Offsets have been added to separate the data vertically. Solid horizontal lines indicate the signal for  $\tau_{23} < 0$  before addition of an offset.

was consistent over the measured temperature range for each sample. Interestingly, the data for all samples except 12x6x1.7 were well described by the fit function that included oscillations with a fixed energy  $\hbar\omega_p = 4.1$  meV. For sample 12x6x1.7, a term to describe oscillations of the signal was not required. In the previous section, we attributed the oscillations seen in the density dynamics of sample 34x8x1.7 to longitudinal acoustic phonons confined by the thickness of the NPLs. As the NPLs in this subset have the same thickness, we expected the energy of any observed oscillations to be the same as for sample 34x8x1.7. The oscillation energy was therefore fixed for these fits, and described the data well as shown in Fig. 3.27. The observation of oscillations of the same frequency in the density dynamics of almost all NPLs of thickness 5.5 ML is consistent with the attribution of the oscillations to thickness confined acoustic phonons.

### 3.4.3 Temperature Dependence

The linewidths  $2\hbar\gamma_{1,2}$  obtained from the dephasing, and  $\hbar\Gamma_1$  obtained from the density dynamics of the NPLs in the FWM SDS are shown as a function of temperature in Fig. 3.28 for comparison. The calculated ZPL weights are also shown, and the same data for sample 34x8x1.7 is shown in Fig 3.28 c) from the previous section for comparison. We noticed from this comparison that all NPL samples exhibit a ground state exciton dephasing time limited by the lifetime of the exciton. This result confirms lifetime limited exciton dephasing as an effect present in NPLs of 5.5 ML thickness. In addition, we noticed that, as expected, the ZPL weights show a decrease with increasing temperature as phonon mediated transition become more important.

Let us now discuss an important result of these measurements which is the observed evidence that the ground state exciton transition in these NPLs is a giant oscillator strength transition (GOST). We have already mentioned that the short dephasing times compared to spherical quantum dots observed in sample 34x8x1.7 indicate GOST. The increase in the strength of these transitions is expected to be proportional to the ratio of extension of the exciton COM within the NPL area to  $a_x^2$ . We do not expect the Bohr radius of the ground state exciton to vary between the different NPL lateral sizes since the lateral sizes are large compared to the Bohr radius (see section 3.2.3). We therefore expected that the strength of the ground state exciton transition would increase with the lateral size of the NPLs which would be observed as faster radiative decay times in NPLs of larger lateral size. Fig. 3.29 shows the homogeneous linewidths  $2\hbar\gamma_2$  at 5 K, the ZPL weight  $Z$ , and the lifetime limited linewidth  $\hbar\Gamma_1$  for all NPLs for which we acquired FWM measurements as a function of the NPL area. An approximately linear increase within error of the homogeneous linewidth can be seen with increasing NPL area. The data for all samples except sample 30x12x1.7 with the largest area fits this trend. The ZPL weight also shows an approximately linear increase with NPL area accordingly. This data confirms the observation of GOST in these NPLs. Interestingly, the ZPL content drops for the largest NPL which is not expected, and points to a localization of the excitons in the NPLs.

Samples 24x14x1.7 and 30x12x1.7 initially comprised NPLs dissolved in a hexane solution. The hexane was replaced with Toluene before the preparation of these NPLs in PS films for measurement as described in section 3.1.1. It is possible that there is a link between the unexpectedly small homogeneous linewidth of the ground state exciton transition observed for sample 30x12x1.7 and the solvent replacement



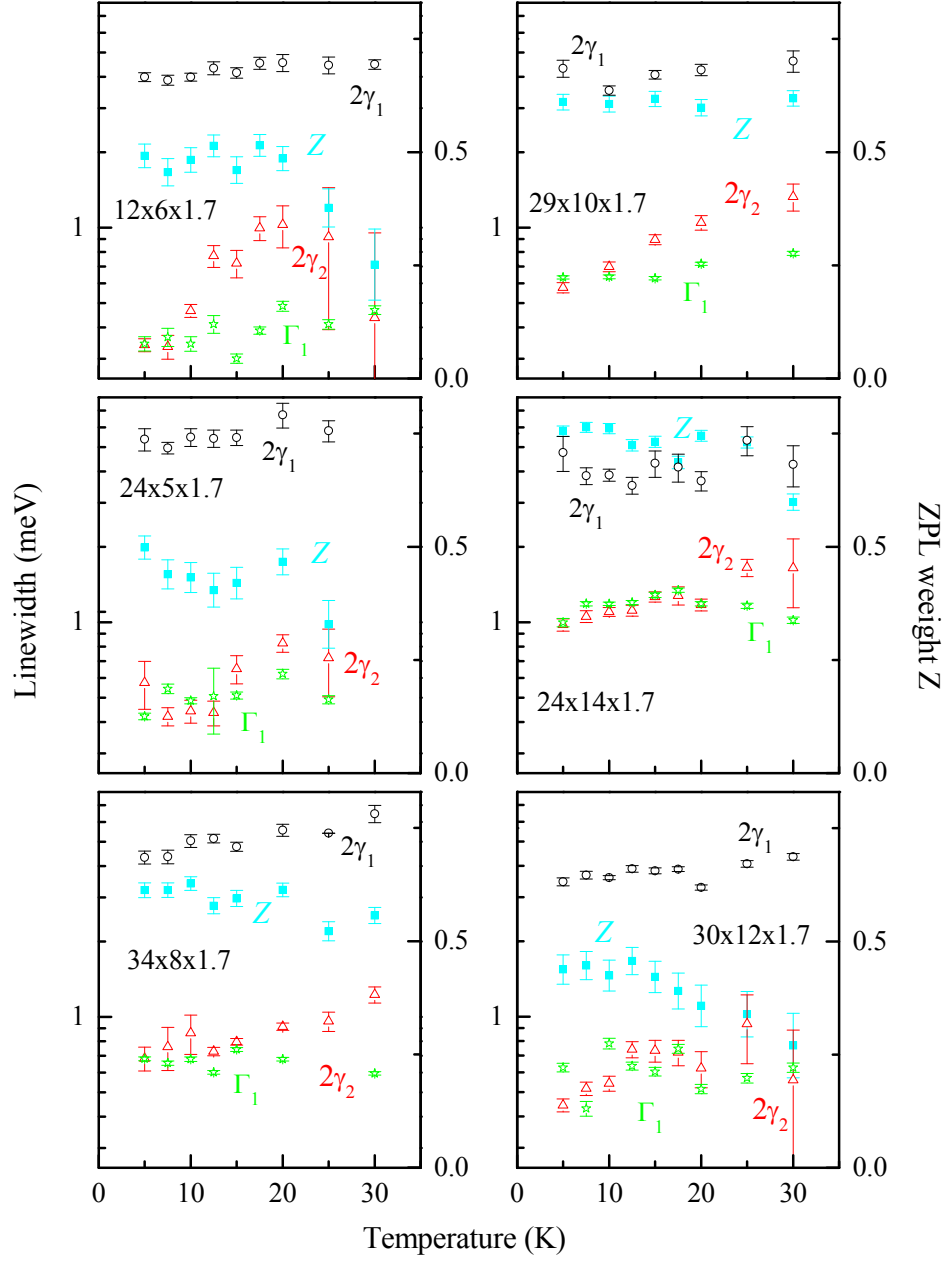


**Figure 3.28:** The homogeneous linewidths  $2\hbar\gamma_{1,2}$ , the ZPL weight Z, and the lifetime-limited linewidth  $\hbar\Gamma_1$  for the FWM SDS as indicated.

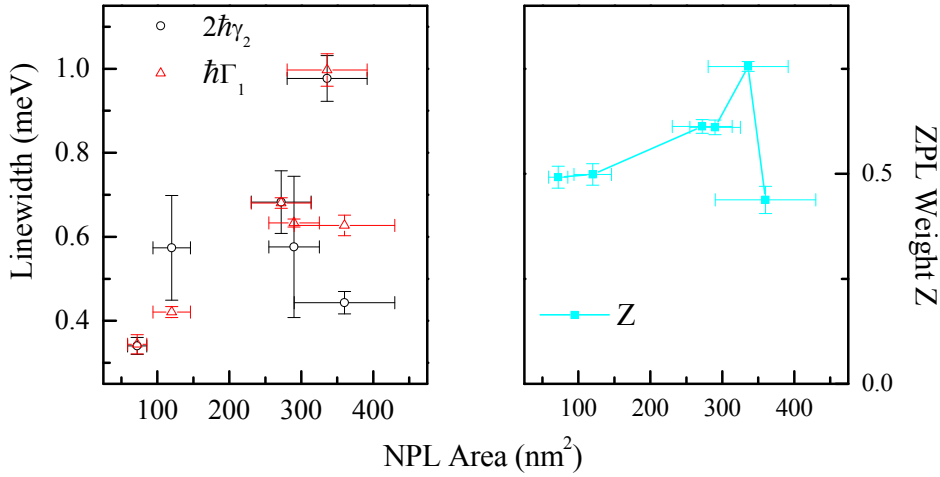


**Figure 3.29:** The homogeneous linewidths  $2\hbar\gamma_2$  and the ZPL weight  $Z$  extracted from the dephasing measurements at 5 K, and the lifetime-limited linewidth  $\hbar\Gamma_1$  from the DG measurements at 5 K are shown as a function of NPL lateral area.

procedure. Let us briefly restate the procedure here for convenience. A small amount of NPL solution was placed inside a 1 ml glass vial which was placed on a hot plate at about 30° C. The hexane was allowed to evaporate until the volume was reduced to half the original level before toluene was added to increase the volume back to the original level. This process was iterated. The nitrogen atmosphere for this process was provided by directing a light flow of Nitrogen using a thin pipe of diameter 5 mm into the open mouth of the vial. It could be the case that during this process for sample 30x12x1.7, the nitrogen atmosphere was not adequately setup, and some oxidation of the NPLs took place resulting in a change in the dephasing dynamics. Another possibility is that the surface ligands were removed resulting in a larger lateral disorder and therefore exciton localization, thus reducing the radiative rate of each localized state.

## Chapter 4

# CdSe/CdS core shell quantum dots in rods

Numerous studies of the optical properties of CdSe/CdS quantum dot in rods (QDR) exist in the literature. There are a large number of absorption and various types of photoluminescence studies such as the recent fluorescence line narrowing study performed by the group of Aguila *et al* [41] in order to probe the exciton and phonon fine structure in these structures. An example of a pump probe study is a study performed by the group of Lupo *et al* [81] in which the authors claim that the holes are localised in the core whereas the electrons are delocalised and penetrate into the CdS shell.

The three beam FWM technique we have used to study the QDR samples is not found frequently in literature. This technique has been used by members of our group to investigate spherical CdSe/CdS core shell dots in ref[54], and CdSe/ZnS dots in ref[4]. In this chapter we present the results of similar measurements, as for the NPL samples in the previous chapter, on the QDR samples in order to reveal the exciton dynamics. Simultaneous measurements of exciton dephasing and population dynamics of these samples do not yet exist in the literature making the following section relevant and interesting.

### 4.1 Studied quantum dot in rod samples

#### 4.1.1 Growth techniques

Quantum dots can be self assembled during epitaxial crystal growth or produced through colloidal synthesis. They can also be created using other methods such as direct lithography. Quantum dots appear during Stranski-Krastanow crystal film growth using Molecular Beam Epitaxy (MBE) or Metalorganic Chemical Vapour Deposition (MOCVD). Using the example of MBE growth, a semiconductor material can be deposited onto a crystal substrate. The semiconductor molecules begin to form thin layers on top of the crystal substrate, and attempt to match the lattice constant of the substrate. The strain energy increases linearly with the thickness, and at some point a structure with a larger surface and less strain has the lower energy. After this point, the semiconductor molecules form clusters which leads to the formation of quantum dots. For example, InAs dots can be grown using MBE on a GaAs substrate.

Colloidal synthesis instead requires precursors which comprise the required atomic

species, a solvent and ligands or organic surfactants. The different compounds are added to a reaction chamber where the temperature of the reaction can be controlled. During the reaction, the precursors break down into monomers which subsequently nucleate in order to start the crystal growth process. In order to grow CdSe dots, dimethylcadmium ( $\text{Me}_2\text{CD}$ ) and bis(trimethylsilyl)selenium ( $\text{TMS}_2\text{Se}$ ) may be used as precursors as in ref [82]. The solvent acts as a medium in which the reactants can be dispersed. The organic ligands or surfactant provide control over the growth process. The ligands bind to the nanocrystal surface but can also unbind to allow the addition of more atoms to the nanocrystal. The type of ligands used will determine the solubility of the quantum dots in different solvents, so they must be carefully selected. A common combination of solvent and surfactant as in ref [82] is tri-n-octylphosphine oxide (TOPO) and tri-n-octylphosphine (TOP). It should be noted that this technique requires a specific time sequence to first nucleate, then slowly grow the dots. The growth has to be controlled in order to avoid Ostwald-ripening which starts when the monomer concentration in the liquid is in equilibrium with the dots. The bigger dots with smaller surface energy and thus less vapour pressure grow at the expense of the smaller dots, broadening the size distribution.

#### 4.1.2 Studied Samples

Transmission Electron Microscopy (TEM) images of the investigated Quantum Dot in Rod (QDR) samples are shown in Fig. 4.1. Out of the three investigated samples, two had similar average core sizes of 5.71 nm and 5.72 nm diameter, total diameter 5.87 nm and 7.3 nm, and total length of 13.9 nm and 12.84 nm respectively. These will be referred to as samples c6sh14 and c6sh13. The third investigated sample had a core radius of 3.43 nm with a total diameter of 5.86 nm and length 25.5 nm. From the TEM images, it can be seen that sample c6sh13 has more of a cone like shape. The position of the cores for all samples is typically 10% of the rod length away from one end. For example, sample c6sh13 will have the edge of the core roughly 1.3 nm away from one end of the structure, meaning that the centre of the core should be positioned roughly 4 nm away from one end of the rod. The core is centred within the overall diameter of the rod, and the c-axis is along the rod.

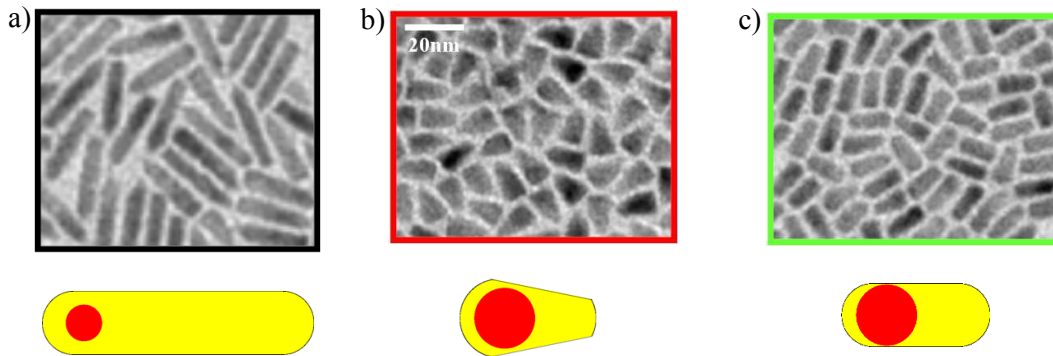


**Figure 4.1:** TEM images in a) b) and c) of samples c3sh26, c6sh13 and c6sh14 respectively. Sketches of the QDRs are shown below their respective TEM images. Scale bar for all TEM images in b).

The QDR samples were grown by a seeded growth technique [3]. The growth method comprises heating a solution of CdO, trioctylphosphine oxide, hexylphosphonic acid, and octadecylphonic acid to a temperature between 350°C to 380°C. CdSe

| Sample | CdSe<br>core<br>diameter | CdS<br>shell<br>diameter | Length  |
|--------|--------------------------|--------------------------|---------|
| c3sh26 | 3.4 nm                   | 5.9 nm                   | 25.5 nm |
| c6sh13 | 5.7 nm                   | 7.3 nm                   | 12.8 nm |
| c6sh14 | 5.7 nm                   | 5.9 nm                   | 13.9 nm |

**Table 4.1:** Parameters of investigated QDR samples.

quantum dots are added to a second solution of sulfur dissolved in trioctylphosphine. Immediately after the QDs are added to the second solution, the second solution is added to the heated flask containing the first solution. The mixture is then allowed to return to its original temperature. The reaction is allowed to continue for several minutes afterwards. The surfactants are chosen so that the CdS crystal grows asymmetrically along the c-axis of the wurtzite lattice. The concentration of CdS (by managing reactant concentrations) is kept small enough to avoid nucleation, so that CdS can only grow on the CdSe cores already present

For the studied samples, different core diameters were obtained by adjusting the temperature and the growth time of the CdSe nanocrystal synthesis. By adjusting the CdSe core, and Cadmium and sulfur precursor ratios, the shell dimensions were varied during the seeded growth of the CdSe/CdS core shell nanocrystals.

## 4.2 Linear optical properties

The room temperature absorption and PL spectra as well as absorption spectra at 10 K of the investigated samples are shown in Fig. 4.2. The three studied samples are labelled c6sh14, c6sh13, and c3sh26. The name indicates the core diameter and the shell length to the nearest nanometer (see section 4.1.2). From the room temperature measurements, we observe a stokes shift of approximately 30 meV for c6sh14, 71 meV for c6sh13, and 27 meV for c3sh26. The TEM images in Fig 4.2 show a larger inhomogeneous distribution for sample c6sh13 than for the other two. We attribute the larger Stokes shift seen for this sample to this greater inhomogeneity.

For the samples with the larger core size, namely c6sh14 and c6sh13, the lowest energy absorption features are at similar energies whereas for sample c3sh26 the feature appears at an energy roughly 100 meV higher. It is possible to estimate the difference in energy of the heavy hole bands due to the different core size by using Eq. 1.25 for the energy eigenvalues of a spherical QD. We use the effective mass of a heavy hole in CdSe of  $0.45 m_e$ . For the two core diameters 5.71 nm and 3.43 nm, the difference in energy of the heavy hole band is approximately 45.4 meV which is approximately 55 meV away from the difference seen in the heavy hole exciton absorption in the measurements. This calculation does not take into account the presence of the CdS shell, or any difference in the binding energy of the heavy hole exciton between the different core sizes. Note that the excitonic absorption peak occurs at an energy which is the band gap minus the binding energy of the exciton. Theoretical calculations presented in [83] indicate a difference in ground state exciton energy in CdSe quantum dots of these sizes of approximately 200 meV. As already discussed, the presence of the shell will reduce the confinement energy. It can be seen from Fig 4.2 that the absorption profile for all three samples shifts to higher energies from room temperature to 10 K. The CdS shell causes an increase in

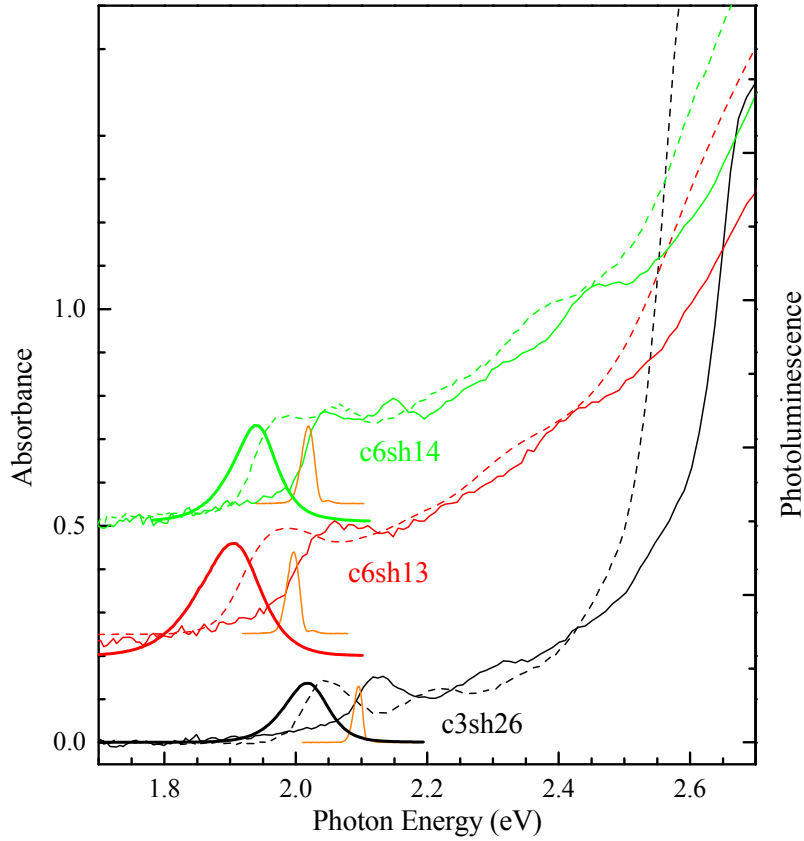


**Figure 4.2:** Absorption and PL spectra of the three investigated QDR samples at 295K are shown as dashed lines and thick solid lines respectively. Absorption spectra at 10 K in thin polymer film is shown using thin solid line. The data for the different samples are vertically displaced for clarity. The spectra of the laser used to excite the samples for FWM measurements are shown in orange lines.

the absorption at energies above 2.5 eV. For the three samples c3sh26, c6sh13 and c6sh14, the ratio of the shell to core volume is 16, 1.8 and 1.0 respectively.

### 4.3 Exciton dephasing

The exciton dephasing was measured using the photon echo technique discussed in section 1.3 for a range of different temperatures. The samples were excited with laser pulses that were centred at an energy on the low energy side of the heavy hole excitonic absorption peak. The excitation spectra are shown in Fig. 4.2. This was done in order to minimize the excitation of the close lying light hole excitonic state.

Examples of the measured dephasing dynamics are shown in Fig. 4.4 wherein the data shows the photon echo area as the TI-FWM signal dependent on  $\tau_{12}$  at a fixed  $\tau_{23} = 2$  ps to exclude non-resonant nonlinearities. This exemplary selection of data has been chosen to highlight features of the dephasing dynamics discussed below. The samples were excited with each beam having a time-averaged intensity in the range 51 to 205 W/cm<sup>2</sup> at the sample which is within the third order nonlinear response regime. Power dependent measurements were performed in order to ensure

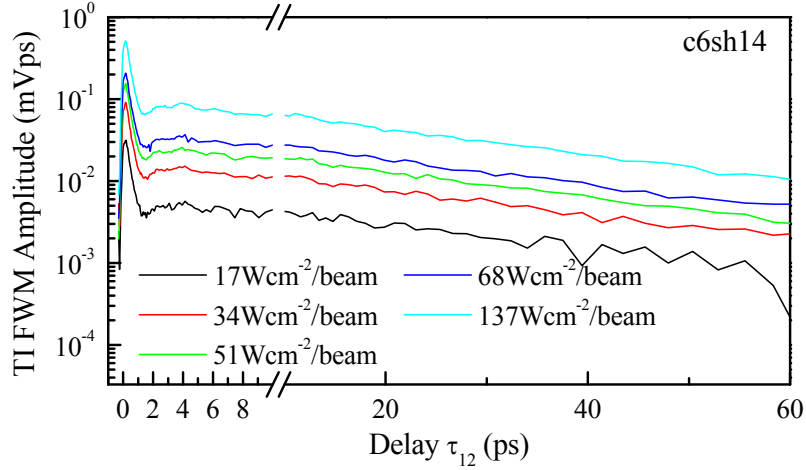


**Figure 4.3:** Power dependent measurements of time-integrated FWM field amplitude vs pulse delay  $\tau_{12}$  for sample c6sh14 as indicated.

that the dynamics did not change based on the power used due to for example, local heating. Fig. 4.3 shows an exemplary set of power dependent measurements that confirm a same slope in the delay range above approximately 10 ps. The QDRs are assumed to be randomly oriented within the polymer film (the sample preparation method is described in section 3.1.1), and to minimize the selective excitation of linearly polarized transitions, we used circularly polarized excitation pulses.

There are a few key features to be noted in the data. There is a fast initial decay of the photon echo area within 1-2 ps followed by damped oscillations within the first 10 ps. At longer delay times, it can be seen that for temperatures greater than 10 K the decay is clearly exponential, however the dephasing dynamics at longer delays for low temperatures (as exemplified by the 5 K data shown) are more complicated. The dynamics at long delays for the low temperature measurements (below 10 K) seen in Fig. 4.4 could not be described by a sum of two or three exponential decay components (as was the case for the NPL samples in the previous chapter). To take account of these features, a more complex fit function was needed than a simple sum of several exponential decays as was used to fit the NPL dephasing curves in section 3.3.2.

#### 4.3.1 Dephasing fit function

In order to describe the dephasing dynamics, we used a Gaussian distribution of the polarization decay rates  $\gamma = 1/T_2$  in the ensemble. These rates are related to the zero phonon line (ZPL) where the FWHM is given by  $2\hbar\gamma$ . To obtain the fit function for decay rates with such a distribution, we evaluated the following integral:

$$\int_0^\infty e^{-\frac{(\gamma-\gamma_0)^2}{2\Delta^2}} e^{-2\gamma\tau_{12}} d\gamma \quad (4.1)$$

where the integral is performed from zero to exclude negative values of  $\gamma$  which are not physically meaningful. We normalize the lineshape area to 1 by dividing the above by

$$\int_0^\infty e^{-\frac{(\gamma-\gamma_0)^2}{2\Delta^2}} d\gamma \quad (4.2)$$

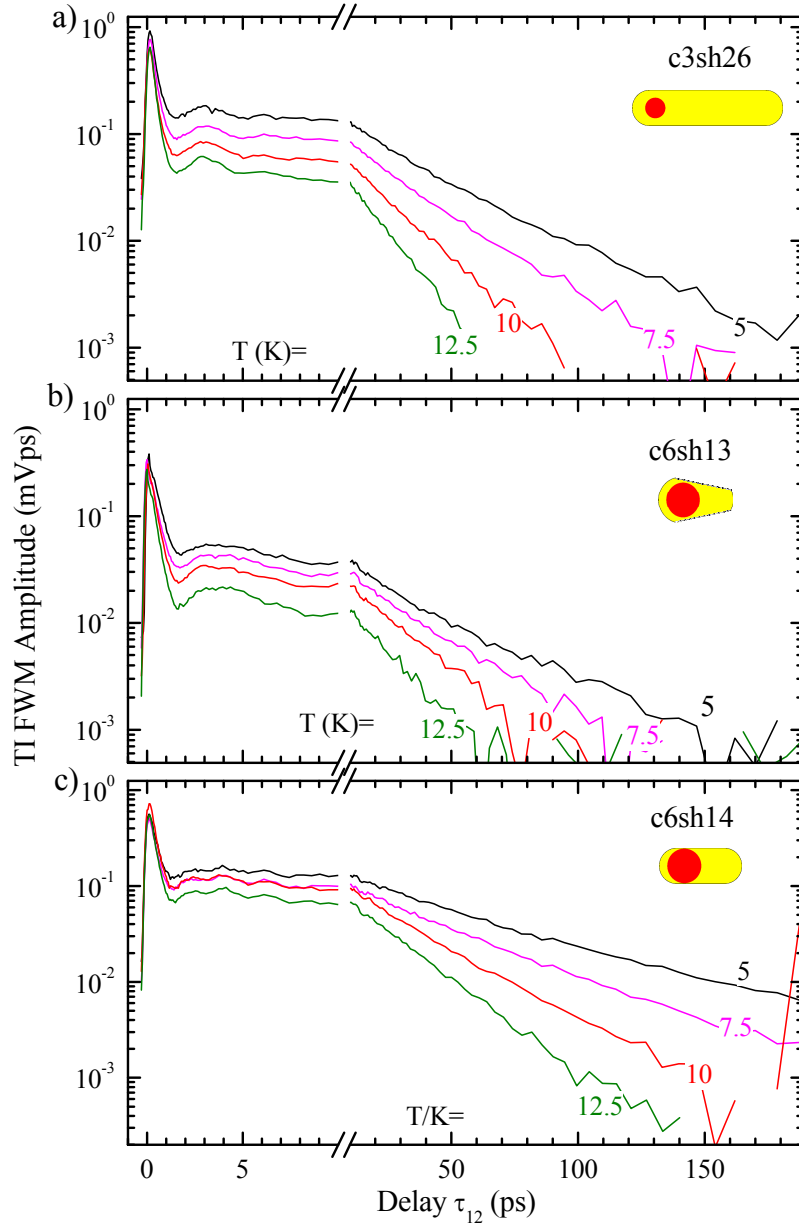


**Figure 4.4:** Photon echo area as time-integrated FWM field amplitude vs pulse delay  $\tau_{12}$  for a range of temperatures. a) for sample c3sh26, in b) for c6sh13, and in c) for c6sh14.



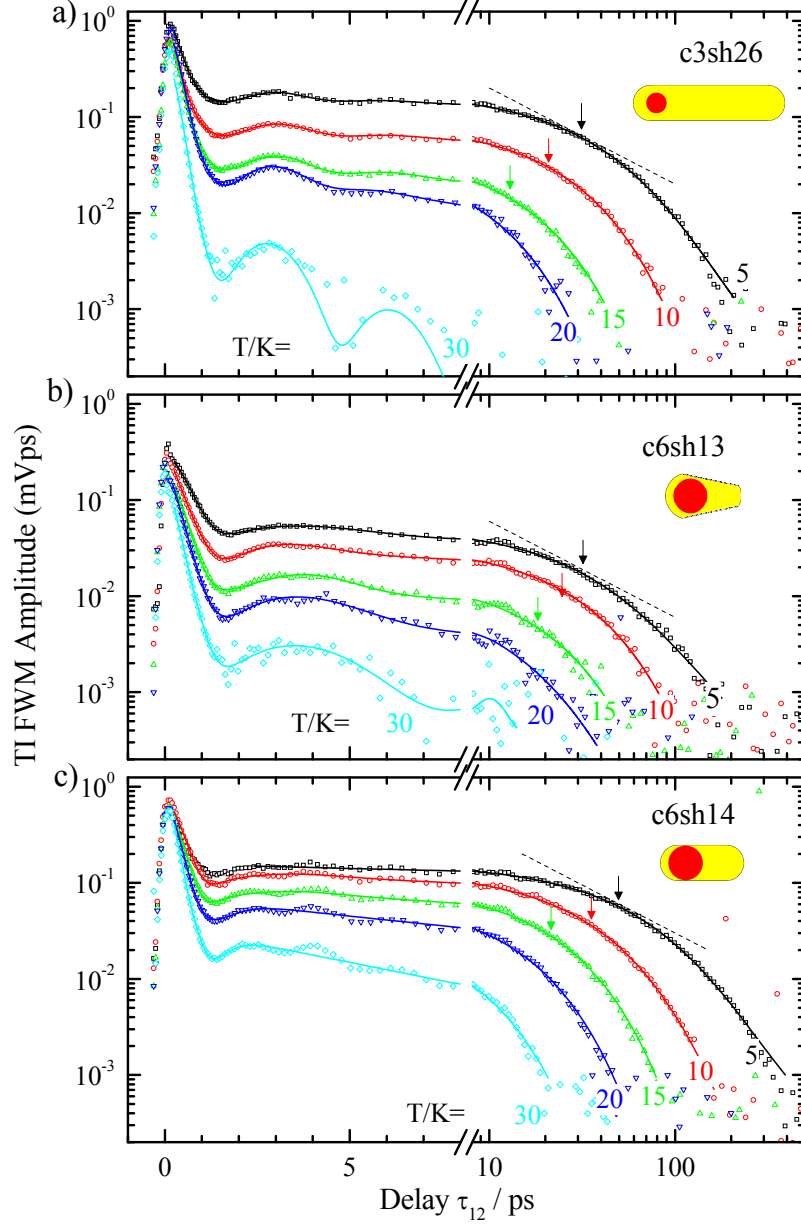


**Figure 4.5:** Photon echo area as time-integrated FWM field amplitude vs pulse delay  $\tau_{12}$  for a range of temperatures. a) for sample c3sh26, in b) for c6sh13, and in c) for c6sh14. Fits to the data are represented by solid lines. The arrows indicate the point at which  $\tau_{12} = 1/\gamma_0$  which is the decay time constant. The dashed lines indicate the gradient -1. The data shown is the same as the data in Fig. 4.4 but for a different range of temperatures.

The resulting fit function is:

$$D_H = e^{\left(\frac{\Delta^2 x^2}{2} - x\gamma\right)} \frac{\left[1 - \operatorname{erf}\left(\frac{\Delta^2 \tau_{12} - \gamma_0}{\sqrt{2}\Delta}\right)\right]}{\left[1 - \operatorname{erf}\left(\frac{-\gamma_0}{\sqrt{2}\Delta}\right)\right]} \quad (4.3)$$

The fit function above allowed the non exponential decay at long delays ( $\tau_{12}$ ) at low temperatures to be described. At low temperatures a finite width  $\sigma_\gamma$  of the distribution of  $\gamma$  is required to make the fits, whereas at higher temperatures the photon echo area decays exponentially with a single time constant. This means that for  $T > 10$  K,  $\sigma_\gamma$  the temperature dependent dephasing does not show a significant distribution of  $\gamma$ .

The fast initial decay of the signal seen in the dephasing curves can be attributed to dephasing of the phonon-assisted transition [4]. In QDs, the ZPL appears on top of a much broader non-lorentzian lineshape. This broad band is due to phonon assisted transitions. The electron and hole wave functions in the exciton [84], specifically their distribution in wavevector space, determines the shape of the broad band. For a parabolic confinement potential, one would expect Gaussian electron and hole wave functions giving a Gaussian shaped phonon broad band. In the investigated samples however, we expect a step like potential for the hole as it is strongly confined inside the core due to the large valence band offset between CdSe and CdS. As a result of this sharper potential, the wavefunction has more extended tails in wavevector space. To reflect this in the shape of the phonon broad band, we used a  $\cosh^{-2}$  lineshape which has more extended tails than a Gaussian lineshape which was used in [85].

To take account of the oscillations observed at short delays, we include a term oscillating at a specific frequency  $\omega_p$  that experiences Gaussian damping with an inhomogeneous broadening  $\sigma_p$ . We attribute these oscillations to a specific mode in the phonon assisted band. In the resulting fit function shown in Eq. 4.4,  $A_{bb}$  and  $A_p$  are the weights of the phonon broad band and the phonon oscillation components respectively.  $\sigma_{bb}$  represents the broadening of the phonon broad band. The part of the function describing the homogeneous decay of the polarization (Eq 4.4) is represented by  $D_H$ .

$$A = A_0 \left(1 + A_{bb} \cosh^{-2}[\tau_{12}\sigma_{bb}]\right) \times \left(1 + A_p \cos[\tau_{12}\omega_p + \phi] e^{-\tau_{12}^2 \sigma_p^2}\right) \times D_H \quad (4.4)$$

The weight of the zero phonon line can be calculated using the fact that the FWM amplitude after the fast initial decay due to the phonon broad band is  $Z^3$ , where  $Z$  is the ZPL weight, times the initial amplitude. The weight  $Z$  is then determined as follows:

$$Z = [(1 + A_{bb}) \times (1 + A_p \cos \phi)]^{-\frac{1}{3}} \quad (4.5)$$

### 4.3.2 Dephasing fits and temperature dependence

The dephasing data is well described by the fit function as can be seen from the fits shown in Fig 4.5, wherein the decay constant is the value of  $\tau_{12}$  at the point where the gradient of the curve is -1. This is indicated on the plot with arrows, and the dashed lines have a gradient of -1. Fig. 4.6 shows in further detail fits to the data describing the non-exponential behaviour observed at low temperatures. The linewidths of the distribution of  $\gamma$ , i.e.  $2\hbar\sigma_\gamma$ , are shown in the inset of Fig 4.6.

These linewidths are roughly constant as a function of temperature, however their error increases with temperature due to the faster dephasing. This means that the dephasing which is due to the temperature activated mechanisms does not have a significant distribution of decay rates in the ensemble. We attribute the dephasing at low temperature to phonon assisted transitions from the bright state we excite to a lower lying dark state in energy [4]. Based on this we would expect there to be a non zero  $\sigma_\gamma$ , i.e. a significant distribution of  $\gamma$ , at higher temperatures if this is the only dephasing mechanism.

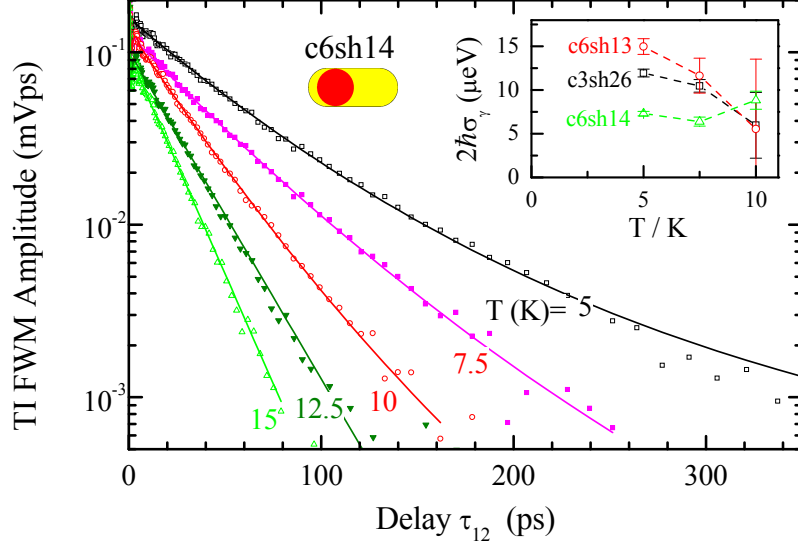


**Figure 4.6:** Photon echo area as time-integrated FWM field amplitude vs pulse delay  $\tau_{12}$  is displayed for sample c6sh14 on a linear delay scale unlike Fig 4.5. The inset shows the linewidth of the Gaussian distribution of the decay rate  $\gamma_0$  in the ensemble.

The observed trend for  $\sigma_\gamma$  makes sense once the expected fine structure of these QDRs is considered. Fig 1.9 b) shows the size dependent fine structure of CdSe dots. The data shown takes into account the size dependent non sphericity of the dots. The asymmetry in shape can significantly change the fine structure. We can see that there are higher lying bright and dark states to which the excitons may transition as the temperature is increased. Having multiple channels of dephasing leads to an averaging of the variation in decay rates within the ensemble. It must also be noted that the phonon assisted transitions to higher states, which contributes to the dephasing, are not as sensitive to small variations in the excitonic energy levels due to the finite phonon linewidth.

Fig. 4.7 shows a temperature dependent summary of the relevant fit parameters obtained from the fits. From Fig. 4.7 a) we note the temperature dependence of the homogeneous linewidth of the three samples. These have been fit with a temperature activated behaviour as was done for the NPL samples using Eq. 3.19 to which additional terms identical to the second term can be added in order to account for additional activation energies. The fits reveal two activation energy values of 2.3 meV and 12.3 meV for the c3sh26 sample, and one activation energy with a value of 3.1 meV and 3.9 meV for samples c6sh14 and c6sh13 respectively. It is interesting to note that the dark bright splitting for small core dots, which is the splitting between the  $\pm 2^L$  and the  $\pm 1^L$  states, is reported to be 3 meV for dots

of diameter 3.3 nm with a rod diameter of 4.5 nm in [42]. In the same work, the authors also report that the splitting should decrease if the thickness of the shell is increased. Since for sample c3sh26 the core is slightly larger but the rod diameter is significantly larger, i.e. 5.86 nm, the fitted value of 2.3 meV is consistent. Calculations in the work of Shabaev *et al* [43] showing size dependent dark bright splitting for different conduction band offsets, also put the dark bright splitting for dots of this size in the region of 2 meV for a conduction band offset of 100 meV.

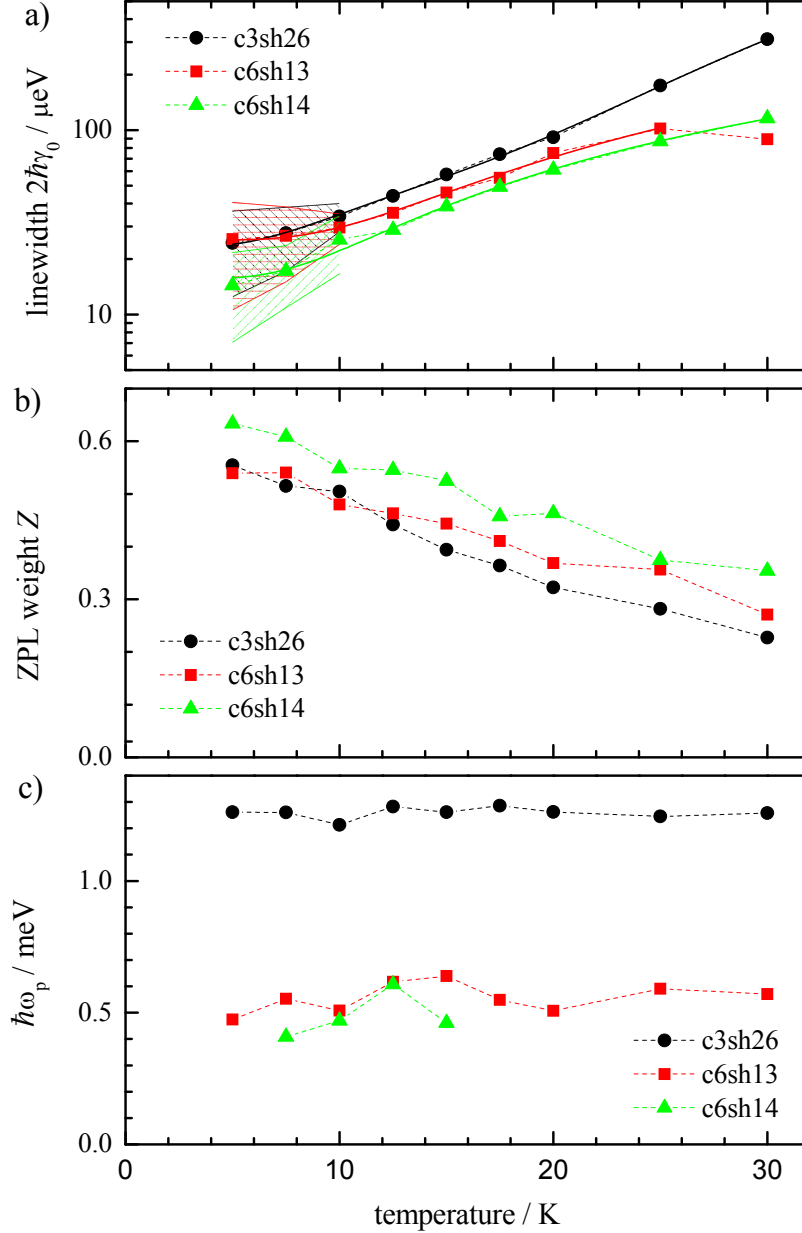


**Figure 4.7:** a) homogeneous linewidths  $2\hbar\gamma_0$  obtained from the fits to the dephasing measurements. The data points are connected by dashed lines and the temperature activated fits are shown using solid lines. The shaded area indicates the linewidth of the distribution of  $\gamma_0$  as  $2\hbar(\gamma_0 \pm \sigma_\gamma)$ . b) deduced ZPL weight, and c) energies of the fitted oscillations at short delays seen in Fig 4.5.

Further examination of the fine structure calculations in Fig 1.9 b) show that

the level  $\pm 1^U$ , which is a bright state, moves further in energy from the probed  $\pm 1^L$  state as the core diameter is reduced from 5.7 to 3.43 nm. It is possible that the larger activation energy observed for c3sh26, as well as the activation energies for samples c6sh13 and c6sh14, are the energy splittings between the  $\pm 1^L$  and  $\pm 1^U$  levels. It must be noted that the dark state  $0^L$  is between the two aforementioned bright states. Evidence for the existence of an energy level 12 meV away from the  $\pm 1^L$  state can be seen in the work of Aguila *et al* [41] who show FLN spectra of similar small core dots. This peak is not well resolved, but appears as a broad tail to a phonon assisted transition from the lowest  $\pm 2^L$  dark state. It is also worth noting that the dark bright splitting for the larger core samples is expected to be smaller than the 2 meV fitted for the small core dots, and therefore not extractable from the data fits because data below 5 K is not available.

Since the difference in the core size of samples c6sh13 and c6sh14 is negligible, any observed difference in the splitting must be due to the differences in the CdS shell. As already mentioned, with increasing shell thickness the splitting between levels should decrease as a result of weaker confinement due to the electron wave function extending into the shell (which represents a smaller energy barrier for electrons and holes than the surrounding polymer). We note however that for the sample with the greater total thickness of the shell, namely sample c6sh13 with a total rod diameter of 7.3 nm, the fitted activation energy is 3.9 meV, higher than c6sh14 with a total shell thickness of 5.87 nm that has a fitted activation energy of 3.1 meV. Since we attribute these activation energies to a higher excitonic energy state, this result is unexpected. We note however that although the total rod diameter for c6sh13 is greater, the shape of the CdS shell of the two samples is quite different as can be seen from the TEM images in Fig 4.1. c6sh13 has more of a cone like shape as compared to the more rod like shape of sample c6sh14. Because of the shape of c6sh13, the total diameter of the CdS shell around the position of the core will be less than 7.3 nm. This shape also means that the volume of CdS around the core is smaller for this sample compared to c6sh14 even if the small difference in total length of 1 nm is taken into account. Because of the reduced volume of the CdS, the exciton would be expected to be more strongly confined than for sample c6sh14 causing a larger splitting between energy levels. If the shapes of the samples are accounted for, the observed energy order of the fitted activation energies can thus be explained.

It can be seen from Fig 4.7 b) that the ZPL weight for all three samples decreases with increasing temperature. This is an expected result since phonon assisted transitions are more likely at higher temperatures. We also note from Fig 4.7 c) that the fitted energies of the phonon oscillations at short delays are independent of temperature. For sample c6sh14 the values at 5 K and those above 15 K are not displayed as these had a fit error similar to the value itself. A more detailed discussion of the phonons is presented in the following section.

## 4.4 Exciton density dynamics

The exciton population dynamics, or density dynamics, in the QDR samples were investigated by measuring the FWM as a function of  $\tau_{23}$ . Measurements for each sample were taken at a range of temperatures. The measurements were taken for  $\tau_{12} = 0$  to probe the density dynamics most independent of internal relaxation between the fine structure exciton states, and for  $\tau_{12} \neq 0$  to probe the internal

relaxation.

#### 4.4.1 Temperature dependent density dynamics

TI-FWM as a function of  $\tau_{23}$  for  $\tau_{12} = 0$  for the samples c3sh26, c6sh13 and c6sh14 are shown in Fig. 4.8 for various temperatures. The data for all samples can be described by two exponential decays at delays longer than 4 ps. The initial dynamics up to 4 ps were surprising because there is a rise in the FWM signal after about 0.5 ps, which in a simple picture would imply an increase in the exciton population of the probed bright exciton state well after the excitation pulses of 150 fs duration have passed. This late signal rise follows an initial decay of the signal. Data for sample c3sh26 shows a stronger initial decay, and a weaker subsequent rise compared to the two larger core samples.

In order to extract the temperature dependence of the longer dynamics, the data were fit with the function:

$$S(t) = \sum_{n=1}^j A_n \exp\left(\frac{\tau_{ac}^2}{2T_n^2}\right) - \frac{t}{T_n} \left[ \frac{1}{e^{\frac{T_p}{T_n}} - 1} + \operatorname{erf}\left(\frac{t}{\tau_{ac}} - \frac{\tau_{ac}}{2T_n}\right) \right] \quad (4.6)$$

where  $\tau_{ac}$  is the excitation pulse autocorrelation time, and  $T_p$  is the laser period. Note that this is similar to Eq. 3.16 used to fit the density dynamics for the NPL samples with the difference being the lack of an oscillatory component. We fitted the data with four components  $j = 4$  ( $n = 1, 2 \dots 4$ ). The components 1 and 2 describe the initial dynamics, whereas components 3 and 4 describe the longer decays. The signal rise in the initial dynamics is reproduced by negative values of  $A_2$ , and the pile-up term  $\frac{1}{e^{\frac{T_p}{T_n}} - 1}$  was excluded for the  $A_2$  component. The resulting fits to all the presented data are shown in Fig. 4.8. Fig. 4.9 shows the data along with the fits for a temperature of 15 K for each sample so that the fits may be compared in more detail. Although at this point in the analysis the physical cause of the initial dynamics is not clear, the fit function described the temperature dependent data well. We fixed the value of the signal rise time constant to the same value for all the fits for each of the three samples. The temperature dependence of the longest lifetime extracted from the fits is shown in Fig. 4.10. We noticed that the long lifetime increases with increasing temperature.

In the exciton level fine structure of these QDR nanocrystals, there is a spin-forbidden dark exciton state below the bright exciton state that we probe. We have already attributed the measured dephasing of the bright state to relaxation of excitons into this lower lying dark state in the previous section. For this fine structure arrangement, as the temperature increases, more excitons will be promoted back up to the bright state causing the population lifetime to shorten as the excitons in the bright state have a much larger radiative rate than in the dark state. The observed decreasing decay rate  $\Gamma_4$  with increasing temperature is therefore opposite to what was expected. A population lifetime that becomes longer with increasing temperature would be explained by the presence of a dark state higher in energy than the excited bright state, with no dark state below the excited bright state. In the fine structure of hole trions in the QDRs the ground hole trion state is bright with several higher lying dark states. A hole trion is a quasi-particle which comprises one electron and two holes. The calculated hole trion fine structure taken from [86] is given in Fig. 4.11. We thus attribute the long term dynamics to an ensemble including both trions and excitons, which both have their distinct dynamics.

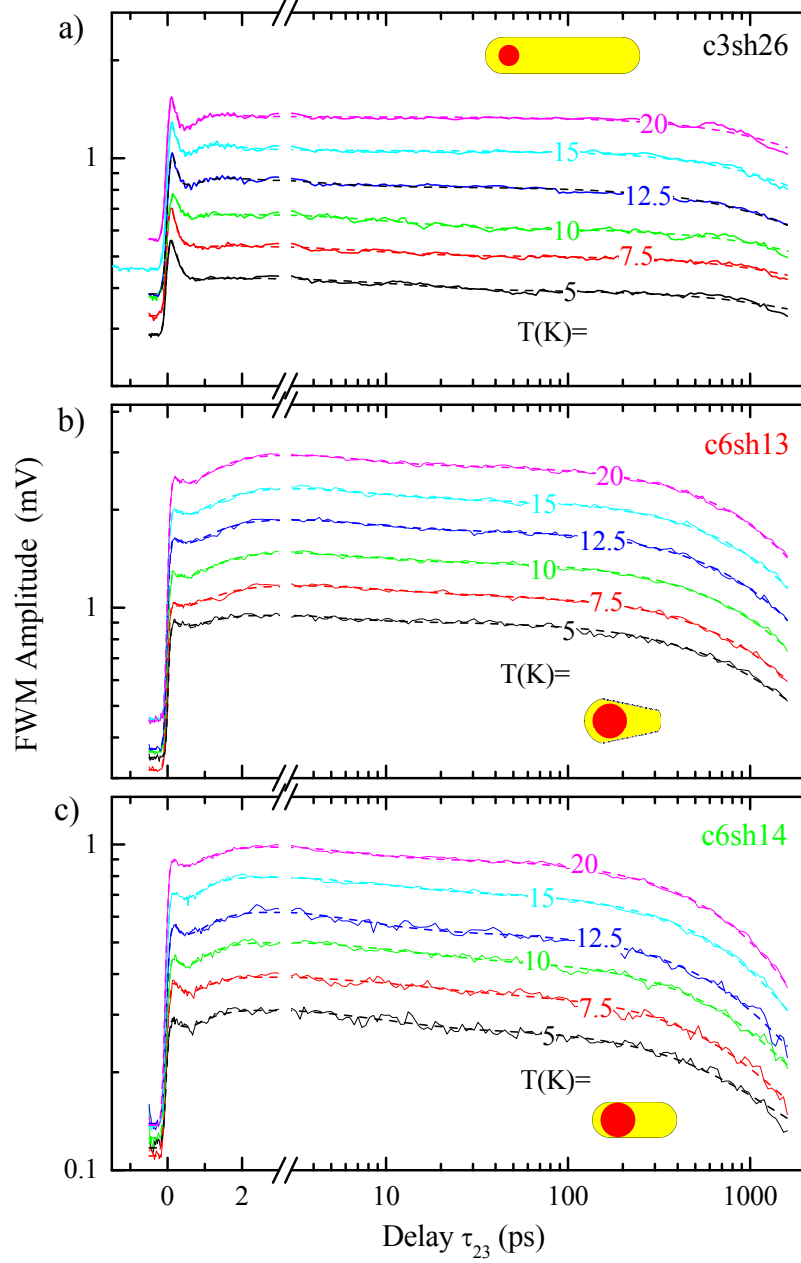


**Figure 4.8:** FWM amplitude as a function of the delay  $\tau_{23}$  is shown for different temperatures as indicated for sample c3sh26 in a), sample c6sh13 in b), and sample c6sh14 in c) using solid lines. Data for temperatures greater than 5 K is shifted vertically for clarity. Fits to the data made using Eq 4.6 are shown using dashed lines.

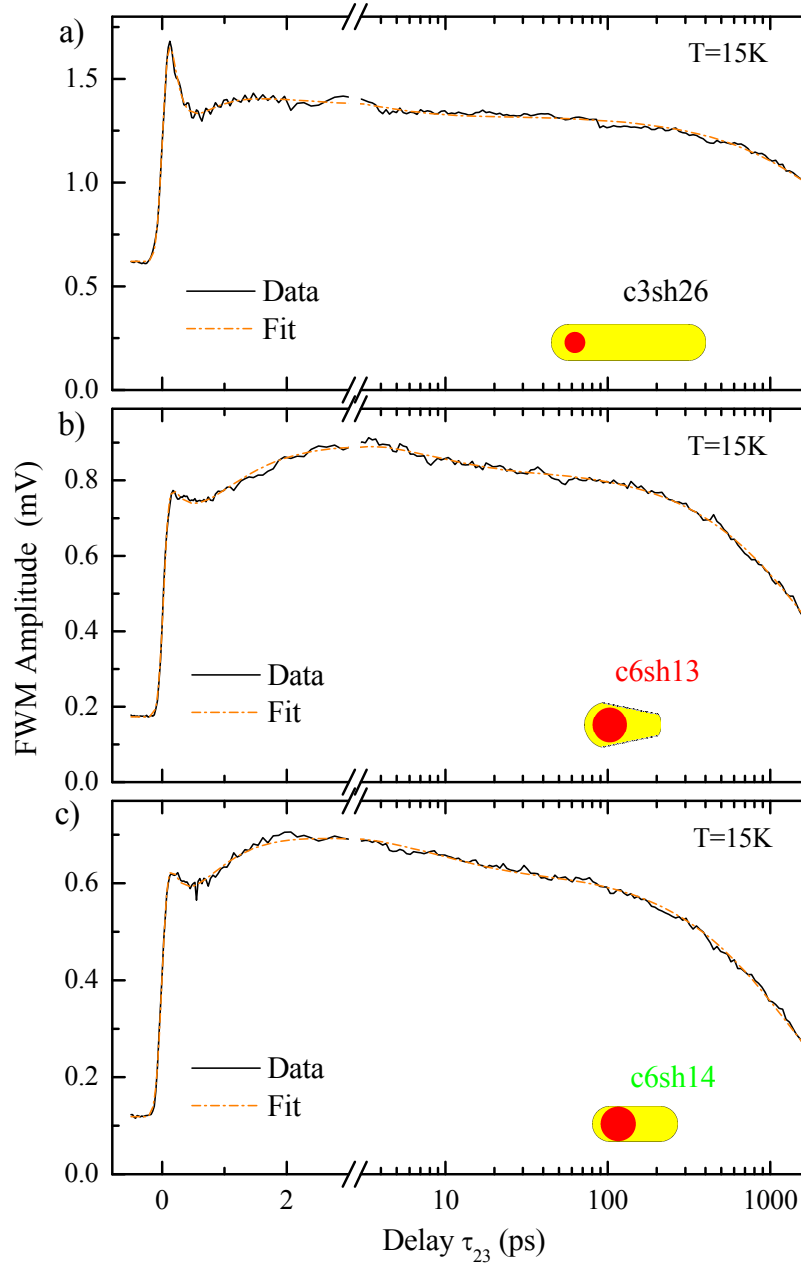


**Figure 4.9:** The FWM amplitude as a function of the delay  $\tau_{23}$  acquired at 15 K is shown for sample c3sh26 in a), for sample c6sh13 in b), and for sample c6sh14 in c) using solid black lines. Fits to the data made using Eq 4.6 are shown using orange dashed lines.



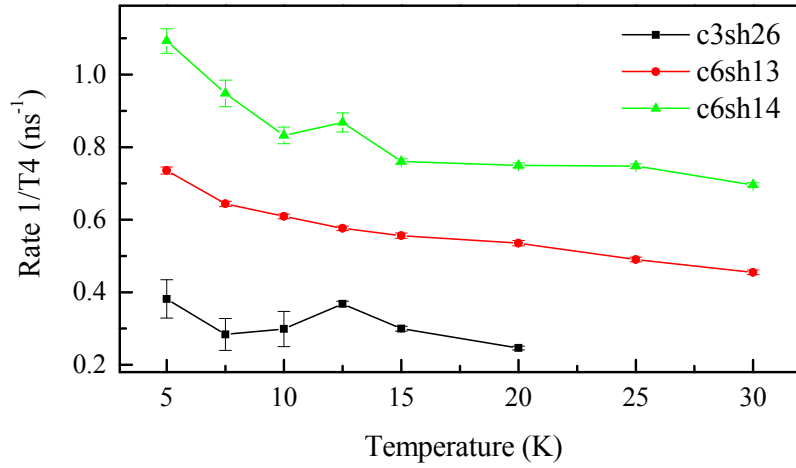


**Figure 4.10:** The longest decay time  $T_4$  obtained from the fits shown in Fig 4.8 as a function of temperature for sample c3sh26 in a), for sample c6sh13 in b), and for sample c6sh14 in c).

This figure has been redacted by the author for copyright reasons

**Figure 4.11:** Sketch of the hole trion fine structure for CdSe quantum dots [86]. The energy separations between levels are not to scale. Bright states are indicated by solid lines, dark states by dashed lines. The subscripts on the symbols for electron (e) and holes (h) represent the single involved particle states, and the superscripts represent the number of particles in the state. N is the total number of particles.

#### 4.4.2 Initial dynamics

One possible explanation for the delayed rise in the exciton population signal after an initial decay is sequential scattering of the exciton within a 3-level system as sketched in Fig 4.12. In this model we included the exciton fine structure levels  $\pm 2$ ,  $\pm 1^L$  and  $\pm 1^U$  (see Fig 1.9). To calculate the time evolution of a signal proportional to the exciton population in this three level model, we solved the following rate

equations:

$$\begin{aligned}
\frac{\delta N_1}{\delta t} &= -\gamma_{12}N_1 + \gamma_{21}N_2 - \gamma_{13}N_1 + \gamma_{31}N_3 \\
\frac{\delta N_2}{\delta t} &= \gamma_{12}N_1 + \gamma_{32}N_3 - \gamma_{21}N_2 - \gamma_{23}N_2 \\
\frac{\delta N_3}{\delta t} &= -\gamma_{32}N_3 + \gamma_{23}N_2 + \gamma_{13}N_1 - \gamma_{31}N_3
\end{aligned} \tag{4.7}$$

where  $N_{1,2,3}$  are the populations of levels 1, 2 and 3, and  $\gamma_{12,13,32}$  are the relaxation rates as indicated in Fig. 4.12.  $\gamma_{21,31,23}$  are the rates of thermal excitation of excitons into higher lying energy states respecting detailed balance.

$$\begin{aligned}
\gamma_{21} &= \gamma_{12} \exp\left(-\frac{E_1 - E_2}{k_B T}\right) \\
\gamma_{31} &= \gamma_{13} \exp\left(-\frac{E_1 - E_3}{k_B T}\right) \\
\gamma_{23} &= \gamma_{32} \exp\left(-\frac{E_3 - E_2}{k_B T}\right)
\end{aligned} \tag{4.8}$$

where  $E_{1,2,3}$  are the energies of levels 1, 2 and 3 respectively. The analytical solution to Eq. 4.9 was calculated for two different sets of initial conditions:

$$N_1(0) = 1, \quad N_2(0) = 0, \quad N_3(0) = 0 \tag{4.9}$$

$$N_1(0) = 0, \quad N_2(0) = 0, \quad N_3(0) = 1 \tag{4.10}$$

Eq. 4.9 states that the exciton population is created by the excitation pulse in level 1 whereas Eq. 4.10 states that the population is created in level 3. Levels 1 and 3 are both bright and therefore will be excited by the light pulses. To describe the initial dynamics seen in the density curves, the following function was used:

$$\begin{aligned}
y(\tau_{23}) &= a \left[ \kappa N_1(\tau_{23}) + (1 - \kappa) \bar{N}_1(\tau_{23}) \right] + \\
&\quad b \left[ \kappa N_2(\tau_{23}) + (1 - \kappa) \bar{N}_2(\tau_{23}) \right] + \\
&\quad c \left[ \kappa N_3(\tau_{23}) + (1 - \kappa) \bar{N}_3(\tau_{23}) \right]
\end{aligned} \tag{4.11}$$

where  $N_{1,2,3}$  are the solutions to Eqs. 4.7 for the initial conditions given in Eq. 4.9, and  $\bar{N}_{1,2,3}$  are the solutions for the initial conditions 4.10.  $\kappa$  thus represents the fraction of excitons in level 1 at zero time. The fits made to the initial dynamics of samples c3sh26 and c6sh13 with this 3 level model are shown in Fig 4.13. The fits shown were made with the energy level splitting between the three levels fixed to the values reported in section 4.3.2 for the three investigated samples. The energy splittings between the states  $\pm 1^L$  and  $\pm 1^U$  were 2.3 meV, 3.1 meV and 3.9 meV for samples c3sh16, c6sh14 and c6sh13 respectively as reported in section 4.3.2. The dark-bright splitting, between the levels  $\pm 2^L$  and  $\pm 1^L$ , was 2.3 meV for sample c3sh26. For the other two samples, the dark-bright splitting is expected to be about 0.7 meV [43]. The initial dynamics are not well described by this model. The fits shown for the initial dynamics of sample c6sh13 deviate from the data at longer delays. For the initial dynamics of sample c3sh26, the model was unable to reproduce the minima in the signal which occur in between the initial fast decay and the signal rise. We thus concluded that the delayed rise in the signal could not consistently be explained by

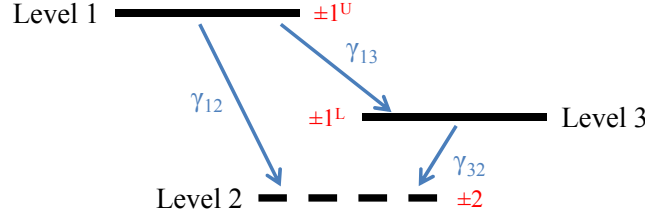


**Figure 4.12:** A sketch of a three level model for the exciton density dynamics within the finestructure of the QDR samples. The dashed line indicates the spin forbidden dark  $\pm 2$  state, and the solid lines represent the bright  $\pm 1^U$  and  $\pm 1^L$  states.  $\gamma_{12,13,23}$  are the rates of relaxation between the levels as indicated.

excitons first relaxing to the lowest lying dark state before being thermally excited back up to one of the bright states namely levels 1 and 3 in Fig 4.12.

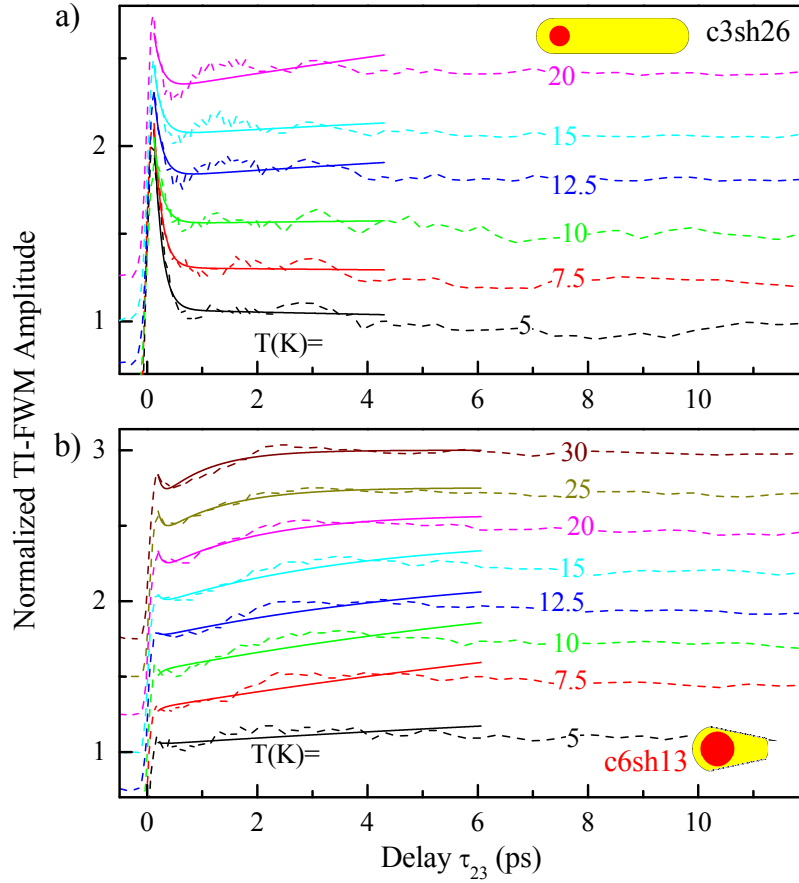


**Figure 4.13:** TI-FWM as a function of  $\tau_{23}$  at  $\tau_{12} = 0$  with fits made with the 3 level model Eq 4.12 to the initial dynamics for sample c3sh26 in a), and for sample c6sh13 in b). Offsets have been added to the normalized data in order to separate them vertically on the scale shown.

An alternative mechanism resulting in the delayed rise is the influence of acoustic phonons. We hypothesise that phonons created due to the exciton population generated due to the excitation pulses would change the lattice spacing in a way that increased the oscillator strength of the exciton transition causing the observed delayed increase in the signal proportional to the population. Although the initial

rise in the signal is quite apparent, lasting oscillations cannot be seen in the data. We decided to compare the time at which features already attributed to acoustic phonons in the dephasing dynamics occurred with the time in the evolution of the density dynamics at which the signal rise is observed. This comparison can be seen for all three QDR samples in Fig 4.14. The  $\tau_{12}$  axis for the dephasing curves is shown aligned with  $0.5\tau_{23}$  (for the density curves). The phases of the polarizations created by the first excitation pulse are allowed to evolve for a time  $2\tau_{12}$ . Therefore, equivalent features will appear at half the value of the delay  $\tau_{12}$  in the dephasing curves compared to the delay  $\tau_{23}$  in the density curves if they are the result of the first excitation pulse. It can be seen for samples c6sh13 and c6sh14 that the maximum of the density signal rise coincides in time with the dip seen in the dephasing curves attributed to phonon oscillations in the previous chapter. For sample c3sh26 however, this is not the case. The rise in the signal concludes at a time roughly equal to half of the time at which the minima in the dephasing curves is seen. Even if this rise was due to phonons as a result of the second excitation pulse, the maximum density signal would appear at the same value of delay  $\tau_{23} = \tau_{12}$  as the minima in the dephasing curves.

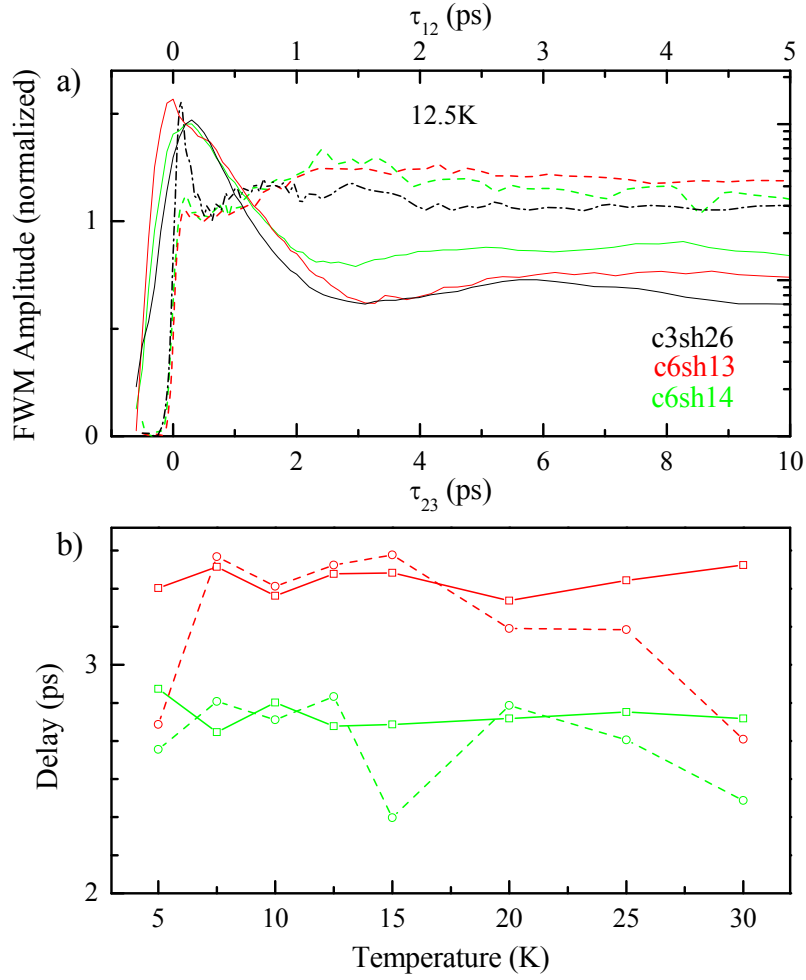


**Figure 4.14:** FWM as a function of  $\tau_{23}$  (density) at  $\tau_{12} = 0$ , and TI-FWM vs  $\tau_{12}$  (dephasing) is shown in a) using dashed and solid lines respectively. The data for the three samples is colour coded as indicated. Fig b) shows the delays at which the signal rise concludes in the density dynamics (squares), and the delays ( $2\tau_{12}$ ) at which the minima occurs in the dephasing dynamics (circles) as a function of temperature.

Although there was evidence to attribute the initial dynamics to an interplay between phonon oscillations and other fast population dynamics for samples c6sh13 and c6sh14, the initial dynamics for all investigated samples will have to include both effects discussed.

#### 4.4.3 Bright to dark relaxation time

The relaxation time of excitons from the  $\pm 1^L$  probed bright state to the lower lying  $\pm 2^L$  dark state can be extracted through measurements of the exciton density dynamics for  $\tau_{12} \neq 0$ . We have attributed the exciton dephasing to this transition. To explain how such measurements allow the extraction of this relaxation time, let us begin with the arrival of the excitation pulses at the QDR sample. As depicted in Fig 4.15 a), the pulses P1 and P2 generate a population of excitons in the bright exciton state. When the third pulse (Probe) arrives it can stimulate excitons to emit and transition to the ground state, but it can also excite the transition from the exciton to the biexciton state as shown in Fig 4.15 b) and c). This is possible

if the biexciton binding energy is less than the spectral width of the laser pulse. A biexciton is a Coulomb bound pair of excitons. As time evolves after the arrival of the Probe, the polarizations due to the exciton and biexciton states interfere and cause the total polarization to oscillate in time with the exciton-biexciton beat frequency, see Fig 4.15 d). This beating is simply due to the frequency difference between these two states. In the three beam FWM technique the photon echo, which occurs at a time equal to  $\tau_{12}$  after the arrival of the probe, is being detected. The generated polarization depicted in Fig 4.15 d) is therefore detected at  $t = \tau_{12}$ . At  $t = 0$ , half of the transition is bleached because one of the two available electron states in the ground state is filled which leads to transparency (i.e the exciton to ground state transition can occur, but the transition to the biexciton state cannot). The polarizations due to the exciton and biexciton are thus out of phase, and the total polarization is at a minimum. By varying  $\tau_{12}$ , it is possible to measure the density dynamics of the system at a time when the polarizations due to the exciton and biexciton are in phase, and effects that result from the presence of the biexcitonic state can be observed.

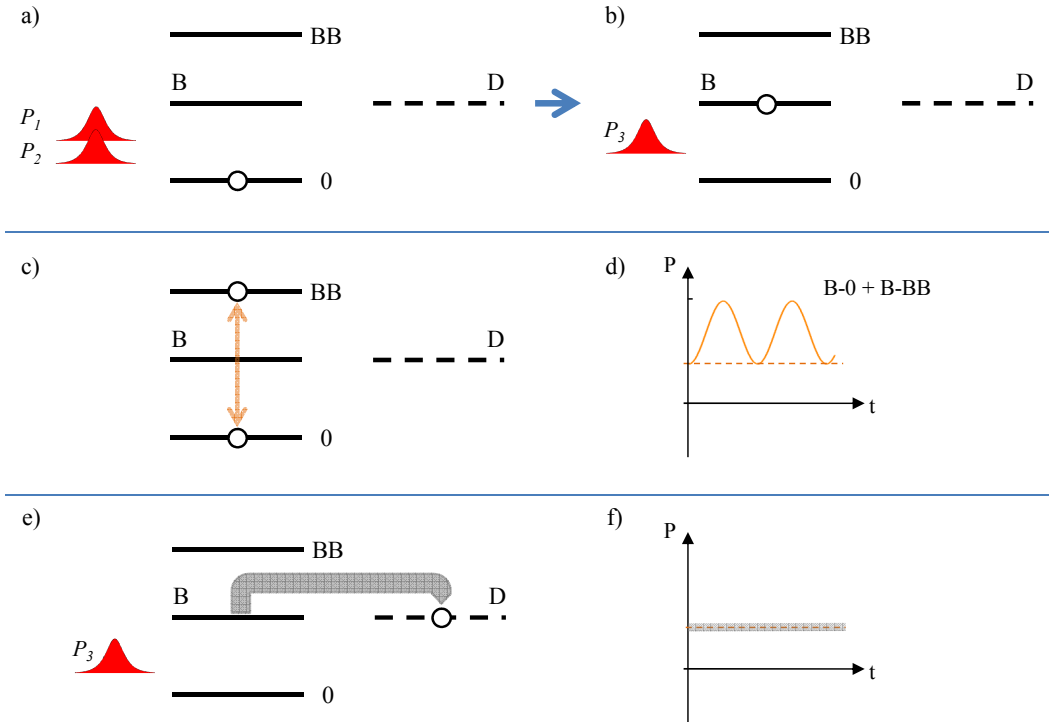


**Figure 4.15:** A sketch depicting the evolution of the exciton. The time axis in the sketch shown in d) has values  $t = \tau_{12}$ .

Now suppose that we have selected  $\tau_{12}$  such that a maximum contribution to the polarization from the exciton-biexciton interference is observed. As  $\tau_{23}$ , the delay between the excitation pulses and  $P_3$  is increased, excitons will relax into the dark state before the arrival of the Probe as depicted in Fig 4.15 e). When in the dark state, the excitons become transparent to the  $P_3$  pulse meaning that transitions from the exciton to the ground state, and from the exciton to the biexciton state are not coupling to light. The signal proportional to the polarization (the measured TI-FWM, or photon echo area) will therefore decrease as a function of  $\tau_{23}$  with a time constant equal to the bright-dark relaxation time. This relaxation time will

appear in addition to the population decay time which is always observed in the FWM signal measured as a function  $\tau_{23}$  in this experiment.

In order to extract the bright-dark relaxation time, we measured the density dynamics for a value of  $\tau_{12}$  which resulted in the strongest additional decay component compared to the signal decay observed for  $\tau_{12} = 0$  for a range of temperatures for all three investigated QDR samples. To analyse this data, we took the ratio of the data obtained for  $\tau_{12} \neq 0$  to the data for  $\tau_{12} = 0$ . Let us refer to these ratios as  $R(\tau_{12}, \tau_{23})$ . This was done to remove the population decay components present in both measurements that have been discussed in the previous two subsections. The comparison of some examples of the resultant ratios  $R(\tau_{12}, \tau_{23})$  and the normalized density dynamics at  $\tau_{12} = 0$  are displayed in Fig 4.16 a), b) and c) where a decay can clearly be seen. We noticed that oscillations were apparent at short delays in some of the ratio curves  $R(\tau_{12}, \tau_{23})$  which we will study in further detail in the following subsection. To fit these ratio curves, we included an oscillating term as well as two exponential decays in the fit function below.

$$R(\tau_{23}) = \left[ 1 + A_{\text{osc}} \exp\left(-\frac{\tau_{23}^2}{\sigma_{\text{osc}}^2}\right) \cos\left(\frac{2\pi\tau_{23}}{T_{\text{osc}}} + \phi\right) \right] \times [A_{\text{bd1}} \exp(-\tau_{23}\Gamma_{\text{bd1}}) + A_{\text{bd2}} \exp(-\tau_{23}\Gamma_{\text{bd2}})] + R(0) \quad (4.12)$$

where  $\sigma_{\text{osc}}$  is the damping rate of the oscillation of period  $T_{\text{osc}}$ , and  $\Gamma_{\text{bd1}}$  and  $\Gamma_{\text{bd2}}$  are the FWM signal decay rates. Examples of these fits are displayed in Fig 4.16 a), b) and c).

The exciton dephasing time obtained in section 4.3.2 provides a lower limit to the lifetime of the bright exciton state  $\pm 1^{\text{L}}$  using the relationship between the dephasing rate  $\gamma$  and the exciton lifetime  $\Gamma$ . Interestingly, the fitted decay rate  $\Gamma_{\text{bd1}}$  for the ratio  $R(\tau_{12}, \tau_{23})$  is similar to the bright exciton lifetime obtained from the dephasing measurements. A comparison of the temperature dependent linewidths  $\hbar\Gamma_1$  derived from the dephasing measurements and  $R(\tau_{12}, \tau_{23})$  is shown for all three investigated samples in Fig 4.16 d), e) and f). This comparison shows consistency between the dephasing time of the phonon assisted spin relaxation of the bright exciton state  $\pm 1^{\text{L}}$  to the dark state  $\pm 2^{\text{L}}$  and the bright to dark population relaxation time.

To observe the exciton-biexciton beats depicted in the sketch shown in Fig 4.15 d), we analysed the dependence of  $A_{\text{bd1}}$  on the delay  $\tau_{12}$ . As shown in Fig 4.17, a dependence in the amplitude of  $\Gamma_{\text{bd1}}$  can be seen for sample c3sh26 most clearly, and also for sample c6sh13. The observed data for sample c3sh26 is consistent with a period of about 2-3 ps. The beat periods (corresponding to a biexciton binding energy of  $\pm 1.5$  meV) for the other two samples could not be estimated due to the limited data range. This can be interpreted as a longer exciton-biexciton beat period for the larger core samples. This means that the exciton-biexciton energy splitting in the larger core QDRs is smaller than the splitting of 1.2 meV in the smaller core QDR namely c3sh26.

#### 4.4.4 Acoustic phonon oscillations

The oscillations observed at small delays  $\tau_{23}$  in the ratios  $R(\tau_{12}, \tau_{23})$  seen in Fig 4.16 a), b) and c) were only clearly visible in the data for a few temperatures. Due to the relatively high noise in the data, we calculated the average of the ratio over different temperatures. The average ratios  $R(\tau_{12}, \tau_{23})$  for all three investigated samples shown

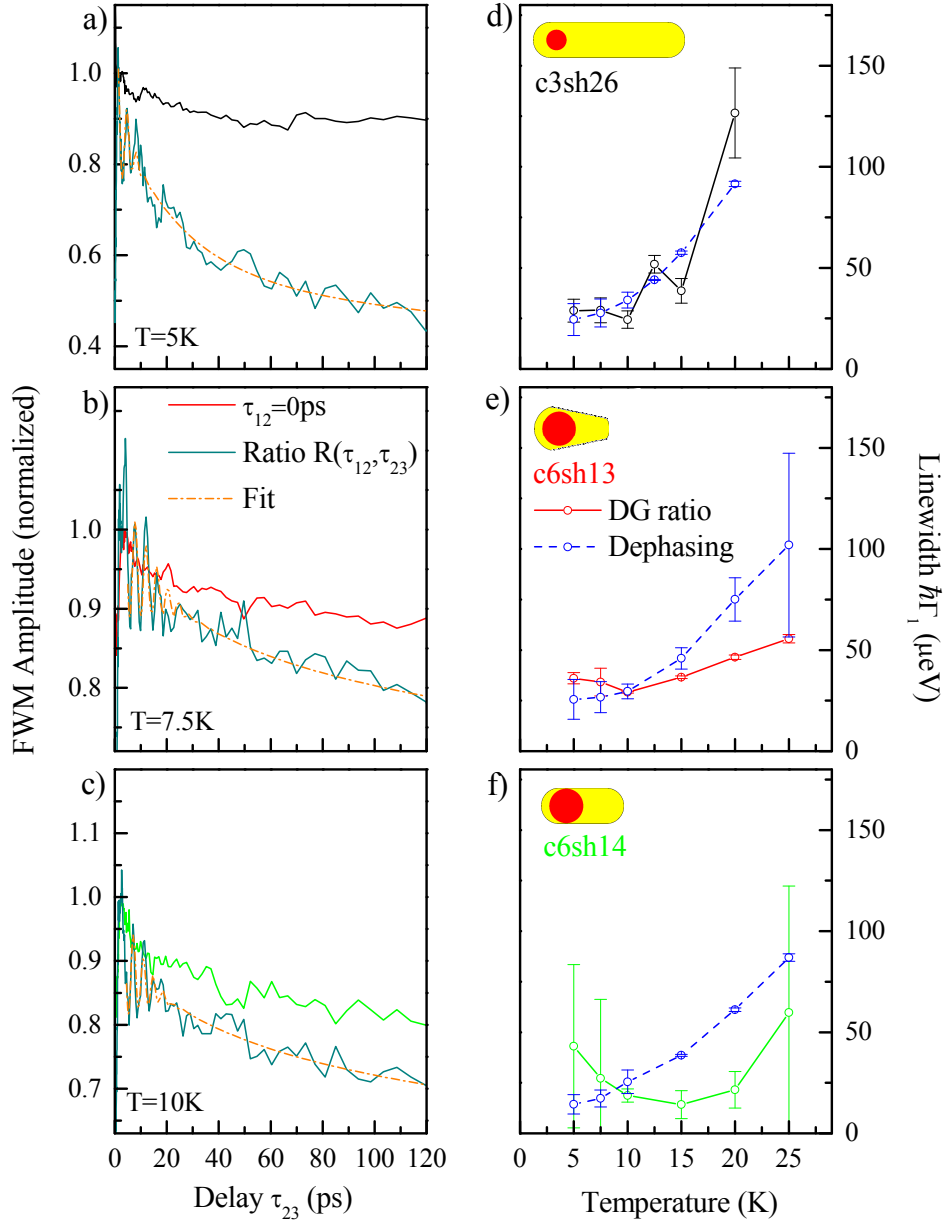


**Figure 4.16:** a), b) and c) show the normalized density curves at  $\tau_{12} = 0$  using solid black, red and green lines for samples c3sh26, c6sh13, c6sh14 respectively. The ratios of the density curves  $R(\tau_{12}, \tau_{23})$  are shown using the dark cyan lines with fits to the ratios shown using orange dash-dot lines. d), e) and f) show the temperature dependent linewidths of the bright-dark relaxation lifetime derived from the ratios shown to the left using solid lines, and derived from the dephasing measurements using the blue dashed lines for the three samples.



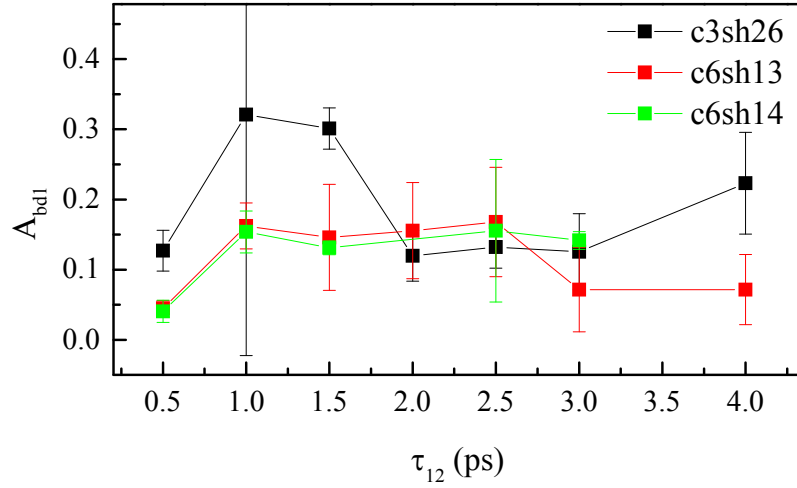


**Figure 4.17:** The amplitude of the bright-dark relaxation lifetime ( $\Gamma_{\text{bd1}}$ ) obtained from  $R(\tau_{12}, \tau_{23})$  fits made for different non-zero values of  $\tau_{12}$  at 10 K as a function of  $\tau_{12}$  are shown for the three investigated samples.

| Parameter                | c3sh26              | c6sh13                    | c6sh14               |
|--------------------------|---------------------|---------------------------|----------------------|
| $A_{\text{osc1}}$        | $0.1570 \pm 0.0032$ | $0.0529 \pm 0.0012$       | $0.0605 \pm 0.0012$  |
| $p_1$ (ps)               | $3.036 \pm 0.013$   | $4.194 \pm 0.011$         | $4.3146 \pm 0.0100$  |
| $\phi_1$                 | $3.166 \pm 0.025$   | $19.652 \pm 0.044$        | $46.409 \pm 0.027$   |
| $\sigma_1$ (ps $^{-1}$ ) | $3.464 \pm 0.058$   | $11.80 \pm 0.23$          | $10.86 \pm 0.23$     |
| $A_{\text{osc2}}$        | $0.0494 \pm 0.0023$ | $1.87 \pm 0.22$           | $0.0194 \pm 0.0009$  |
| $p_2$ (ps)               | $7.50 \pm 0.12$     | $8.388 \pm 0.022$ (fixed) | $10.087 \pm 0.076$   |
| $\phi_2$                 | $6.658 \pm 0.060$   | $2.165 \pm 0.011$         | $36.981 \pm 0.064$   |
| $\sigma_2$ (ps $^{-1}$ ) | $5.59 \pm 0.23$     | $1.615 \pm 0.035$         | $18.36 \pm 0.90$     |
| $O$                      | $0.0008 \pm 0.0002$ | $-0.0006 \pm 0.0002$      | $-0.0009 \pm 0.0002$ |

**Table 4.2:** Summary of the fit parameters used for the fits shown in Fig 4.18 a), b) and c) according to Eq. 4.13.

in Fig 4.18 clearly display oscillations at short delays. Fourier transforms (FT) were performed on these data sets so that the different frequency components of the observed oscillations could be examined. Fig 4.18 c), d) and f) shows the FTs of the averaged ratios  $\bar{R}(\tau_{12}, \tau_{23})$  for all three samples. The averaged  $R(\tau_{12}, \tau_{23})$  were fit with the following fit function:

$$\begin{aligned}
 R(\tau_{23}) = & A_{\text{osc1}} \cos\left(\frac{2\pi\tau_{23}}{p_1} + \phi_1\right) \exp\left(-\frac{\tau_{23}^2}{2\sigma_1^2}\right) \\
 & + A_{\text{osc2}} \cos\left(\frac{2\pi\tau_{23}}{p_2} + \phi_2\right) \exp\left(-\frac{\tau_{23}^2}{2\sigma_2^2}\right) + O
 \end{aligned} \quad (4.13)$$

where Gaussian damping is used for both oscillation terms as opposed to exponential damping which lead to underdamped fits. A summary of the fit parameters used to make the fits shown in Fig. 4.18 with this function is given in Table 4.2.

We compare the oscillations attributed to acoustic phonons that were observed in the dephasing measurements in section 4.3 to the features seen in these FTs. In order to analyse the oscillations in the dephasing curves in Fig. 4.5 in further detail, we fit regions of these data where oscillations were visible with Eq. 4.3 as shown in the insets of Fig. 4.19 a), b), and c). We then divided the data by these fits, and fit the resulting ratios with the function given in Eq. 4.13. Fig. 4.19 d), e) and f)

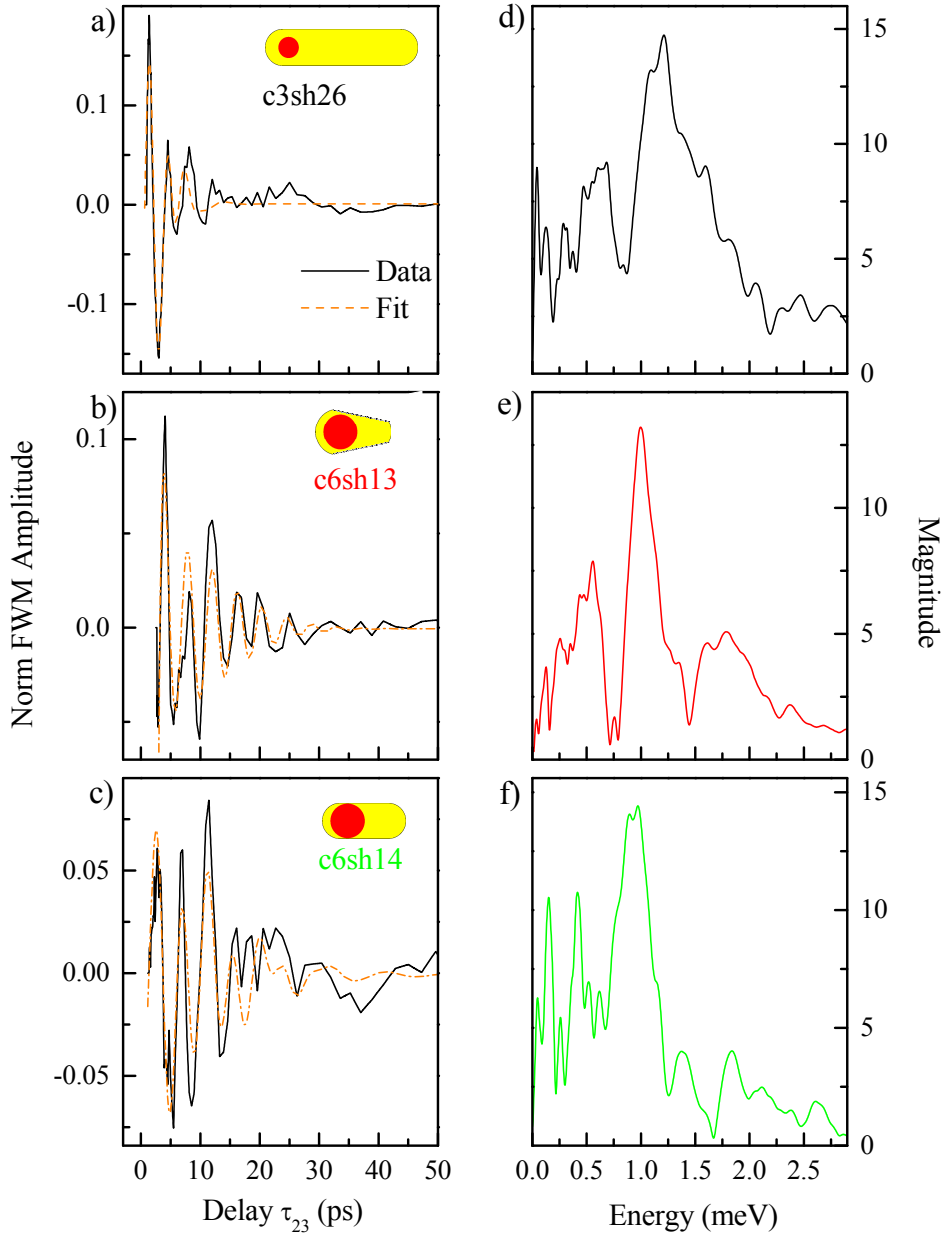


**Figure 4.18:** The mean average ratios of the density curves  $\bar{R}(\tau_{12}, \tau_{23})$  are shown after the subtraction of a biexponential decays for sample c3sh26 in a), c6sh13 in b), and c6sh14 in c). Fits to the data are shown using orange dash-dot lines. Figs d), e), and f) show the amplitudes of the Fourier transforms of the data shown to their left.

show a temperature dependent summary of the oscillation energies extracted from the fits shown to the left of these figures, and the oscillation energies extracted from the fit to the  $\bar{R}(\tau_{12}, \tau_{23})$  curves shown in Fig 4.18. For sample c6sh14, the oscillation period obtained from the analysis of the dephasing data for the higher energy mode (namely Mode 1 as indicated in Fig 4.19) was roughly half of the value obtained from the analysis of the  $\bar{R}(\tau_{12}, \tau_{23})$  curves. This period was increased by a factor of 2 before the oscillation energies as shown in Fig 4.19 f) were calculated. This was done recognising the possibility of acoustic phonons being generated as a result of the exciton density created by either P1 or P2. The signal is detected at a time  $2\tau_{12}$  after the arrival of P1 when the photon echo is generated. Therefore, phonons generated by the first pulse will appear as oscillations of the FWM signal with a period half that of the actual oscillation period in the TI-FWM versus  $\tau_{12}$  data.

Based on the observation of oscillations in both the dephasing and density data, and the correlation between the oscillation energies obtained from the two separate data sets, we concluded that the oscillations observed in the  $\bar{R}(\tau_{12}, \tau_{23})$  curves are due to the same acoustic phonons modes observed in the dephasing measurements. Analysing the dephasing data from section 4.3 in further detail allowed us to extract a second oscillation period not taken into account in the fits shown in Fig 4.5. The acoustic phonons are created as a result of the perturbation to the crystal equilibrium position upon exciton population generation by the excitation pulses (P1 and P2) that impinge on the QDR samples. Furthermore, we observed oscillations due to acoustic phonons generated P2 in all cases except for the case of Mode 1 in sample c6sh14 in which we attribute the higher energy oscillations to phonons generated by the first excitation pulse because this yields consistency with the oscillations observed in the density dynamics.

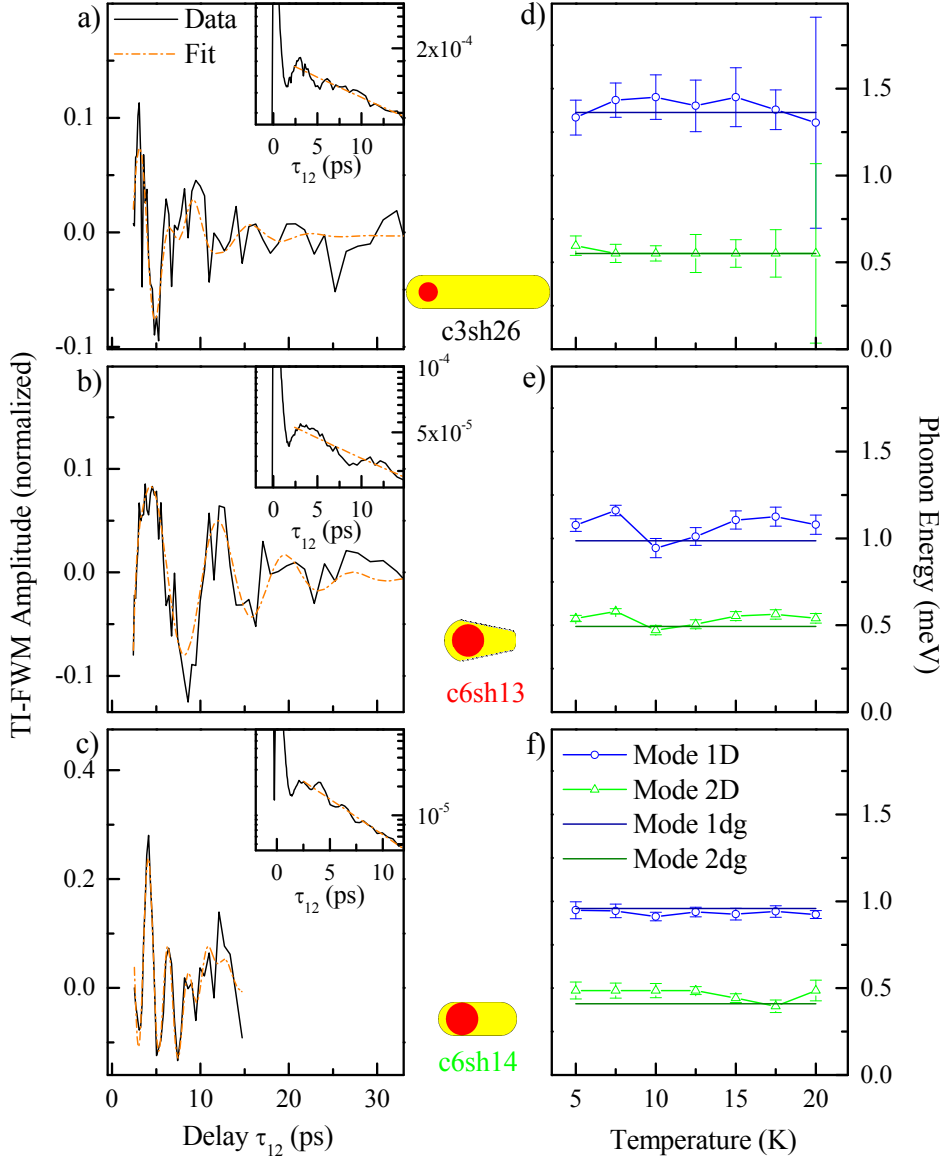


**Figure 4.19:** The ratios of the dephasing curves to the fits that are shown in the insets of a), b) and c) are shown along with fits made with Eq. 4.13 in a), b) and c) for samples c3sh26, c6sh13 and c6sh14 respectively. The blue and green lines with data points in d), e) and f) show the oscillation energies as a function of temperature extracted from fits to the full data set of temperature dependent dephasing curves analysed as shown to the left. The oscillation energies extracted from the density dynamics data as shown in Fig 4.18 are plotted as dark blue and green lines. The two modes are labelled Mode 1 and 2 with the ending D (dg) indicating the origin of the data as the dephasing (density) data set.

## Chapter 5

# Scanning probe microscope development

In this chapter, we outline the development of a scanning probe microscope (SPM) capable of simultaneous optical and scanning probe measurements undertaken such as electrostatic force microscopy (EFM) and atomic force microscopy (AFM) during the course of this PhD. This home built instrument was previously, in part set up in the MPhil project [87], and developed further with the goal to study correlation between single QD emission and their charging, specifically the QDR samples investigated in chapter 4. In the first section of this chapter, we will present essential background information about SPM. We will then describe the types of measurements the instrument is intended for, and motivate it's development. In the following sections we will move on to outlining the principles of operation of the instrument, and it's characteristics that allow for simultaneous scanning probe and optical measurements. We will then describe the changes made to the instrument from its initial state to improve its performance, and future work that must be performed beyond the timescale of this PhD to allow the instrument to perform its intended function.

### 5.1 Background theory

SPM involves the use of a solid probe, typically a fine tip, which is scanned over a surface in order to produce an image. Several different types of SPM techniques exist including atomic force microscopy (AFM), scanning tunneling microscopy (STM), electrostatic force microscopy (EFM). The homebuilt instrument described here was designed to implement AFM and EFM.

#### 5.1.1 Atomic force microscopy

AFM relies on the force distance relation between the tip and the sample surface. A feedback system is implemented in order to maintain a constant force on the tip by adjusting tip sample distance as it is scanned over the surface. There are several modes of AFM operation [88]. Non contact mode operates in the attractive part of the force curve as shown in Fig. 5.2. The tip is attached to a cantilever of known force constant. The cantilever is made to oscillate close to it's resonant frequency which is typically 300kHz. This is achieved using a dither piezo. Feedback is based on modulations in the amplitude, frequency or phase of oscillation during a scan. The feedback system will adjust the height of the tip to maintain an amplitude or

frequency setpoint. The amplitude or frequency of the cantilever can be detected for example by detecting laser light reflected from the back of the cantilever.

This figure has been redacted by the author for copyright reasons

**Figure 5.1:** A scanning electron microscopy (SEM) image of a dynamic mode cantilever manufactured by Olympus [89]

The tip and sample can be said to be in contact when their separation is such that the force between them is repulsive. Thus, contact mode AFM operates in the repulsive part of the force curve where the cantilever is deflected away from the sample surface. The strong repulsive force can cause deformation of the tip and possibly also of the sample surface with time.

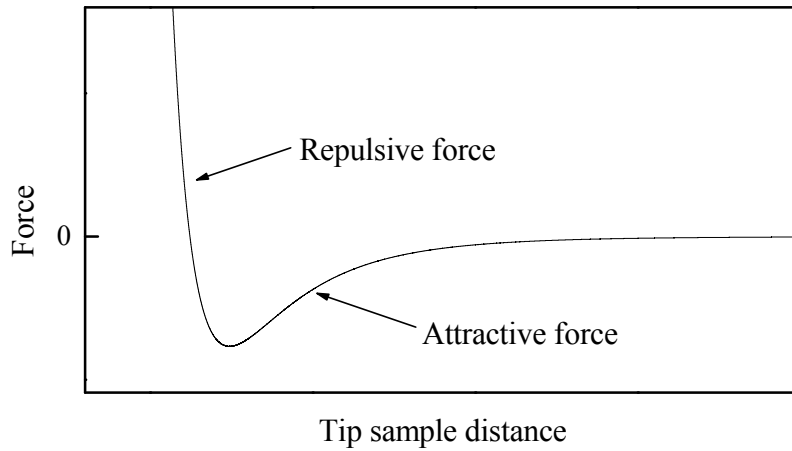


**Figure 5.2:** A sketch of the force distance relation. The negative gradient of a Leonard-Jones potential is plotted.

In tapping mode AFM, the cantilever is made to oscillate with the tip closer to the sample than in non contact mode. At the closest distance to the sample surface, the tip enters the repulsive regime. This is therefore also referred to as intermittent contact mode. The cantilevers used are stiffer than those used for other AFM modes and the amplitude of oscillation is large when compared to non contact mode; typically tens of nanometers. The advantage of this is that the tip is less likely, than in non contact mode, to become stuck in a layer of liquid which can often form on the sample surface in ambient conditions. In tapping mode, the tip also experiences reduced lateral force when compared to contact mode, giving greater resolution.

### 5.1.2 Electrostatic force microscopy

For electrostatic force measurements, a potential difference is applied between the tip and the sample. A long range force is then present which depends on the change in capacitance with tip sample separation. An expression for this force can be derived by taking the derivative with respect to the tip sample separation  $z$ , of the energy stored in a capacitor:

$$F_{\text{el}} = \frac{1}{2} \frac{\partial C}{\partial z} V^2 \quad (5.1)$$

Where  $F_{\text{el}}$  is the electrostatic force, and  $V$  is the potential difference between the tip and the sample which is the sum of contact potential and any applied potential [90]. The frequency shift  $\Delta\nu$  of the tuning fork depends on the force gradient, as given by the expression:

$$\frac{\Delta\omega}{\omega_0} = -\frac{1}{4} \frac{\frac{\partial^2 C}{\partial z^2} V^2}{k} \quad (5.2)$$

where  $k$  is the spring constant,  $\omega_0$  is the unperturbed resonant frequency of the cantilever, and  $\Delta\omega$  is defined as the difference between the measured frequency and the resonant frequency without the influence of a force gradient. A conductive tip is required for this mode as well as a means of applying a voltage bias. EFM measurements are beneficial in any field where it is useful to know the charge distribution of samples.

## 5.2 Working principles of the instrument

In this section we will describe the home built SPM instrument and its working principles. We will describe how the arrangement of its components allows for simultaneous SPM and optical measurements.

### 5.2.1 Setup

The instrument is mounted inside a homebuilt vacuum chamber which is on an air damped optics table. The top part of the chamber can be removed to access the instrument. Once pumped using a turbo pump/membrane pump combination, pressures down to  $10^{-5}$  mbar can be achieved after approximately half a day. The instrument parts are mounted on a damping stage suspended by three springs which attach to vertical poles extending from the base of the vacuum chamber. The damping stage also has three pairs of parallel metallic plates positioned evenly around the stage as shown in Fig. 5.3. In between the metal plates there are magnets which are held by the vacuum chamber base. These magnets do not physically contact any part of the damping stage. When the metal plates move relative to the magnets, Eddy currents form in the metal plates. The magnetic fields produced as a result of these currents oppose that of the permanent magnets, and dampen the motion of the stage. The distance had been adjusted to lead to a Q-factor of about 2-5, which is best for minimum transfer of vibrations in the relevant frequency range (see [87])

The vertical column labelled VC in Fig 5.3 a) holds a home built coarse positioner which functions by a 'stick slip' mechanism. Attached on the underside of the home built positioner (HBP) is an attocube ANSxyz100 scanning piezo (SP) capable of  $40\mu\text{m}$  of movement in the x and y directions, and  $24\mu\text{m}$  in the z-direction (the direction that defines the tip sample distance). A custom made printed circuit board (PCB) holder labelled PCBh in Fig 5.3 b) can be attached to the bottom

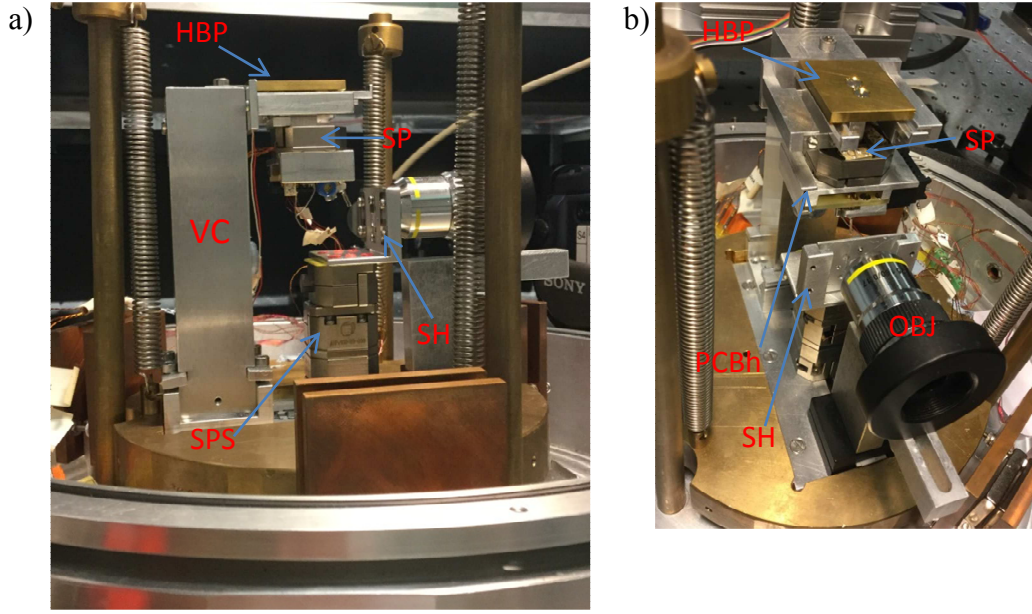


**Figure 5.3:** Pictures from different angles of the combined AFM and optical instrument in a) and b)

of the SP as shown. This holder is made to hold a PCB onto which a quartz tuning fork (QTF) with an AFM tip can be mounted using a custom made QTF holder (discussed in further detail in section 5.3.4). A stack of attocube ANPxyz100 postioners labelled SPS forms a base for the sample holder labelled SH. The sample holder allows samples to be mounted vertically so that they are accessible to the SPM tip from the left side as shown in Fig 5.3, while still being optically accessible from the other side as long as the sample substrate is transparent. The objective labelled OBJ can be used to focus light onto the sample, as well as collect light from the sample for imaging and optical excitation. The HBP and the sample positioning stack (SPS) allow the tip and sample respectively to coarsely approach each other, whereas the scanning is handled by the SP which has a much better resolution. This arrangement facilitates simultaneous SPM and optical measurements on an appropriately prepared sample.

### 5.2.2 Quartz tuning forks

The home built instrument relies on the changes in oscillation frequency of the SPM probe for the feedback required to maintain a constant distance of the SPM tip from the sample surface. The probe consists of a quartz tuning fork (QTF) with a tip attached to one of the prongs, pointing parallel to the direction of oscillation. The resonant frequency of a QTF is dependent on its spring constant. If the probe experiences a force gradient, for example due to a change in tip sample distance, the spring constant is changed as follows [91]:

$$k = k_0 - \frac{\partial F}{\partial z} \quad (5.3)$$

In analogy with a mass on a spring, the resonant frequency is given by  $\omega_0 = \sqrt{\frac{k}{m}}$  with  $m$  being the effective mass of the cantilever. Thus, the shift in frequency depends



on the force gradient as given [92]:

$$\frac{\Delta\omega}{\omega_0} = -\frac{1}{2} \frac{dF}{dz} \frac{1}{k} \quad (5.4)$$

The piezoelectric effect can be used in the tuning fork to produce mechanical oscillations by providing a sinusoidal voltage signal. The motion of the prongs then results in a current proportional to the oscillation because of the electrostrictive effect, which is the reverse of the piezoelectric effect. This current signal can be used for detection, removing the need for an optical readout. A self sensing probe is a major advantage for a cost effective SPM instrument. Furthermore, an optical readout can interfere with the optical imaging in our instrument.

The QTFs utilized are the same as the ones typically used in time keeping devices. The ones used in this work were obtained from Farnell, and have a resonant frequency of 32.768kHz and a quality factor in vacuum of about 100,000. The QTFs used in this work have a prong length of about 5-6 mm. It's possible [93] to model the frequency response of the QTFs using a circuit comprising an inductor, capacitor and resistor in series (LCR circuit) like the one shown in Fig. 5.4

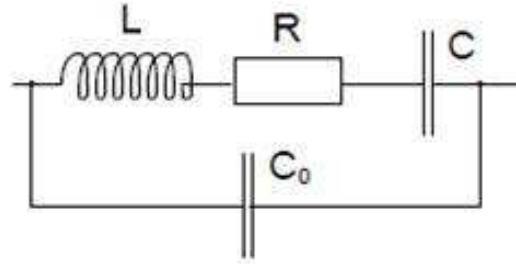


**Figure 5.4:** Diagram of LCR resonant circuit with additional parallel capacitance.

In this circuit, the resistor is related to the dissipative forces, the series capacitance to the spring constant, and the inductance to the effective mass of the tuning fork [94]. The parallel capacitance  $C_0$  represents the parasitic capacitance in the system. The frequency response can be obtained by calculating the total impedance of this circuit as follows:

$$Z = \frac{R}{\left(1 - \omega^2 C_0 L + \frac{C_0}{C}\right) + \omega^2 C_0^2 R^2} + i \frac{\left[\left(\omega L - \frac{1}{\omega C}\right) \left(1 - \omega^2 C_0 L + \frac{C_0}{C}\right) - \omega C_0 R^2\right]}{\left(1 - \omega^2 C_0 L + \frac{C_0}{C}\right) + \omega^2 C_0^2 R^2} \quad (5.5)$$

We characterised these QTFs by measuring their frequency response. A tuning fork was driven by a voltage controlled oscillator (VCO) through one of its electrodes, and a current output was taken from the other electrode to be input into a lock-in amplifier. The reference signal for the lock-in was provided by the same VCO that was used to drive the QTF. The resultant data was fitted using the expression (5.5). These fits are shown in Fig 5.5 a), and 5.5 b) for data taken in vacuum and ambient conditions respectively. Because of the circuit used to collect this data, one would expect there to be a large parallel capacitance which is indeed observed. The frequency response of the equivalent circuit was also simulated using Fortran90 code using the parameter values resulting from the fits in Fig 5.5. The results of the simulations along with the measured data can be seen in Fig. 5.6.

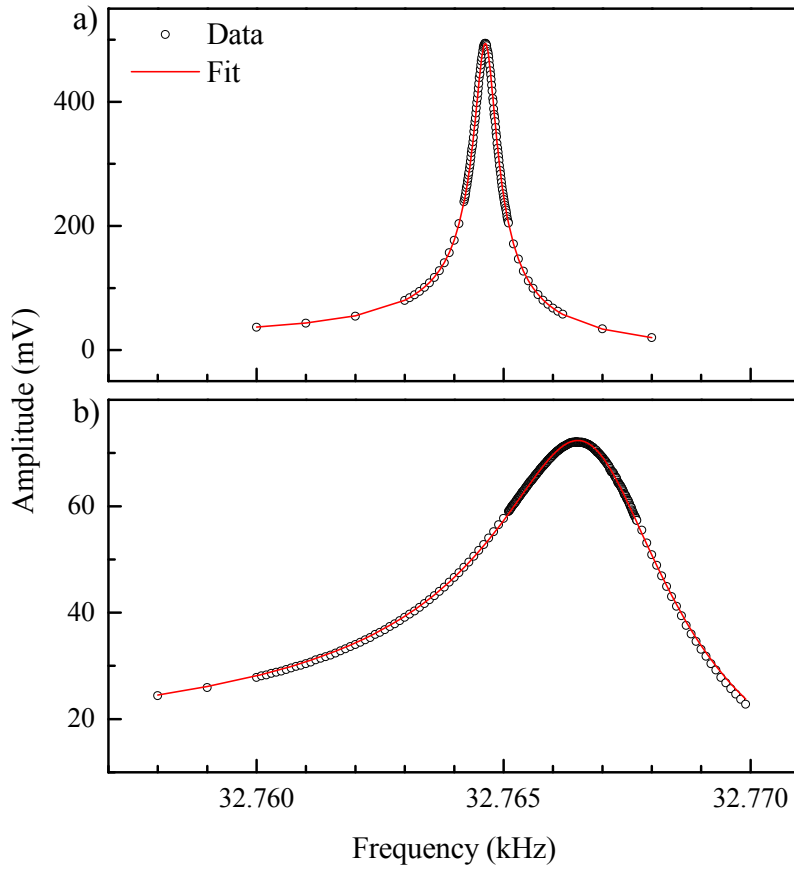


**Figure 5.5:** a) amplitude of the signal from the QTF measured by the lock-in versus the frequency with which the QTF was driven with the VCO. The data is for a QTF in vacuum conditions. The solid line is the fit to the data made using Eq. 5.5. The parameter estimates were:  $L = 2860$  H,  $R = 6949\Omega$ ,  $C = 8.249 \times 10^{-15}$  F and  $C_0 = 1.568 \times 10^{-11}$  F. The quality factor was 84,700. b) shows the same data but with the QTF in ambient conditions (removed from casing). The parameter estimates were:  $L = 2699$  H,  $R = 56695\Omega$ ,  $C = 8.74 \times 10^{-15}$  F and  $C_0 = 1.389 \times 10^{-11}$  F. The quality factor was 9,800.

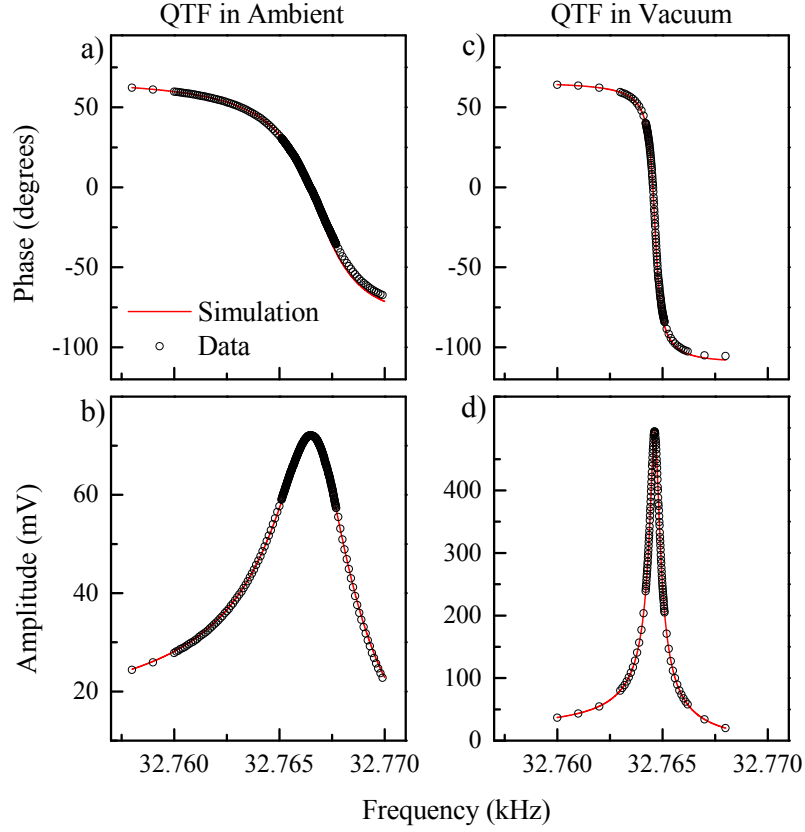


**Figure 5.6:** Amplitude and phase of the current output from the QTF measured by the lock-in versus the driving frequency. The solid lines show the results of simulations of the equivalent circuit with the parameters estimated from the fits in Fig. 5.5 a) and b).

### 5.2.3 Electronics setup

As discussed in section 5.1.1, the frequency shift of a tuning fork is proportional to the force gradient experienced by the probe, see Fig. 5.7. Relying on changes in resonant frequency rather than amplitude also results in faster detection since it adjusts instantaneously. The QTF is driven using a circuit based on the design by Jersch et al [95]. One of the outputs of this circuit is a signal proportional to the QTF oscillation. This signal is fed into a Phase Locked Loop (PLL) which outputs a dc signal proportional to the frequency shift of the QTF.

This figure has been redacted by the author for copyright reasons

**Figure 5.7:** The top plot shows a force curve and its equivalent frequency shift for a combined AFM/STM instrument by Gomez et al [96]

The electronics setup is outlined using a block diagram seen in Fig. 5.8. The details of the PLL are as follows. The signal proportional to the QTF oscillation is input into a lock-in amplifier along with a reference signal generated by a voltage controlled oscillator (VCO). The output is taken from the phase output of the lock in, which is also fed back to the external modulation input of the VCO to create the loop. First, the QTF and reference signals are multiplied in the lock-in, e.g.

$$SR = A_s \sin(\omega_s t + \phi_s) \times A_r \sin(\omega_r t + \phi_r) \quad (5.6)$$

Where the phases in general are functions of time,  $S$  is the signal and  $R$  the reference [97]. In the above  $A_s$ ,  $\omega_s$  and  $\phi_s$  are the amplitude, frequency and phase of the signal respectively.  $A_r$ ,  $\omega_r$  and  $\phi_r$  are the amplitude, frequency and phase of the reference respectively. The resulting signal after this multiplication is passed through a low pass filter to obtain only the dc part which is shown below.

$$X = \frac{A_s A_r}{2} \cos(\phi_s - \phi_r) \quad (5.7)$$

In a dual phase lock-in amplifier, the signal is also multiplied by a reference [98], phase shifted by  $90^\circ$ . The output signal of the second channel can therefore be written as

$$Y = \frac{A_s A_r}{2} \sin(\phi_s - \phi_r) \quad (5.8)$$

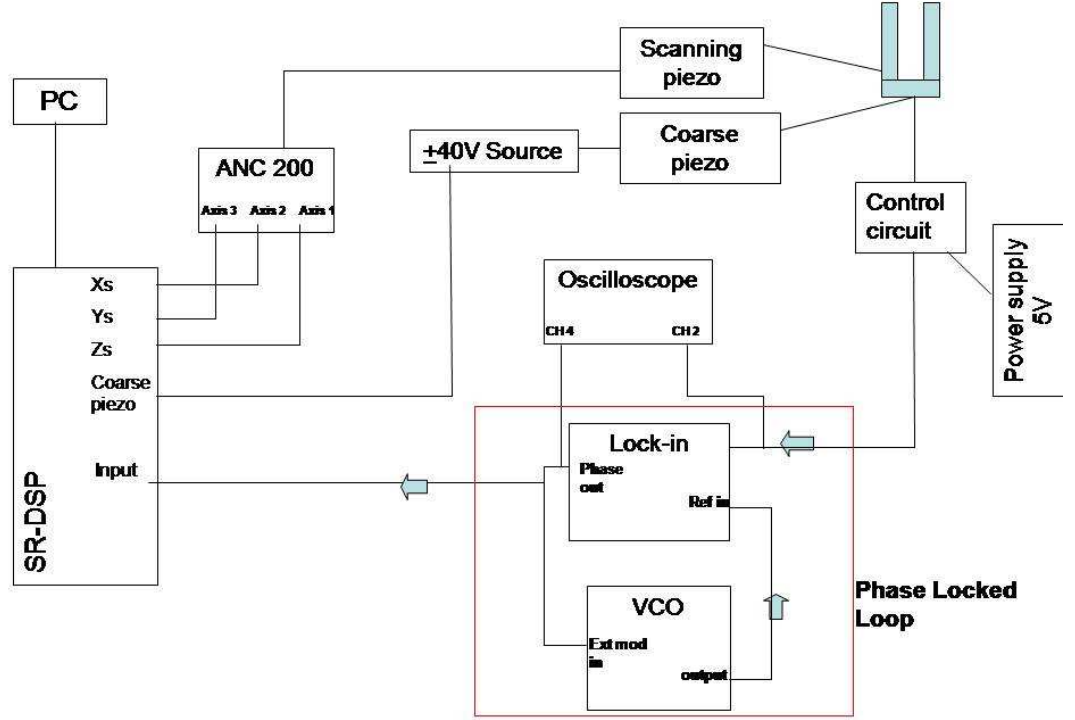


Figure 5.8: A block diagram of the electronics setup [87]

The phase output of the lock-in can be calculated using  $\phi_{out} = \arctan(Y/X)$ . Since the frequency of a signal is the time derivative of the phase i.e  $f = \frac{1}{2\pi} \frac{d\phi}{dt}$ , the phase output signal  $\phi_{out}$  is dependent on the frequencies of the two input signals.

The external modulation input of the VCO converts a dc voltage signal into an increase or decrease in the frequency of its output. In order to describe the feedback loop, one can write  $\frac{d\omega_r}{dt} = -\alpha(\omega_s - \omega_r)$  where  $\alpha$  is the product of the VCO gain ( $G$  with units of frequency over voltage, i.e. rad/sV) and the phase to voltage conversion factor  $V_\phi$  of the lock-in phase output, i.e.  $\alpha = V_\phi G$ . We used a Stanford Research System SR530 lock-in for which  $V_\phi = 2.9 \text{ mV/rad}$ . The solution to the above equation for a constant  $\omega_s$  is:

$$\omega_r = \omega_s - [\omega_s - \omega_{r0}] e^{-\alpha t} \quad (5.9)$$

Where  $\omega_{r0}$  is the initial reference frequency at  $t=0$ . Thus, the frequency of the reference approaches the frequency of the signal with an exponential response time constant of  $1/\alpha$  which is the response time of the PLL. The reference frequency will therefore follow the signal frequency with this response time. The difference in the initial reference and signal frequencies is given by  $\omega_s - \omega_{r0} = \alpha \phi_{out}$ . This also limits the frequency range to  $\pm \pi \alpha$ . It must be noted that Eq. 5.9 does not account for the response time of the lock-in amplifier. For SPM operation, the reference frequency is initially set to the same value as the QTF frequency to result in close to zero lock-in phase such that  $\alpha \phi_{out}$  is the frequency shift.

The parameters which control the behavior of the PLL are the integration time of the lock-in, which determines the amount of time taken for the phase output to settle at a constant value, and the gain  $G$  of the VCO. The behavior of the PLL setup was tested by generating a frequency modulated signal with a square waveform of a modulation amplitude of 2 Hz, which was input into the PLL, and monitoring the response. The responses obtained for a few different parameters are shown in

Fig. 5.9. The comparison of different gain settings indicates that with too little gain, the response is slow whereas with high gain, the output signal overshoots the correct value before settling. The comparison of different time constants shows that for long integration times, the output oscillates about the correct value for a significant time before settling, and vice versa for short integration times. The integration time of the lock in must be shorter than the response time of the PLL defined by  $\alpha$ .

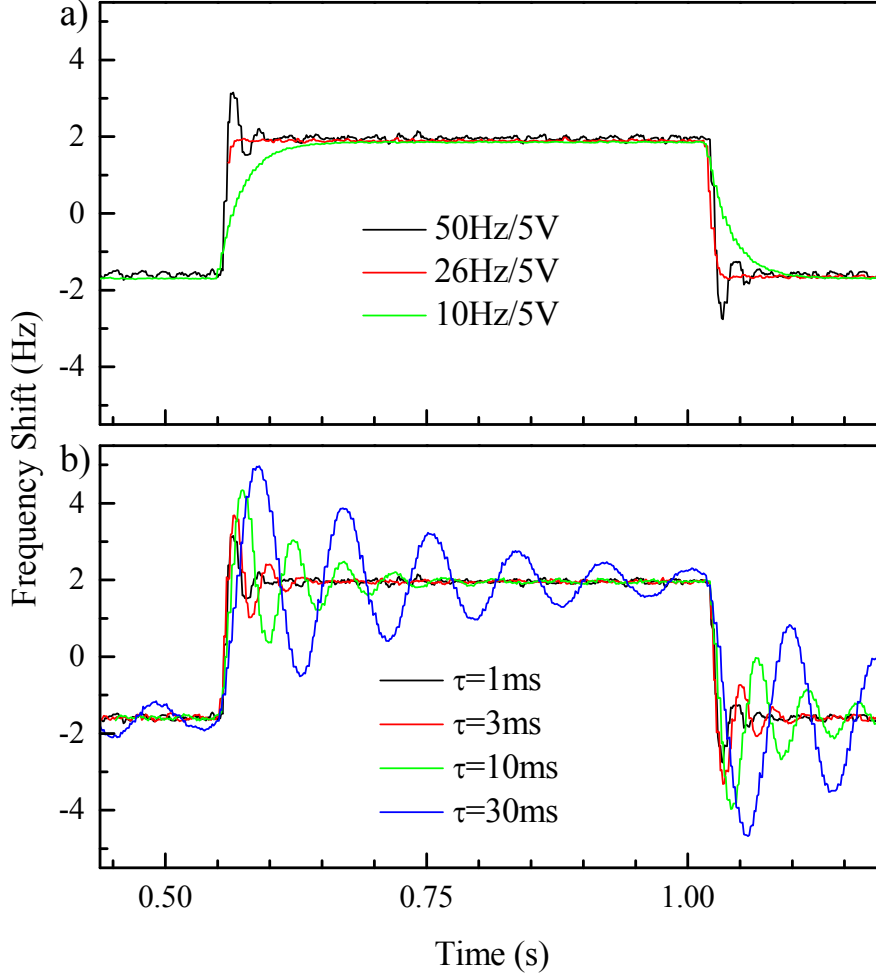


**Figure 5.9:** a) reference frequency of the PLL, with an input signal modulated in frequency between  $\pm 2\text{Hz}$  at a rate of 1 cycle per second. The PLL output for different gain settings and a lock-in integration time of 1ms is shown. b) as a) but for varying integration times and a fixed gain of 50Hz/5V. Note that gain was specified in units of Hz/V rather than rad/sV as discussed in the text.

The instrument is controlled by the open source GXSM software written for SPM applications. The software allows control of the positioning devices linked to the QTF sensor as well as the feedback and scanning parameters. The feedback control loop, which is a proportional integral control, is implemented by a DSP board. The frequency shift signal is an input for the DSP board and is used for the feedback. A frequency setpoint is defined by the user in the GXSM software which the DSP attempts to achieve by adjusting the z-position (tip sample separation) of the SP controlled through the ANC200 amplifier. Feedback can be obtained in the repulsive or attractive region of the frequency shift curve, with the attractive region

presenting the disadvantage of a tip crash if the tip travels past the minima of the curve. During an approach, steps of the coarse piezo are followed by an extension forward of the tip using the SP. If the surface is not found, the tip retracts and the process is repeated.

### 5.3 Developments of the instrument

The images of the combined SPM and optical instrument presented thus far have represented the instrument as it exists after a number of modifications from its status at the beginning of this thesis which was the result of [87]. In this section we will describe the problems with the instrument, and the related modifications made.

#### 5.3.1 Modifications to the electronics

The open source control software GXSM allows for many different measurement types, one of which is a scan of the variation of the frequency shift signal of the tuning fork with distance from the sample. These were the measurements first attempted on the instrument. Frequency shift curve measurements were made using commercial AFM tips attached to the QTFs using two part epoxy glue with a 150 micron thick glass coverslip as the sample surface (note that a bare coverslip was used as a mock sample surface). These measurements often did not show the attractive part of the frequency shift curve (see Fig. 5.7). An example of these measurements is shown in Fig. 5.10. It was also noticed that stable feedback in the repulsive regime could not be achieved. The frequency difference signal showed jumps to a high value followed by a return to a frequency difference value below the set point, which coincided with the tip extending and retracting repeatedly. It appeared as if the tip was snapping in towards the sample surface and sticking to it. This problem could not be resolved by adjusting the control parameter settings of the proportional integral control loop used by GXSM, or by adjusting the parameters of the PLL.

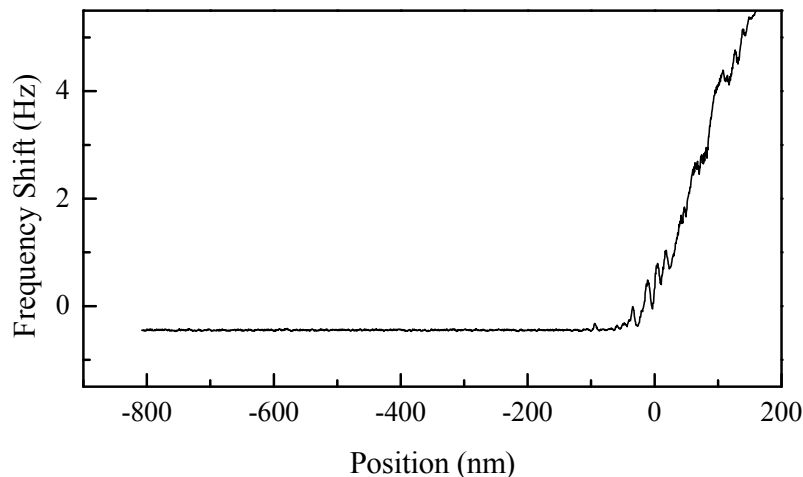


**Figure 5.10:** Frequency shift versus tip sample distance is plotted. The graph is an example of a frequency shift curves obtained using GXSM software. The approach of the tip started from an arbitrary position away from the sample, and the scale shows the distance travelled by the tip towards the sample surface.

A manual method of obtaining frequency shift curves was attempted by moving

the tip towards the sample using the scanning piezo controller (Attocube ANC200) which controls the sample positioning stack (SPS). The tip was moved the smallest possible step size of 1.5 nanometers and a scan of the frequency shift signal with time was recorded at each position. The method allowed the measurement of the expected profile of a frequency shift curve. However, it was observed that as the tip was manually moved closer to the sample surface in discrete steps, there would be a separation at which the frequency shift signal would gradually (over 10s of seconds) increase and settle at a value high enough to imply contact with the surface in the repulsive regime. It was also noticed that when subsequently retracting the tip manually, the frequency shift signal would remain at a constant high value (in the repulsive regime) as the tip sample separation was increased. The frequency shift signal would not return to a lower value until the separation was much greater than the separation at which the gradual increase was observed during the approach. These observations also implied that the tip and sample were sticking to each other when in contact.

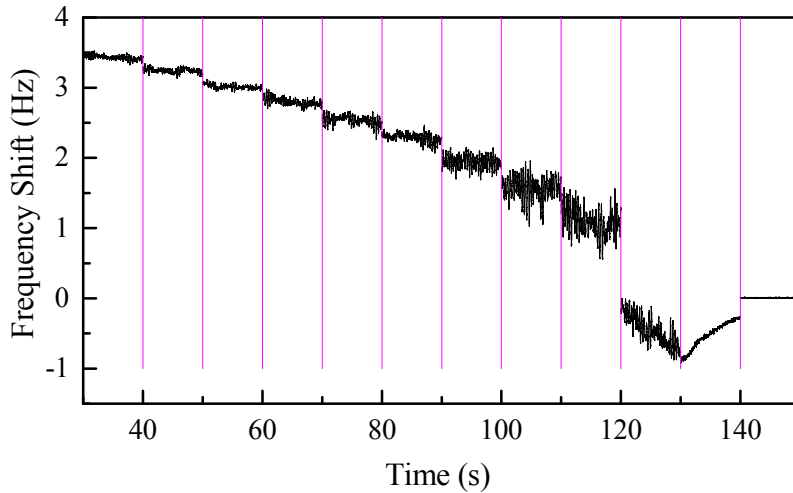


**Figure 5.11:** Frequency shift versus time. The vertical magenta lines separating 1.5 nm steps in the position of the tip towards the sample surface.

In order to investigate the sticking, measurements were made in vacuum to eliminate the possibility of a water film causing the observed problem. No significant alterations of the results were found. Suspecting contamination of either the tip or the sample surface we subsequently replaced them. A frequency shift curve over the expected separation range was then measured as shown in Fig. 5.12. Subsequent measurements led to the observation of the sticking problem yet again.



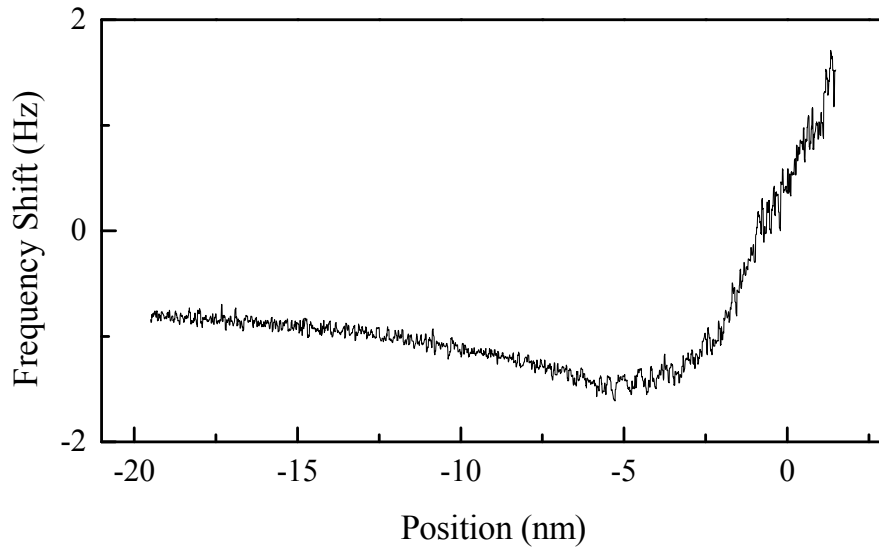


**Figure 5.12:** A frequency shift curve obtained at the first approach with a newly prepared commercial AFM tip.

Later scans, while attempting to approach the sample for feedback in the attractive regime, showed that after the tip had contacted the sample surface on the initial approach, indicated by a sudden jump in the frequency shift signal, a frequency shift curve like profile could be measured and feedback at the frequency set point achieved; see Fig. 5.13. The distance over which this profile was measured was approximately 50 nanometers as seen in Fig. 5.14, far larger than expected for a typical frequency shift curve. It was speculated that such a long range force could be due to changes in the charge state of either the tip or the sample surface after the initial contact causing a type of electrostatic force. Such unwanted frequency shift curves could be predictably measured on the sample with the tip for which the measurements are shown in Fig 5.12. In commercial SPM instruments the sample is usually grounded which prevents the build up of charge. The home built SPM in its initial state had no provision for grounding either the tip or the sample. Based on the observations, a build up of charge was a reasonable explanation. It was possible with this frequency shift curve profile to achieve stable feedback in the repulsive regime.

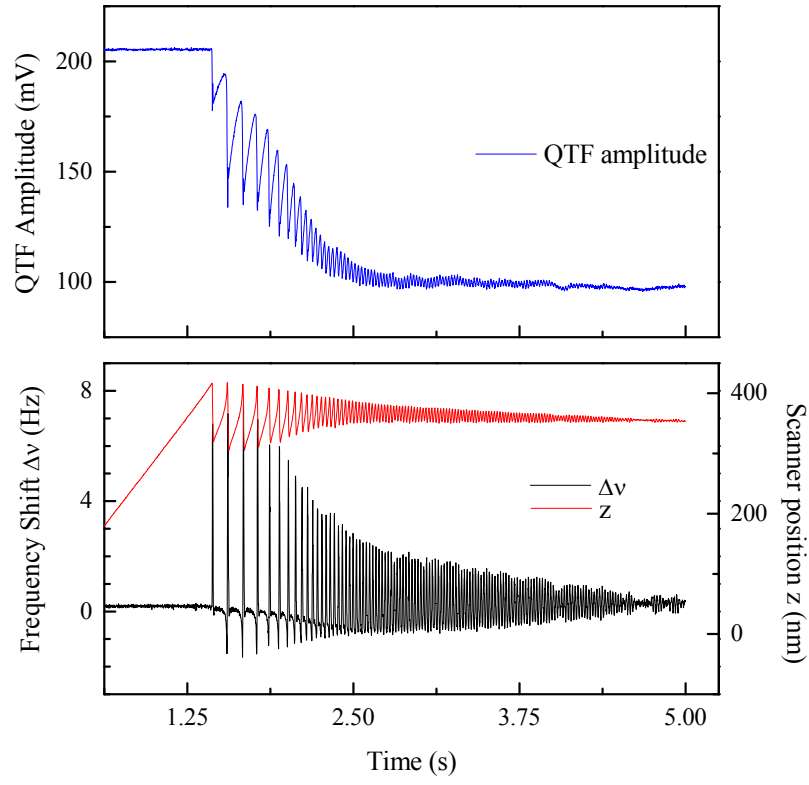


**Figure 5.13:** A time scan is shown during an approach of a commercial silicon AFM tip towards a glass coverslip sample surface. The QTF amplitude, tip position and frequency shift signal are shown.

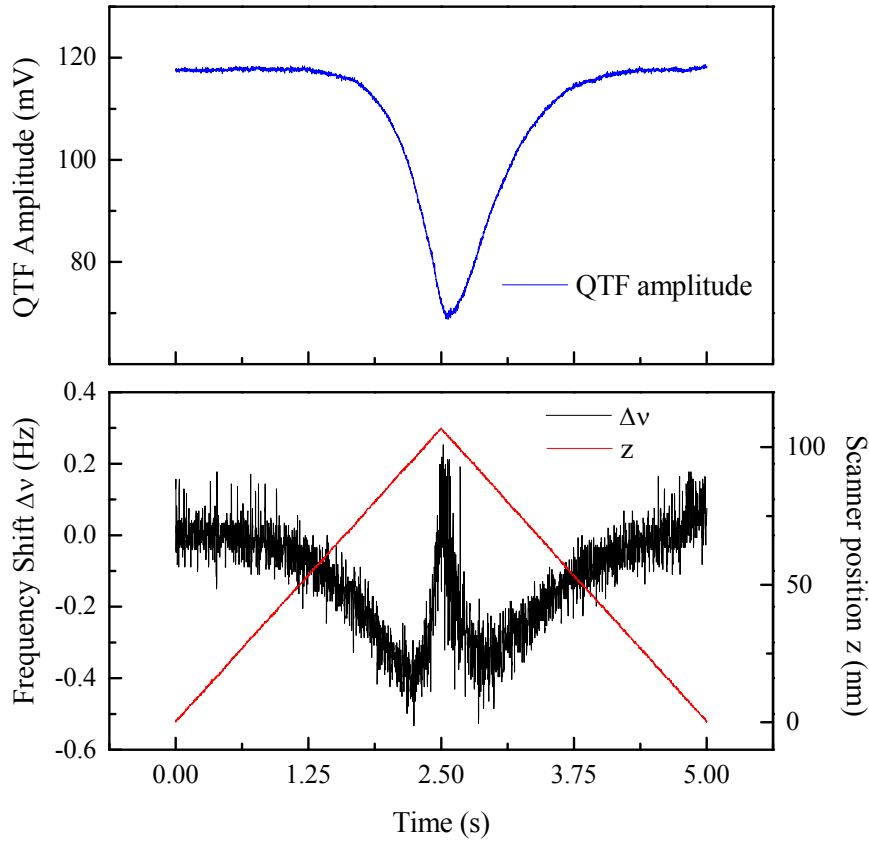


**Figure 5.14:** A frequency shift curve after suspected damage to the AFM tip. The graph includes QTF amplitude and damping signals.

We also noticed during the course of these initial tests that the minimum detectable QTF oscillation amplitude was 8 nm limited by the electronics noise. A much lower QTF oscillation amplitude of 0.1 nm has been reported in the literature for SPM applications [91]. The drive circuit as it initially existed was not capable of driving the QTF with a lower amplitude. Let us now discuss the drive circuit used for the QTF in further detail, and outline the modifications made.

Jersch et al, in [95], propose a circuit which can drive tuning forks to oscillate at as low as thermal vibration amplitudes, for SPM applications. The circuit based on this design was implemented on a printed circuit board (PCB) mounted inside an aluminium box for electrical screening. This was then connected via BNC to a port mounted on the outside of the vacuum chamber which connected to the QTF via some cables of length greater than 20 cm. Due to the fact that the entire drive circuit was housed outside the vacuum chamber, the lengthy cables between the QTF and the circuit added extra parallel capacitance, and increased the electronic pickup. The circuit, as inherited at the beginning of the project is shown in the diagram in Fig. 5.15. The circuit is designed such that the drive to the QTF is kept constant even as the quality factor changes during an approach. The output of the circuit gives a signal which is proportional to the QTF oscillation and is used as the input to the PLL. Since the possible amplitudes outlined by Jersch et al, and also those reported generally in literature for SPM applications (for example in ref [91] and [96]), are much smaller than the noise floor measured for the circuit in this configuration, it was necessary to modify the layout. It was noticed that oscillations of the tuning fork cease before the minimum gain setpoint is reached; in other words

the minimum attainable amplitude was limited by the noise of the setup. In light of this, several modifications to the circuit were made. The first was to create a new output after the first current amplifier in the circuit and test whether this could be used as the input to the PLL. The reason for this was to have a signal which has a fixed proportionality to the physical amplitude of oscillation of the QTF instead of having additionally the variable gain of the feedback amplifier.

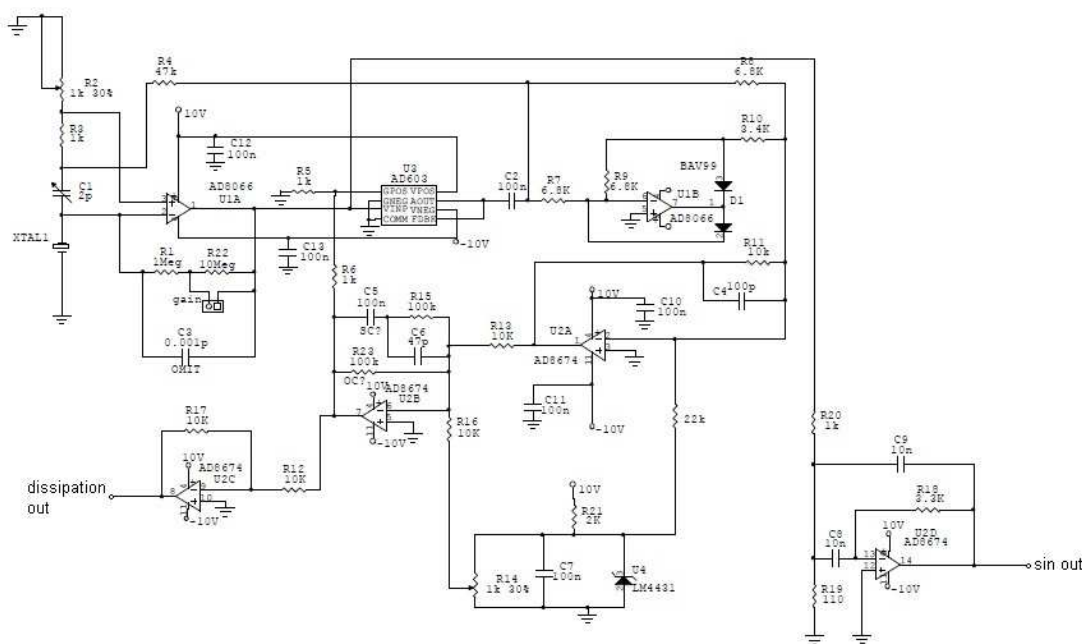


**Figure 5.15:** The QTF drive circuit as used in the work of Everson et al in [87].

In order to reduce the noise in the oscillation amplitude detection, a band pass filter, centered at the QTF resonant frequency (32kHz), was inserted before the rectifier part of the circuit. No band pass filter was previously present anywhere in the control loop of the circuit. The operational amplifier part of the circuit from which the QTF oscillation signal was taken, see Fig. 5.15, was adjusted to give the appropriate filter characteristics and placed before the rectifying part of the circuit; directly after the AD603 amplifier, see Fig. 5.17. When compared with the previous minimum achievable amplitude, a reduction of approximately 30% was observed with these modifications alone. In addition, to remove the parallel capacitance due to the lengthy cables between the QTF and the first current amplifier, we decided to put this amplifier onto the same PCB on which the QTF probe would be mounted underneath the SP on the instrument. The circuit diagrams of these two modified drive circuit parts are shown in Fig 5.17. Importantly, we also decided to connect the prong of the QTF to which the SPM tip would be attached to ground. Also, the signals were floated to avoid ground loops by differential amplifiers. For the connection to ground to prevent build up of charge we would need to use conductive tips electrically contacted to the relevant prong of the QTF. The SPM tips to be used with the instrument will be discussed in the next section.

Instead of housing the part of the circuit shown in Fig 5.17 b) in a cuircuit box connected to the outside of the vacuum chamber, as was the case with the drive circuit before the described modifications (see Fig 5.16 a)), we built a stand alone circuit control unit with easily accesible controls, and BNC ports for different inputs

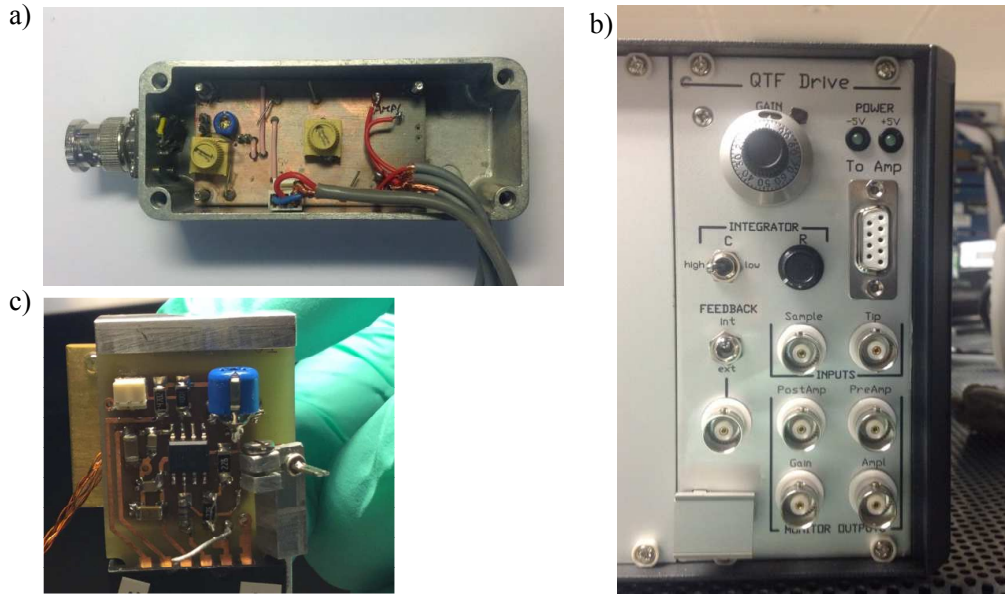


**Figure 5.16:** Image of circuit housing used for the circuit shown in Fig 5.15 prior to any modifications is shown in a). b) shows an image of the circuit control unit constructed to house the circuit shown in Fig 5.17 b). c) current amplifier on the PCB with the QTF sensor. The labels shown on the circuit control unit correspond to the labels shown in Fig 5.17 b).

and outputs as seen in Fig 5.16 b). A multipole vacuum connector replaced the BNC port to allow the part of the circuit housed in the stand alone circuit box to be connected to the current amplifier circuit in Fig 5.17 a) mounted on to the SP. To characterize the noise performance of this new circuit setup, we attempted to measure the thermal motion of a QTF connected to the drive circuit. We did this by measuring the frequency noise power of the pre-amp output shown in Fig 5.16 b) using a lock-in amplifier with the set point of the drive to the QTF set to its minimum value. The reference signal for the lock-in was provided by a VCO which allowed the user to manually change the reference frequency. The measured frequency response of the QTF with no drive is shown in Fig 5.18. The observation of the thermal motion of the QTF with the new drive circuit setup confirmed the ability of the new circuit setup to drive the QTFs at amplitudes limited by the thermal motion.

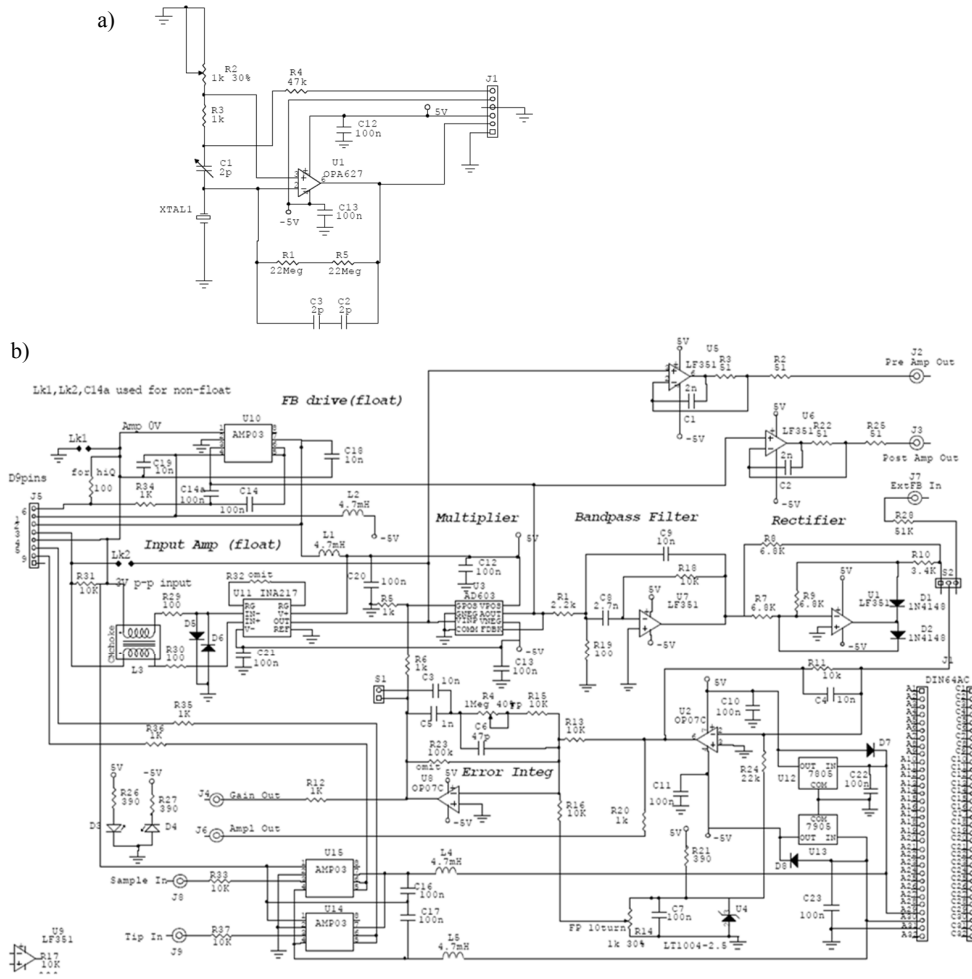


Figure 5.17: The QTF drive circuit after outlined modifications

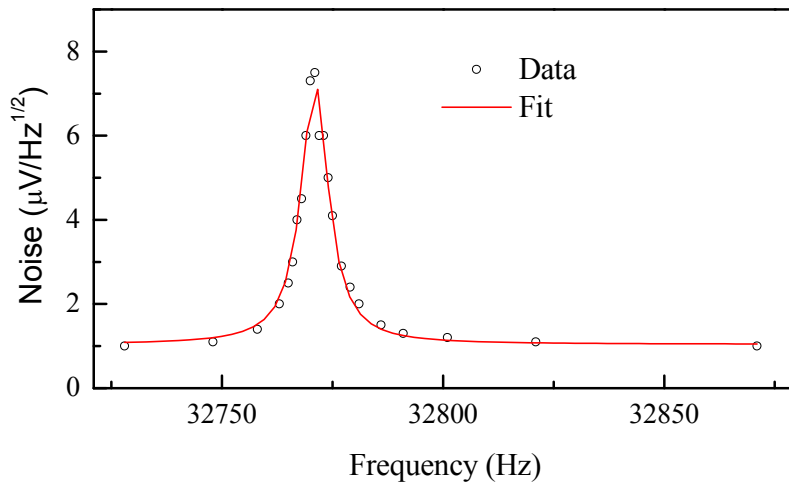
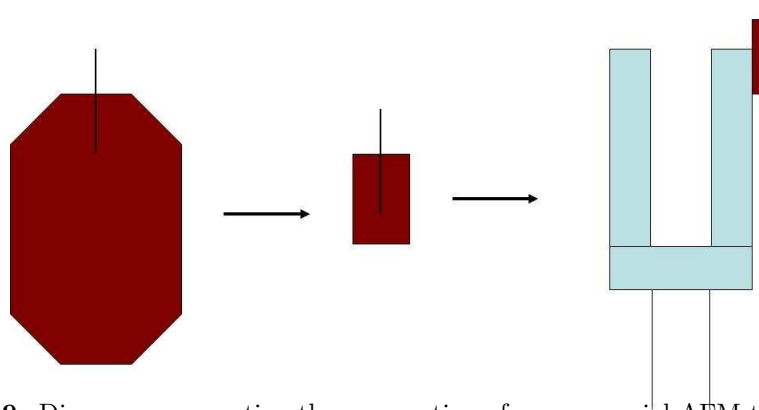


Figure 5.18: Frequency response of a QTF with no drive. The fit to data was made with a lorentzian lineshape centered at  $2.99 \pm 0.10$  Hz with a FWHM of  $7.42 \pm 0.41$  Hz, an offset of  $1.04 \pm 0.10 \mu\text{V}/\text{Hz}^{1/2}$ , and an amplitude of  $72.6 \pm 3.9 \mu\text{V}/\text{Hz}^{1/2}$

### 5.3.2 Scanning probe microscopy tips

As mentioned in the previous section, not having a provision for either the SPM tip or the sample surface to be grounded resulted in the build of charge on either the tip or the sample surface. This prevented the instrument from achieving stable feedback to keep a constant tip sample separation. In the modifications to the QTF drive circuit described already, we added the provision for the SPM tip to be connected to ground, and for the sample holder to be biased. Let us now describe the SPM tips that were initially used with the instrument and their limitations before moving on to discuss the newly developed SPM tips.

The tips initially used with the homebuilt instrument were commercial silicon AFM non contact mode tips. As depicted in the sketch shown in Fig 5.19, these tips comprise a cantilever and tip attached to a silicon base. In order to minimize the excess mass put onto the QTF, the silicon wafer had to be chipped carefully away around the cantilever using a scalpel. This was done to prevent significant changes to the QTF resonant frequency and quality factor. This left a small part of the base with the cantilever and tip attached that could subsequently be attached to one of the prongs of the QTF using two part epoxy glue. Despite the effort made to minimize the mass, the resonant frequency of the QTF still reduced by approximately 2kHz. This method of preparing tips was not ideal due to the low success rate in reducing the silicon wafer without damaging the tip, the reduction of the quality factor by the assymetric loading, and the fact that the tip was still on a cantilever which was free to oscillate but with a much higher frequency. It was not known how the cantilever and QTF oscillations would couple. In addition, silicon dust produced during the cutting which could contaminate the tip was a concern since it was often not possible to rinse the tip with a liquid without removing the cantilever from the remaining wafer completely. In addition, these commercial tips were not conductive and therefore could not be grounded. If this method was used with similar conductive commercial tips, the use of glue to attach the tip to the QTF prong would prevent electrical contact.



**Figure 5.19:** Diagram representing the preparation of a commercial AFM tip.

In light of these issues, we decided to pursue the development of carbon fibre tips that could be produced in house. Gomez *et al* in [96] present a procedure to produce carbon fibre tips which they demonstrate can be used for simultaneous AFM and STM operation. The tips can have a tip apex radius of about 55 nm. Platinum Iridium (PtIr) etched wire tips had been used previously with this instrument, however carbon fibre tips would be more durable due to a higher Young's modulus approximately 280GPa as measured by Gomez *et al* [96]. In addition, 7 micron

diameter carbon fibres can be used to etch tips compared to the 25 micron diameter of PtIr wire, reducing the mass and asymmetry introduced to the sensor. Carbon fibre tips are reported to survive a few crashes with sample surfaces and they are also conductive lending themselves for use in EFM applications. This also means that carbon fibre tips can be grounded. These tips are also relatively inexpensive and easy to produce.

In order to produce SPM tips in house, carbon fibre yarn with easily extractable single fibres was purchased from Advent RM, with single fibre diameter of 7 microns. An etching procedure, similar to that outlined by Gomez *et al*, was attempted to etch tips. The setup included a dc power supply with its negative terminal connected to a Gold ring of approximately 4-5mm diameter, made from 125 micron diameter wire. The positive terminal was connected to a wire to which a few millimeters of a single carbon fibre was connected using silver epoxy paint. This piece of wire was mounted onto a micromanipulator (Singer Mk1), which offers 4 to 1 reduction in movement, in order that the position of the carbon fibre could be finely controlled. A film of Potassium Hydroxide (KOH) solution of concentration 4M was suspended in the gold ring, and the end of the fibre was positioned inside the film. The power supply was then switched on to commence the etching which finished when a piece of fibre broke off into the liquid leaving behind the etched tip which was then rinsed with deionized water. The etching itself took up to 10 seconds. The etching setup is shown in Fig. 5.20

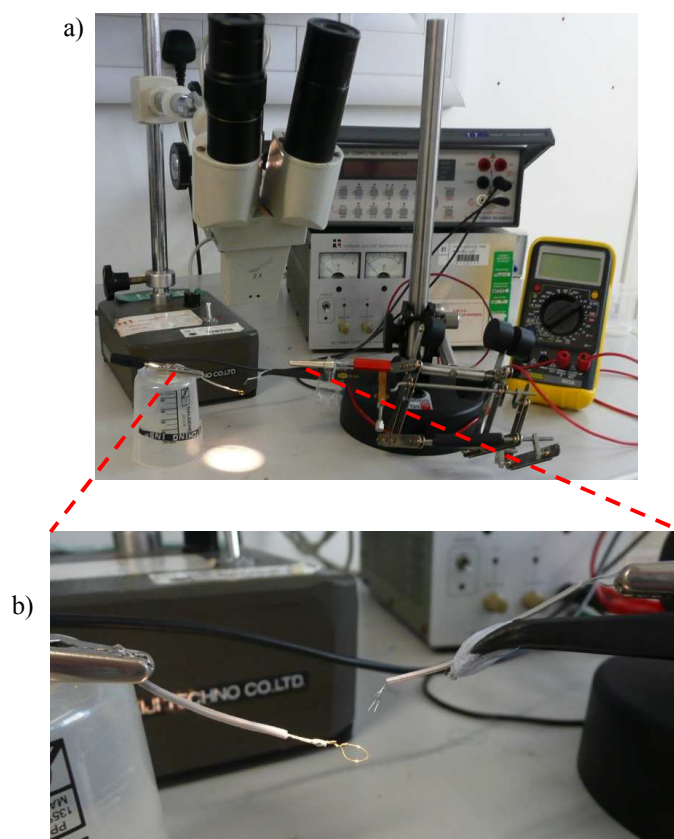


**Figure 5.20:** Images of the carbon fibre tip etching setup. a) shows an overview of the described etching setup, and b) shows an expanded view of the gold wire ring as indicated.



We initially experimented with different voltage settings that could be used for the carbon fibre tip etching. The voltage used in ref[96] was 4 V. The tip shapes produced from a number of different voltage settings were investigated using an optical microscope. Samples which showed promising shapes were then selected for Scanning Electron Microscopy (SEM) imaging which revealed the variation in the tip apex with different voltages. Initially, we attempted etching tips with voltage settings up to 10 V. Shapes due to the crystalline structure of the carbon fibre were observed for the tips etched with lower voltage settings. SEM images shown in Fig 5.21 display the tip shapes obtained with settings of 5, 6 and 7 V. These irregular shapes may be due to the slower etching, not diffusion limited, giving preferential etching of specific crystallographic surfaces. Tips produced using the higher voltages shown in Fig. 5.21 showed a more uniform shape, however the tip apex was of the order of 100 nanometers as can be seen in Fig. 5.21 c). An ideal tip apex size would be of the order of tens of nanometers. Further experimentation revealed a potential difference of 9 V applied between the KOH solution inside the Gold wire ring and the carbon fibre during etching gave better results as shown in Fig 5.22. Tips of this quality could be produced with a 75% success rate with this procedure. For voltage settings higher than 9V, the etching tended to be very fast with the production of large amount of gas bubbles which perturbed the fibre during etching causing unwanted shapes. The estimated apex size of the tip shown in Fig 5.22 is 50 nm. We were satisfied that tips of this quality would be adequate for use with the home built SPM instrument.

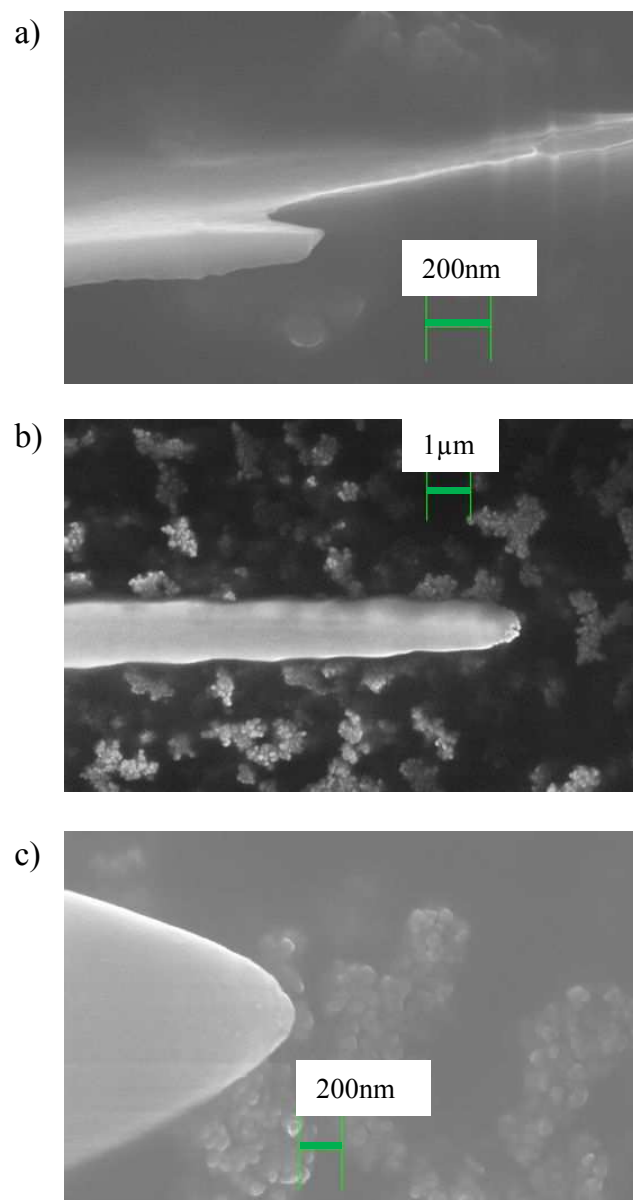


**Figure 5.21:** SEM images of carbon fibre tips are shown. a) shows a tip etched with a 5 V setting, b) with 6 V, and c) with 7 V applied between the KOH solution and the carbon fibre.

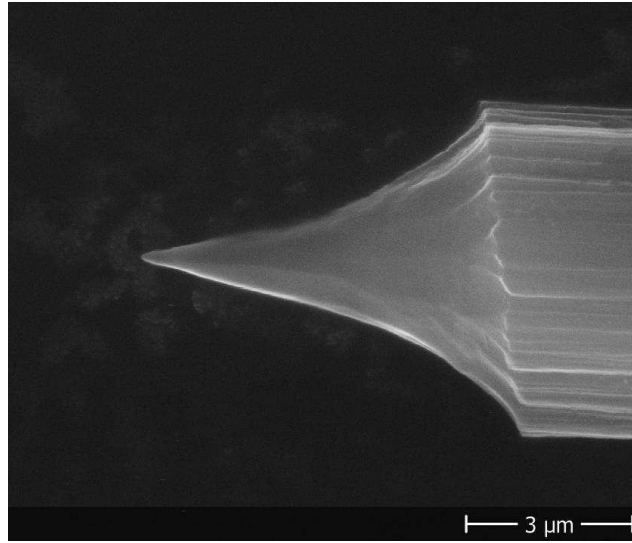


**Figure 5.22:** SEM image of carbon fibre tip produced at an etching voltage of 9 V with KOH of concentration 4 M.

### 5.3.3 Home built positioner

The design of the home built positioner shown in Fig 5.3 of the instrument setup was an evolution of the original home built positioner design which is shown in Fig 5.23. The positioner comprised a center plate labelled CP, and top and bottom plates labelled TP and BP respectively made from brass. The plate CP was attached to the aluminium piece labelled HBPbase using two thin brass plates acting as springs with a piezo squeezed between the centre plate CP and HBPbase as shown in Fig 5.23 b). The aluminium piece HBPbase was designed to attach firmly to the vertical column shown in Fig 5.3. The center plate CP had six sapphire spheres of 3 mm diameter embedded 1.5 mm into its top and bottom surfaces. Three of the spheres were embedded into the top surface as shown in Fig 5.23 b), and the remaining three were embedded into the bottom surface in the same configuration. The top and bottom plates TP and BP each had one triangular and one rectangular cut out on the side which faced the center plate CP. These cut outs can be seen on the BP in the shown image. The triangular cut outs were designed to allow the two sapphire spheres, which were arranged in line with each other along the length of the center plate on its top and bottom surfaces, to track along them as the plates TP and BP moved in relation to the center plate in order to keep the three plates in line. The rectangular cut out made contact with the sapphire sphere shown on the right hand side of the CP. Clearance holes in plate BP allowed the scanner piezo (SP) to be mounted at the bottom of the HBP.

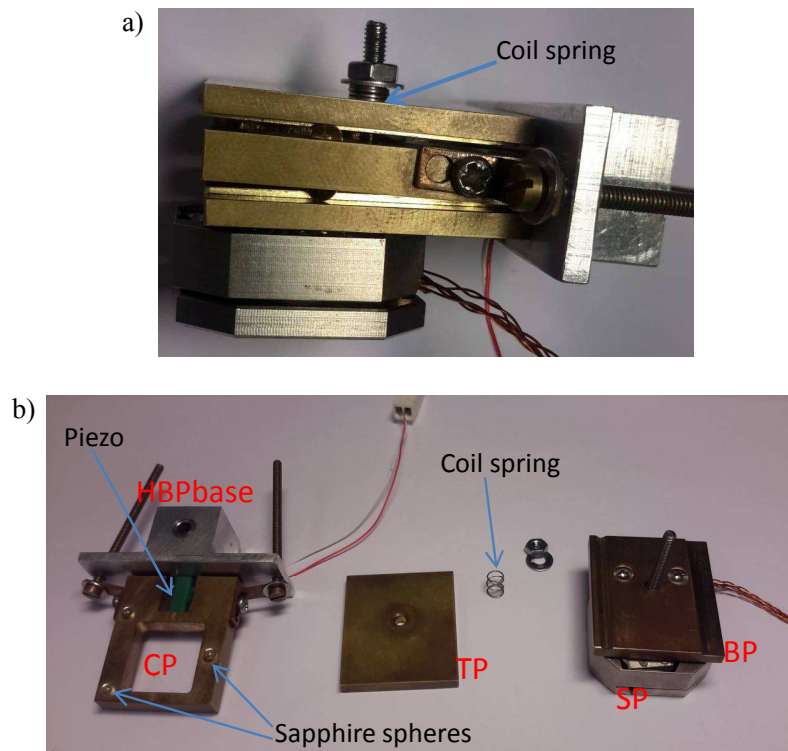


**Figure 5.23:** Pictures of HBP before modifications. a) shows the assembled HBP with the ANSxyz100 SP mounted underneath. b) shows the HBP disassembled with the indicated labels to differentiate the individual parts.

The three plates which comprised the HBP were mounted together with the aid of a coil spring, a washer and a hex nut as shown in Fig 5.23 a). Tightening the nut from the top allowed the plates to be held together due to the compressive force provided by the spring. In order to move the HBP, a sawtooth voltage was applied to the piezo. For the forward motion, the piezo would initially expand causing all three plates to move slightly forward. The piezo would then quickly return to its original size causing the center plate CP to quickly retract due to the force of the springs on either side. The plates TP and BP would remain in the forward extended position as the center plate slid backwards due to the sapphire spheres sliding along the cut outs. As long as a sawtooth voltage was continuously applied to the piezo, the plates TP and BP would continue to move relative to the center plate in this way. The backwards motion was achieved using the same slip stick mechanism by reversing the sawtooth voltage.

The original design of the HBP presented us with limitations. The amount of distance covered by the positioner per step varied with the compressive force applied to the plates through the spring. The nut that determined the amount of force applied needed repeated manual adjustments resulting in inconsistency in the distance moved per step. These adjustments were required as the force necessary to hold the plates together was close to the amount of force that resulted in enough friction to halt the movement of the positioner altogether. With the maximum force applied that still allowed movement, the bottom plate BP would often hang too low at the front which caused the bottom plate BP to become misaligned with the center plate during movement as shown in Fig 5.24. The problems made this design of the positioner impractical to use with the SPM instrument.

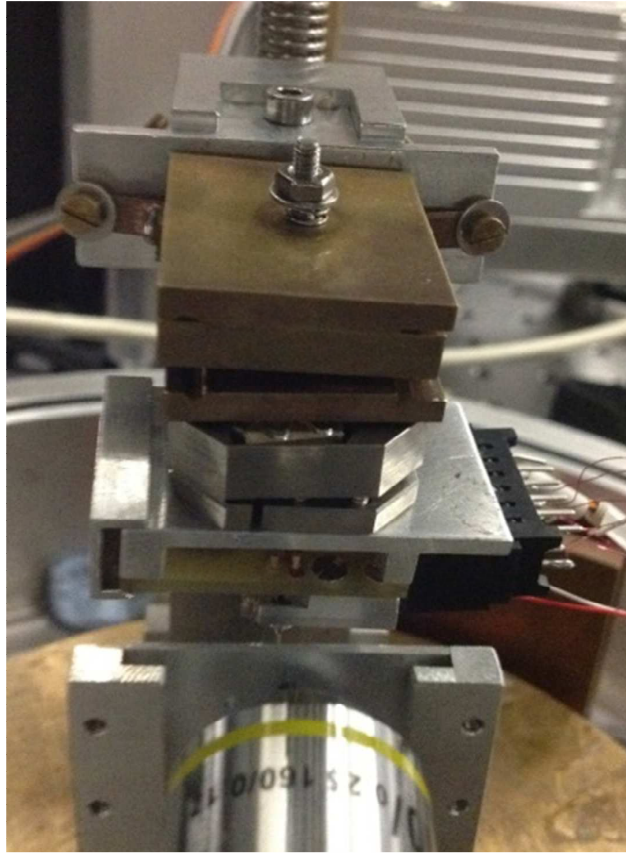


**Figure 5.24:** Picture demonstrating the misalignment of components of the HBP during operation.

We needed to make the construction lighter in order for it to function correctly and consistently. We constructed a new center plate (nCP), as shown in Fig 5.25 a) and b), made from aluminium in order to reduce its mass to allow faster motion. In the new design, the sapphire spheres were placed on the new top plate (nTP) instead of the nCP. The nCP had triangular and rectangular cut outs as shown in Fig 5.25 a) to allow the nTP to slide using the sapphire spheres as contact points. Stopper arms (SA) were built into the nCP to prevent the nTP from travelling past its intended range. Two stopper arms SA extended forward from the nCP allowing the cut outs for the sapphire spheres to be extended further forward than in the previous design. These SAs terminated with an upturned lip to prevent the nTP from sliding too far forward and slipping off the nCP. With the sapphire spheres now placed in the moving plate, the gravitational load distribution was not changing with the motion unlike in the previous design.

The newly designed aluminium base arms labelled BA in Fig 5.25 b) mounted onto the aluminium piece HBPbase connected to the new center plate through four 150 micron thick steel springs as shown. The need for the bottom plate BP was removed completely with the inclusion of a bridge piece labelled BRDG in Fig 5.26 c). The bridge piece connected the nTP to the SP mounted an adequate distance below the nCP. Adequate contact between the cut outs of the nCP and the sapphire spheres was provided by the weight of the construction that comprised the new top plate, the bridge piece, and the SP with the SPM sensor construction (to be discussed in detail later) mounted underneath it.

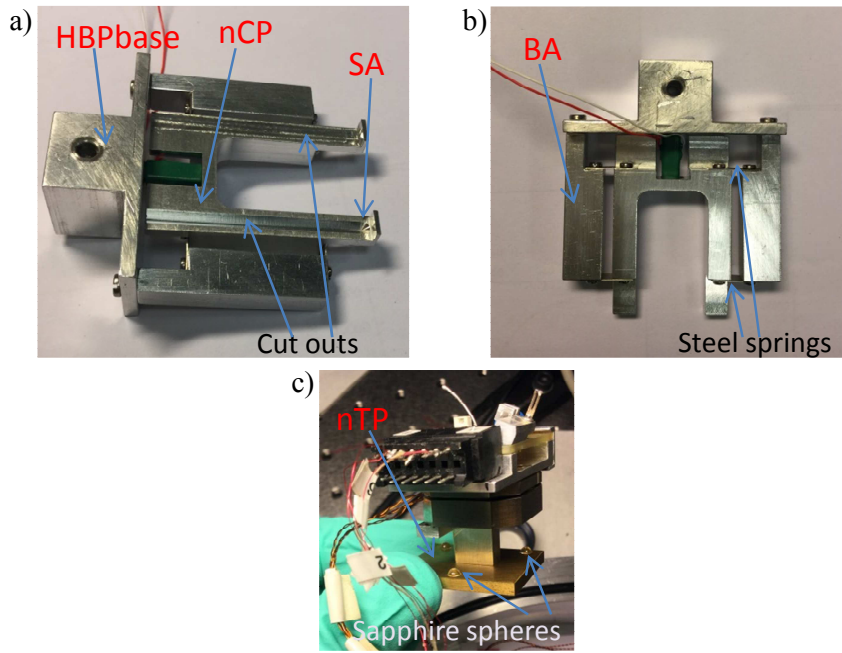


**Figure 5.25:** Picture from the top of the new center piece construction is shown in a), and from the bottom in b). c) shows the placement of the sapphire spheres on the new top plate.

The newly designed HBP overcame the problems encountered with the original design, and resulted in consistent motion both forward and backwards. Because the part of the construction that moves and thus attaches to the SP and the SPM probe simply rests on the center plate, it can easily be lifted and removed as demonstrated in Fig 5.26 b). This provides much improved accessibility compared to the previous design in which the construction needed to be removed from the vertical column VC in Fig 5.3 to access the SPM probe. Part of the ongoing development process will be a calibration of the distance moved forwards and backwards per step given a specific voltage input for the piezo which is controlled using the GXSM control software. However, preliminary tests showed consistent and smooth motion of the HBP in both directions of movement.

#### 5.3.4 Quartz tuning fork holder

The SPM sensor which comprised a QTF with a glued on silicon AFM tip was originally mounted into a cubic aluminium mount shown in Fig 5.27. This mount was then glued onto a blank PCB using two part epoxy glue. This PCB was subsequently mounted onto the underside of the SP. The cubic aluminium mount had two parts as indicated in Fig 5.27 joined using four screws with an opening in between the edges of the two parts on the top surface. The base of the QTF sat in this opening and was held in the mount as the tightening of the screws joined the two pieces of the holder together. Glueing the QTF holder onto the PCB meant that to replace the QTF probe the holder had to first be detached from the PCB by breaking the bond formed by the glue. This was because the design of the holder meant that both pieces of the holder were glued onto the PCB as shown in Fig 5.27.



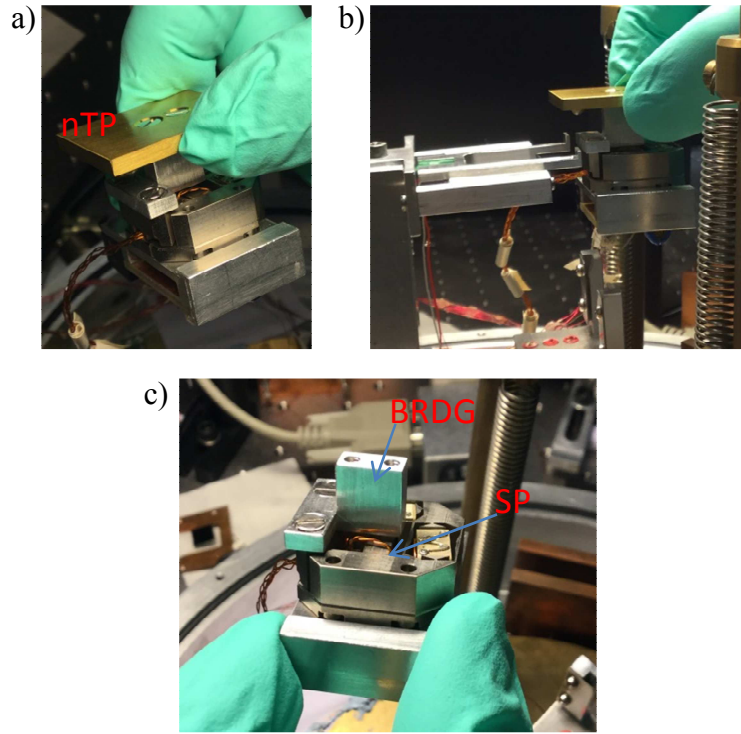


**Figure 5.26:** Picture of the removable top plate construction of the new HBP comprising the new top plate, bridge piece, SP and the PCB holder construction (described in 5.3.5) is shown in a). b) picture illustrating the removal of the new top plate construction from the new center plate. c) shows a close up of the bridge piece.

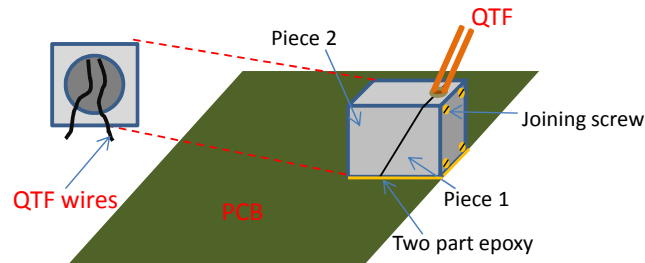


**Figure 5.27:** A sketch of the previous design of the QTF holder. The alternative view indicated by the red dashed lines shows the face of the holder opposite to the one with the joining screws.

As part of the modifications to the QTF drive circuit, a PCB with a current amplifier circuit to be mounted underneath the SP was designed (see Fig. 5.17). We designed a new holder for the QTF to be mounted onto this PCB using a pair of screws as shown in Fig 5.28 a) and b). It allows removal of the QTF probe without the need to dismount the holder from the PCB, and also allows short connections to the current amplifier (which is on the PCB in the new design) to minimize stray capacitances and electrical pickup. Images showing the details of the design of the new QTF holder can be seen in Fig 5.29.

Loosening the holding screw HS indicated in Fig 5.29 a) allows easy removal of the QTF, and tightening this screw securely hold the QTF in place. The holder is designed so that the angle between the front QTF prong and the sample surface is

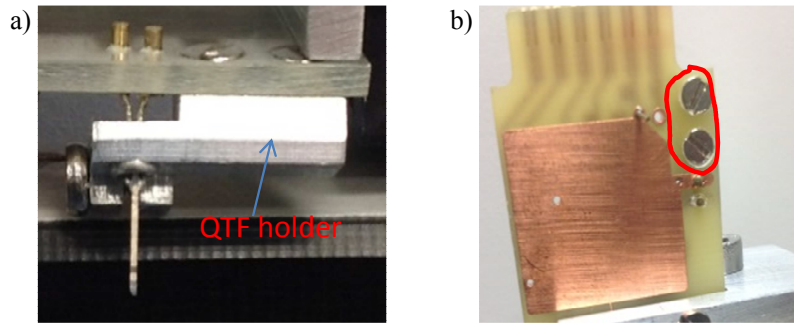


**Figure 5.28:** a) Picture of the QTF holder seen from a sample surface as arranged in Fig. 5.3. b) picture of the screws used to mount the QTF holder on the side of the sensor PCB opposite to the side on which the QTF holder is mounted.

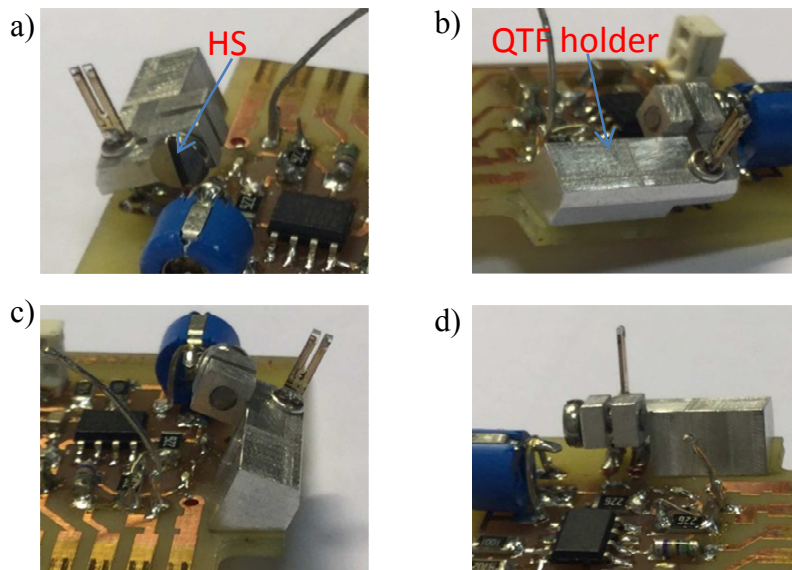


**Figure 5.29:** Pictures of the QTF holder mounted onto the sensor PCB from various directions.

about  $30^\circ$  when mounted onto the instrument as shown in Fig 5.3. Fig 5.28 a) shows the orientation of the construction as seen from the sample surface position. This design also allows manipulation of the connection wires of the QTF which extend from the bottom of its base.

### 5.3.5 Printed circuit board holder

Instead of attaching the sensor PCB (with the mounted QTF probe) directly to the SP, we decided to construct a PCB holder which would allow easy removal of the PCB from the setup. The PCB holder is shown in Fig 5.30. Fig 5.30 a) shows the two pieces that comprise the holder, namely a base with two protruding arms and clearance holes to allow it to be mounted to the SP using screws, and an aluminium clamp to secure the PCB against the protruding arms.

A 10 pin connector is glued using two part epoxy glue onto one side of the holder as shown in Fig 5.30 b). The PCB is designed so that it can easily be pushed into the connector. The 10 pin connector connects to a vacuum Fisher connector on the base of the vacuum chamber through enamel copper wires. The PCB can be held



within this construction when inserted into the 10 pin connector, however the clamp is needed to hold it securely. The full PCB holder construction when mounted onto the instrument is shown in Fig 5.30 c) and d).

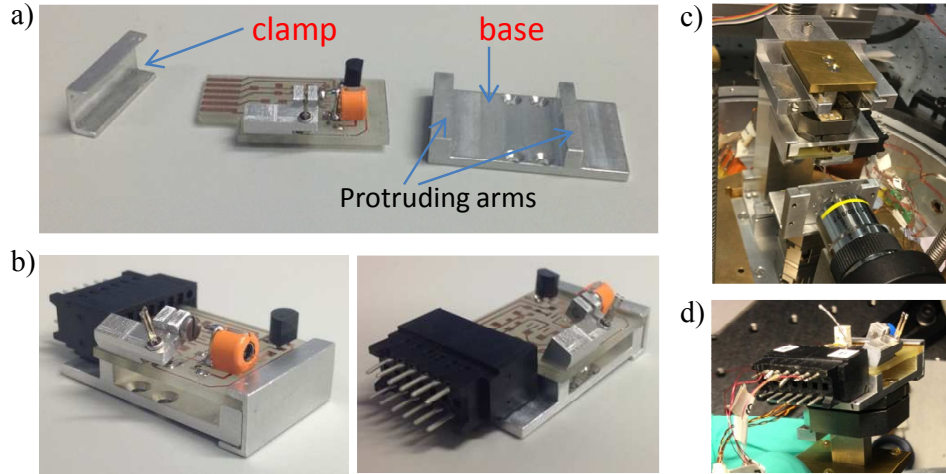


**Figure 5.30:** The image in a) shows the components of the PCB holder construction. b) shows two views of the PCB holder with the PCB mounted thereon. Figures c) and d) shows different views of the PCB holder construction mounted onto the SP. Note that a mock PCB is shown in the pictures

### 5.3.6 Sample holder and preparation setup

The sample holder originally used with the home built instrument is shown in Fig 5.31. It comprised two brass arms shown in Fig 5.31 a) and b). The two arms were free standing and not connected to each other. A 1 mm thick polystyrene sheet was screwed onto the SPS before the sample holder was mounted on top. The polystyrene sheet also had clearance holes that extended beyond the sides of the SPS so that the brass arms of the sample holder could be mounted onto it using screws. The purpose of using the plastic sheet was to electrically isolate the sample mount from the SPS. A sample could be mounted onto the piece shown in Fig 5.31 c) before being mounted onto the brass arms shown in a) and b).

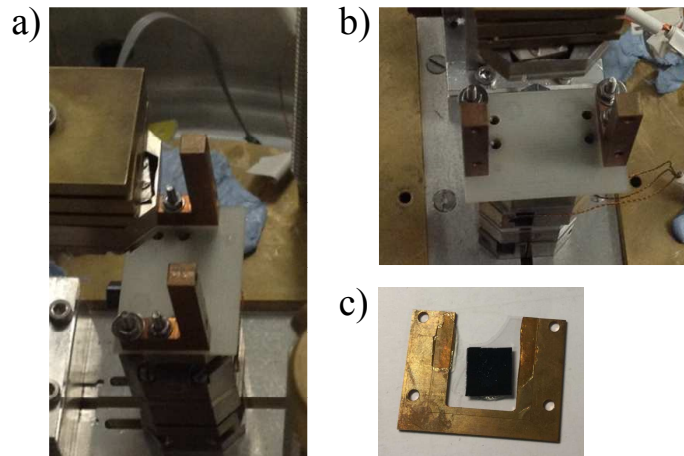


**Figure 5.31:** Pictures of the previous sample mounting construction.

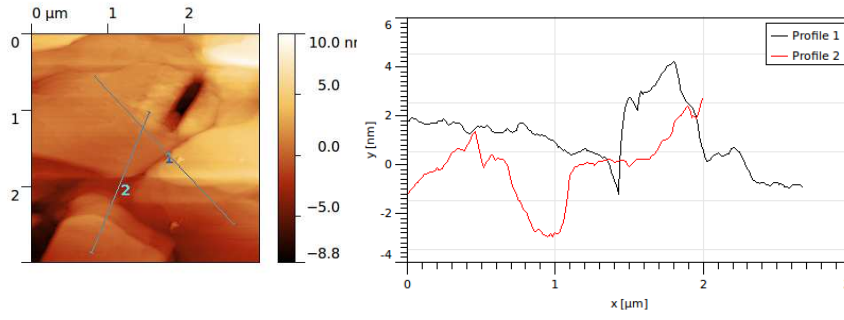


**Figure 5.32:** AFM image and two dimensional line profiles of the indicated regions of the graphene coated quartz coverslips are shown.

Before creating a new design for the sample holder, we decided to investigate the possibilities for a transparent yet conductive sample substrate that could be used for EFM studies. In addition to these requirements, the substrate ideally needed to have a roughness of less than 3 nm for SPM application. This was crucial as the home built instrument was being developed to investigate QDR samples which may have diameters as small as 4 nm. We concluded that quartz coverslips coated with a monolayer of graphene would be suitable. 25x25 mm quartz coverslips of thickness 150 microns (specified as thickness no.1 130-170 microns) were purchased from UQG Optics. Their surface roughness (as measured using a commercial SPM instrument) was 2 nm. These coverslips were shipped to Graphene Supermarket who deposited monolayers of graphene on one of the surfaces of these coverslips. The roughness of the graphene layers was also characterised using a commercial SPM instrument and was less than 2 nm as shown in Fig 5.32.

The size of the substrate required for SPM studies of QDR samples was expected to be no larger than 6 mm. We therefore decided that in order to conserve the graphene coated coverslips, we would cut the 25x25 mm coverslips into 6.25x6.25 mm pieces as required. To cut the coverslips to the required size without disturbing the graphene layer, we constructed the setup shown in Fig 5.33. This setup comprised an aluminium coverslip cutting base CCB, a spacer made from steel of thickness 150 microns, a bendable steel clamp piece, and two blocks of PTFE of different dimensions named the presser piece PP and the breaker piece BP. The dimensions of the base and the spacer were selected so that the distance between the edge of the spacer and the edge of the base was 6.25 mm when arranged as shown in Fig 5.33 b). A piece of coverslip would rest on the base flush against the spacer with the PTFE block PP resting on top clamped down with the steel clamp screwed into the base as shown in Fig 5.33 b). A diamond scribe would then be used to make a cut on the surface of the coverslip using the edge of the clamp as a guide. The larger PTFE block BP was then to be used to gently press down on the coverslip protruding from the setup in order to make a break in line with the cut drawn by the diamond scribe. In this way, the graphene coated coverslips could be cut into squares of size 6.25x6.25 mm. PTFE was chosen as the material that would come in contact with the graphene layer as it has a low friction coefficient and would not disturb the graphene layer.

The sample holder designed for coverslip pieces of thickness 150 microns to be mounted is shown in Fig 5.34. It features a sample plate which has a cut out that allows square cover slip pieces to sit in it as shown. The square hole on the rear side of the plate is to allow optical access from the side opposite the SPM sensor. The

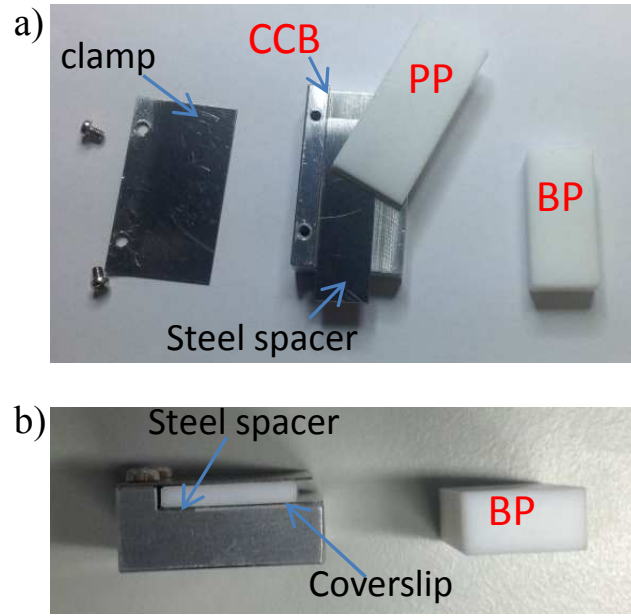


**Figure 5.33:** Image showing the components of the coverlip cutter is shown in a). b) shows an image of the cutter setup with a coverslip mounted.

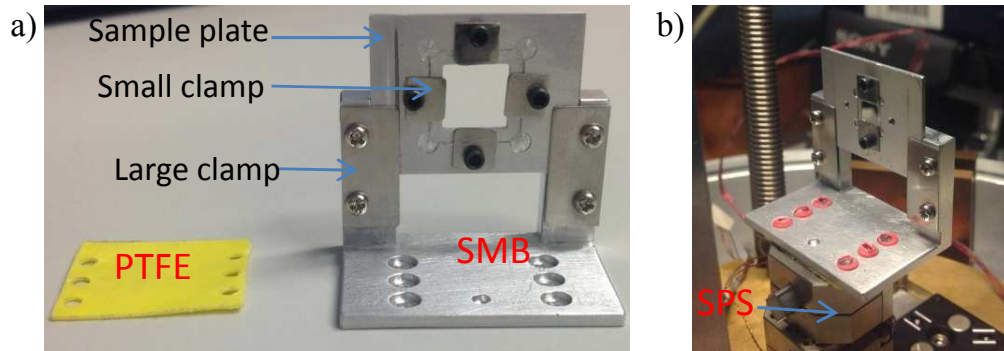


**Figure 5.34:** Image of the components of the sample holder as indicated shown in a). b) shows the sample holder mounted onto the sample piezo stack SPS.

small flexible steel clamps shown press down on the coverslip to hold it in place, and also electrically contact the graphene to the sample plate. The sample mount base SMB has two arms that extend vertically upwards and are shown with larger steel clamps attached. The shape of these arms allows the sample plate to slide in and out of the SMB easily while the clamps hold the plate firmly when it is in position. Six countersunk screws encased in heatshrink firmly mount the SMB to the SPS as shown in Fig 5.34 b). There is a piece of PTFE between the base and the SPS. This PTFE piece and the heatshrink electrically isolates the sample holder from the SPS. The new sample holder design holds the sample firmly in place while providing easy access. It also allows a potential difference to be applied to the surface simply by contacting any part of the holder with a wire supplying the bias voltage.

### 5.3.7 Tip mounting setup

A setup was devised to aid the mounting of an etched carbon fibre tip onto a QTF. The setup is shown in Fig 5.35. As previously described, the carbon fibre tip etching procedure involved the use of a micromanipulator which allowed a user to finely control the position of the carbon fibre. For convenience, it was thought best not to remove the etched carbon fibre from the micromanipulator setup before mounting it onto a QTF for use with the instrument. A tip mounting stage was constructed which would allow an etched carbon fibre tip to be mounted onto a QTF already mounted on to the sensor PCB using the QTF holder. The mounting stage comprised a rod shaped brass column, and an aluminium holder for the sensor PCB. The holder allowed the QTF prongs to remain in place when the holder was rotated to align it with the orientation of the fibre tip.

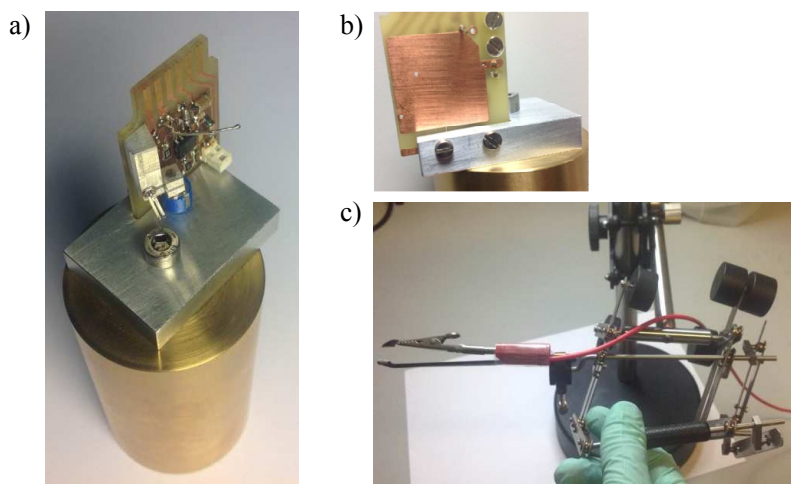


**Figure 5.35:** Pictures of tip mounting setup. a) shows an overview of the construction with b) showing a rear view. Image c) illustrates the use of the singer mk1 micromanipulator.

During the mounting procedure, the carbon fibre tip was positioned onto the correct prong of the QTF using the micromanipulator, and the QTF was rotated to adjust the relative orientation. The stereo microscope shown in Fig 5.20 a) was used to help guide the tip towards the QTF. The tip was then connected to the QTF prong using silver paint. Care had to be taken not to shortcut the QTF drive and readout contacts. Subsequently, the length of carbon fibre attaching the QTF prong to the wire piece held by the micromanipulator was cut using scissors. An example of a carbon fibre tip mounted onto a QTF using silver paint is shown in Fig. 5.36.

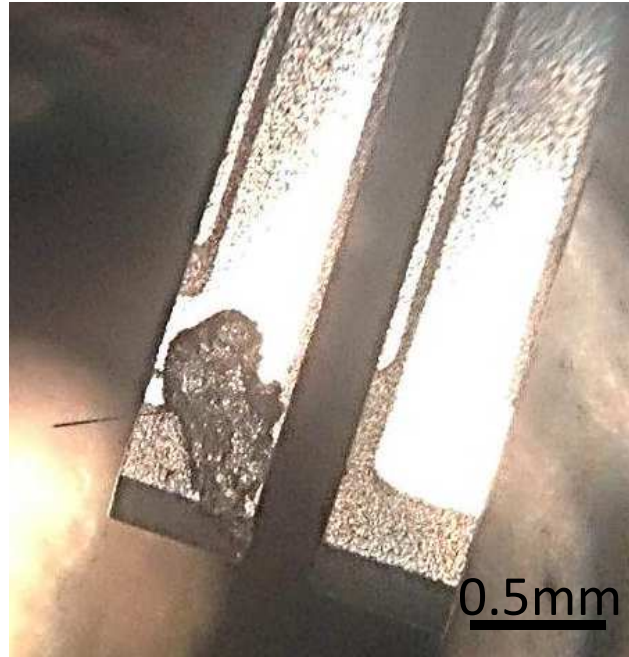


**Figure 5.36:** An image of an etched carbon fibre tip mounted on to a QTF prong using silver paint.

### 5.3.8 Future work

To progress with the development and use of the described instrument, the next steps would be to characterize several aspects of the performance of the instrument. First, a frequency shift versus distance curve should be measured using an etched carbon fibre tip. The minimum amplitude of the QTF while driven using the new drive circuit setup should be quantified. This may be done by measuring frequency shift versus distance curves for different levels of drive provided to the QTF. Briefly, if an approach towards a sample surface is made from the same starting point with different QTF amplitudes, a particular frequency shift value will be observed at different distances towards the sample from the starting point depending on the amplitude.

In addition to characterizing the AFM operation of the instrument, progress would have to be made with the optical part of the instrument. For the instrument to be used for the types of measurements it's intended for, it must be developed to be made capable of photoluminescence (PL) measurements. This is set up, both spectrally resolved and time-resolved, using TCSPC and a PMT (not used in the present project).

A detection scheme for electrostatic force measurements must also be developed in order to track the position of charges within a single QDR as it blinks while being photo-excited.

This instrument benefits greatly from cost effective parts that have been built in house and can easily be modified further to improve its performance. It is hoped that the modifications made allow the instrument to achieve an SPM resolution of the order of nanometers, as well as realise its capability for simultaneous scanning probe (specifically EFM) and optical measurements on QDR samples.



# Summary

A three beam four wave mixing technique (FWM) has been utilized in order to study exciton dynamics in a variety of colloiddally grown semiconductor nanostructures. Absorption and Photoluminescence (PL) studies of the investigated samples are also reported. The investigated structures included several monolayer thick CdSe nanoplatelets (NPLs) which have only been reported in the literature for the past eight years approximately. Also investigated were quantum dot in rod (QDR) samples which comprised a CdSe core within a rod shaped shell of CdS, with the CdSe core being offset to one side along the length of the rod like shell.

We introduced a model for fitting the absorption spectra of NPLs that could describe the features of the spectra well. The fitting of the absorption spectra with this model allowed us to extract parameters relating to the excitons within these quantum well like structures, such as the binding energies of the heavy hole and light hole excitons. Absorption spectra for a range of thicknesses as well as lateral size were reported. We found that excitons within these structures are predominantly confined by the thickness of the NPLs, with confinement within the lateral size becoming an important factor as one of the lateral dimensions approaches the exciton Bohr radius. For varying thickness and lateral size, we observed the exciton absorption energies increase with increasing confinement. In general, we extracted binding energies of about 250 meV for heavy, and about 350 meV for the light hole excitons.

We subsequently presented in detail the results of three beam FWM experiments on a sample comprising NPLs of lateral dimensions 34 nm by 8 nm with a thickness of 1.67 nm. We observed a lifetime limited ground state exciton dephasing at low temperature of about 1 ps, which is 4 orders of magnitude shorter than the radiative lifetime of CdSe spherical nanocrystal (about 10 ns). This observation was evidence of an effect known as "giant oscillator strength transitions" (GOST) wherein the radiative lifetime of excitons decreases with increasing extension of the exciton centre of mass [45]. We also observed oscillations in FWM data, which we attributed to acoustic phonons confined within the thickness of the NPLs.

To further investigate GOST within CdSe NPLs, we studied samples of different lateral sizes. We observed short, lifetime limited dephasing times at low temperature for all our samples, supporting the results we reported in [45]. In addition, we observed a decrease of the low temperature dephasing time with increasing NPL area affirming the observation of the GOST effect. The size dependence also supported the attribution of the observed oscillations in the TI-FWM as being due to acoustic phonons confined within the thickness, since data relating to the different lateral sizes (but same thickness) could be fit using the same oscillation energy.

The three beam FWM on CdSe/CdS QDR samples was performed to measure the exciton dynamics. A Gaussian distribution of polarization decay rates in the

ensemble was used to describe time integrated FWM data relating to dephasing dynamics. We observed that the data could be fit using a (non-exponential) decay given by the Gaussian distribution for temperatures below 10 K. The data reverted to being well described by an exponential decay at higher temperatures showing that the temperature activated dephasing has a small inhomogeneous distribution. Homogeneous linewidths of about  $20 \mu\text{eV}$  for these samples were observed at low temperature. Using the activation energies obtained from the temperature dependence of the homogeneous linewidths, we found approximate agreement with known fine structure splittings in the Literature.

The measured density dynamics of the QDR samples showed for short pulse delays (less than about 5 ps) a fast initial decay of the signal followed by a signal rise. This unexpected result was attribute to an interplay between the presence of acoustic phonons and fast population dynamics related to the fine structure of the QDRs. In addition, the density dynamics at longer delays were attributed to an ensemble including both trions and excitons, which both have their distinct dynamics. Further analysis of the density dynamics data revealed a low temperature homogeneous linewidth due to bright to dark relaxation (within the known fine structure of the QDRs) . By comparing these linewidths to the dephasing dynamics, we concluded that the measured exciton dephasing was due to relaxation of excitons from a probed bright state ( $\pm 1^L$ ) to a lower lying dark state ( $\pm 2^L$ ). Furthermore, a comparison of oscillations observed in both the dephasing and density dynamics signals revealed correlation between the oscillation energies, leading us to conclude that the same acoustic phonon modes were observed therein.

We described an instrument intended for simultaneous scanning probe microscopy (SPM), specifically electrostatic force microscopy, and optical measurements. This instrument was intended to investigate the correlation between charging and the optical behaviour of colloidal quantum dots. We outlined the working principles of the homebuilt instrument, and described in detail modifications made to it (from its initial state) in order to allow it to be used for its intended purpose.

In conclusion, the linear optical properties and exciton dynamics of different semiconductor nanostructures were studied. A model to describe the absorption spectra of CdSe NPLs was developed, which allowed the extraction of parameters relating to excitons confined within the thickness of the NPLs. Giant oscillator strength transitions were observed in NPLs with a lifetime limited dephasing of the ground state excitons at low temperature of about 1 ps, using transient resonant FWM in heterodyne detection. A decrease in the low temperature dephasing time with increasing NPL area affirmed the observation of the GOST effect. Secondly, in CdSe/CdS QDR samples, dephasing dynamics at low temperature were described by a Gaussian distribution of decay rates. Density dynamics showed a fast initial decay followed by a signal rise attributed to an interplay between acoustic phonons and fast population dynamics related to the QDR fine structure. Density dynamics at longer delays were attributed to an ensemble including both excitons and trions. The low temperature dephasing was attributed to relaxation of excitons from a bright state to a lower lying dark state. Finally, a homebuilt SPM instrument was modified to allow simultaneous optical and scanning probe imaging for the study of correlation between charge state and optical properties of nanostructures.

# Bibliography

- [1] Jagdeep Shah. *Ultrafast Spectroscopy of Semiconductors and Semiconductor Nanostructures*. Springer, 1996.
- [2] S. Ithurria and B. Dubertret. Quasi 2d colloidal cdse platelets with thicknesses controlled at the atomic level. *J. Am. Chem. Soc.*, 130:16504–16505, 2008.
- [3] L. Carbone, C. Nobile, M. De Giorgi, F. Della Sala, G. Morello, P. Pompa, M. Hytch, E. Snoeck, A. Fiore, I. R. Franchini, M. Nadasan, A. F. Silvestre, L. Chiodo, S. Kudera, R. Cingolani, R. Krahne, and L. Manna. Synthesis and micrometer-scale assembly of colloidal cdse/cds nanorods prepared by a seeded growth approach. *Nano Lett.*, 7(10):2942–2950, 2007.
- [4] F. Masia, N. Accanto, W. Langbein, and P. Borri. Spin flip limited exciton dephasing in cdse/zns colloidal quantum dots. *Phys. Rev. Lett.*, 108:087401, 2012.
- [5] N. Accanto. Exciton coherence and relaxation in colloidal cdse quantumdots studied by photon echo spectroscopy. Master’s thesis, Università degli Studi di Firenze, 2011.
- [6] Wikipedia webpage: Doping (semiconductor), September 2015.
- [7] Hyperphysics webpage, 2015.
- [8] Cubic crystal system. Online web page.
- [9] via Wikimedia Commons By Solid State (Own work) [Public domain]. Wurtzite polyhedra.
- [10] via Wikimedia Commons By Benjah-bmm27 (Own work) [Public domain]. Zinc-selenide-unit-cell-3d-balls.
- [11] Claus Klingshirn. *Semiconductor Optics*. Springer, 2004.
- [12] D. Vogel, P. Kruger, and J. Pollmann. Self-interaction and relaxation-corrected pseudopotentials for ii-vi semiconductors. *Phys. Rev. B*, 54(8):5495, 1996.
- [13] M. Schulz O. Madelung, U. Rössler, editor. *Landolt-Börnstein - Group III Condensed Matter*, volume 41B. SpringerMaterials, 1999.
- [14] A. Szemjonov, T. Pauporte, I Ciofini, and F. Labat. Investigation of the bulk and surface properties of cdse: insights from theory. *Phys. Chem. Chem. Phys.*, 16:23251–23259, 2014.
- [15] Mark Fox. *Optical Properties of Solids*. Oxford University Press, 2010.



- 
- [16] A. Achtstein, A. Schliwa, A. Prudnikau, M. Hardzei, M. Artemyev, C. Thomsen, and U. Woggon. Electronic structure and exciton phonon interaction in two-dimensional colloidal cdse nanosheets. *Nano Lett.*, 12:3151, 2012.
- [17] Shun Lien Chuang. *Physics of Photoni Devices*. Wiley, 2012.
- [18] S. Ithurria, G. Bousquet, and B. Dubertret. Continuous transition from 3d to 1d confinement observed during the formation of cdse nanoplatelets. *J. Am. Chem. Soc.*, 133:3070–3077, 2011.
- [19] M. Pelton, S. Ithurria, R. D. Schaller, D. Dolzhenkov, and D. V. Talapin. Carrier cooling in colloidal quantum wells. *Nano. Lett.*, 12:6158–6163, 2012.
- [20] M. D. Tessier, B. Mahler, B. Nadal, H. Heuclin, S. Pedetti, and B. Dubertret. Spectroscopy of colloidal semiconductor core/shell nanoplatelets with high quantum yield. *Nano. Lett.*, 13:3321–3328, 2013.
- [21] B. Mahler, B. Nadal, C. Bouet, G. Patriarche, and B. Dubertret. Core/shell colloidal semiconductor nanoplatelets. *J. Am. Chem. Soc.*, 134:18591–18598, 2012.
- [22] B. Abecassis, M. D. Tessier, P. Davidson, and B. Dubertret. Self-assembly of cdse nanoplatelets into giant micrometer-scale needles emitting polarized light. *Nano Lett.*, 14:710–715, 2014.
- [23] L. Biadala, F. Liu, M. D. Tessier, D. R. Yakovlev, B. Dubertret, and M. Bayer. Recombination dynamics of band edge excitons in quasi-two-dimensional cdse nanoplatelets. *Nano Lett.*, 14:1134–1139, 2014.
- [24] Sung Jun Lim, Wonjung Kim, and Seung Koo Shin. Surface-dependent, ligand-mediated photochemical etching of cdse nanoplatelets. *J. AM. CHEM. SOC.*, 134:7576–7579, 2012.
- [25] A. Lyashchova, A. Dmytruk, I. Dmitruk, G. Klimusheva, T. Mirnaya, and V. Asaula. Optical absorption induced bleaching and photoluminescence of cdse nanoplatelets grown in cadmium octanoate matrix. *Nanoscale Research Letters*, 9:88, 2014.
- [26] Jianying Ouyang, Md. Badruz Zaman, Fu Jian Yan, Dennis Johnston, Grace Li, Xiaohua Wu, Don Leek, Christopher I. Ratcliffe, John A. Ripmeester, and Kui Yu. Multiple families of magic sized cdse nanocrystals with strong bandgap photoluminescence via noninjection one-pot syntheses. *J. Phys. Chem. C*, 112(36):13805–13811, 2008.
- [27] Zheng Li and Xiaogang Peng. Size/shape-controlled synthesis of colloidal cdse quantum disks: Ligand and temperature effects. *J. AM. CHEM. SOC.*, 133:6578–6586, 2011.
- [28] S. A. Cherevkov, A. V. Fedorov, M. V. Artemyev, A. V. Prudnikau, and A. V. Baranov. Anisotropy of electron-phonon interaction in nanoscale cdse platelets as seen via off-resonant and resonant raman spectroscopy. *Phys. Rev. B*, 88(4):041303, 2013.
-

- [29] L. T. Kunneman, M. D. Tessier, H. Heuclin, B. Dubertret, Y. V. Aulin, F. C. Grozema, J. M. Schins, and L. D. A. Siebbeles. Bimolecular auger recombination of electron/hole pairs in two-dimensional cdse and cdse/cdzns core/shell nanoplatelets. *J. Phys. Chem. Lett.*, 4:3574–3578, 2013.
- [30] S. Ithuria, M.D. Tessier, B. Mahler, R.P.S.M. Lobo, B. Dubertret, and A.L. Efros. Colloidal nanoplatelets with two-dimensional electronic structure. *Nat. Mater.*, 10:936–941, 2011.
- [31] J. Feldmann, G. Peter, E. O. Gobel, P. Dawson, K. Moore, C. Foxon, and R. J. Elliott. Linewidth dependence of radiative exciton lifetimes in quantum wells. *Phys. Rev. Lett.*, 59:2337, 1987.
- [32] A. I. Ekimov, F. Hache, M. C. Schanne-Klein, D. Ricard, C. Flytzanis, I. A. Kudryavtsev, T. V Yazeva, A. V Rodina, and Al.L Efros. Absorption and intensity-dependent photoluminescence measurements on cdse quantum dots: assignment of the first electronic transitions. *Journal of Optical Society of America B*, 10:100–107, 1993.
- [33] A.L. Efros. Luminescence polarization of cdse microcrystals. *Phys. Rev. B*, 46(12):7448, 1992.
- [34] D. J. Norris, Al. L. Efros, M. Rosen, and M. G. Bawendi. Size dependence of exciton fine structure in cdse quantum dots. *Phys. Rev. B*, 53(24):16347, 1995.
- [35] M. Kuno M. Nirmal D. J. Norris Al. L. Efros, M. Rosen and M. Bawendi. Band-edge exciton in quantum dots of semiconductors with a degenerate valence band: Dark and bright exciton states. *Phys. Rev. B*, 57(7):4843, 1996.
- [36] M. Nirmal, D. J. Norris, M. Kuno, M. G. Bawendi, Al. L. Efros, and M. Rosen. Observation of the "dark exciton" in cdse quantum dots. *Phys. Rev. Lett.*, 75(20):3728, 1995.
- [37] Ying Luo and Lin-Wang Wang. Electronic structures of the cdse/cds core-shell nanorods. *ACS Nano.*, 4(1):91–98, 2010.
- [38] M. P. Halsall, J. E. Nicholls, J. J. Davies, P. J. Wright, and B. Cockayne. Photoluminescence studies of cds/cdse wurtzite superlattices; evidence for large piezoelectric effects. *Surf. Sci.*, 228(1):41–44, 1990.
- [39] W. Langbein, M. Hetterich, and C. Klingshirn. Many-body effects and carrier dynamics in cdse/cds stark superlattices. *Phys. Rev. B*, 51:9922–9929, 1995.
- [40] C. d. M. Donega. Synthesis and properties of colloidal heteronanocrystals. *Chem. Soc. Rev.*, 4:1512, 2011.
- [41] A. G. del Aguila, B. Jha, F. Pietra, E. Groeneveld, C. de Mello Donega, J. C. Maan, D. Vanmaekelbergh, and P. C. M. Christianen. Observation of the full exciton and phonon fine structure in cdse/cds dot-in-rod heteronanocrystals. *ACS Nano.*, 8(6):5921–5931, 2014.
- [42] G. Raino, T. Stoferle, I. Moreels, R. Gomes, Z. Hens, and R. F. Mahrt. Controlling the exciton fine structure splitting in cdse/cds dot-in-rod nanojunctions. *ACS Nano.*, 6(3):1979–1987, 2012.

- 
- [43] A. Shabaev, A. V. Rodina, and A. L. Efros. Fine structure of the band-edge excitons and trions in cdse/cds core/shell nanocrystals. *Phys. Rev. B*, 86:205311(14), 2012.
- [44] Mark Fox. *Quantum Optics*. Oxford University Press, 2011.
- [45] A. Naeem, F. Masia, S. Christodoulou, I. Moreels, P. Borri, and W. Langbein. Giant exciton oscillator strength and radiatively limited dephasing in two dimensional platelets-supplement. *Phys. Rev. B*, 91:121302(5), 2015.
- [46] W. Langbein, J. M. Hvam, and R. Zimmermann. Time-resolved speckle analysis: A new approach to coherence and dephasing of optical excitation in solids. *Phys. Rev. Lett.*, 82(5):1040–1043, 1999.
- [47] G. Kocherscheidt, W. Langbein, G. Mannarini, and R. Zimmermann. Spectral speckle analysis of resonant secondary emission from solids. *Phys. Rev. B*, 66:161314 (1–4), 2002.
- [48] D. Gammon, E. S. Snow, B. V. Shanabrook, D. S. Katzer, and D. Park. Homogeneous linewidth in the optical spectrum of a single gallium arsenide quantum dot. *Science*, 273:87–89, 1996.
- [49] M. Bayer and A. Forchel. Temperature dependence of the exciton homogeneous linewidth in ingaas/gaas self-assembled quantum dots. *Phys. Rev. B*, 65:041308 (1–4), 2002.
- [50] S. T. Cundiff. Coherent spectroscopy of semiconductors. *Opt. Express*, 16:4639–4664, 2008.
- [51] W. Langbein. Coherent optical spectroscopy of semiconductor nanostructures. *Rivista del nuovo cimento*, 33:255–312, 2010.
- [52] P. Borri. *Coherent light-matter interaction in semiconductor quantum dots*. PhD thesis, Dortmund, 2003.
- [53] A. E. Siegman. *Lasers*. Oxford, 1986.
- [54] N. Accanto, F. Masia, I. Moreels, Z. Hens, W. Langbein, and P. Borri. Engineering the spin-flip limited exciton dephasing in colloidal cdse/cds quantum dots. *ACS Nano*, 6:5227, 2012.
- [55] F. Masia, W. Langbein, and P. Borri. Multiphoton microscopy based on four-wave mixing of colloidal quantum dots. *Appl. Phys. Lett.*, 93:021114 (3), 2008.
- [56] F. Masia, W. Langbein, P. Watson, and P. Borri. Resonant four-wave mixing of gold nanoparticles for three-dimensional cell microscopy. *Opt. Lett.*, 34:1816–1818, 2009.
- [57] F. Masia, W. Langbein, and P. Borri. Measurement of the dynamics of plasmons inside individual gold nanoparticles using femtosecond phase-resolved microscope. *Phys. Rev. B*, 85:235403 (11), 2012.
- [58] F. Masia, W. Langbein, and P. Borri. Polarization-resolved ultrafast dynamics of the complex polarizability in single gold nanoparticles. *Phys. Chem. Chem. Phys.*, 15:4226–4232, 2013.
-

- [59] J. Yang, J. S. Son, J. h. Yu, J. Joo, and T. Hyeon. Advwells in the colloidal synthesis of two-dimensional semiconductor nanoribbons. *Chem. Mater.*, 25:1190–1198, 2013.
- [60] R. Benchamekh, N. A. Gippius, J. Even, M. O. Nestoklon, J. M. Jancu, S. Ithuria, B. Dubertret, Al. L. Efros, and P. Voisin. Tight-binding calculations of image-charge effects in colloidal nanoscale platelets of cdse. *Phys. Rev. B*, 89:035307, 2014.
- [61] M.D. Tessier, C. Javaux, I. Maksimovic, V. Loriette, and B. Dubertret. Spectroscopy of single cdse nanoplatelets. *ACS Nano*, 6(8):6751, 2012.
- [62] E. Baghani, S. K. O Leary, I. Fedin, D. V. Talapin, and M. Pelton. Auger-limited carrier recombination and relaxation in cdse colloidal quantum wells. *J. Phys. Chem. Lett.*, 6:1032–1036, 2015.
- [63] C. Bouet, M. D. Tessier, S. Ithuria, B. Mahler, B. Nadal, and B. Dubertret. Flat colloidal semiconductor nanoplatelets. *Chem. Mater.*, 25:1352–1271, 2013.
- [64] M. D. Tessier, L. Biadala, C. Bouet, S. Ithurria, B. Abecassis, and B. Dubertret. Phonon line emission revealed by self-assembly of colloidal nanoplatelets. *ACS Nano*, 7(4):3332–3340, 2013.
- [65] S. Ithuria and D. V. Talapin. Colloidal atomic layer deposition (c-ald) using self-limiting reactions at nanocrystal surface coupled to phase transfer between polar and nonpolar media. *J. AM. CHEM. SOC.*, 134:18585–18590, 2012.
- [66] E. Cassette, B. Mahler, J-M. Guigner, G. Patriarche, B. Dubertret, and T. Pons. Colloidal cdse/cds dot-in-olate nanocrystals with 2d-polarized emission. *ACS Nano*, 6(8):6741–6750, 2012.
- [67] Z. Chen, B. Nadal, B. Mahler, H. Aubin, and B. Dubertret. Quasi-2d colloidal semiconductor nanoplatelets for narrow electroluminescence. *Adv. Funct. Mater.*, 24:295–302, 2014.
- [68] Iwan Moreels and Sotirios Christodoulou. Istituto italiano di tecnologia, via morego 30, it-16163 genova, italy.
- [69] K. Leosson, J.R. Jensen, W. Langbein, and J.M. Hvam. Exciton localization and interface roughness in growth interrupted gaas/alas quantum wells. *Phys. Rev. B*, 61:10322, 2000.
- [70] R.F. Schnabel, R. Zimmermann, D. Bimberg, H. Nickel, R. Losch, and W. Schlapp. Influence of exciton localization on recombination line shapes: Ingaas/gaas quantum wells as a model. *Phys. Rev. B*, 46(15):9873–9876, 1992.
- [71] A. Pasquarello and L. C. Andreani. Variational calculation of fano linewidth: Application to excitons in quantum wells. *Phys. Rev. B*, 44(7):3162–3167, 1991.
- [72] B. R. Nag. *Physics of Quantum Well Devices*. Springer Science and Business Media, 2001.
- [73] <http://hyperphysics.phy-astr.gsu.edu/hbase/atmos/blusky.html>. online.

- 
- [74] S Adachi. *Handbook on Physical Properties of Semiconductors*, volume 3. Kluwer Academic, 2004.
  - [75] R. W. Schoenlein, D. M. Mittelman, J. J. Shiang, and A. P. Alivisatos. Investigation of femtosecond electronic dephasing in cdse nanocrystals using quantum-beat-suppressed photon echoes. *Phys. Rev. Lett.*, 70(7):1014–1017, 1993.
  - [76] V. N. Gladilin, S. N. Klimin, V. M. Fomin, and J. T. Devreese. Optical properties of polaronic excitons in stacked quantum dots. *Phys. Rev. B*, 69:155325 (1–5), 2004.
  - [77] W. Langbein, C. Mann, U. Woggon, M. Klude, and D. Hommel. Radiative coupling of excitons in znse double quantum wells. *Phys. Status Solidi A*, 190:861–866, 2002.
  - [78] H. P. Wagner, A. Schatz, R. Maier, W. Langbein, and J. M. Hvam. Interaction and dephasing of center-of-mass quantized excitons in wide quantum wells. *Phys. Rev. B*, 57(3):1791–1796, 1998.
  - [79] L. C. Andreani. *Confined Electrons and Photon: New Physics and Applications*. Plenum, 1995.
  - [80] L. C. Andreani, G. Panzarini, and J. M. Gerard. Strong-coupling regime for quantum boxes in pillar microcavities: Theory. *Phys. Rev. B*, 60:13276, 1999.
  - [81] M. G. Lupo, F. Scotognella, M. Zavelani-Rossi, G. Lanzani, L. Mannac, and F. Tassone. Band edge ultrafast pump probe spectroscopy of core/shell cdse/cds rods: assessing electron delocalization by effective mass calculations. *Phys. Chem. Chem. Phys.*, 14:7420–7426, 2012.
  - [82] C. B. Murray, D. J. Norris, and G. Bawendi. Synthesis and characterization of nearly monodisperse cde (e = s, se, te) semiconductor nanocrystalites. *J. AM. CHEM. SOC.*, 115:8706–8715, 1993.
  - [83] U. E. H. Laheld and G. T. Einevoll. Excitons in cdse quantum dots. *Phys. Rev. B*, 55:5184–5204, 1996.
  - [84] A. Vagov, V. M. Axt, and T. Kuhn. Impact of nanoplatelets on the nonlinear optical response of single quantum dots and dot ensembles. *Phys. Rev. B*, 67:115338 (16), 2003.
  - [85] P. Borri, W. Langbein, U. Woggon, V. Stavarche, D. Rueter, and A. D. Wieck. Exciton dephasing via phonon interaction in nanocrystal quantum dots: Dependence on quantum confinement. *Phys. Rev. B*, 71:115328, 2005.
  - [86] A. Zunger, M. Califano, A. Franceschetti. Lifetime and polarization of the radiative decay of excitons, biexcitons, and trions in cdse nanocrystal quantum dots. *Phys. Rev. B*, 75:115401(7), 2007.
  - [87] R. Everson. Scanning probe microscopy of semiconductor quantum dots. Master’s thesis, Cardiff University, 2012.
  - [88] [www.nanoscience.com](http://www.nanoscience.com). Online.
  - [89] [probe.olympus-global.com](http://probe.olympus-global.com). Online.
-

- [90] Yongho Seo and Wonho Jhw. Electrostatic force microscopy using a quartz tuning fork. *Applied Physics Letters*, 80(23):4324–4326, 2002.
- [91] H. Edwards, L. Taylor, and W. Duncan. Fast, high-resolution atomic force microscopy using a quartz tuning fork as actuator and sensor. *Journal of Applied Physics*, 82(3):980–984, 1997.
- [92] T. Melin, M.Zdrojek, and D. Brunel. Electrostatic force microscopy and kelvin force microscopy as a probe of the electrostatic and electronic properties of carbon nanotubes. *Scanning Probe Microscopy in Nanoscience and Nanotechnology*, 14-16, 2010.
- [93] J. Rychen, T. Ihn, P. Studerus, A. Herrmann, and K. Ensslin. A low-temperature dynamic mode scanning force microscope operating in high magnetic fields. *Review of Scientific Instruments*, 70:2765–2768, 1999.
- [94] J. Rychen. *Combined Low-Temperature Scanning Probe Microscopy and Magneto-Transport Experiments for the Local Investigation of Mesoscopic Systems*. PhD thesis, Swiss Federal Institute of Technology Zürich.
- [95] J. Jersch, T. Maletzky, and H. Fuchs. Interface circuits for quartz crystal sensors in scanning probe microscopy applications. *Review of Scientific Instruments*, 77:083701, 2006.
- [96] A. Castellanos-Gomez, N. Agraït, and G. Rubio-Bollinger. Carbon fibre tips for scanning probe microscopy based on quartz tuning fork force sensors. *Nanotechnology*, 21:145702, 2010.
- [97] Unlocking the phase lock loop- part1 [www.complextoreal.com](http://www.complextoreal.com). Online.
- [98] <http://www.bruker-axs.com>. Online, June 2012.